JAERI-Conf
95-008

INDC(JPN)-173/U

PROCEEDINGS OF THE 1994 SYMPOSIUM ON NUCLEAR DATA

November 17-18, 1994, JAERI, Tokai, Japan

March 1995

(Eds.) Masayoshi KAWAI* and Tokio FUKAHORI

日本原子力研究所
Japan Atomic Energy Research Institute

本レポートは，日本原子力研究所が不定期に公刊している研究報告書です。
入手の問合わせは，日本原子力研究所技術情報部情報資料課（〒319-11 茨城県那珂郡東海村）あて，お申し越しください。なお，このほかに財団法人原子力弘済会資料センター（〒319-11 茨城県那珂郡東海村日本原子力研究所内）で複写による実費頒布をおこなっております。

This report is issued irregularly.
Inquiries about availability of the reports should be addressed to Information Division, Department of Technical Information, Japan Atomic Energy Research Institute, Tokai-mura, Naka-gun, Ibaraki-ken 319-11, Japan.

編集兼発行　日本原子力研究所
印　　刷　いばらき印刷㈱

JAERI-Conf 95-008

Proceedings of the 1994 Symposium on Nuclear Data
November 17-18, 1994, JAERI, Tokai, Japan

(Eds.) Masayoshi KAWAI* and Tokio FUKAHORI

Japanese Nuclear Data Committee
Tokai Research Establishment
Japan Atomic Energy Research Institute
Tokai-mura, Naka-gun, Ibaraki-ken

(Received February 22, 1995)

The 1994 Symposium on Nuclear Data was held at Tokai Research Establishment, Japan Atomic Energy Research Institute (JAERI), on 17th and 18th of November, 1994. This symposium was organized by Japanese Nuclear Data Committee and Nuclear Data Center, JAERI. In the oral sessions, presented were 15 papers on nuclear data research in Bangladesh, nuclear data for actinoids, integral testing of JENDL-3.2, nuclear reaction theory, nuclear data needs in material science application and topics on measurement of fission neutron multiplicity, IFMIF Project and nuclear structure data evaluation. In the poster session, presented were 34 papers concerning experiments, evaluations and benchmark tests on nuclear data. All of the 49 papers are compiled in the proceedings.

Keywords: Nuclear Data, Symposium, Proceedings, Nuclear Reaction, Theory, Actinoid, JENDL-3.2, Material Science, IFMIF Project, Nuclear Structure Data, Experiment, Evaluation, Benchmark Tests, Neutron, Proton, Cross Section, Fission

---

* Toshiba Corporation

JAERI-Conf 95-008

1994年核データ研究会報文集

1994年11月17日～18日、日本原子力研究所、東海村

日本原子力研究所東海研究所
シグマ研究委員会
（編）川合　將義*・深堀　智生

（1995年２月22日受理）

1994年核データ研究会が、1994年11月17日と18日の両日、日本原子力研究所東海研究所において開催された。この研究会は、日本原子力研究所のシグマ研究委員会と核データセンターが主催して開いたものである。口頭発表では、バングラデシュにおける核データ研究、アクチニドの核データ、ＪＥＮＤＬ-3.2の積分テスト、核反応理論、材料研究からの核データニーズ、トピックスとして核分裂中性子数の測定、ＩＦＭＩＦ計画と核構造核データ評価活動の15件の報告があった。ポスター発表では、34件の発表があり、それらは、核データの測定、評価や評価済み核データのベンチマークテストに関するものであった。本報文集は、それら全部で49件の論文をまとめたものである。

東海研究所：〒319－11　茨城県那珂郡東海村白方字白根２－４
＊（株）東芝

Program Committee

Masayoshi KAWAI (Chairman)	Toshiba Corporation
Satoshi CHIBA	Japan Atomic Energy Research Institute
Tokio FUKAHORI	Japan Atomic Energy Research Institute
Tetsuo IGUCHI	University of Tokyo
Hideki IIMURA	Japan Atomic Energy Research Institute
Shin IWASAKI	Tohoku University
Yutaka NAKAJIMA	Japan Atomic Energy Research Institute
Shigeaki OKAJIMA	Japan Atomic Energy Research Institute
Makoto SASAKI	Mitsubishi Atomic Power Industries, Inc.
Etsuro SAJI	Toden Software Inc.
Naoki YAMANO	Sumitomo Atomic Energy Industries, Ltd.

プログラム委員会

川合　將義（委員長）	（株）東芝
千葉　敏	日本原子力研究所
深堀　智生	日本原子力研究所
井口　哲夫	東京大学
飯村　秀紀	日本原子力研究所
岩崎　信	東北大学
中島　豊	日本原子力研究所
岡嶋　成晃	日本原子力研究所
佐々木　誠	三菱原子力工業（株）
佐治　悦郎	東電ソフトウェア（株）
山野　直樹	住友原子力工業（株）

Contents

目　　次

1. Preface

The 1994 symposium on nuclear data was held at Tokai Research Establishment, Japan Atomic Energy Research Institute (JAERI), on 17th and 18th of November, 1994. The symposium was organized by Japanese Nuclear Data Committee and Nuclear Data Center, JAERI. The program of the symposium is listed below. In the first oral session, an invited speak was made on nuclear data research in Bangladesh together with the 3 presentations on nuclear data for actinoids. In the other sessions, total 10 papers were presented on integral testing of JENDL-3.2, nuclear reaction theory, nuclear data needs in material science application and topics on measurement of fission neutron multiplicity, IFMIF Project and nuclear structure data evaluation. In the poster session, presented were 34 papers concerning nuclear data experiments, evaluations and benchmark tests on nuclear data. All of the 49 papers and summary talk are compiled in this proceedings.

Program

Oral Presentation ([Presentation(min.)+Discussion(min.)])

Nov. 17 (Thu.)

9:45～ 9:55　1. Opening Address　H. Yoshida(JAERI)

9:55～11:55　2. Topics (1)　Chairman: Y.Kikuchi(JAERI)

2.1 Nuclear Data Activity at Atomic Energy Research Establishment, Savar, Dhaka [25+5]　N.I. Molla(INST)

2.2 Actinide Nuclear Data Evaluation for BROND and Beyond [25+5]　V.M. Maslov(RPCPI)

2.3 Calculations of Nuclear Data for the Reactions of Neutrons and Protons with Heavy Nuclei at Energies from 1 MeV up to 2 GeV [25+5]　V.A. Konshin(JAERI)

2.4 Inelastic Interaction of Neutrons with Actinide Nuclei Studied by Means of High Resolution Gamma-Spectroscopy in Neutron Beam [25+5]　A.A.Filatenkov(KRI)

11:55～13:00　lunch

13:00～14:30　3. Integral Testing of JENDL-3.2 (1)　Chairman: A. Zukeran(Hitachi)

3.1 Benchmark Tests of JENDL-3.2 for Thermal and Fast Reactors [50+10]
H. Takano(JAERI)

3.2 Measurement and Analysis of ^{238}U Capture to ^{239}Pu Fission Rate Ratio at Fast Critical Assembly [25+5] T. Sakurai(JAERI)

14:30～15:00 4. Integral Testing of JENDL-3.2 (2) Chairman: M. Nakagawa(JAERI)

4.1 Usage of JENDL Dosimetry File for Material Dosimetry in JOYO [25+5]
S. Suzuki(PNC)

15:00～15:15 coffee break

15:15～16:15

4.2 Integral Data Testing of JENDL-3.2 for Fusion Reactor and Shielding Applications [50+10] Y. Oyama(JAERI)

16:15～18:00 5. Nuclear Reaction Theory Chairman: Y. Watanabe(Kyushu Univ.)

5.1 Quantum and Statistical Theories for Nuclear Reaction [50+10]
M. Kawai(Kyushu Univ.)

5.2 Analysis of the Nucleon-induced Nuclear Reactions by the Quantum Molecular Dynamics [40+5] S. Chiba(JAERI)

18:15～20:15 Reception at Akogi-ga-ura Club

Nov. 18 (Fri.)

9:10～11:10 6. Poster Session

1～22 : Lobby of Main Seminar Room

23～34 : Meeting Room No.5

11:10～11:55 7. Topics (2) Chairman: T. Osawa(Kinki Univ.)

7.1 Measurement of $\nu(m^*)$ for Thermal Neutron Induced Fission of ^{239}Pu [40+5]
K. Nishio(Kyoto Univ.)

11:55～13:00 lunch

13:00～15:00 8. Nuclear Data Needs from Non-energetic Fields (Material Science Research) Chairman: I. Kimura(Kyoto Univ.)

8.1 Cold Neutron Production and its Application [50+10] M. Furusaka(KEK)

8.2 Radiation Damage Study of Materials [50+10] N. Sekimura(Univ. of Tokyo)

15:00～16:20 9. Topics (3) Chairman: N. Kishida(CRC Research Institute)

9.1 Fusion Materials Irradiation Facility - IFMIF Program - [45+5]
K. Noda(JAERI)

9.2 Japanese Activity on Nuclear Structure Data Evaluation [25+5]
K. Kitao(Data Engineering)

16:20～16:35 10. Summary Talk A. Takahashi(Osaka Univ.)

Poster Session

9:10-11:10 on Nov. 18 at Lobby and Meeting Room No.5 in Research Bldg. 1

1 Precise Measurement of Neutron Total Cross Sections of Pb-208 and Pb-nat
K. Kobayashi(Kyoto Univ.)

2 Measurements of keV-Neutron Capture γ Rays of Fission Products
M. Igashira(TIT)

3 Sensitivity Analysis of JENDL-3.2 in Fast Reactor
T. Takeda and T. Kitada(Osaka Univ.)

4 Analysis of Reaction Rate Ratio C8/F (^{238}U Capture/Total Fission) by using the JENDL-3.2
K. Nakajima(JAERI)

5 Evaluation of Prompt Neutron Spectra for Actinides
T. Ohsawa(Kinki Univ.)

6 Semi Classical Model of the Neutron Resonance Compound Nucleus
M. Ohkubo(JAERI)

7 Measurements of Double Differential Charged Particle Emission Cross Sections by Incident D-T Neutrons
T. Kondoh, A. Takahashi (Osaka Univ.) and
H. Nishizawa (Mitsubushi Electric Co.)

8 Measurement of Neutron-induced Charged-particle Emission Cross Sections
M. Baba, I. Matsuyama, T. Sanami, S. Matsuyama,
T. Kiyosumi, Y. Nauchi and N. Hirakawa(Tohoku Univ.)

9 Measurement of Double-differential Neutron Emission Cross Sections of Fe and Nb for 11.5 MeV Neutrons
S. Matsuyama, D. Soda, M. Baba, M. Ibaraki,
Y. Nauchi, S. Iwasaki and N. Hirakawa(Tohoku Univ.)

10 Measurement of Helium Production Cross Section with Helium Accumulation Method
Y. Takao, Y. Kanda, K. Yamaguchi, T. Yonemoto, H. Etoh and M. Miwa(Kyushu Univ.)

11 Measurement of Activation Cross-sections for Several Elements between 12 and 20 MeV
S. Iwasaki, S. Matsuyama, T. Ohkubo, H. Fukuda, M. Sakuma and M. Kitamura(Tohoku Univ.)

12 Measurement of (p,p') Spectra from Boron Isotopes
N. Koori, K. Ichiba(Tokushima Univ.), Y. Watanabe, H. Shinohara, T. Michibata, H. Ijiri, K. Sagara, H. Nakamura, K. Maeda and T. Nakashima(Kyushu Univ.)

13 Benchmark Test of JENDL-3.2 with Pulsed Sphere Experiment at OKTAVIAN
C. Ichihara(Kyoto Univ.), S. Hayashi(Rikkyo Univ.), J. Yamamoto(Setsunan Univ.), I. Kimura(Kyoto Univ.) and A. Takahashi(Osaka Univ.)

14 Suprathermal Fusion Reactions in Laser-imploded D-T Pellets: Applicability to Pellet Diagnosis and Necessity of Nuclear Data
Y. Tabaru, Y. Nakao, H. Nakashima and K. Kudo (Kyushu Univ.)

15 Systematics of Activation Cross Sections around 14 MeV Neutrons
Y. Kasugai, H. Yamamoto, K. Kawade(Nagoya Univ.) and Y. Ikeda(JAERI)

16 Measurement of Beta-decay Half-lives of Short-lived Nuclei by Using High-Rate Spectroscopy Amplifier
S. Ito, M. Yasuda, H. Yamamoto, K. Kawade(Nagoya Univ.), T. Iida and A. Takahashi(Osaka Univ.)

17 Measurement of Formation Cross Section Producing Short-lived Nuclei by 14 MeV Neutrons - Na, Si, Te, Ba, Ce, Sm, W, Os
Y. Satoh, T. Matsumoto, Y. Kasugai, H. Yamamoto, K. Kawade (Nagoya Univ.), A. Takahashi and T. Iida (Osaka Univ.)

18 Measurement of C(n,z) Reaction Double Differential Cross Section at 40 and 64 MeV
T. Kiyozumi, M. Baba, T. Iwasaki, T. Sanami, S. Matsuyama, N. Hirakawa, T. Nakamura(Tohoku Univ.), Su. Tanaka, H. Nakashima, S. Meigo and Sh. Tanaka(JAERI)

2. Papers Presented at Oral Session

2. 1 International Session

2. 1. 1 Nuclear Data Activity at Atomic Energy Research Establishment, Savar, Dhaka

S.I. Bhuiyan, and N.I. Molla

Institute of Nuclear Science & Technology
Atomic Energy Research Establishment
Ganakbari, Savar, G.P.O. Box 3787
Dhaka, Bangladesh.

ABSTRACT

The nuclear data activity at AERE, Savar is briefly presented in this paper. Major thrust is on the customization of cross section libraries for general purpose reactor and shielding calculations. The processing codes that are available are NJOY91.91, some AMPX-Modules and the modules in SCALE-PC. Recent measurements on cross section data over the energy range 13-15 MeV at the Institute of Nuclear Science & Technology have been reviewed. Measurements and calculations are based on the determination of excitation functions of neutron induced reactions on the elements and isotopes of FRT-relevant structural materials.

1. INTRODUCTION

Nuclear Data is the most essential fundamental infrastructure for any country having nuclear program. With this philosophy in mind Bangladesh Atomic Energy Commission has initiated a modest activity in the field of Nuclear Data with the following principal objectives: (i) Preparation of Processed Nuclear Data Libraries for Research Reactor, LWRs and Shielding calculations. (ii) Generation of a fine group pseudo-problem-independent cross-section library based on basic data files such as JENDL3, ENDF/B-VI, JEF2, etc. that can be used in radiation transport applications. (iii) Customization of problem dependent coupled Neutron-Photon Multi-groups cross section libraries to interface with specific neutronic codes. (iv) Production of few-group group constants for general purpose reactor analysis, global reactor calculations and safety parameters studies. (v) Verification and validation of LWR calculation Methods, Processing Code Systems and the major basic data files JENDL, ENDF, and JEF. (vi) Measurements of 14 MeV Neutron cross section by Activation Technique.

The overall scheme for this data activity is summarized in Fig.1. In the process of shielding library production, care will be taken to serve the interest of the Fast and Fusion reactor community.

Some activities on these six areas are very briefly presented in this paper.

2. THE PROCESSING CODE SYSTEM

(a) NJOY91.91: The state-of-the-Art comprehensive computer Code Package NJOY91.91[1] is available at AERE, Savar. The basic nuclear data libraries (such as JENDL3,

ENDF/B-V, JEF-2, etc.) represent the underlying nuclear data from physics view point, but practical calculations usually require special job libraries for particle transport codes or reactor core physics codes. This is the mission of NJOY - to take the basic data from the nuclear data library and convert it into the forms needed for applications. The NJOY code consists of a set of modules, each a self-standing code, performing a well defined processing task. They are linked to one another by input and output files and a few common constants. The modules are as follows:

NJOY / RECONER / BROADR / UNRESR / HEATR / THERMR / GROUPR GAMINR / ERRORR / COVR / MODER / DTFR / CCCCR / MATXSR / RESXS ACER / POWR / WIMSR / PLOTR / MIXR / PURR.

(b) Organisation of Pseudo-AMPX System: We developed a system with limited capability in our IBM 4341 main frame computer which we named Pseudo-AMPX System[2-3] (Fig.2). The system is automated and has ten AMPX-modules operating under a driver control. A procedure permits any number of modules of the system to be executed in a single job step. The modules are:

AIM / AJAX / BONAMI-S / CHOX / NITAWL / MALOCS / RADE / DIAL / ALPO

Some locally developed modules has been added to the system as can be seen in Fig.2. This work was performed in close cooperation with RSIC, ORNL, USA.

(c) SCALE-PC: This system performs criticality Safety Analysis Sequences and includes the following processing modules:

BONAMI / NITAWL-II / XSDRNPM / ICE / AIM

3. SOME RECENT NUCLEAR DATA ACTIVITIES

(a) Generation of a library for 3-MW TRIGA Mark-II Research Reactor and validation through core and Safety Parameter Studies.

A data base is generated[4-5] for the 3-MW TRIGA MARK-II research reactor in Bangladesh. The library is created using the WIMS-D/4 code. Cross sections are calculated from zero burnup to 37% of initial ^{235}U in 20 burnup steps. The created TRIGA library is tested through practical calculations and is compared with experimental values or with values in the Safety Analysis Report (SAR). Excess reactivity of the fresh core configuration is measured and determined to be 10.27$, while a value of 10.267$ is obtained using the generated library. By choosing burnup steps of 0, 50, 350, and 750 MWh, the whole operating history is covered. The calculated temperature defect at 1 and 3 MW is 1.15 and 3.59$ compared with the experimental values of 1.02 and 3.64$, respectively. The xenon value obtained at 1 and 3 MW is 2.21 and 3.20$, respectively, compared with 3.57$ at 3 MW in the SAR. The TRIGA code with its new library is used for calculating fast and thermal flux distributions and were found close to values from the SAR. The temperature coefficient of LEU fuel calculated for three different burnup steps shows good agreement with SAR. Total peaking factors calculated as products of axial, radial, and hot rod peaking factors for four configurations are: (a) the compact core with graphite reflector, 3.15; (b) the same core with water reflector, 3.39; (c) the core with a central thimble, graphite reflector, 5.01; and (d) the same core with a water

reflector, 5.29. In the SAR, the total peaking factor for the compact core is 3.5 and with a central thimble, 5.63. Excellent agreement between calculations and measurements establishes the validity of the library. Figs. 3 and 4 show the performance of the generated library using TRIGA experiment as benchmark.

(b) The Effect of Bound and Free Hydrogen Cross Section on Fuel Temperature Reactivity Co-efficient of 3MWt TRIGA Research Reactor.

We have studied the fuel temperature reactivity co-efficient, as function of burnup and temperature[6]. Also considerable efforts were made to study the effect of processing the hydrogen cross section on fuel temperature reactivity coefficient, α_f. The fuel meat of TRIGA Mark II Research Reactor contains zirconium hydride as the principal moderator. This needs some special treatment in the cross section preparation. First we calculated α_f considering the cross section of hydrogen as in zirconium hydride. Then α_f was calculated considering the cross section of hydrogen as in water. It was found that the use of these two cross sections yield entirely different fuel temperature characteristics, specially in lower temperature region. Fig. 5 shows the variations of α_f at different temperatures. The same type of discrepancy has been found at other burn up steps, 1000 MWd and 2000 MWd also.

(c) WIMS Library update project:

The WIMS is one of the most widely used general purpose thermal reactor analysis code. Several deficiencies of WIMS library were observed by the users: (i) the cross section library is based on old nuclear data (ii) several nuclides, typical for power and research for power and research reactor calculations are absent in the library (iii) Errors in some of the very important resonance integrals like ^{238}U. (iv) absence of the self-shielding effect of resonance scattering cross section. After a development period of 10-15 years, the availability of several recent evaluated improved basic nuclear data files, such as: ENDF/B-VI, and JENDL-3 offer the possibility of improving the WIMS data library. IAEA Nuclear Data Section has taken an initiative to perform the task of coordinating a number research laboratories from different countries to up-date the WIMS 69-group cross section library.

Bangladesh is participating in this project and has contributed the following:

The definition of the integral parameters which are compared to the measured values are as follows:

k	infinite medium multiplication factor,
k_{eff}	finite medium effective multiplication factor,
ρ^{28}	ratio of epithermal to thermal ^{238}U capture,
δ^{25}	ratio of epithermal to thermal ^{235}U fission,
δ^{28}	ratio of ^{238}U fission to ^{235}U fission,
C^*	ratio of ^{238}U capture to ^{235}U fission.

The multiplication factor k_{eff} is the most important benchmark integral parameter. It comprises all reactor physics parameters of the problem geometry, isotopic composition, cross sections of all isotopes, spectrum etc. For this reason, it is very sensitive to the WIMS input modeling.

WIMS k_{eff} is overestimated for TRX-1 and BAPL-1 which are both rather tight lattices compared to TRX-2 and BAPL-3, where k_{eff} is underestimated. The dependence of the error in k_{eff} on latice pitch or fuel/water ratio either stems from the resonance calculation method in WIMS (Dancoff corrections), methods for the effective diffusion constant and leakage calculations or from the cross sections which are used in this calculations.

The influence of different input options is not so strong in the case of other benchmark parameters (ρ^{28}, δ^{28}, δ^{25}, C^*), as they depend only on the spectrum and on the particular isotope microscopic cross-sections.

The WIMS ρ^{28} is on average underestimated, indicating that the resonance cross-sections are probably underestimated, yielding overestimated k_{eff} in tight lattices, where the spectrum is harder and ρ^{28} is large. Going to lattices with a bigger lattice pitch (such as TRX-2 or BAPL-3), ρ^{28} becomes smaller and the error in the resonance integral becomes less important.

The conclusion that the epithermal and the resonance capture cross sections in WIMS U-238 data are incorrect which can not be definitely confirmed but it is consistent with the observed indications. Among them it is important to note that the epithermal capture of U-238 is underestimated also due to the definition of the U-238 absorption cross section in the WIMS library. Per definition, the (n, 2n) cross section is subtracted from the absorption cross section. The neutron balance and the total cross section are preserved by taking the extra neutron into account in the transfer matrix. However the definition affects the calculated reaction rates, where the complete absorption cross section should be used and is not available in the WIMS library.

(d) A comparative study of WIMS-Library group constants processed through NJOY'91 from ENDF/B-VI and JENDL-3 for ^{16}O, ^{56}Fe, ^{58}Ni, ^{27}Al, ^{11}B, & ^{9}Be.

In the context of the WIMS library update project, it is essential to investigate the group constants generated from ENDF/B-VI and JENDL-3 [7].

The output of the POWR module was processed by WIMSLIC[5] to produce the 69-group format WIMS library for the following elements: ^{16}O, ^{56}Fe, ^{58}Ni, ^{27}Al, ^{11}B, and ^{9}Be. Fig.6 shows how the used modules were linked for flow of data to prepare the WIMS library. The lethargy values were taken from GROUPR Run (MF-3, MT252) for the WIMSLIC Run. P_o cross section for 296° K have been investigated. The parameters that have been compared are Potential Scattering, slowing down power/Lethargy width, Transport cross sections, absorption cross sections, and group-to-group scattering matrices. The ratio of ENDF/B-VI and JENDL-3 and the percentage of deviations have been produced. The study reveals that the WIMS-library group constants generated from ENDF/B-VI and JENDL-3 have fairly good agreement with severe discrepancies in some cases under study. For ^{16}O the agreement is very good for all the parameters. Only the Σ_{tr} in fast group differs by 10%. For ^{56}Fe the overall agreement is good; in some fast groups the transport cross section differs with a maximum difference of 42%. ^{58}Ni have some bad disagreements in absorption cross section in the fast and resonance groups (maximum of 70% in group 13). ^{27}Al have very bad disagreement in the fast group absorption cross section (maximum 326% in group 5). A good agreement is observed in the group constants of ^{11}B except the fast group absorption cross section, where a disagreement as high as 225% can be seen in group 2. For ^{9}Be all the parameters show a very good agreement except

the fast group absorption cross section with maximum difference of 58% in group 1. In all the cases studied the scattering matrix both in the fast group and thermal groups do not show any significant disagreement. The reason for the consistent disagreement between ENDF/B-VI and JENDL-3 in the fast and resonance groups absorption cross section should be investigated further.

4. 14 MeV NEUTRON CROSS SECTION DATA MEASUREMENT

Measurement of cross section data for fast neutron induced reactions as a function of neutron energy are important for applications in fission and fusion reactor technology as well as validation support of nuclear model calculations. Keeping this aim in view we initiated and continued neutron cross section data measurements around 14MeV [8-13] with the technical assistance of IAEA and nuclear data group at Julich, FRG.

Activation technique is used in the cross section data measurements. High purity target materials, foils/power, together with neutron flux monitor foils are irradiated at different emission angles in a ring geometry arrangement over a period of several minutes to twelve hours. Neutrons are produced by the J-25 Neutron Generator using D-T reaction at 110 keV deuterons and beam current between 150-400 μA.

The effective neutron energies at the emission angles are verified by measuring the ratio of the ^{89}Zr to ^{92m}Nb specific activities induced both in Zr and Nb foils by (n,2n) reactions. Neutron fluences are measured by using ^{27}Al(n,α)^{24}Na and ^{93}Nb(n,2n)^{92m}Nb reactions. The radioactivity measurements for the reaction products are mainly based on the use of MCA based high resolution HPGe detector gamma ray spectrometry.

Excitation functions of the reactions measured over the energy range 13-15 MeV in the recent years are given in Table-1. Measured values, literature data[14-34] and the results obtained via nuclear model calculations on some reactions are shown as a function of neutron energy in Figs.7-20.

5. CONCLUDING REMARKS

The fundamental infrastructure for the Nuclear data processing, evaluation, generation of problem dependent library, and their validation through benchmark testing has been established in Bangladesh. At present we have limited capability to take part in the global nuclear data activity. In this stage collaboration with the advanced data analysis centers like, Nuclear Data Center, JAERI, Japan, will contribute significantly to promote our Nuclear data activity. The most important step to promote this activity will be to establish a regional nuclear data center for Asia and Pacific (ANDC) to meet the growing need of the region. It may be mentioned here that in a recent IAEA Technical Committee Meeting held in Dhaka such need was strongly felt and establishment of ANDC was recommended. Under the circumstances it is concluded and proposed that the Nuclear Data Center, JAERI may come forward to give leadership for the establishment of ANDC, under its own umbrella.

6. REFERENCES

1) R.E. MacFarlane, D.W.Muir and R.M. Boicourt, "NJOY91.91 - A Code System for Producing Pointwise and Multigroup Neutron and Photon Cross Sections from ENDF/B Evaluated Nuclear Data", Los Alamos National Laboratory, PSR-171, RSIC, ORNL, USA (Oct. 1993).

2) S.I. Bhuiyan, M. Musa, M. Alamgir, A.R. Khan, M. Rahaman, M.M. Sarker, Z.G. Ara and J.E. White, " Development of an Automated Modular System for Preparation of a Special Problem Dependent Customized Cross Section Library", Proc. Int. Sym. on Recent Advances in Physics, 15-19 Janurary, 1990, Dhaka, Bangladesh.

3) S.I. Bhuiyan, M. Musa, M. Alamgir, A.R. Khan, M. Rahaman, M.M. Sarker, Z.G. Ara and M.A. Mannan, " Organization of the Pseudo AMPX-System", Tech. Rep., AERE / TR-2, March 1993.

4) S .I. Bhuiyan et al ,"Generation of a Library for Research Reactor calculations and Some Application in the Core and Safety Parameters Studies of the 3MW TRIGA MARK II Research Reactor", Nuc. Tech., Vol. 97, 253 (1992).

5) S.I. Bhuiyan, A.R.Khan, M.M. Sarker, M. Rahman, Z.G.Ara, M. Musa, M.A.Mannan, and I. Mele, "Preperation of a Cross Section Library for 3 MW TRIGA Reactor and Validation Through Some Applications", Nuc. Data for Sci. & Tech., ISBN 0-387-55100-x Springer Verlag New York, (1992).

6) M.R. Sarder, S.I. Bhuiyan, M.Rahman, and M.M. Sarker,"The Effect of Bound and Free Hydrogen Cross Section on Fuel Temperature Reactivity Co-efficient of TRIGA Research Reactor," Proc. Int. Conf. on Nuc. Data for Sci. & Tech., May 9 - 13, 1994, USA (In press).

7) S.I. Bhuiyan, M. Rahman, M.R. Sarder, "A comparative study of WIMS-LIB Group Constant processed through NJOY'91 from ENDF/B-IV and JENDL3.1 for ^{16}O, ^{56}Fe, ^{58}Ni, ^{27}Al, ^{11}B and ^{9}Be", Proc. Int. Conf. on Nuc. Data for Sci. & Tech., May 9 - 13, 1994, USA (In press).

8) N.I. Molla, R.U. Miah, S. Basunia, M. Hossain and M. Rahman, Proc. Int. Conf. on Nuclear Data for Science and Technology, 9-13 May, 1994, Gatlinburg, USA (In press).

9) S.M. Qaim, M. Uhl, N.I. Molla and H. Liskien, Phys. Rev. C46, No.4, 1398 (1992).

10) N.I. Molla, S.M. Qaim, H. Kalka, Phys. Rev. C45 No.6, 3002 (1992).

11) N.I. Molla, S.M. Qaim and M. Uhl, Phys. Rev. C42, No.4, 1540 (1990).

12) N.I. Molla S. M. Qaim, H. Liskien and R. Widera, Applied Radiation and Isotopes, 42 No. 4, 337 (1991).

13) N.I. Molla, R.U. Miah and M. Rahman, Proc. Int. Conf. on Nuclear Data for Science and Technology, 13-17 May 1991, Julich, FRG P 355.

14) J. Csikai, S. Nagi, Nucl. Phys. A91, 222 (1967).

15) V. Levkovskii, et al. Sov. J. Nucl. Phys. 8, 4 (1969).

16) B.P. Bayhurst and R.J. Prestwood, J. Inorg. Nucl. Chem. 23, 173 (1961).

17) Y. Ikeda, C. Konno, K. Oishi, T. Nakamura, H. Miyade, K. Kawade, H. Yamamoto and T. Katoh, JAERI Report 1312, March 1988.

18) M. Bormann et al. Hand book on Nuclear Activation Cross Sections, IAEA Technical Report Series 156 (1974).

19) S.K. Ghorai et al. Nucl. Phys. A266, 53 (1976).

20) D.R. Nethway, Nucl. Phys. A190, 635 (1972).

21) Z. Wenrong et al. IAEA INDC(CPR)-16, Vienna (1989).

22) E.T. Bramlitt, R.W. Fink, Phys. Rev. 131, 2649 (1963).

23) Fujino et al. NEANDC(J)- 51U, 60 (1977).

24) Kanda et al. Nucl. Phys. A185, 177 (1972).

25) L. Husain, A. Bari and P.K. Kuroda, Phys. Rev. C1, 1233 (1970).

26) W. Lu et al. Phys. Rev. C1, 358 (1970).

27) S.M. Qaim and G. Stocklin, Proc. 8th Symp. on Fusion Technology, Norrdijkevhout, Netherland, EUR 5182e, 939 (1974).

28) H. Liskien, R. Wolfle, R. Widera and S.M. Qaim, Appl. Radiat. Isot. 41, 1, 83 (1990).

29) Amemiya et al. J. Nucl. Sci., and Tech., 19, 781 (1982).

30) P. Cuzzocrea et al. Ibid, A103, 616 (1967).

31) F. Fukuda et al. Report INDC(JAP)-420 (1978).

32) J. CSikai, Proc. of Symp. on Nuclear Data, Nov. 18-19, 1993, JAERI, Japan INDC(JPN)-169/L, P408.

33) A. Susumu, K. Ishibashi and T. Katoh, J. Nucl. Sci. and Tech., 19, 781 (1982).

34) Gerhard Erdmann, Neutron Activation tables vol.6 (1976).

Table 1. Excitation Functions of the Reactions Measured and Associated Decay Data Used in the Cross Section Calculations.

Reaction	Half-life	Gamma ray in keV (% abundance)	Reaction	Half-life	Gamma ray in keV (% abundance)
$^{45}Sc(n,2n)^{44g}Sc$	3.93 h	1157.0 (99.9)	$^{70}Zn(n,2n)^{69m}Zn$	13.90 h	438.9 (100)
$^{45}Sc(n,2n)^{44m}Sc$	58.60 h	271.4 (86.6)	$^{70}Ge(n,2n)^{69}Ge$	39.20 h	574.0 (11.8)
$^{45}Sc(n,\alpha)^{42}K$	12.36 h	1524.7 (18.8)	$^{72}Ge(n,\alpha)^{69m}Zn$	13.90 h	438.9 (100)
$^{45}Sc(n,p)^{45}Ca$	163.00 d	E_{β}^{-1} =258(100)	$^{74}Ge(n,\alpha)^{71m}Zn$	3.97 h	386.3 (93.0)
$^{47}Ti(n,p)^{47}Sc$	3.42 d	159.4 (70.0)	$^{76}Ge(n,2n)^{75}Ge$	82.80 m	264.8 (12.0)
$^{48}Ti(n,p)^{48}Sc$	43.70 h	983.3 (100.0)	$^{89}Y(n,2n)^{88}Y$	106.6 d	898 (93.0)
$^{51}V(n,\alpha)^{48}Sc$	43.70 h	983.3 (100.0)	$^{90}Zr(n,2n)^{89m}Zr$	4.18 m	587.8 (89.5)
$^{56}Fe(n,p)^{56}Mn$	2.58 h	846.6 (99.0)	$^{90}Zr(n,2n)^{89}Zr$	3.27 d	909.0 (99.0)
$^{59}Co(n,2n)^{58m+g}Co$	70.78 d	810.7 (99.4)	$^{90}Zr(n,p)^{90m}Y$	3.19 h	482.5 (90.0)
$^{59}Co(n,p)^{59}Fe$	44.60 d	1099.2 (56.5)	$^{90}Zr(n,\alpha)^{87m}Sr$	2.81 h	388.4 (83.0)
$^{59}Co(n,\alpha)^{56}Mn$	2.58 d	846.6 (99.0)	$^{94}Zr(n,p)^{94}Y$	19.0 m	918.2 (73.6)
$^{58}Ni(n,2n)^{57}Ni$	36.00 h	1377.6 (77.9)	$^{94}Zr(n,\alpha)^{91}Sr$	9.48 h	1024.3 (33.0)
$^{58}Ni(n,p)^{58m+g}Co$	70.78 d	810.7 (99.44)	$^{96}Zr(n,2n)^{95}Zr$	65.50 d	756.7 (54.6)
$^{58}Ni(n,n'p)^{57}Co$	271.65 d	122.0 (85.6)	$^{93}Nb(n,2n)^{92m}Nb$	10.13 d	934.5 (99.2)
$^{61}Ni(n,p)^{61}Co$	1.65 h	67.4 (90.0)	$^{93}Nb(n,\alpha)^{90m}Y$	3.19 h	482.5 (90.0)
$^{62}Ni(n,p)^{62}Co$	13.90 m	1172.9 (79.0)	$^{92}Mo(n,p)^{92m}Nb$	10.13 d	934.5 (95.5)
$^{65}Cu(n,2n)^{64}Cu$	12.74 h	511.0 (35.7)	$^{92}Mo(n,\alpha)^{89m}Zr$	4.18 m	587.8 (93.0)
$^{65}Cu(n,p)^{65}Ni$	2.52 h	1115.8 (15.1)	$^{92}Mo(n,\alpha)^{89m+g}Zr$	78.43 h	909.2 (99.0)
$^{65}Cu(n,\alpha)^{62g}Co$	13.90 m	1172.0 (99.0)	$^{94}Mo(n,2n)^{93m}Mo$	6.95 h	263.0 (56.7)
$^{64}Zn(n,2n)^{63}Zn$	38.50 m	669.6 (8.5)	$^{95}Mo(n,p)^{95m+g}Nb$	34.97 d	765.8 (99.0)
$^{64}Zn(n,p)^{64}Cu$	12.74 h	511.0 (35.7)	$^{96}Mo(n,p)^{96}Nb$	23.55 h	778.4 (97.0)
$^{68}Zn(n,\alpha)^{65}Ni$	2.52 h	1115.8 (15.1)	$^{97}Mo(n,p)^{97m+g}Nb$	73.60 m	657.9 (98.2)
			$^{98}Mo(n,\alpha)^{95}Zr$	65.5 d	756.7 (54.6)

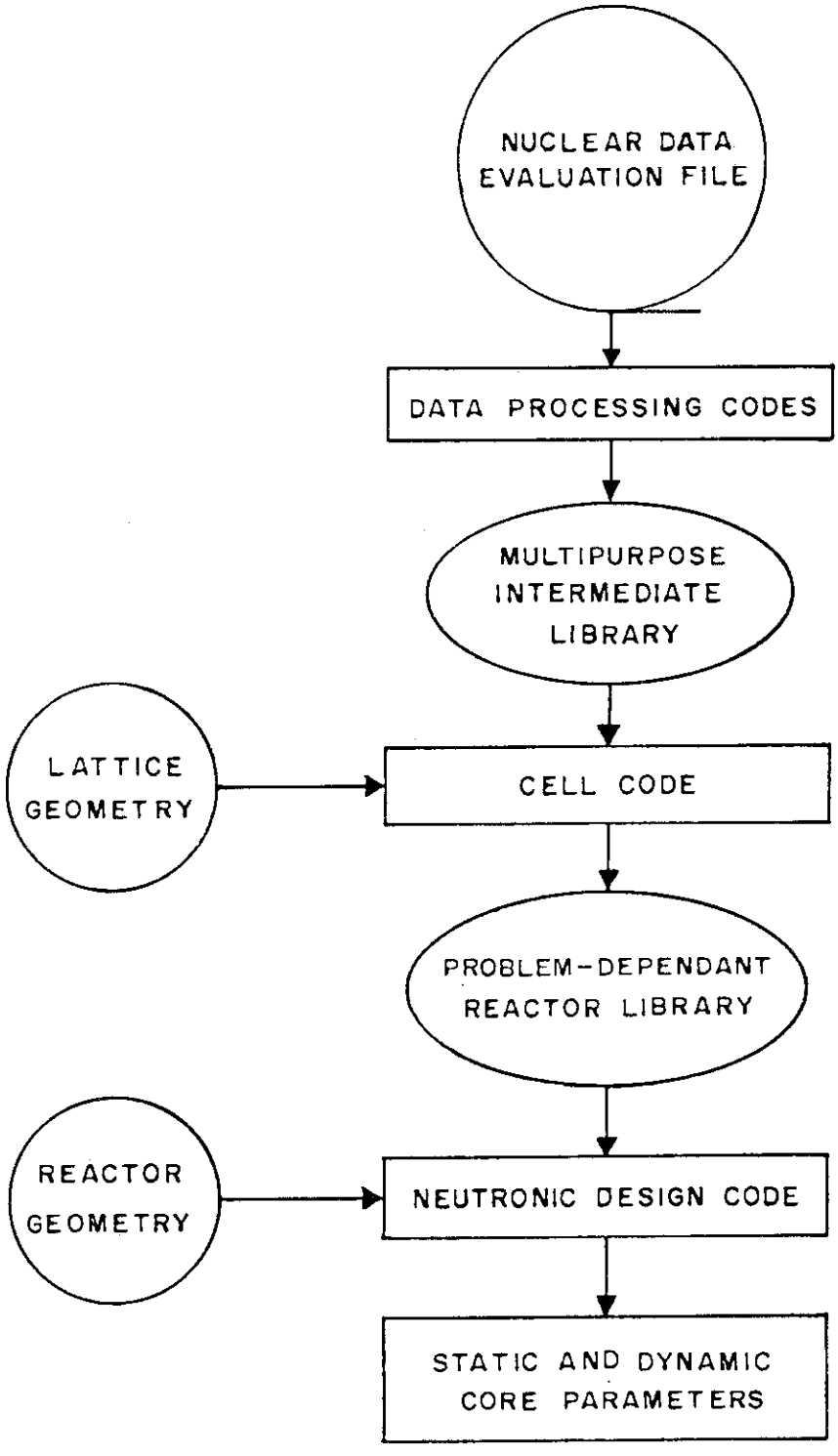

FIG. 1: FLOW-CHART OF THE NEUTRONIC DESIGN SCHEME.

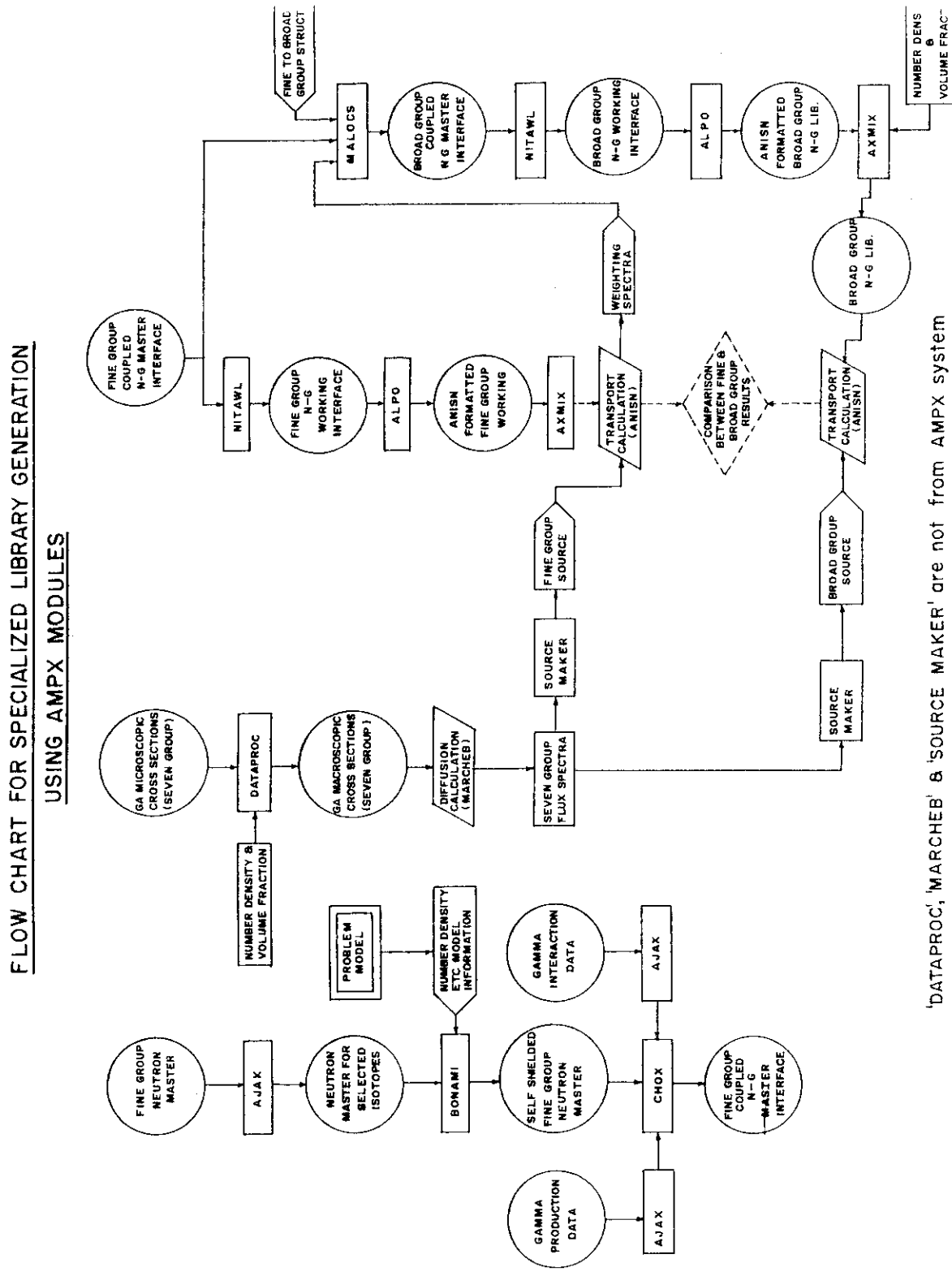

'DATAPROC', 'MARCHEB' & 'SOURCE MAKER' are not from AMPX system

FIG. 2

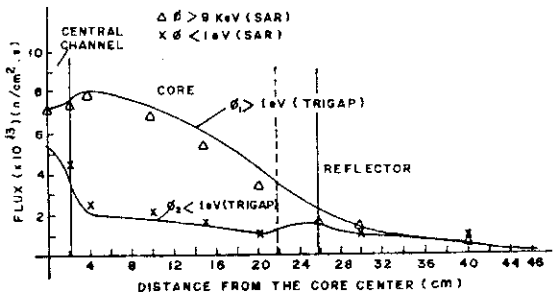

FIG. 3 : COMPARISON OF CALCULATED FLUX DISTRIBUTION AND PROJECTED VALUES FOR A TRIGA CORE CONFIGURATION.

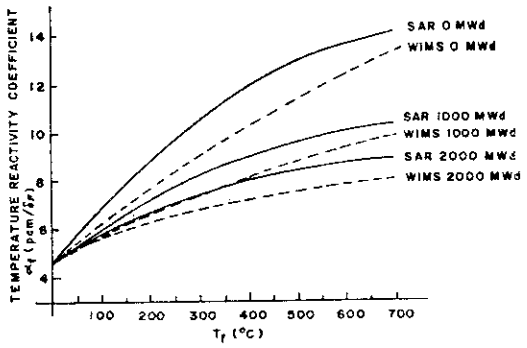

FIG. 4 : TEMPERATURE COEFFICIENT FOR LEU FUEL AT DIFFERENT BURN-UP STEPS.

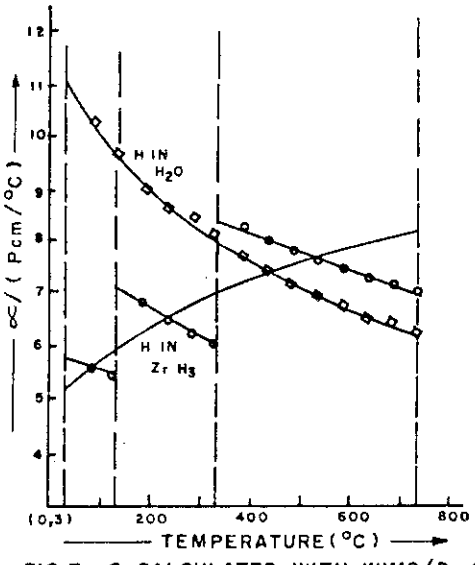

FIG. 5 : α_f CALCULATED WITH WIMS/D-4 USING CROSS-SECTION FOR H (i) IN ZrH LATTICE (ii) IN H_2O

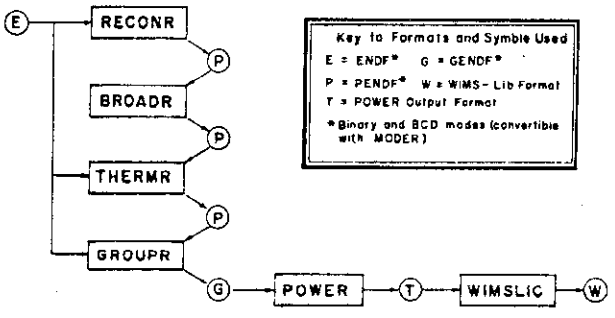

FIG. 6 : THE FLOW OF DATA IS PREPARING TO WIM - LIB. GROUP CONSTANT.

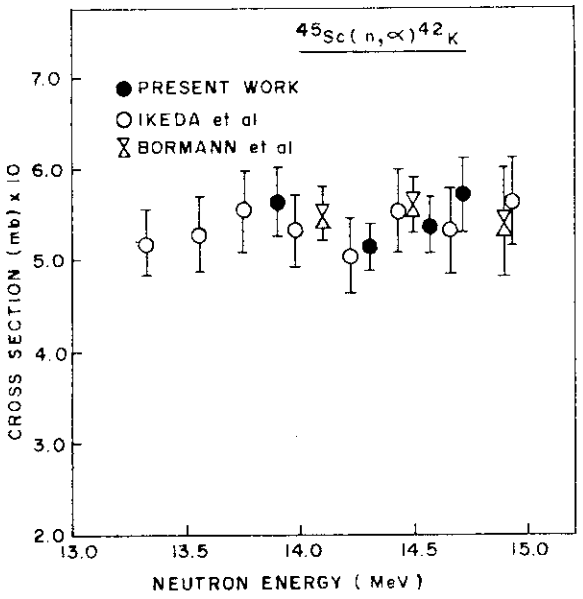

Fig.7. Excitatation function of $^{45}Sc(n,\alpha)^{42}K$ reaction.

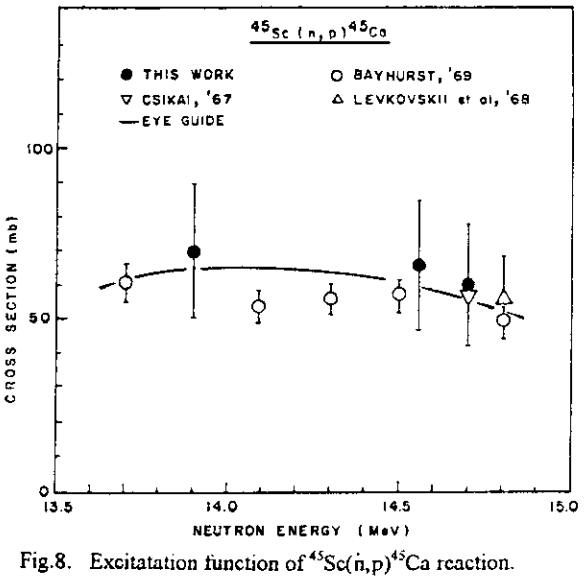

Fig.8. Excitatation function of $^{45}Sc(n,p)^{45}Ca$ reaction.

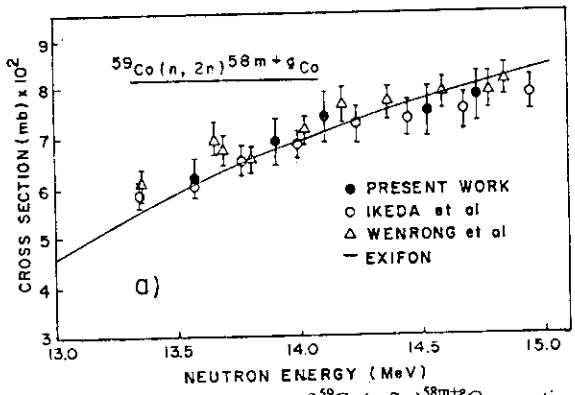

Fig.9. Excitatation function of $^{59}Co(n,2n)^{58m+g}Co$ reaction.

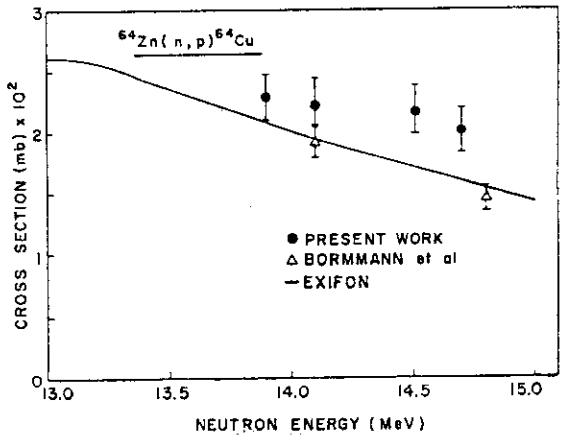

Fig.10. Excitatation function of $^{64}Zn(n,p)^{64}Cu$ reaction.

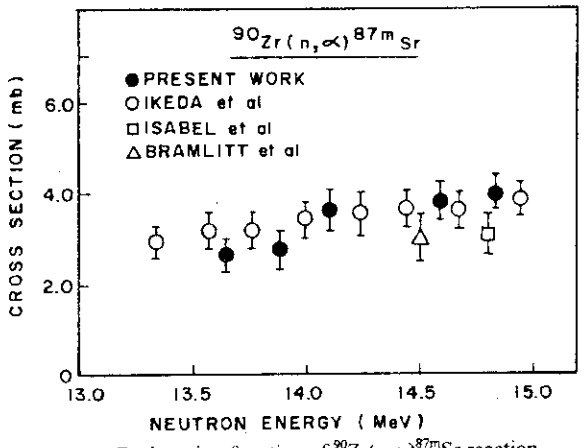

Fig.11. Excitatation function of $^{90}Zr(n,\alpha)^{87m}Sr$ reaction.

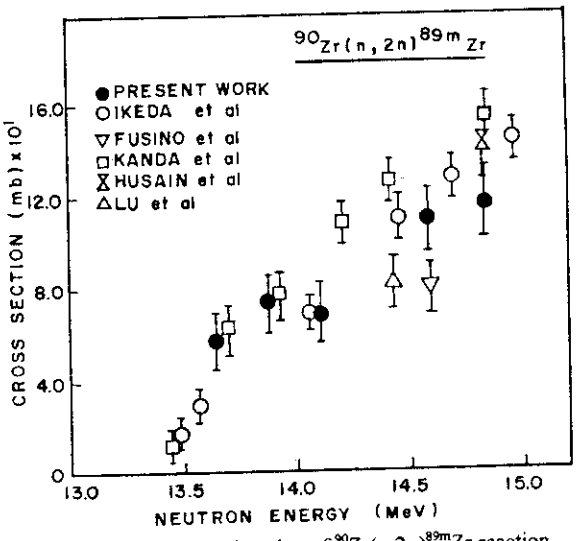

Fig.12. Excitatation function of $^{90}Zr(n,2n)^{89m}Zr$ reaction.

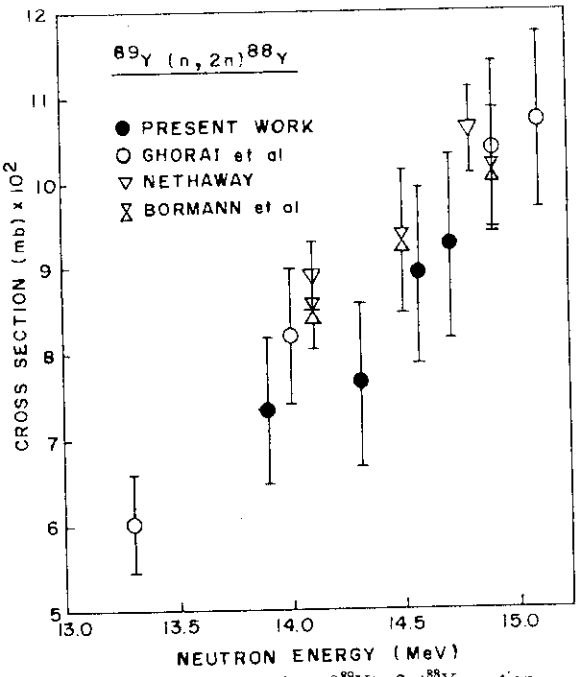

Fig.13. Excitatation function of $^{89}Y(n,2n)^{88}Y$ reaction.

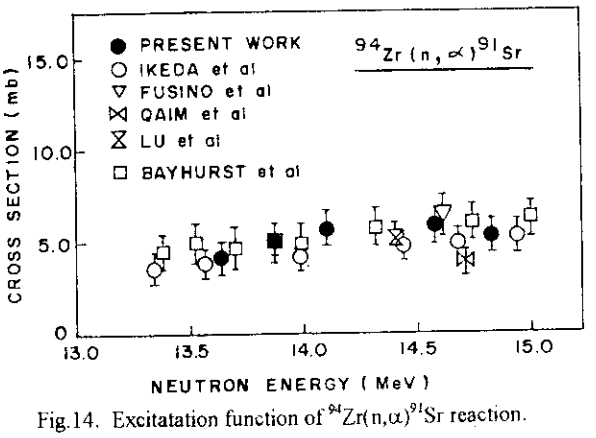

Fig.14. Excitatation function of $^{94}Zr(n,\alpha)^{91}Sr$ reaction.

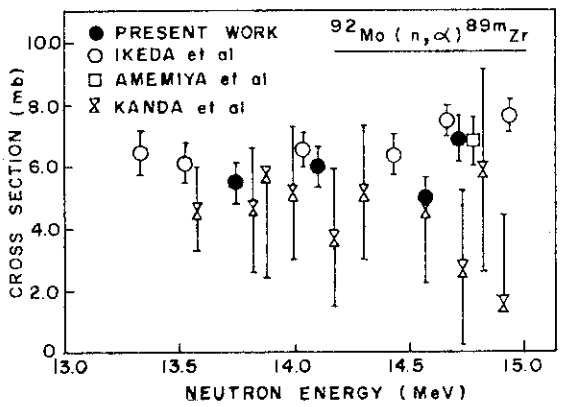

Fig.15. Excitatation function of $^{92}Mo(n,\alpha)^{89m}Zr$ reaction.

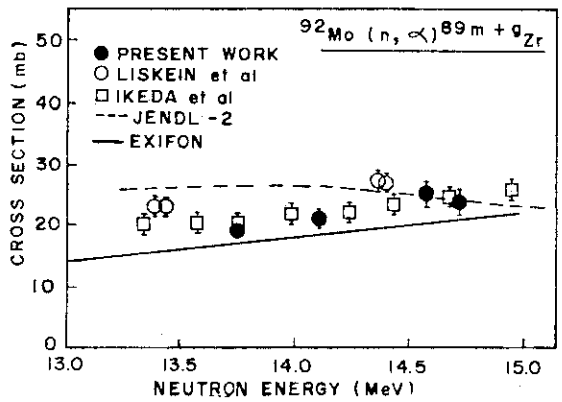

Fig.16. Excitatation function of $^{92}Mo(n,\alpha)^{89m+g}Zr$ reaction.

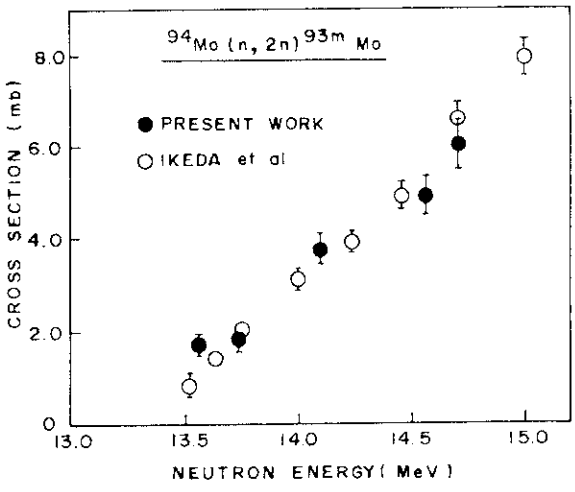

Fig.17. Excitatation function of $^{94}Mo(n,2n)^{93m}Mo$ reaction.

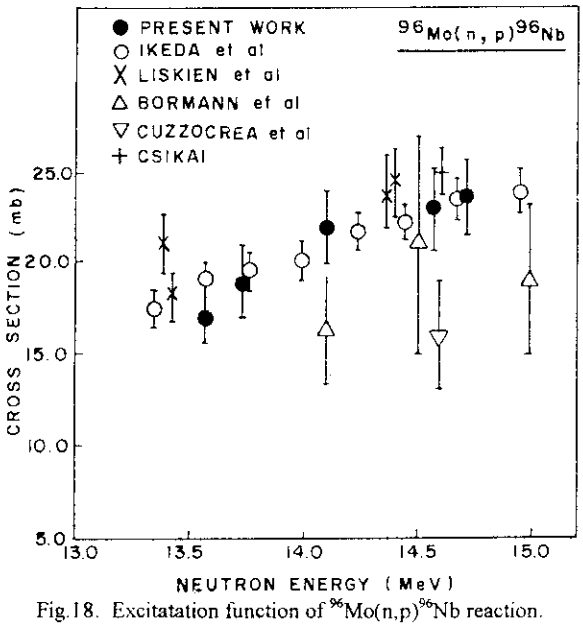

Fig.18. Excitatation function of $^{96}Mo(n,p)^{96}Nb$ reaction.

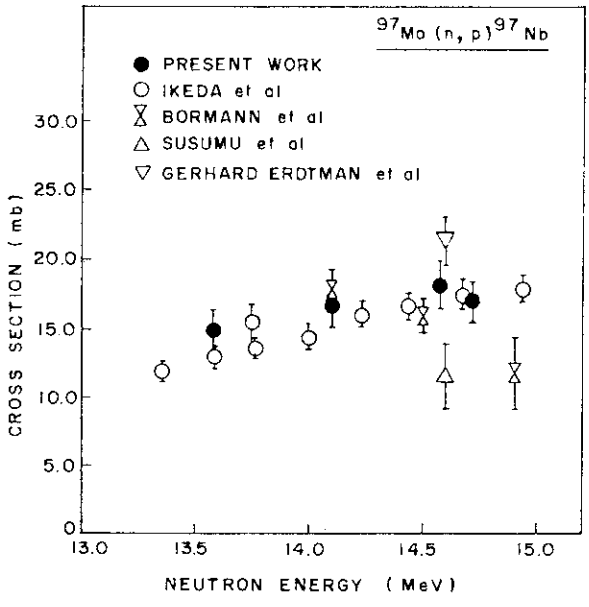

Fig.19. Excitatation function of $^{97}Mo(n,p)^{97}Nb$ reaction.

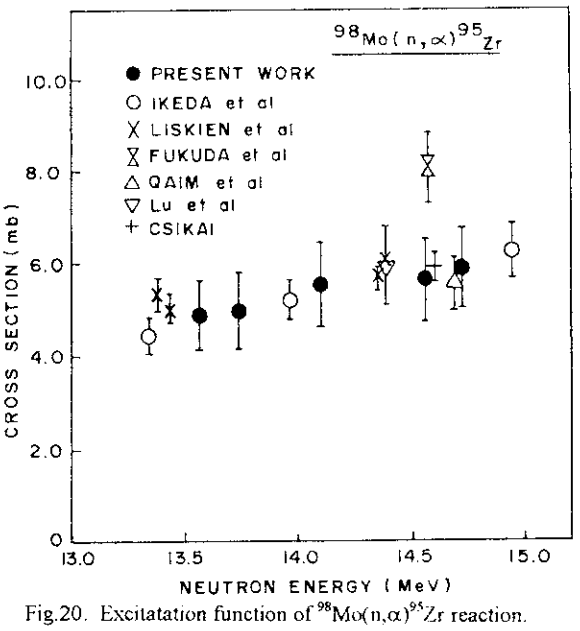

Fig.20. Excitatation function of $^{98}Mo(n,\alpha)^{95}Zr$ reaction.

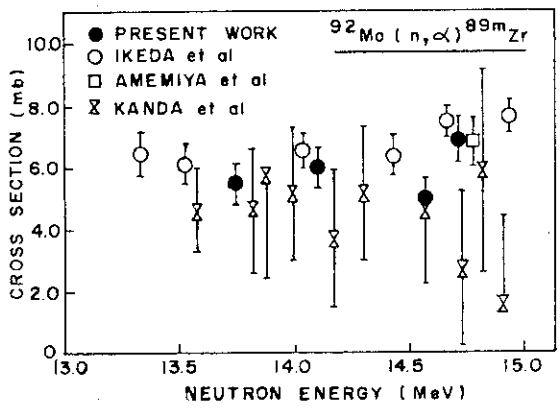

Fig.15. Excitatation function of ^{92}Mo(n,α)^{89m}Zr reaction.

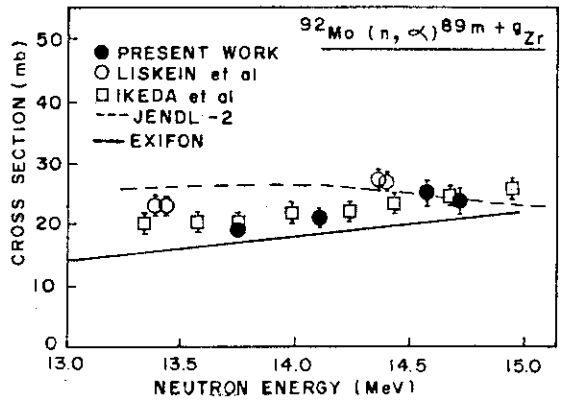

Fig.16. Excitatation function of ^{92}Mo(n,α)$^{89m+g}$Zr reaction.

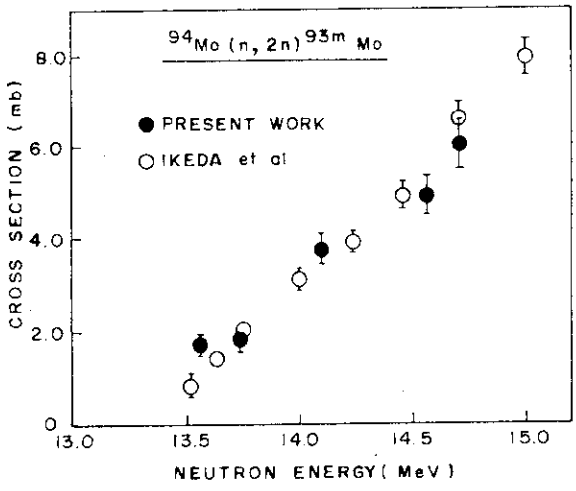

Fig.17. Excitatation function of ^{94}Mo(n,2n)^{93m}Mo reaction.

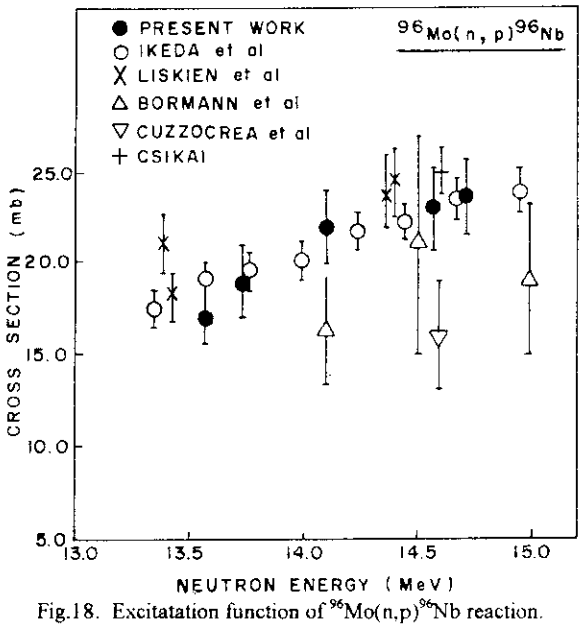

Fig.18. Excitatation function of ^{96}Mo(n,p)^{96}Nb reaction.

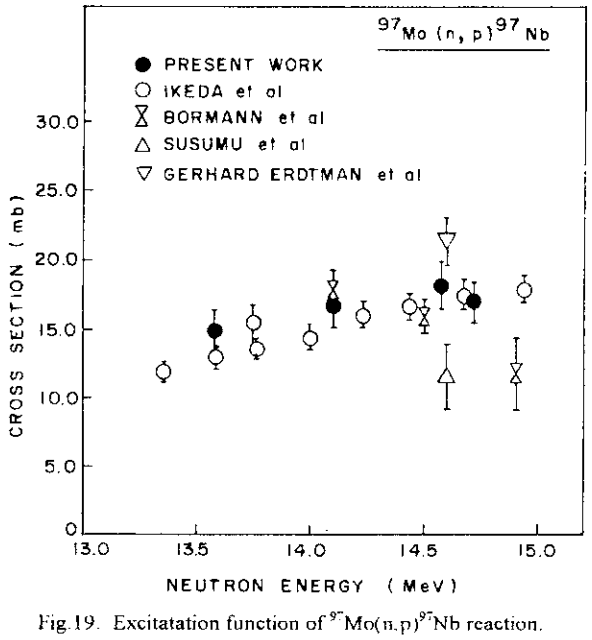

Fig.19. Excitatation function of ^{97}Mo(n,p)^{97}Nb reaction.

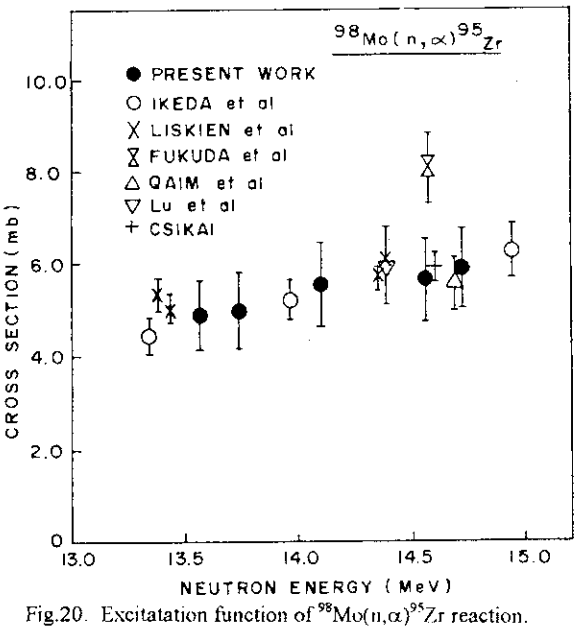

Fig.20. Excitatation function of ^{98}Mo(n,α)^{95}Zr reaction.

2.1.2 Actinide Nuclear Data Evaluation for BROND and Beyond

V.M. Maslov

Radiation Physics and Chemistry Problems Institute
220109, Minsk-Sosny, Belarus, CIS

The neutron cross sections of minor actinides U, Pu, Am, Cm have been calculated in the energy range of 0.01 to 20 MeV. The optical cross sections were calculated with coupled channel model. Since in case of minors the fission data fit is virtually the only constraint for (n,xn), x= 1,2,3 and (n,γ) calculations, the theoretical tools employed were tested in case of consistent analysis of total, (n,f), (n,γ), (n,n'), (n,2n) and (n,3n) data for major actinides. The role of statistical model parameters testing is exemplified.

1. Introduction

Until recently the target of activity of Nuclear Data Evaluation Laboratory of the former Institute of Nuclear Engineering were mainly major actinides. The actinide data files prepared for BROND library are the following (the year of release in parentheses): ^{239}Pu, ^{241}Pu, ^{242}Pu (1980), ^{240}Pu (1981), ^{235}U (1985), ^{236}U (1987), ^{238}Pu, ^{242}Cm (1988), ^{244}Cm (1989), ^{233}U (1991). Since then a number of methods, parameter systematics and calculation tools were developed[1], which could be used for evaluation of minor actinide data. These data are urgent for actinide burner concept optimization, but unfortunately, with the rear exception (^{242}Cm, ^{244}Cm, for example[2,3]) they were never produced as the files for major actinides. Virtually, only fission data, if any, are available for minor actinides, they would be used as a constraint for (n,γ), (n,n'), (n,2n) and (n,3n) reaction cross sections.

In the present analysis the $^{232\text{-}238}$U, $^{236\text{-}244}$Pu, $^{241\text{-}243}$Am and $^{242\text{-}248}$Cm nuclides are covered. The total cross section, shape elastic and reaction cross sections were calculated with a coupled channel optical potential parameter systematics[4]. It was obtained when fitting total and differential scattering cross sections for major actinides. Although actual β_2 and β_4 deformation parameter values should be checked at least against S_0 and S_1 values.

The analysis was divided into two parts, i.e. 1) up to the emissive fission threshold and 2) above emissive fission threshold. In the first part total, reaction, elastic and inelastic scattering, direct inelastic scattering for 4 or 5 ground state band levels, capture and fission cross sections were calculated. Code STAT[5] was used. In the second part fission, inelastic scattering, (n,2n) and (n,3n) cross sections were calculated with modified version of STAPRE[6] code.

2. Cross sections below emissive fission threshold

The first "plateau" fission cross section analysis is accomplished within a Hauser-Feshbach formalism, the double-humped fission barrier model is used. The detailed description of the model is given elsewhere[7,8]. Here only the main points would be discussed.

The level densities of fissionning nuclides at inner and outer saddles as well as that of the residual nuclides were

calculated with a phenomenological model[9] :

$$\rho(U,J,\pi) = K_{rot}(U,J)\ K_{vib}(U)\ \rho_{qp}(U,J,\pi) \qquad (1)$$

where $K_{rot}(U,J)$ and $K_{vib}(U)$ are factors of rotational and vibrational enchancement of level density and $\rho_{qp}(U,J,\pi)$ is the quasi-particle level density, which was "renormalized" at low energies to fit the cumulative sums of low lying levels. The residual nuclides were assumed axially deformed, the main level density parameter $a(B_n)$ was defined by fitting D_{obs}, except those cases, like ^{245}Pu and ^{245}Cm compound nuclides, when resulting $a(B_n)/A$ (A-mass number) looks like a spike as compared with neighbouring nuclide values. In such cases simple systematics for $\tilde{a}/A = 0.484 - 0.00162/A$ was used. The liquid drop shell corrections were calculated with the liquid-drop mass parameters[10]. The asymmetries of fissionning nuclides at saddles were defined according to SCM calculations of fission barriers[11].

Then the available fission data for U and Pu targets were analysed. Some peculiar features arise here for neutron-poor nuclides data ^{232}U(n,f) and ^{236}Pu(n,f). They exhibit a non-threshold cross section behaviour at low energies, which corresponds to rather low inner barrier heights (lower than the outer one), meanwhile, they gain axial symmetry at inner saddles[11]. As shown on the figs.1,2 the model employed is capable to reproduce also rather steep slope of ^{232}U(n,f) data[12] above 2 MeV. The scatter of data on ^{236}Pu(n,f) prohibits more reasonable fitting of data, since at lower energies fission cross section values are as high as that of reaction cross section. In case of other U, Pu and Am nuclides the data are fitted rather well from 0.01 MeV up to 5 MeV.

In case of Cm targets the extreme paucity of fission data hinders an extensive analysis. In case of N-even Cm targets the bomb-shot data[16] are consistent with data, measured with electron linac as a neutron source and lead slowing down time spectrometer[17]. The fig.3 shows the typical comparison of calculated and measured data for ^{246}Cm(n,f) data. Also with our approach we can't reproduce over-barrier structures in Cm bomb-shot data[16].

Actually there is no adjustable parameter in neutron channel in case of most U and Pu targets. In case of minor actinides extreme care should be taken, so that the matching energy of continuum level density description would be lower than the energy, where the missing of low-lying levels occurs[18]. If the matching energy is too high, the significant part of inelastic cross section may be misinterpreted as elastic scattering cross section. This would be the case if CASTHY code approach is used. In convenient approach the fission channel parameters would be aberrated. Fig.4 shows what happens in case of ^{243}Cm(n,n') reaction if missing of levels in residual nuclide ^{243}Cm above 0.4 MeV is ignored and matching energy of 1 MeV is adopted. The same happens in other cases, for example, ^{241}Pu(n,n') etc. The proposed approach fits the data on (n,n') reactions for ^{233}U, ^{235}U and ^{238}U, which justifies it's application for the minors.

Capture data for ^{238}U and ^{236}U provide an opportunity to develop the approach to predict (n,γ) reaction cross sections in case of even targets. The Poenitz data[19] (see fig.5) show a fair agreement with JENDL-3 evaluation and our calculated curve up to

1 MeV. The radiation strength function $S_{\gamma 0}$ used is 9.5×10^{-4}. At higher energies JENDL-3 curve seems to underestimate the data, since it is a fit of some older Poenitz' data. Above 1 MeV incident neutron energy when calculating capture width the competition of (n,γf) and, more important, (n,γn') reactions should be included. In an opposite case calculated curve drastically overestimates the capture cross section. To resolve the remaining discrepancy (see fig.5) one should model the residual even-even nuclide ^{238}U level density at 1.3-2.8 MeV excitation energy, i.e. above pairing gap. Within pairing gap collective levels are modelled with a constant temperature model[18]. Above pairing gap the two-quasi-particle state density could be modelled with a simple formulas[20]. As a result the (n,n') and, which is more important, (n,γn') competition will increase and we will get a fair agreement with data[19]. The same effects are observed in case of ^{236}U(n,γ), but there are systematic discrepancies in measured (n,γ) data around 1 MeV.

The (n,γ) cross section for N-odd fissile targets could be fitted with inclusion of (n,γf) reaction competition. The measured data are actually $\alpha=\sigma_\gamma/\sigma_f$ data and above 0.1 MeV they are rather old[21]. The ^{235}U(n,γ) cross section could be well reproduced, but in case of ^{233}U(n,γ) to reproduce the 'dip' in data[21] above 0.6 MeV one needs a $S_{\gamma 0}$ value, which is ~50% lower than that fitting data[21] at lower energies (see fig.6).

3. Cross sections above emissive fission threshold

For fixed statistical model parameters of residual nuclides, fissionning in (n,nf), (n,2nf) etc. reactions, the realistic trend of non-emissive fission cross section σ_f^1 is critical for reproducing the measured fission cross sections up to 20 MeV. The consistent description of the most complete set of measured data on (n,f), (n,2n) and (n,3n) reaction cross sections for the ^{235}U and ^{238}U target nuclei and secondary neutron spectra for the latter target gives a strong ground to consider the estimate of σ_f^1 and contribution of the first neutron pre-equilibrium emission as fairly realistic. The model is described in detail elsewhere[8,22]. At least, the new ^{232}Th(n,2n) data were reproduced fairly well without aditional parameter variation[23], the fission cross section being the only constraint.

In case of N-odd, Z-even targets the method[20] of resolving the well-known discrepancy between measured data on ^{239}Pu(n,2n) and convenient statistical model calculations could be applied. Near-threshold behaviour of the (n,2n) cross section is interpreted as being due to jump-like excitation of two-quasi-particle states in residual even-even nuclide. The same effect is observed[24] in case of ^{235}U(n,2n) data (see fig.7). The calculated ^{233}U(n,2n) cross section, governing the ^{232}U build-up in U-Th fuel cycle, is rather different from JENDL-3 (see fig. 8)

Almost no new data have appeared since previous analyses of U, Pu, Am and Cm data. The method of fission calculation[22] prooved reasonable in case of $^{232\text{-}238}$U(n,f) data and $^{238\text{-}244}$Pu data. The validity of the model for Z-odd target was demonstrated[25] in case of consistent ^{237}Np(n,f) and ^{237}Np(n,2n)^{236}Np^s data analysis[25] and $^{241\text{-}243}$Am(n,f) data analysis[26]. For most of the nuclides there is a consistency between calculated and measured fission data. However the numerous discrepancies in calculated and JENDL-3 evaluated (n,xn) cross sections being notified. The severe

discrepancy persists in case of ^{242m}Am(n,f) above the onset of (n,nf) reaction. The same kind of discrepancy still persists in case of ^{245}Cm(n,f). The analysis of the other existing evaluated Cm data shows the inadequacy between JENDL-3, ENDF/B-VI and statistical calculations with reasonable fission and neutron channel parameters.

4.Conclusion

I guess, that existing data base and knowledge data base are sophisticated enough to produce more justified neutron data for minor actinides, like Pa, U, Np, Pu, Am and Cm.

5. Acknowledgements

The author acknowledges with thanks the support of JAERI,under Foreign Researcher Inviting Program, and helpful cooperation with JAERI Nuclear Data Center staff.

References

1. Bakhanovich L.A., Klepatskij A.B., Maslov V.M. et al. In:Nucl. Data for Sci. & Technology,Julich,1991,p.915 (1992).
2. Klepatskij A.B., Kolesov A.M., Maslov V.M. et al. INDC(CCP)-316 (1989).
3. Bakhanovich L.A., Klepatskij A.B., Maslov V.M. et al. Jadernye Constanty,N 1, 36 (1989).
4. Klepatskij A.B., Sukhovitskij E.Sh., private communication.
5. Klepatskij A.B., Maslov V.M., Sukhovitskij E.Sh., private communication.
6. Uhl M., Strohmaier B. Report IRK-76/01 (1976).
7. Ignatjuk A.V., Klepatskij A.B., Maslov V.M. et al. Sov. J. Nucl. Phys.42, 360 (1985).
8. Ignatjuk A.V., Maslov V.M. In: Nuclear Data Evaluation, Methodology, Brookhaven, USA, Oct,1992.,p.440 (1993).
9. Ignatjuk A.V., Istekov K.K., Smirenkin G.N. Sov.J. Nucl. Phys. 29, 450 (1979).
10. Myers W.D., Swiatecki W.J. Ark.Fyz.,v.36, 342 (1967).
11. Howard W.M., Moller P. Atomic Data and Nuclear Data Tables,v.25, 219 (1980).
12. Fursov B.I.,Baranov E.Yu.,Klemyshev M.P. et al. Sov. J. At. Energy, v.61, 383 (1986).
13. Vorotnikov P.E.,Dubrovina S.M.,Otroshchenko et al. v.12, 474 (1970)
14. Gromova S.M. et al. Sov.J. At.Energy, v.68, 223 (1990).
15. Vorotnikov P.E. et al., in: Proc. Int. Conf. on Neutron Physics, Kiev, 1987, v.3, p.76, (1988).
16. Fomushkin E.F.,et al, Sov. J. Nucl. Phys. 36,338 (1980).
17. Maguire H.T. et al., Nucl. Sci. Engn. v.89, 293 (1985)
18. Antsipov G.V. et al. INDC(CCP)-182 (1982)
19. Poenitz W.P. et al. Nucl.Sci.Engng.,v.78, 329 (1981).
20. Maslov V.M. Z. Phys. A347, 211 (1994).
21. Hopkins J.C., Diven B.C. Nucl. Sci. Engng., v.12, 169 (1962).
22. Ignatjuk A.V., Maslov V.M. Sov. J. Nucl. Phys. 47,224 (1990).
23. Maslov V.M. Ann. Nucl.Energy, v.19, 181 (1992).
24. Maslov V.M. Nuclear Data for Sci.& Technology., Gatlinburg,USA, 13-17 May, 1994.
25. Maslov V.M. Nuclear Constants, 4, 18, (1987).
26. Klepatskij A.B. and Maslov V.M. In: Nuclear Data for Sci. & Technology,Julich,Germany 1991,p.881 (1991).
27. Maslov V.M. Ann. Nucl.Energy, v.20, 163 (1993).

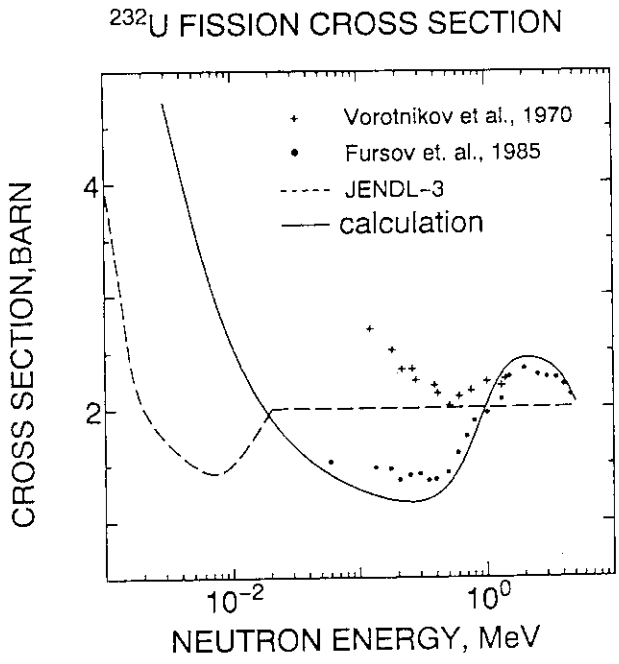

Fig. 1

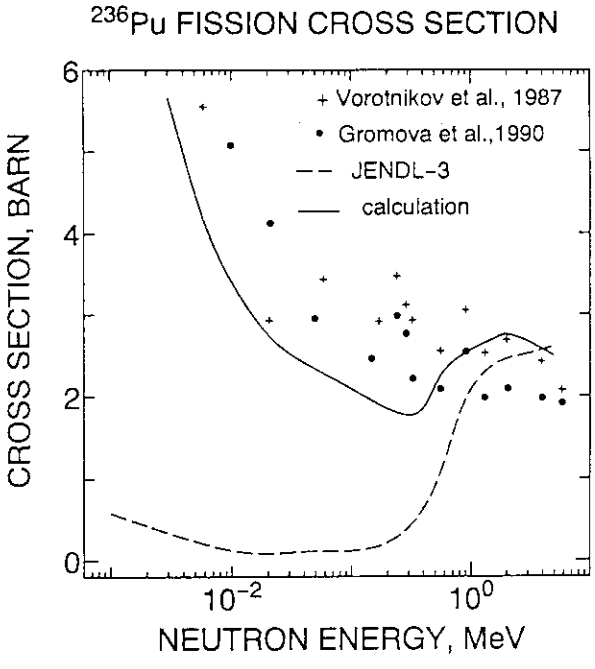

Fig. 2

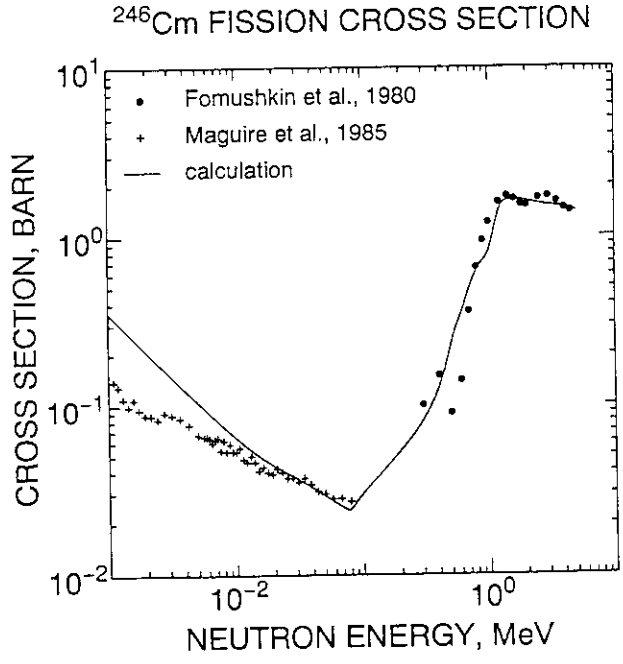

Fig. 3

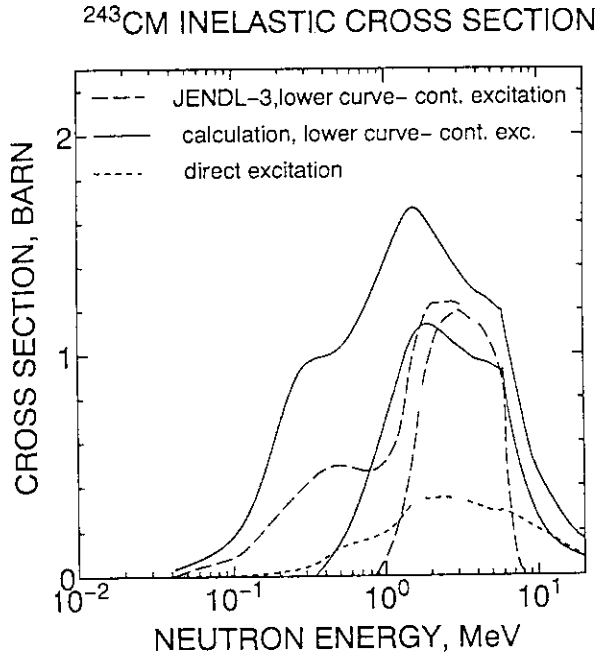

Fig. 4

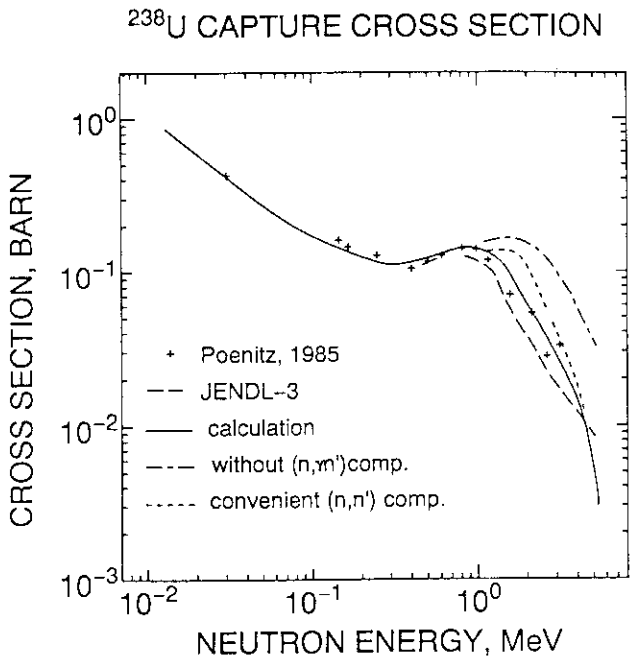

Fig. 5

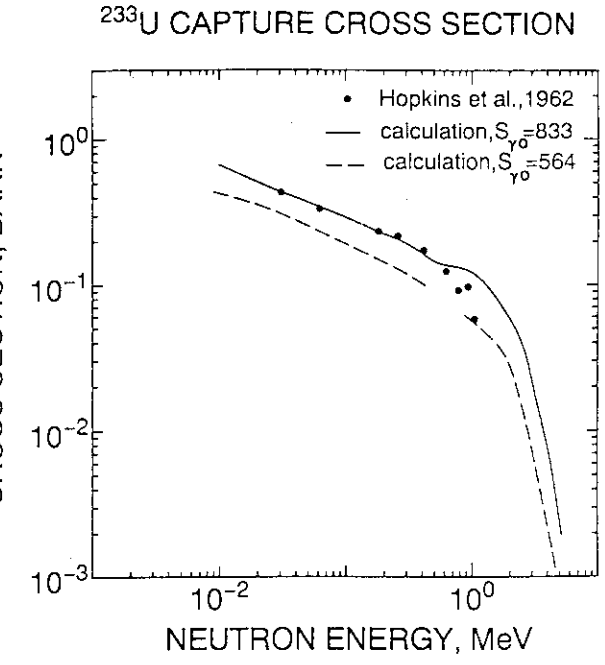

Fig. 6

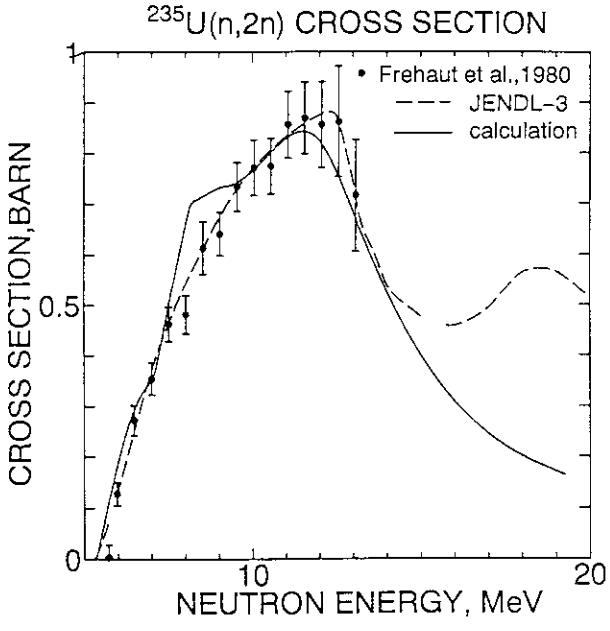

Fig. 7

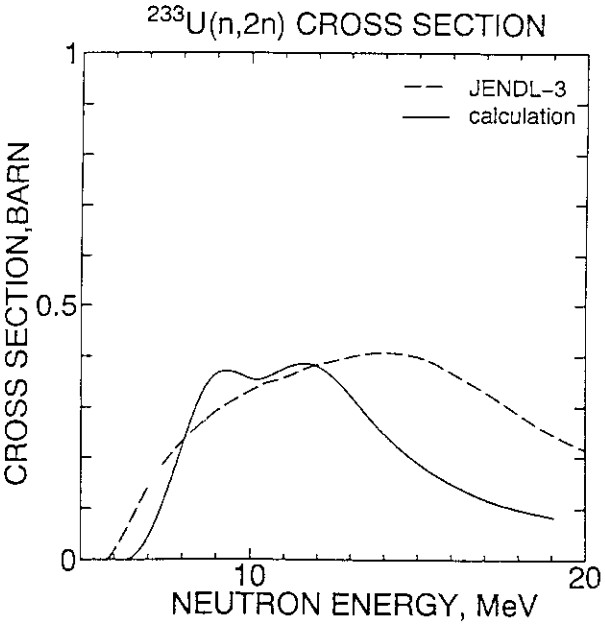

Fig. 8

2.1.3 Calculations of Nuclear Data for the Reactions of Neutrons and Protons with Heavy Nuclei at Energy from 1 MeV up to 2 GeV

V.A. KONSHIN
Japan Atomic Energy Research Institute
Tokai-mura, Naka-gun, Ibaraki-ken 319-11

Abstract

Several nuclear model codes were applied to calculations of nuclear data in the energy region from 1 MeV to 2 GeV. At energies from 1 to 20 MeV the statistical model code STAPRE was used for calculations of the neutron cross-sections for fission, (n,2n) and (n,3n) reaction cross-sections for 71 actinide isotopes. In the energy region from 10 to 100 MeV the nuclear theory code GNASH was used to calculate the neutron fission and (n,xn) cross-sections for ^{238}U, ^{235}U, ^{239}Pu, ^{232}Th, ^{237}Np, ^{238}Pu, ^{241}Am, ^{243}Am, ^{245}Cm and ^{246}Cm. At energies from 100 MeV to 2 GeV the intranuclear cascade-exciton model including the fission process was applied to calculations of the interactions of protons and neutrons with actinides and the calculated results are compared with experimental data.

The statistical model code STAPRE [1] taking into account conservation of spin and parity for all nuclear reaction cascades was used for the calculation of the fission, (n,2n) and (n,3n) reaction cross-sections. The neutron transmission coefficients required for the statistical model calculations were obtained using the coupled-channel code ECIS [2] with the potential parameters taken from [3]. The main parameter of the exciton model was fixed by fitting the experimental data for the secondary neutron spectra for ^{238}U at 6 to 14.3 MeV [4]. For the calculation of the level density for residual and fissioning nuclei a generalized superfluid model [5] was used. The model takes into account pairing correlation, odd-even, collective and shell effects and the actinide nuclei are supposed to be an ideal object for application of the superfluid nuclear level density model.

The validity of the model used is demonstrated by a consistent description of all experimental data on the fission and (n,2n) cross-sections available for actinide isotopes. In Fig.1 and 2 the fission cross-sections calculated for ^{239}Pu and ^{237}U are given as an illustration.

The fission barrier parameters were obtained by analyzing the experimental data for the fission cross-sections within the framework of the level density model used. For those nuclei, whose experimental data are not virtually available, the systematics [6] for the first

plateau region, as well as indirect experimental data were used. For the nuclei beyond the experimentally investigated region the accuracy of the fission cross-sections calculated may be not higher than 20 - 30 %.

The multistep Hauser-Feshbach preequilibrium nuclear model code GNASH [7] was used to calculate fission and (n,xn) reaction cross-sections for actinides in the energy region from 5 to 100 MeV. The input information needed is descrete level decay data for all significant residual nuclei formed, ground-state mass, spin and parity tables, direct reaction cross-sections, and optical model transmission coefficients. The transmission coefficients are required from low energies up to 100 MeV and they were obtained using the coupled-channel method with relativistic kinematics [2] and the relevant deformed potential parameters were determined by analysis of the experimental data for the total cross-section of ^{238}U up to 100 MeV. They appeared to be the following:

$$V_R = \begin{cases} 45.87 - 0.3\,E & 0 \le E \le 20\ \text{MeV} \\ 60.84 - 7\,\ln E & 20 \le E \le 100\ \text{MeV} \end{cases}$$

$$W_D = \begin{cases} 2.95 + 0.4\,E & E \le 10\ \text{MeV} \\ 6.95 - 0.082\,(E-10) & 10 \le E \le 90\ \text{MeV} \\ 0.39 & E \ge 90\ \text{MeV} \end{cases}$$

$$W_V = 8.0 \cdot \{1 + \exp[-(E-50)/10]\}^{-1},\ 0 \le E \le 100\ \text{MeV}$$

$$V_{SO} = 7.5\ ;\ r_R=1.256,\ \alpha_R=0.626,\ r_D=1.260,\ \alpha_D=0.556,\ \beta_2=0.216,\ \beta_4=0.080.$$

The introduction of the volume absorption term to the imaginary part of the deformed potential leads to a good agreement with the experimental data for $\sigma_t(^{238}U)$ up to 100 MeV and, surprisingly, to a better description of the experimental data for angular distributions of inelastically scattered neutrons on the first and second levels of ^{238}U [8].

The calculations using the GNASH code were done for ^{238}U, ^{235}U, ^{239}Pu, ^{232}Th, ^{237}Np for which the experimental data for the neutron fission cross-sections above 20 MeV exist [9], and for ^{238}Pu, ^{241}Am, ^{243}Am, ^{245}Cm and ^{246}Cm for which there are no experimental data available in the intermediate energy region.

The comparison of calculated and experimental data for σ_f and (n,xn) reactions, x≤7, for ^{235}U, ^{239}Pu and ^{237}Np is shown in Fig.3-11. The experimental data are reproduced rather accurately up to 100 MeV using the above potential parameters and taking into account the decay of nine compound nuclei. The calculations were made with two options for level density models: the Gilbert and Cameron model [10] and a form of Fermi-gas model by Ignatyuk et al. [5] that includes an energy-dependent level density parameter and the damping out of shell effects at higher excitation energies, which is especially important for the energies considered here. The calculations showed that the use of the Gilbert and Cameron model leads to an overestimation of $\sigma_f(^{238}U)$ by 20 % and the Ignatyuk formulation agrees better with experimental data.

The results obtained using the GNASH code for actinide (n,2n) cross-sections are about 5 - 10 % lower than the results obtained by the STAPRE code and for (n,3n) cross-

sections the GNASH code gives systematically higher values than STAPRE. This is shown in Fig.8, where (n,3n) cross-sections calculated by both codes differ by 40 %, with the fission cross-section being similar in both calculations up to 17 MeV. At energies above 15 MeV the binary reactions are dominated by the preequilibrium component and calculations become increasingly sensitive to the accuracy of that approximation. Therefore the possible reason of the discrepancy between both codes may lie in different options of the preequilibrium model used, namely, a rather simple version of the exciton model used in STAPRE and more advanced version used in GNASH [11], with the state density for the initial ph-configuration corrected to account for variations of the single-particle state density with energy in the potential well and to account for effects due to the finite depth of the nuclear potential [12].

In the energy region from 100 MeV to 2 GeV the intranuclear cascade-exciton model including the fission process [13] is applied to calculations of the interactions of protons and neutrons with ^{232}Th, ^{232}Pa, ^{235}U, ^{238}U, ^{239}Pu, ^{237}Np, ^{238}Np, ^{241}Am, ^{242}Am and $^{242-248}$Cm.

The intranuclear cascade model has been developed in 1960-70th and naturally involved rather substantial simplifications which can presently be removed. For instance, usually in the cascade models a constant, independent on N, Z and E^* of residual nuclei, value of a was used ($a=\alpha_0 A$, with α_0=const). The calculation of the competition between the particle emission and fission of excited nuclei was also based on rather rough assumptions.

The fission cross-section for ^{238}U+p calculated in the present work using the intranuclear cascade model and its sensitivity to different models for macroscopic fission barrier calculations [14-20] in the energy region from 100 MeV to 1 GeV is shown in Fig.12. The phenomenological approach by Barashenkov et al [14,15] and the liquid drop model (LDM) with Myers and Swiatecki parameters [16] lead to too low σ_f, and better results can be achieved using the subroutine BARFIT by Sierk [20] which provides the macroscopic fission barrier heights within the Yukawa-plus-exponential modified LDM, as well as by the approximation by Krappe et al [19].

The change of properties of nuclei with increasing excitation energies influences strongly the nuclear fissility and the $B_f(E^*)$ dependence proposed by Sauer et al [21] was taken into account (~ 5 % in σ_f). The dependence of B_f on the angular momentum L of a fissioning nucleus was calculated using the approximation by Sierk [20], and it appears to be rather strong, with σ_f changing by 30 %.

The results of the calculations using the intranuclear cascade model showed that the dependence of the fission cross-section calculated on the different level density systematics presently available [22-25] is not essential (about 7 % in σ_f at 0.1 - 1 GeV).

The best results for the actinide fission cross-section description for incoming protons and neutrons were obtained by using the fission barrier values by Sierk [20], level density systematics by Iljinov et al [25] with ground state shell and pairing corrections by Truran et al [26], and with taking into account $B_f(E^*)$ and $B_f(L)$ dependencies.

It was assumed that the values of the level density parameters to be the same in both evaporating and fissioning nuclei, namely a_f/a_n = 1.0. This is confirmed by the results of the

theoretical considerations for actinides [27].

The calculated neutron and proton induced fission cross-sections for ^{238}U, ^{239}Pu, ^{237}Np are shown in Fig.13-17 and the yield of Th-isotopes is shown in Fig.18. A good agreement is reached for all nuclei, except for ^{237}Np where the calculated results are lower than the experimental data by 10 %. In Fig.18 the present results for isotope yields are compared with the results by Barashenkov et al.[28] who used a constant value of the a-parameter, and with the results by Hahn and Bertini [29] where the energy-independent ratio Γ_n/Γ_f was employed. The better agreement of present results with the experimental data is demonstrated.

In general, comparison with the experimental data on isotope yields, fission cross-sections and particle multiplicities indicates that the calculations reproduce the trends, and often the details, of the experimental data.

References

[1] Uhl M. and Strohmaier B.: IRK-76/01, Vienna (1976).

[2] Raynal J.: Optical Model and Coupled-Channel Calculations in Nuclear Physics, SMR-9/8, IAEA, Vienna (1970).

[3] Lagrange Ch.: INDC(FR)-56/L (NEANDC 218L) (1982).

[4] Kornilov V.N., Baryba V.Ya and Salnikov O.A.: Neutron Physics, Tcniiatominform, Moscow, V.3, 104 (1980).

[5] Ignatyuk A.V., Istekov K.K. and Smirenkin G.N.: J. Nucl. Phys., 29, 450 (1979).

[6] Kuprijanov V.M., Smirenkin G.N. and Fursov B.I.: J. Nucl. Phys., 39, 281 (1984).

[7] Young P.G. and Arthur E.D.: GNASH; A Preequilibrium, Statistical Nuclear Model Code for Calculation of Cross Sections and Emission Spectra, LA-6947 (1977).

[8] Konshin V.A.: Proc. of the IAEA Workshop on Computation and Analysis of Nuclear Data Relevant to Nuclear Energy and Safety, Trieste, Italy, 1992, World Scientific, p.775 (1993).

[9] Lisowski P.W., Gavron A., Parker W.E., Ullman J.L., Balestrini S.J., Carlson A.D., Wasson O.A. and Hill N.W.: Proc. of a Specialists' Meeting on Neutron Cross-Section Standards for the Energy Above 20 MeV, Uppsala, Sweden, 21-23 May 1991, p.178 (1991).

[10] Gilbert A. and Cameron A.G.W.: Can. J. Phys. 43, 1446 (1965)

[11] Kalbach: Z. Phys. A283, 401 (1977).

[12] Arthur E.D.: Proc. of the ICTP Workshop on Applied Nuclear Theory and Nuclear Model Calculations for Nucl. Thechn. Applications, 15 Feb.-18 March 1988, Trieste, Iatly (1988).

[13] Gudima K.K., Mashnik S.G. and Toneev V.D.: Nucl. Phys. A401, 329 (1983).

[14] Barachenkov V.S., Iljinov A.S., Toneev V.D. and Gereghi F.G.: Nucl.Phys., A206, 131 (1973).

[15] Barashenkov V.S. and Gereghi F.G.: Communication JINR, 94-10781, Dubna (1977).

[16] Myers W.D. and Swiatecki W.S.: Ark. Fyz. 36, 343 (1967).

[17] Pauli H.C. and Ledergerber T.: Nucl. Phys., A175, 545 (1971).
[18] Krappe H.J. and Nix J.R.: Proc. IAEA Symp. on the Phys. and Chemistry of Fission, Rochester, New York, 1973, v.1, p.159 (1974).
[19] Krappe H.J., Nix J.R. and Sierk A.J.: Phys. Rev. C20, 992 (1979).
[20] Sierk A.J.: Phys. Rev. C33, 2039 (1986).
[21] Sauer G., Chandra H. and Mosel U.: Nucl. Phys. A264, 221 (1976).
[22] Ignatyuk A.V., Smirenkin G.N. and Tishin A.S.: Yad. Fiz., 21, 485 (1975).
[23] Ignatyuk A.V., Itkis M.G., Okolovich V.N., Smirenkin G.N. and Tishin A.S.: Yad. Fyz., 21, 1185 (1975).
[24] Cherepanov E.A. and Iljinov A.S.: Preprint INR AS USSR, P-0064, Moscow (1977); Nucleonika 25, 611 (1980).
[25] Iljinov A.S., Mebel M.V., Bianchi N., De Sanctis E., Guaraldo C., Lucherini V., Muccifora V., Polli E., Reolon A.R. and Rossi P.: Nucl. Phys. A543, 517 (1992).
[26] Truran J.W., Cameron A.G.W. and Hilf E.: Proc. of the Intern. Conf. on the Properties of Nuclei far from the Region of Beta-Stability, Leysin, Switzerland, 1970, v.1, p.275 (1971).
[27] Reisdorf W.: Z. Phys. A300, 272 (1981).
[28] Barashenkov V.S., Gereghi F.G., Iljinov A.S. and Toneev V.D.: Nucl. Phys., A222, 204 (1974).
[29] Hahn R.L. and Bertini H.W.: Phys. Rev. C6, 660 (1972).

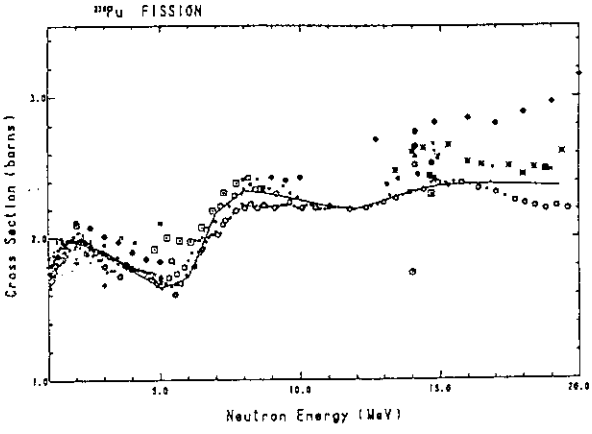

Fig. 1 The fission cross-section of ^{239}Pu calculated using the STAPRE code.

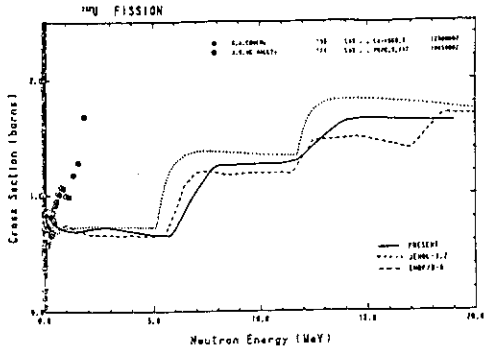

Fig. 2 Comparison of the calculated fission cross-section of ^{237}U with evaluated data

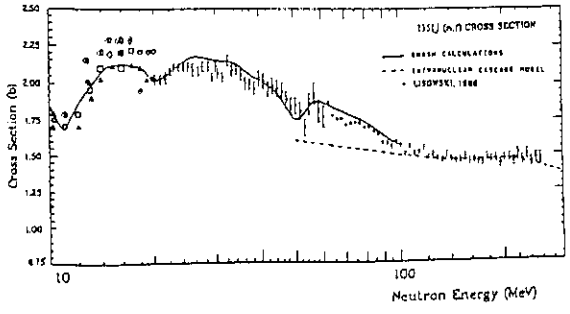

Fig. 3 The fission cross-section of ^{235}U calculated using the GNASH code and the intranuclear cascade model.

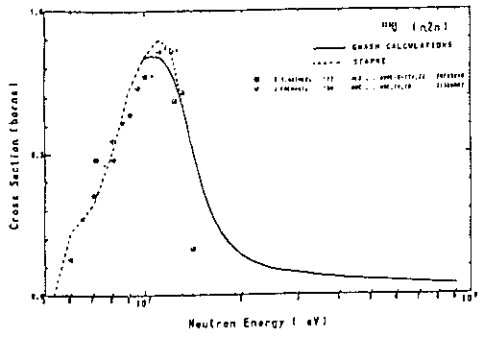

Fig. 4 The (n,2n) reaction cross-section for ^{235}U calculated using the STAPRE and GNASH codes.

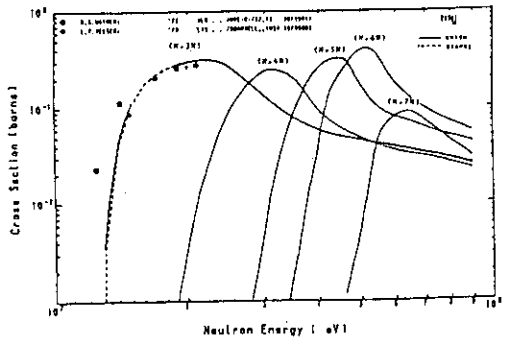

Fig. 5 The (n,xn) reaction cross-sections for ^{235}U.

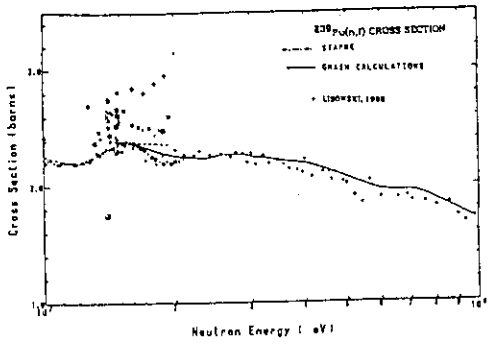

Fig. 6 The fission cross-section of ^{239}Pu.

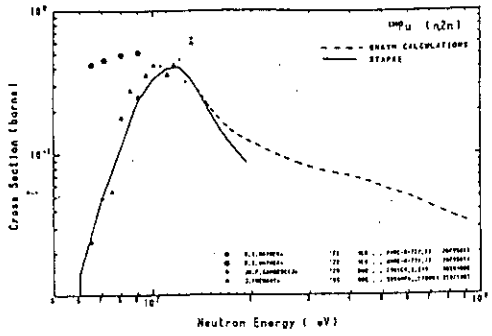

Fig. 7 The (n,2n) reaction cross-section for ^{239}Pu calculated using the STAPRE and GNASH codes.

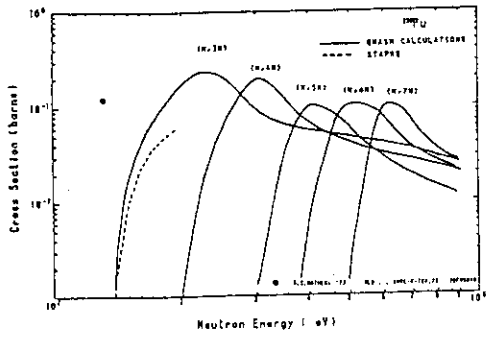

Fig. 8 The (n,xn) reaction cross-sections for ^{239}Pu.

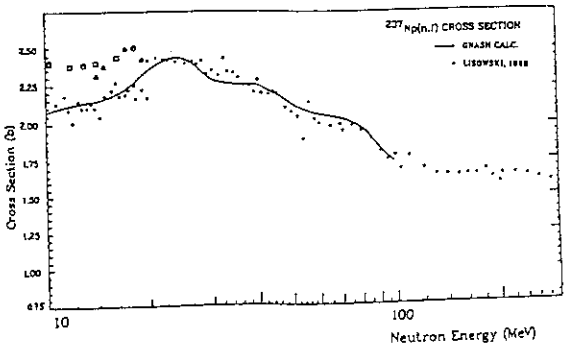

Fig. 9 The fission cross-section of ^{237}Np.

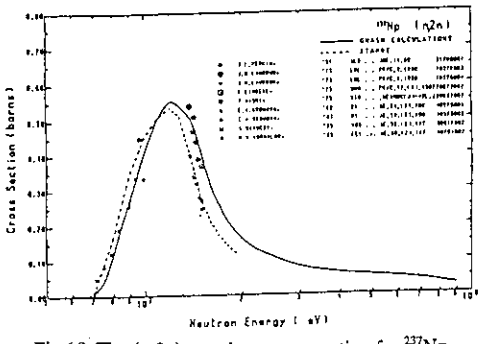

Fig.10 The (n,2n) reaction cross-section for ^{237}Np calculated using the STAPRE and GNASH codes.

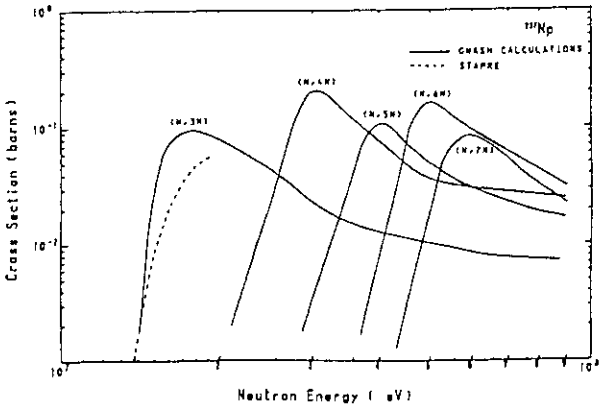

Fig.11 The (n,xn) reaction cross-sections for ^{237}Np.

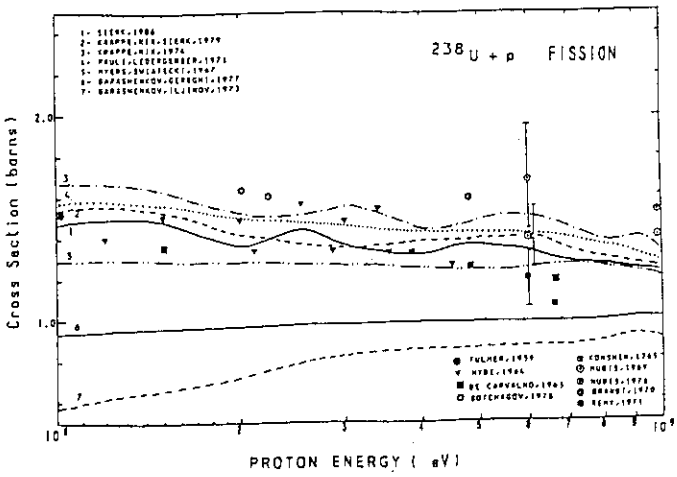

Fig.12 The ^{238}U proton induced fission cross-section dependence on the models for macroscopic fission barrier calculations used in the intranuclear cascade model.

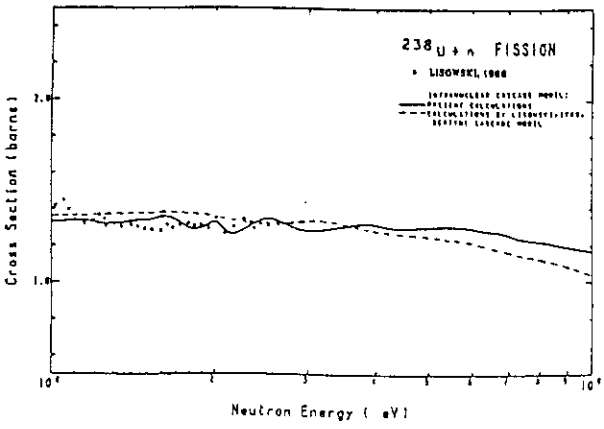

Fig.13 The neutron induced fission cross-sectioon of ^{238}U.

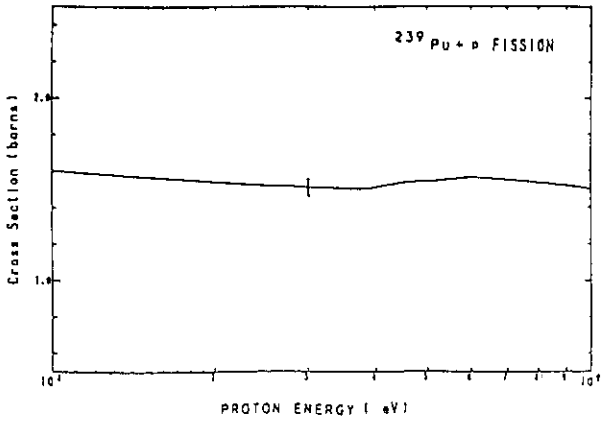

Fig.14 The proton induced fission cross-section of ^{239}Pu.

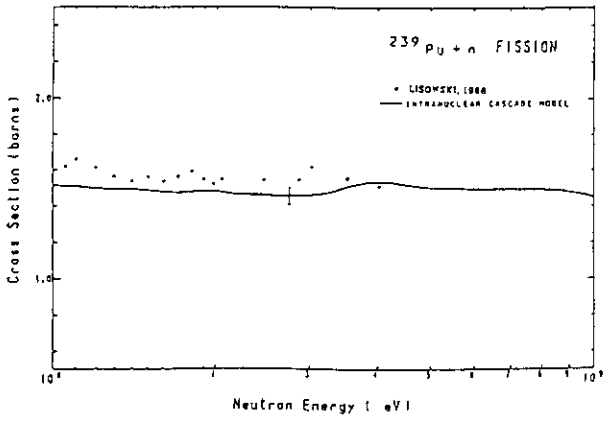

Fig.15 The neutron induced fission cross-section of ^{239}Pu.

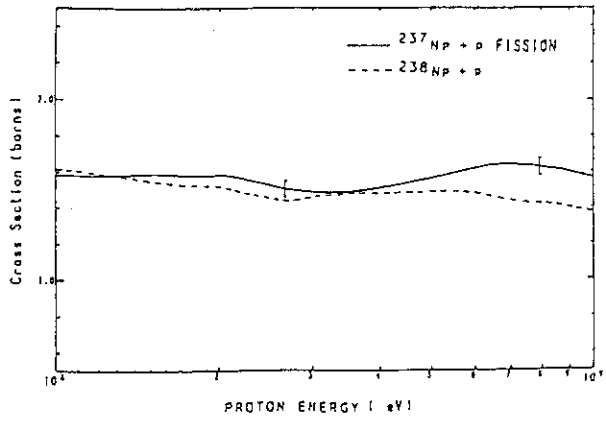

Fig.16 The proton induced fission cross-sections of ^{237}Np and ^{238}Np.

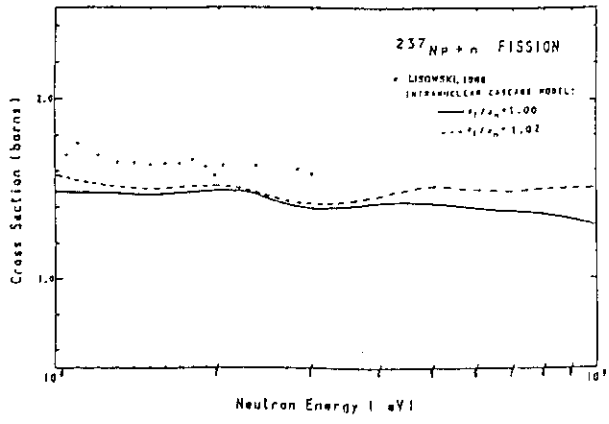

Fig.17 The neutron induced fission cross-section of ^{237}Np.

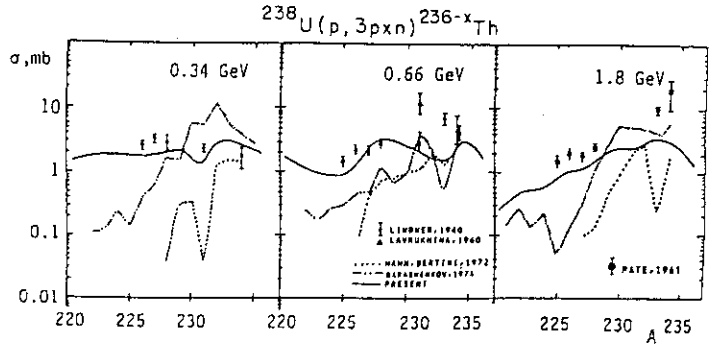

Fig.18 The yield of Th-isotopes in the reaction $^{238}U(p,3pxn)^{236-x}Th$.

2. 1. 4 Inelastic Interaction of Neutrons with Actinoid Nuclei Studied by Means of High Resolution Gamma-spectroscopy in Neutron Beam

Anatoly FILATENKOV, Sergey CHUVAEV
V.G.Khlopin Radium Institute
194021, 2-nd Murinski ave.28, St.Petersburg, Russia

Results are presented for actinoid nuclei gamma-spectra measurements that were curried out using monochromatic neutron sources of the Khlopin Radium Institute. The measurements were performed in neutron energy interval 0.74 - 2.06 MeV and at neutron energies 3.0 MeV and 14.9 MeV. Total gamma ray production cross sections, level population in inelastic neutron scattering, yields of gamma rays from fission fragments, and fission cross sections were obtained.

1. Introduction

The ^{235}U, ^{238}U and ^{232}Th are the principal fuel elements. This defines the practical interest to the investigation carried out. High resolution in-beam gamma spectroscopy is an effective and comparatively cheap method, which gives detailed data on partial neutron inelastic scattering cross sections, nuclear structure and nuclear reaction mechanism. Besides, in case of fissioning nuclei, this method allows to investigate characteristics of nuclear fission such as independent yields and mean angular moment of fission fragments as well as properties of fission fragments itself.

There are several experiments devoted to measurement of gamma spectra of actinoide nuclei interacting with fast neutrons [1-4]. They studied mainly gamma rays accomplishing the inelastic neutron scattering on the ^{232}Th and ^{238}U nuclei. Most detailed, this problem was investigated in works of the Lowel University group[4] where excitation functions were determined in neutron energy interval 0.8 - 2.5 MeV. Later, this group carried out the direct measurement of the inelastic neutron scattering cross sections registering the scattered neutrons[5].

It should be noted that the extraction of partial neutron inelastic cross sections from experiments on gamma spectra measurement requires great attention. The

studied spectra consist of hundreds gamma peaks, most of which are very small. In the picture observed, the gamma lines are involved that are emitted by products of the natural radioactive decay of the target nuclei, by excited fission fragments and by excited target nuclei as well. Characteristics of gamma spectra are well known for the first type of γ-radiation only. It means that full decoding of gamma spectra is hardly possible and missing of gamma lines as well as wrong appointments of them are rather probably. Unfortunately, no one from papers[1-4] contained corrections for population of levels by unobserved gamma transitions from the states lying higher. Only qualitative corrections were made for E0-transitions. Prompt gamma rays of fission fragments were not identified in these works too. Sometimes it could lead to mistakes.

The present paper reviews results of three experiments carried out in the Khlopin Radium Institute at neutron energy 3.0 MeV, 14.9 MeV and in interval of 0.74-2.06 MeV.

2. Measurements at neutron energy 3.0 MeV and 14.9 MeV

Measurements were carried out at the Neutron Generator NG-400 that was operated in the pulse mode. The metallic samples of the ^{232}Th, ^{235}U and ^{238}U were used. They had the cylindrical form and weighted 116.5, 100.2 and 186.7 g, respectively. The gamma spectra were measured in the time window of 25 ns by means of the Ge(Li) detector that was enclosed in the shield made of lead and hydrogen- and boron-containing materials. More detailed, the experimental procedure was described in [6,7,8].

Several hundreds of gamma peaks were revealed in the spectra. At neutron energy 3 MeV, the results could be interpreted comparatively easily because the most intensive gamma peaks of the ^{232}Th and ^{238}U spectra are related to the (n, n'γ) reaction.

2.1 Gamma rays accomplishing inelastic scattering of neutrons

Identification of gamma rays belonging to the inelastic neutron scattering was made using available level schemes of the ^{232}Th and ^{238}U [9,10]. Analyzing energies and intensities of the measured gamma lines, the level scheme of the ^{238}U was modified slightly [11].

However, the level schemes remain incomplete. It is quite obviously at excitation energies higher than 1.2 MeV. To calculate the population of levels more reliable we supposed the continuous distribution of levels for $E^* > 1.2$ MeV with

parameters of the paper [12]. The calculations were made using STAPRE code [13]. The penetration coefficients were taken from the coupled channel optical model [14]. Parametrization of fission barriers and level densities above and between them was done according to [15]. The radiative strength functions were described by the Weisskopf form at normalizing of the absolute radiative widths to the data of [16].

In tables 1 and 2, the experimental cross sections of the ^{232}Th and ^{238}U level population in the (n, n'γ) reaction are compared with the results of calculations. The comparison was made for neutron energy 3.0 MeV. On the whole, the data are in a satisfactory agreement.

At neutron energy 3.0 MeV, the total gamma ray production cross sections were determined using response matrix and regularized unfolding method [17]. In Fig. 1 the experimental total gamma spectra are compared with the calculated ones. Since the fission gamma rays production was not calculated in STAPRE code, it was added to the calculated spectra using the data of [18]. The agreement between the experimental and calculated data is quite suticfactory.

2.2. Fission fragment gamma-rays

The remarkable contamination of gamma rays emitted by fission fragments is a significant peculiarity of gamma spectra of fissile nuclei interacting with neutrons. Its share of the total gamma ray production cross section exceeds often 50%. In spectra, the fission gamma rays appear mainly in form of an intense component with a continuous, exponentially failed energy distribution. The individual gamma peaks could be observed for the fission fragments only that have high yield and concentrate all the possible de-excitation paths on a small number of gamma transitions. It takes place for even-even fission fragments lying on the bumps of mass distribution.

In the spectra, there were about 30 gamma lines identified as belonging to the prompt fission fragment gamma radiation. The identification was made by a comparison of the experimental energy values and excitation cross sections of the gamma transitions with the corresponding values obtained from available data on fission cross sections [19], fission fragments yields [20], and level schemes [21].

In Fig. 2, the yields of gamma transitions $2^+ - 0^+$ that complete usually all gamma cascades in even - even nuclei are compared with the expected independent yields of the corresponding fission fragments. Generally, the agreement is quite satisfactory.

The only remarkable exception is the gamma transition 1279.1 keV of the ^{134}Te. Its yield is steady lower. As was shown in [22], this could be explained by the mean fission fragment angular momentum that was about 5.5 $\hbar$. Another confirmation of this value could be obtained from relative intensities of the gamma transitions 4^+ - 2^+ and 6^+ - 4^+ that were observed for several fission fragments too [24].

3. Measurements in neutron energy interval 0.74 - 2.06 MeV

The measurements were performed at the electrostatic accelerator EG-5 with a steady beam. The ^{3}H(p.n)^{3}He reaction was used to generate monochromatic neutrons. The energy spread of neutron beam was about 30 keV. The data were obtained for 30 values of neutron energy in interval of 0.74-2.06 MeV. Most detailed, with a step of 15-25 keV, they were made in vicinity of fission threshold where anomalies in behavior of excitation function of (n, n'γ) reaction are possible. Simultaneously, fission cross sections of the same nuclides were obtained by means of small ionization chambers with thin fissioning layers.

Two scintillate counters determined relative neutron fluences and transmission functions. The absolute neutron fluence was measured by means of two small ionization chambers with layers of ^{237}Np. For the (n, n'γ) excitation function measurement, a Ge(Li)-detector and metallic cylindrical samples were used. Different background components in complex gamma-spectra were determined using the metallic ^{235}U sample and a plastic container filled with oxalic acid. The geometry of experiment is shown in Fig. 3.

The samples were swapped without irradiation interruption. It was done by means of the rotating sample holder governed by mini-computer DVK-3M. Programs written for it allowed data accumulation and saving, and logging of experiment as well.

The results of the ^{232}Th fission cross section measurement are presented on Fig. 5. On the same Figure, the data of work [23] are shown, where the fission cross section of the ^{232}Th was measured with a high energy resolution. The good agreement is observed between the data.

The ^{238}U fission cross section is presented on Fig. 6 along with the data of the ENDF/B-V [19]. A small difference has been revealed between the data near the fission threshold. This can be connected with the problem of neutron beam energy spread and the correct determination of the mean neutron energy.

Results of the (n, n'γ) cross section measurement are shown on Fig. 7 and 8. Generally, they correspond to the data of [4]. The systematic disagreement for the level 950 keV of the ^{238}U and 1023 keV of the ^{232}Th may be related to the difference in level schemes used.

The role of level population by unobserved γ-transitions is illustrated in Fig. 9. In the calculations, it was supposed that levels have the continuous distribution at excitation energy higher 1.2 MeV with the density of [12].

Summary

Gamma-spectra of the ^{232}Th, ^{235}U and ^{238}U were measured using Ge(Li) detector and computerized set-up at En = 3.0 MeV, 14.9 MeV and 0.7 - 2.1 MeV. Several hundreds of γ-peaks were revealed in the spectra. Among them, the prompt gamma-rays from fission fragments were identified. It was shown that yields of gamma-transitions from the first excited state 2^+ to the ground state 0+ in the even-even fission fragments are very close to the expected independent yields of these fission fragments. The intensities of g-transitions 4^+ - 2^+ and 6^+ - 4^+ inside the ground state rotational bands agree with the assumption that the mean angular moment of fission fragments is equal to 5.5 $\hbar$.

The inelastic scattering gamma rays were identified for the ^{232}Th and ^{238}U. Analysis of their intensities and energies allow to suggest some new levels in the level scheme of the ^{238}U. The partial cross sections were determined for level excitation in the (n, n'γ) reaction. The inelastic scattering cross sections can be obtained from these data after corrections on level population by unobserved γ-transitions from "the continuum" taking into account dependence of the γ-transition probability dependence on the structure of nuclei studied.

The total gamma ray production cross section was determined at neutron energy 3.0 MeV. The comparison with the calculated by STAPRE gamma spectra was made and a satisfactory agreement was found.

Simultaneously with the inelastic gamma spectra measurement, the fission cross sections were determined for the ^{232}Th and ^{238}U with the energy resolution of about 30 keV in the neutron energy interval 0.74 - 2.06 MeV. The data for the ^{232}Th agree well with the data of work [23]. The ^{238}U fission cross section is about 10% lower then the data of [19] in the region near the fission threshold.

References

1) W.R.McMurray, I.J.Van Heerden: Zeitshrift fur Physik 253, p.289 (1972).

2) W.P.Poenitz, J.F.Whalen, and A.B.Smith: Proc. of Int. Conf. on Nuclear Cross Section for Technology, Knoxville, 1979, p. 698 (1980).

3) D.K.Olsen, G.L.Morgan, and J.W.McConnel, Ibid., p. 677.

4) D.W.S.Chan, J.J.Egan, A.Mitler and E.Sheldon: Phys. Rev. C, 26, 841 (1982) / D.W.S.Chan and E.Sheldon: Ibid., p, 861.
5) E Sheldon, L.E.Begian, C.A.Clarcia et al.: J. Phys. G: Nucl. Phys., 11, 237 (1986) / E.Sheldon, L.E.Begian, D.W.S.Chan: Ibid., 12, p.443.
6) E.M.Kozulin, G.A.Tutin, A.A.Filatenkov: Proc. 5th All Union Conf. on Neutr. Phys. (Rus.), part 4, p.242 (1980).
7) Blinov M.V., Filatenkov A.A., Sciborsky B.D., et al.: VANT, Nuclear constants (Rus.), 3(57), p. 3-12 (1984).
8) A.A.Filatenkov, M.V.Blinov, S.A.Yegorov, et al.: Proc. Int. Conf. on Nuclear Data for Science and Technology, May/June 1988, Mito, Japan, p. 79, Salkon, Tokyo (1988).
9) M.R.Smorak: Nuclear Data Sheets, 63, p.139 (1991).
10) E.N.Shurshikov: Nuclear Data Sheets, 53, p.601 (1988).
11) A.A.Filatenkov : 38th All Union Conf. on Nuclear Spectroscopy and Nucl. Sructure (Rus.), p.129 (1988).
12) G.V.Antipov et al. Progr. Report ITMO AN BSSR (Rus.), No. 3 (1982).
13) M.Uhl, B.Stromeier: Report IRK-76/01, Vienna (1976).
14)Ch.Lagrange: NEANDC(E), 228"L" (1982).
15)J.E.Lynn: INDC(USA), N. 092/L, p.345 (1983).
16) T.S.Belanova et al.: Radiative Neutron Capture (Rus.), Moscow (1986).
17) A.I.Tikhonov, V.A.Arsenin: Incorrect tasks' solution methods (Rus.) Moscow (1979).
18) V.V.Verbinsky, H.Weber, R,E.Sund: Phys. Rev. C, 7, p.1173 (1973).
19) Z.Body: Handbook on Nuclear Activation Data, p.29, IAEA, Vienna (1987).
20) E.A.C.Crouch: Atom. Data and Nuclear Data Tables, 19, p.500 (1977).
21) M.Sakai: Atom. Data and Nuclear Data Tables, 31, p.399 (1984).
22) A.A.Filatenkov, S.V.Chuvaev: INDC (NDS)-238L, p.31-36 (1990).
23) J.Blons et al. Nucl.Phys., A414, No. 1, p.1-41 (1984).
24) A.A.Filatenkov : 38th All Union Conf. on Nuclear Spectroscopy and Nucl. Sructure (Rus.), p.127(1988).

Table 1. Level population in the ^{232}Th(n, n'γ) reaction at neutron energy 3.0 MeV

$E_{lev.}$	$I^{\pi}K^{\pi}$		Population (mb)	
			Exper.	Theor.
0	0^+0^+			3095
49.4	2^+0^+			2824
162.1	4^+0^+			1563
333.2	6^+0^+		320(70)	468
556.9	8^+0^+		27(9)	66
714.2	1^-0^-	k	186(13)	133
730.4	0^+0^+	e	23(4)	32
774.1	2^+0^-	e	225(15)	329
774.4	3^-0^-			
785.4	2^+2^+	k	170(15)	136
829.6	3^+2^+		131(9)	154
873.0	4^+0^-	e	22(2)	124
883.6	5^-0^-		100(10)	113
890.1	4^+2^+		110(20)	120
960.4	5^+2^+		65(9)	78
1042.5	7^-0^-		14(4)	25
1072.9	2^+		67(5)	77
1077.3	1^-		61(5)	61
1078.7	0^+		23(4)	17
1105.7	3^-		81(9)	88
1122.8	2^+		83(9)	71
1143.3			41(4)	
1148.3			9(2)	
1182.5	3^-		47(4)	78

Table 2. Level population in the ^{238}U(n, n'γ) reaction at neutron energy 3.0 MeV

$E_{lev.}$ (keV)	$I^{\pi}K^{\pi}$		Population (mb)	
			Exper.	Theor.
0	0^+0^+			2758
44.9	2^+0^+			2539
148.4	4^+0^+			1487
307.2	6^+0^+		310(90)	436
517.9	8^+0^+		30(10)	58
680.1	1^-0^-	k	225(24)	152
731.9	3^-0^-		240(25)	204
775.7	10^+0^+			2
826.8	5^-0^-		100(15)	115
927.0	0^+0^+	e		15
930.8	1^-1^-	k	115(15)	55
950.0	2^-1^-		140(30)	72
966.1	7^-0^-		25(4)	28
967.1	2^+0^+		80(10)	64
993	0^+0^+			13
997.5	3^-1^-		105(20)	80
1037.3	2^+0^+	e	17(7)	53
1057	4^+0^+	e	<15	59
1059.7	3^+3^+	k	140(20)	62
1060.6	2^+2^+	k	100(15)	50
1105.5	4^+3^+		45(10)	48
1106.2	3^+2^+		80(15)	55
1126.5	4^+0^+	e	<25	47
1128.7	2^-2^-		140(15)	45
1150.3	9^-0^-			1
1162.5	5^+3^+		20(8)	24
1167.9	4^+2^+		47(9)	42
1169.7	3^-2^-		60(15)	48
1223.9	2^+		35(4)	41
1239.4	5^+2^+		27(7)	23

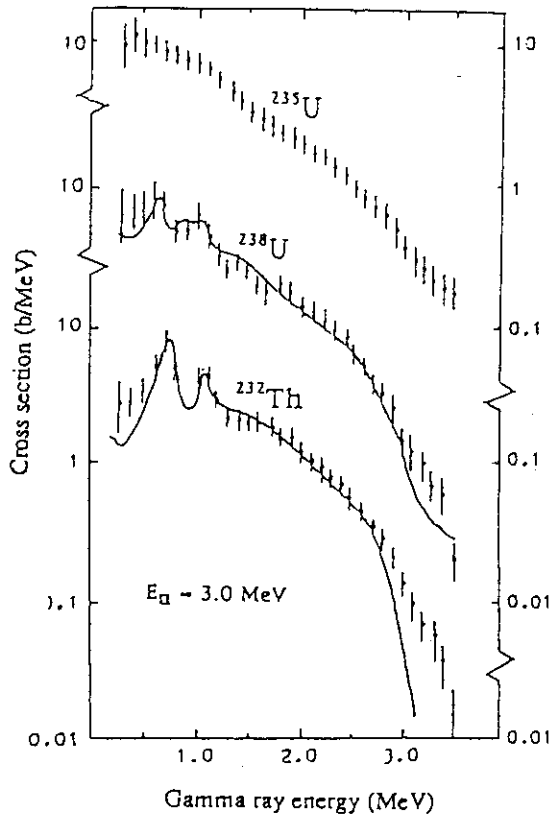

Fig. 1. Total gamma ray production cross section at neutron energy 3.0 MeV. Curve: those calculated by statistical model.

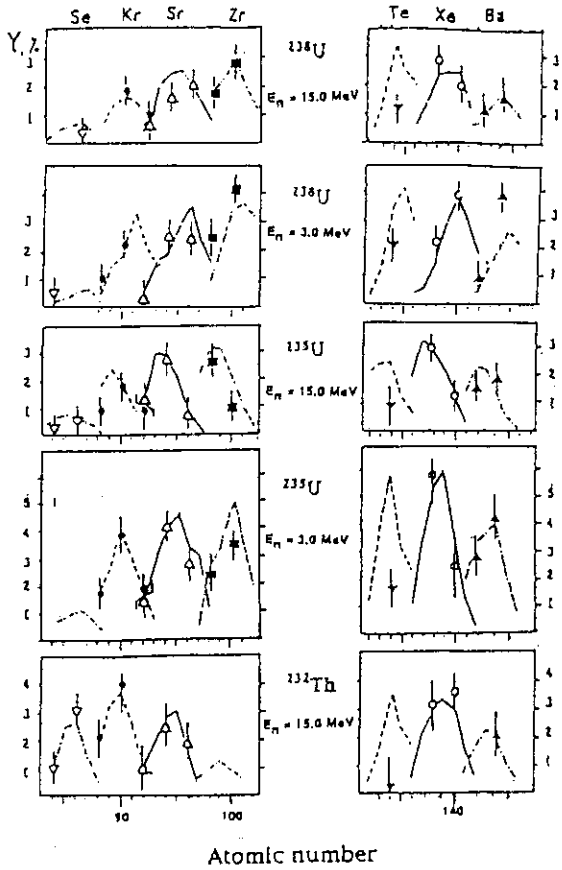

Fig. 2. Experimental yields of γ-transitions $2^+ - 0^+$ in the even-even fission fragments in comparency with the independent yields of the corresponding fission fragments [20].

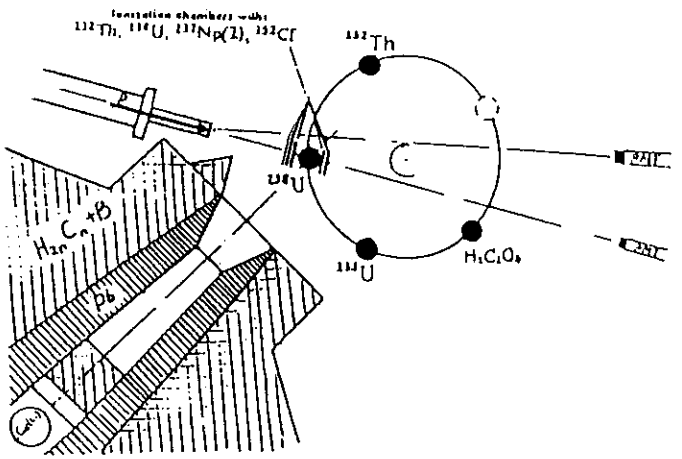

Fig. 3. Geometry of the experiment at EG-5.

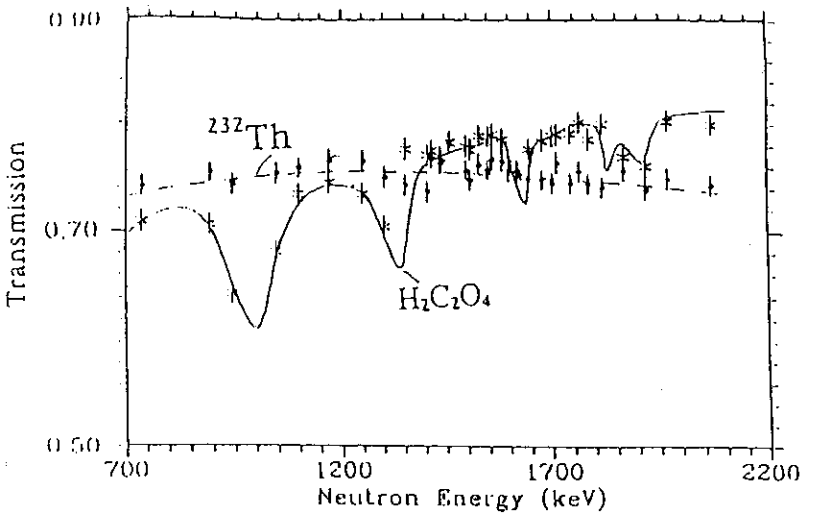

Fig. 4. Reduction of neutron fluence passed trough cylindrical samples of the ^{232}Th (o) and $H_2C_2O_4$ (x). Full and dotted lines - calculation.

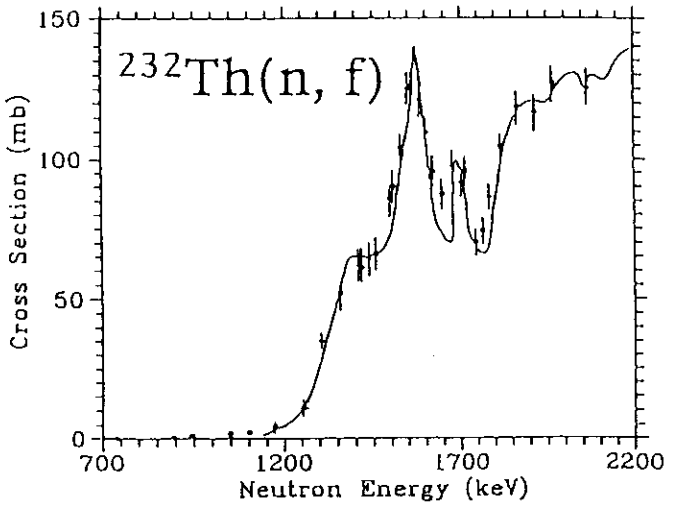

Fig. 5. The fission cross section of the ^{232}Th. Curve - from the work J.Blons et al., Nucl. Phys., A414, p.1 (1984).

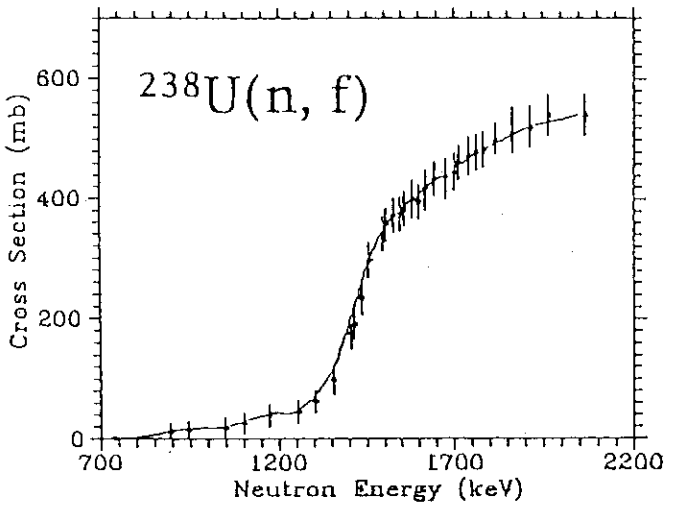

Fig. 6. The fission cross section of the 238U. Curve - ENDF/B-V, Mod. 2, Dosimetry Library.

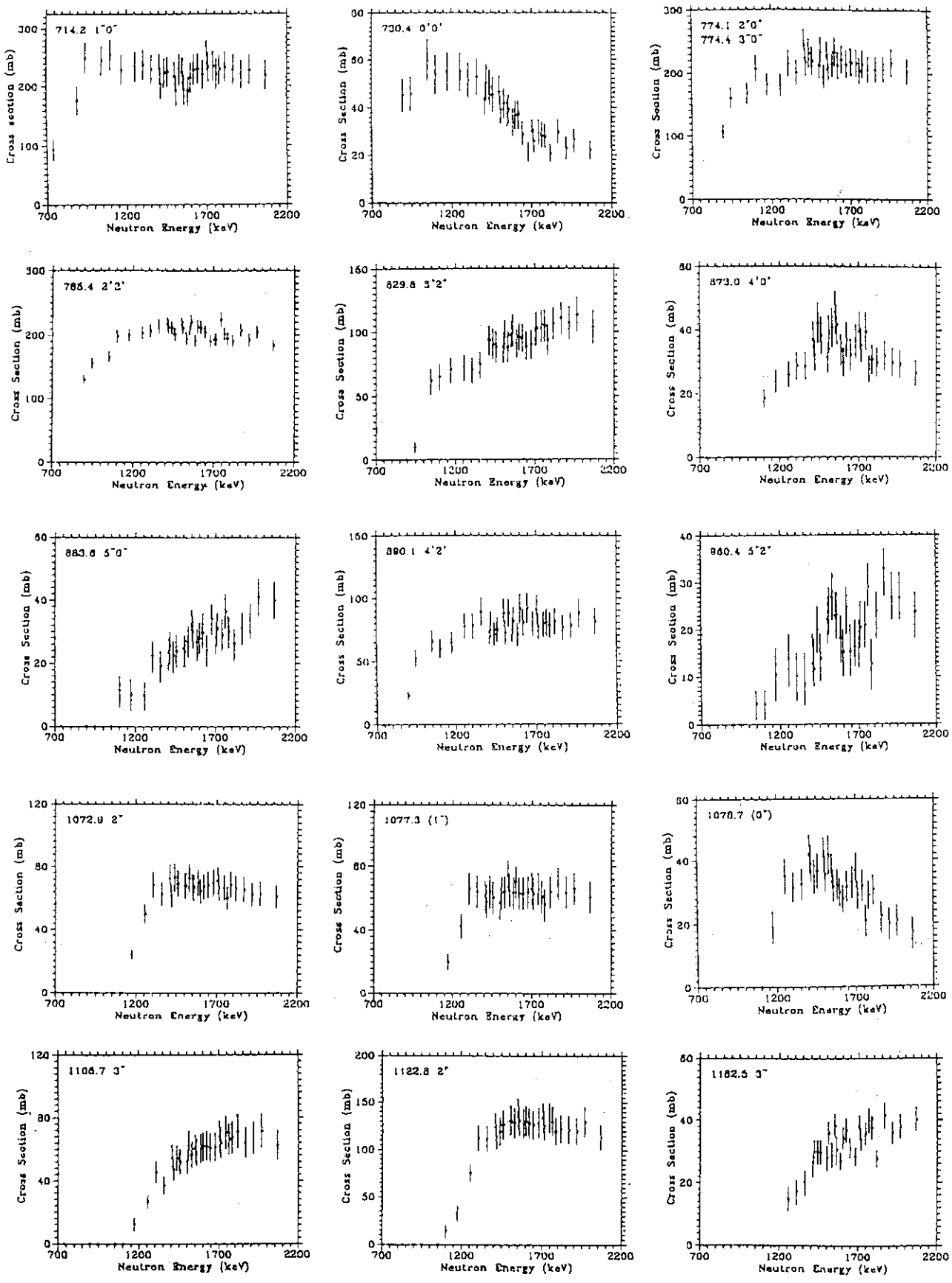

Fig. 7. Excitation functions of the ^{232}Th(n, n'γ) reaction.

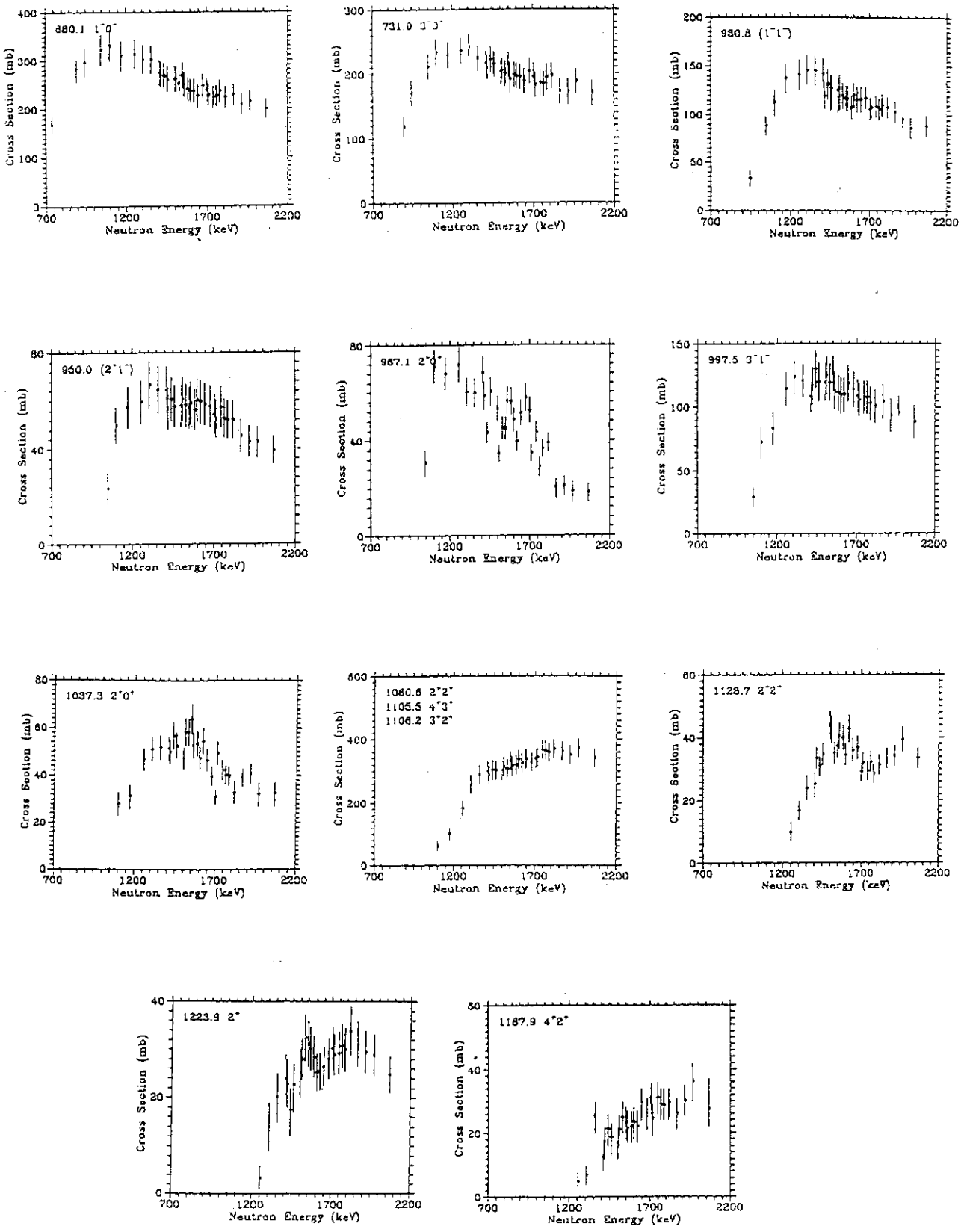

Fig. 8. Excitation functions of the $^{238}U(n, n'\gamma)$ reaction.

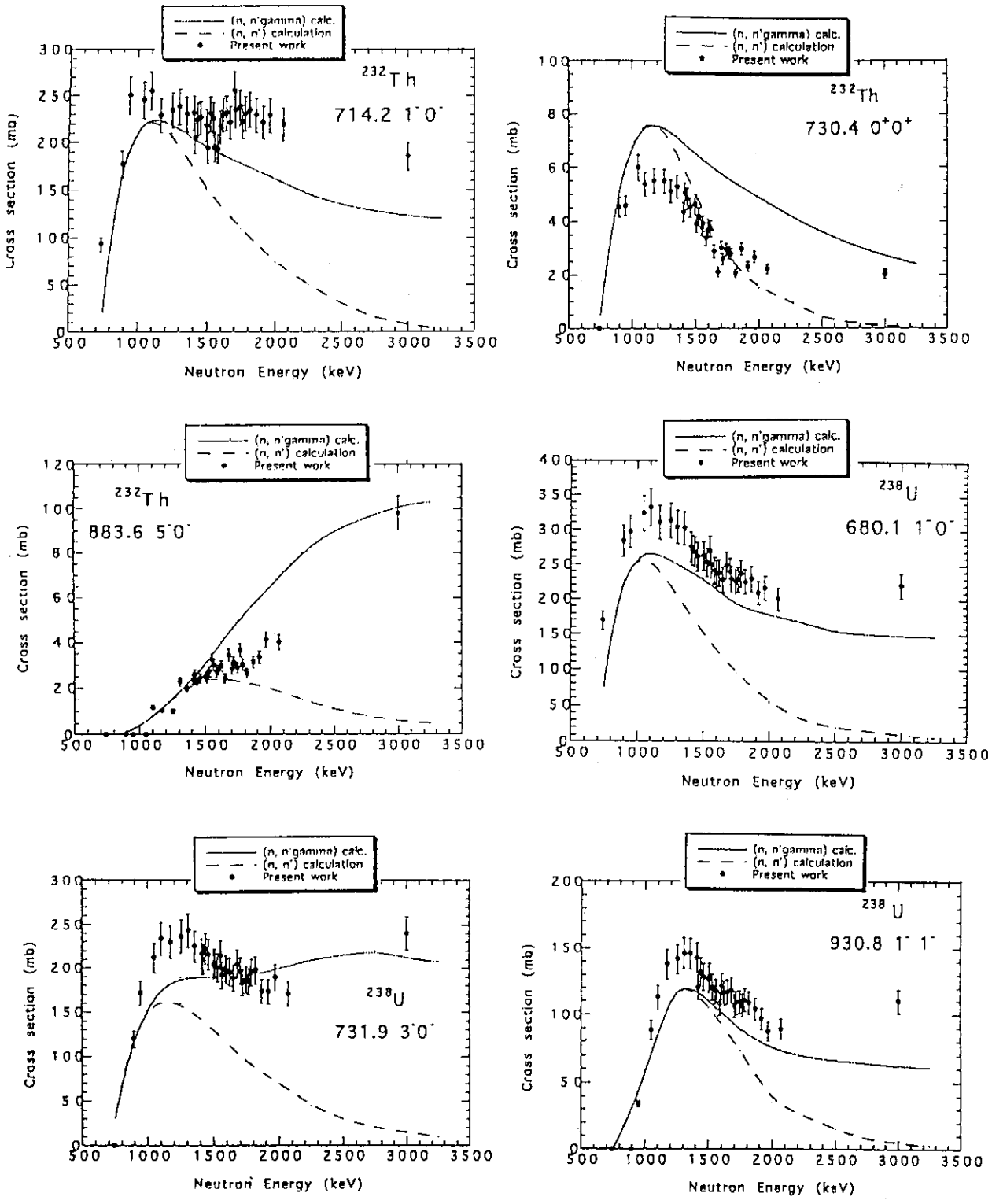

Fig. 9. Excitation functions of the ^{232}Th(n, n'γ) and ^{238}U(n, n'γ) reactions. Points - this experiment; curves - calculation: dotted line - inelastic neutron scattering only; solid line - the level population by γ-transitions from "continuum" ($E^* > 1.2$ MeV) is added.

2. 2 Integral Testing of JENDL-3. 2

2. 2. 1 Benchmark Tests of JENDL-3. 2 for Thermal and Fast Reactors

Hideki Takano
Japan Atomic Energy Research Institute
Tokai, Ibaraki, 319-11, Japan
+81-292-82-6151

Benchmark calculations for a variety of thermal and fast reactors have been performed by using the newly evaluated JENDL-3 Version-2 (JENDL-3.2) file. In the thermal reactor calculations for the uranium and plutonium fueled cores of TRX and TCA, the k_{eff} and lattice parameters were well predicted.The fast reactor calculations for ZPPR-9 and FCA assemblies showed that the k_{eff}, reactivity worth of Doppler, sodium void and control rod, and reaction rate distribution were in a very good agreement with the experiments.

I .INTRODUCTION

A great deal of effort have been required for development and validation of various neutronic calculation methods and nuclear data libraries, and various critical experiments for thermal and fast reactors have been performed to verify these methods and data. Especially, the development of new nuclear data library requires accurate verification and validation

JENDL-3.1[1] was revised on the basis of much feedback information by various benchmark tests[2], and the revised version (JENDL-3.2) was released in June 1994[3]. In this paper, the benchmark tests of the newly evaluated JENDL-3.2 file will be described for thermal and fast reactors.

In thermal critical experiments were selected the uranium fuel cores TRX[4] and TCA-UO_2[5] with water moderated lattice of slightly enriched uranium metal and oxide rods, respectively, and as plutonium fueled cores TCA-MOX[5] with 3.0 wt.% Pu rods and the tight lattice Pu cores of PROTEUS experiments[6]. Furthermore, a lots of critical safety experiments such as ORNL[4] of U-cores, PNL[4] of Pu-cores and M&J[7] of ^{233}U-cores were selected. The benchmark calculations were performed with the continuous energy Monte Carlo code MVP[8] and integral transport code SRAC-93[9]. The results calculated will be described here.

Fast reactor benchmark cores consist of various critical assemblies such as MONJU plot type mock-up core (FCA-VI-2), the large LMFBR mock-up core (ZPPR-9), the FCA-IX cores with a wide variety neutron spectrum shapes, very small cores such as GODIVA, JEZEBEL and FLATTOP with hard neutron spectra. The benchmark calculations were performed by using the 70-group cross section library JFS-3-J32 based on JENDL-3.2. The very small cores were calculated with the MVP code. The basic integral data such as effective multiplication factor, central reaction rate ratios, sodium void reactivity, Doppler reactivity and control rod worth are compared between the calculations and experiments.

II. THERMAL REACTOR BENCHMARK

Various cores were analyzed with some different nuclear libraries; JENDL-2, JENDL-3.1, JENDL-3.2P and JENDL-3.2. JENDL-3.2P is the preliminary version for the final version of

JENDL-3.2. The main difference between both libraries are as follows: In JENDL-3.2 the inelastic scattering cross sections of ^{238}U is smaller than those of JENDL-3.2P, and the fission spectrum of ^{233}U is softer than that of JENDL-3.2P.

A. Uranium (^{235}U) Fueled Cores

Figure 1 shows the k_{eff} and lattice parameters in TRX-2 core calculated with the continuous energy Monte Carlo code MVP. The k_{eff} value of JENDL-3.2 is increased by 0.5% as comparing that of JENDL-3.1, because the capture resonance integral of ^{235}U is considerably decreased in JENDL-3.2 as shown in Table 1. The lattice parameters of ρ-28, δ-25 and δ-28 are better predicted with JENDL-3.2. The k_{eff} values calculated for the TCA with UO_2 rods are slightly overestimated as shown in Fig. 2. The k_{eff} calculated with MVP for the critical safety ORNL cores are shown in Fig. 3. The results for JENDL-3.2 improve a tendency of underestimate observed in JENDL-3.1, excepting for the ratio of H/U = 0.

B. Plutonium Fueled Cores

The k_{eff} values of the TCA cores with the MOX rods in the cell pitch from 1.8 to 2.5 cm are compared in Fig. 4. The calculations were conducted with the MVP code. The results of JENDL-3.2 predict very well the experiments. Figure 5 shows the k_{eff} values calculated for the PNL cores, and they overestimate the experiments in lower ratio values than H/Pu = 1000.

For the tight lattice PROTEUS cores, the k_{eff} values and central reaction rate ratios were calculated with the SRAC-93 code and the results are compared in Tables 2 and 3. JENDL-3.2 predicts very well the k_{eff} for the coolant unvoid and voided cores. The C/E values of the ratio of ^{238}U capture to ^{239}Pu fission reaction rate (C8/F9) depends on the coolant voided fractions.

C. ^{233}U Fueled Cores

Figure 6 shows the k_{eff} values calculated with MVP for ^{233}U cores. It is observed that they are predicted very well in the values of H/^{233}U from 400 to 2000, but they are overestimated in the small values of H/^{233}U.

Ⅲ. FAST REACTOR BENCHMARK

A. GODIVA, JEZEBEL and FLATTOP

Very small cores with hard neutron spectrum were selected as plutonium fueled JEZEBEL,JEZEBEL-Pu,FLATTOP-Pu and THOR, enriched ^{235}U fueled GODIVA,FLATTOP-25 and BIGTEN, and enriched ^{233}U fueled JEZEBEL-23 and FLATTOP-23. These cores were analyzed by using the MVP code, and the results are shown in Fig. 7. The k_{eff} values for Pu cores are slightly underestimated excepting for that of THOR with thorium reflector. The results for ^{235}U cores are in good agreement with the experiments, and those of ^{233}U cores are improved but overestimated still.

B. ZPPR-9 and FCA-VI-2

The k_{eff} values are well predicted with JENDL-3.2 as shown in Table 4. In Table 5, the C/E values for Doppler reactivities of natural UO_2 sample are increased by JENDL-3.2 and become

closer to the experimental values. Because the unresolved resonance region of ^{238}U is expanded up to 150 keV.

The C/E values of central reaction rate ratios for ZPPR-9 are shown in Fig. 8. The fission rate ratios of ^{238}U to ^{235}U and ^{239}Pu are underestimated by about 6 % due to softer fission spectrum of JENDL-3.2 than Madland-Nix one of JENDL-3.1. The ratio of ^{238}U capture to ^{239}Pu fission rate is overestimated by 5 %.

Figure 9 shows the C/E values of the sodium void reactivities with the increase of void regions, and they are satisfactory both of JENDL-3.1 and 3.2.The C/E values of control rod worth are well predicted with JENDL-3.2 as shown in Fig. 10.

Figure 11 shows the C/E values of ^{239}Pu fission rate radial distribution, and JENDL-3.2 overestimates slightly the experiments in the outer core region.

C. FCA-IX

The FCA-IX-1, 2 and 3 are uranium fueled cores with soft spectrum well moderated by graphite. As shown in Fig. 12, the k_{eff} values underestimated by JENDL-3.1 are well predicted with JENDL-3.2. This is due to decreasing the capture resonance integral of ^{235}U in JENDL-3.2 as described at the thermal reactor benchmark.

IV. CONCLUSION

The k_{eff} values of ^{235}U fueled thermal and fast reactor cores were well predicted with JENDL-3.2 as improving the underestimate by JENDL-3.1.

In Pu fueled cores, JENDL-3.2 predicted very well the k_{eff} values for various thermal MOX cores from tight to loose lattice assemblies. And in the fast reactor benchmark, the values calculated with JENDL-3.2 for k_{eff}, Doppler effect, sodium void reactivity, control rod worth and power distribution were in good agreement with the experimental results. But, the reaction rate ratio of ^{238}U capture to ^{239}Pu fission and the threshold fission rate ratio of ^{238}U to ^{235}U was underestimated by 4 and 6 % in ZPPR-9, respectively.

References

1) K. Shibata et al.,"Japanese Evaluated Nuclear Data Library Version-3, JENDL-3," JAERI 1319 (1990).
2) H. Takano et al.,"Benchmark Tests of JENDL-3 for Thermal and Fast Reactors," Proc. Int. Conf. Physics of Reactors, Marseille, April, Vol. 3, PI-21(1990).
3) Y. Kikuchi,"JENDL-3 Revision-2 (JENDL-3.2)," presented at the International Conference of Nuclear Data and Science Technology, Gatlinburg, 1994.
4) "Cross Section Evaluation Working Group Benchmark Specifications," ENDF-202, BNL-19302, 1974.
5) H. Tsuruta et al.: JAERI 1254, 1978.
6) R. Chawla et al.: Nucl. Technology., 67,296(1984) and 73, 296(1986).
7) McNeany and Jenkins: Nucl. Sci. Eng., 65, 441 (1978).
8) T. Mori et al.: J. Nucl. Sci. Technol., 29, 325 (1992).
9) T. Kugo et al.:" A Version to Allow Arbitrary Temperature Treatment and Release of the Latest Version SRAC-93," JAERI-Review 94-009, p64, 1994.

Table 1 Comparison of resonance integrals and thermal cross sections in JENDL-3 nuclear data library (barn)

		2200m/s		R.I.	
		fission	capture	fission	capture
U-235	JENDL-3.1	584.0	96.0	275	152
	JENDL-3.2	584.4	98.81	279	134
U-238	JENDL-3.1	0.110E-6	2.681	2.02	279
	JENDL-3.2	11.8E-6	2.717	1.72	277
Pu-239	JENDL-3.1	746	270	299	185
	JENDL-3.2	747.4	270.3	302.6	181.6
Pu-241	JENDL-3.1	1015	363.0	590	187
	JENDL-3.2	1012.0	361.53	572.6	179.9

Table 2 The C/E values of k-inf calculated with SRAC for PROTEUS 1,2 and 3

Core	Exp.	JENDL-2	JENDL-3.1	JENDL-3.2P	JENDL-3.2
1	1.045±1.1%	1.000	1.003	1.003	1.004
2	0.991±1.5%	0.996	1.000	0.999	1.000
3	0.905±1.1%	0.992	1.011	0.995	1.000

Void fraction: core-1; 0.0 %, core-2; 100 %, core-3; 42.5 %.

Table 3 The C/E values central reaction rate ratios calculated with SRAC for PROTEUS-1, 2 and 3

Reaction	Core	Error(%)	J-2	J-3.1	J-3.2P	J-3.2
C8/F9	1	2.2	0.972	0.976	0.972	0.971
	3	2.0	0.993	0.999	0.994	0.993
	2	1.5	1.036	1.025	1.033	1.029

Table 4 The Comparison of the C/E values of k_{eff} in ZPPR-9 and FCA-VI-2

Core	JENDL-2	JENDL-3.1	JENDL-3.2
ZPPR-9	0.9991	1.0063	0.9967
FCA-VI-2	1.0066	1.0014	0.9992

Table 5 The C/E values of the natural UO_2 Doppler reactivity

Core	Temp.(℃)	JENDL-2	JENDL-3.1	JENDL-3.2
ZPPR-9	300-487	0.91	0.94	0.96
	300-644	0.92	0.95	0.97
	300-794	0.89	0.92	0.94
	300-935	0.93	0.96	0.98
	300-1087	0.92	0.95	0.97
FCA-VI-2	300-823	0.93	0.91	0.95
	300-1073	0.93	0.91	0.95

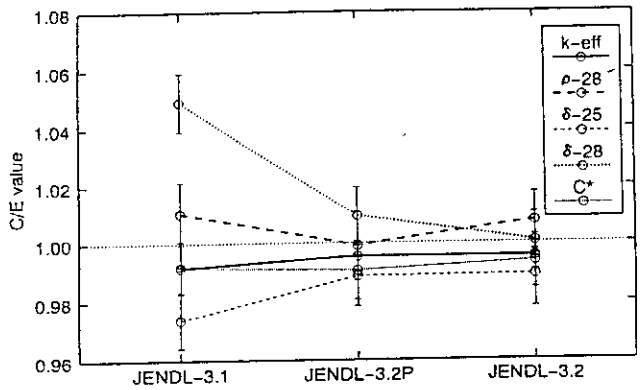

Fig.1 The C/E values of k_{eff} and lattice parameters calculated by the MVP code for TRX-2 core

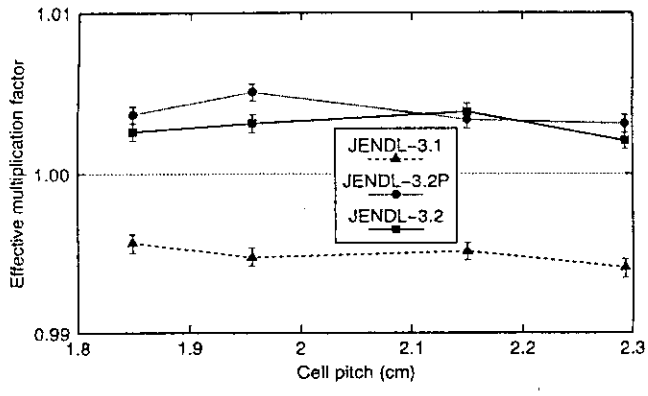

Fig.2 The k_{eff} values calculated by the MVP code for TCA-UO_2 cores

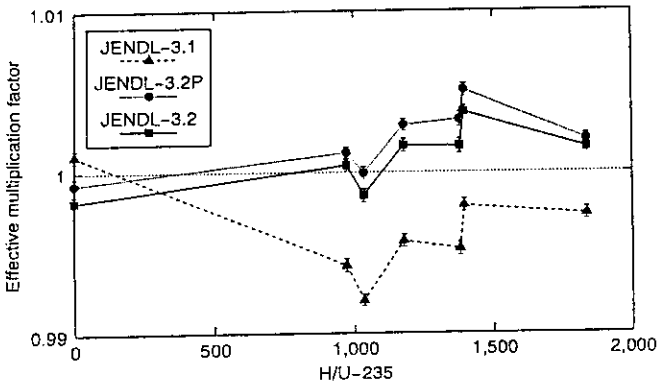

Fig.3 The k_{eff} values calculated with the MVP code for ORNL cores

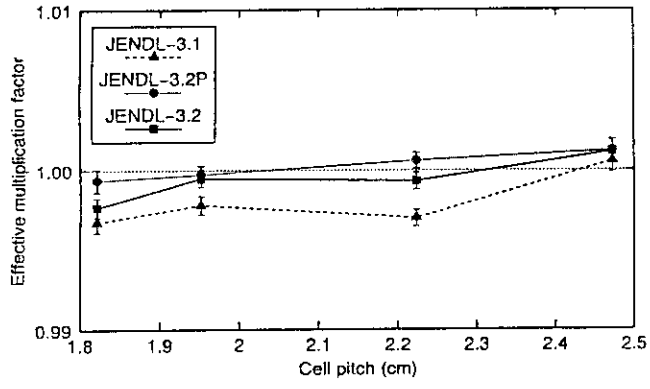

Fig.4 The k_{eff} values calculated with the MVP code for TCA-MOX cores

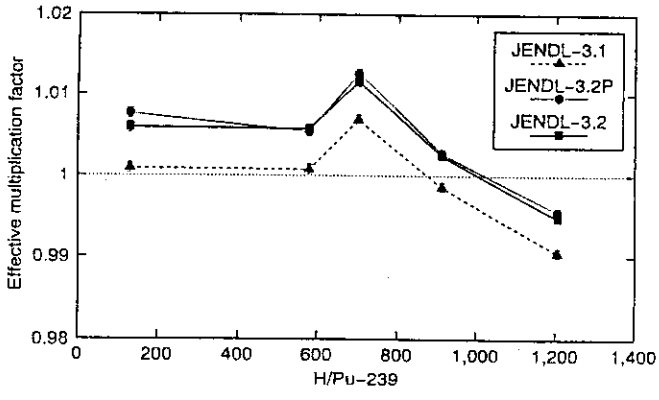

Fig.5 The k_{eff} values calculated with the MVP code for PNL cores.

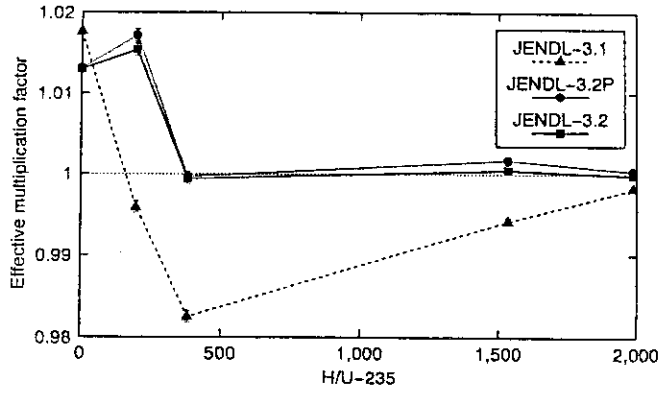

Fig.6 The k_{eff} values calculated with the MVP code for M&J cores.

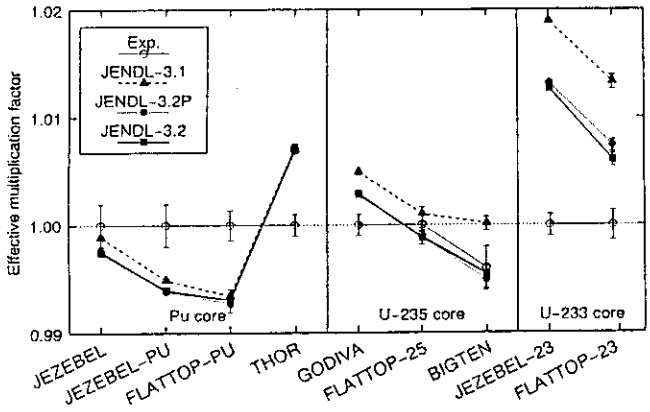

Fig.7 The k_{eff} values calculated with the MVP code for hard neutron spectrum cores

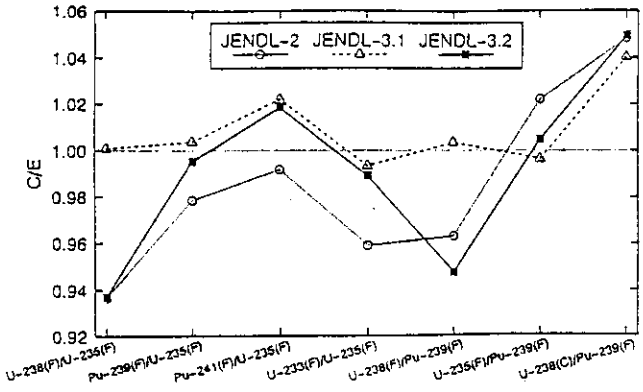

Fig.8 The C/E values of central reaction rate ratios in ZPPR-9

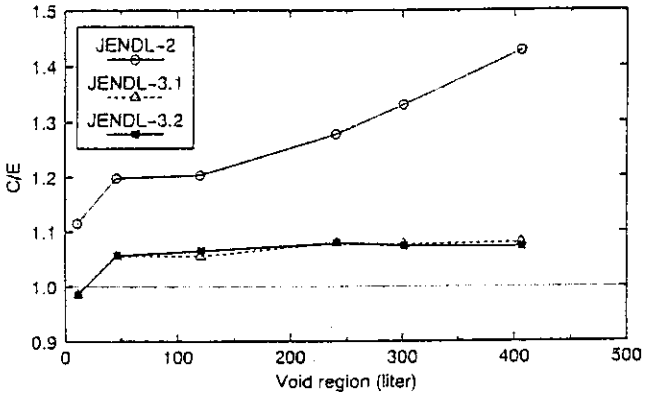

Fig.9 The C/E values of Na-void reactivity in ZPPR-9

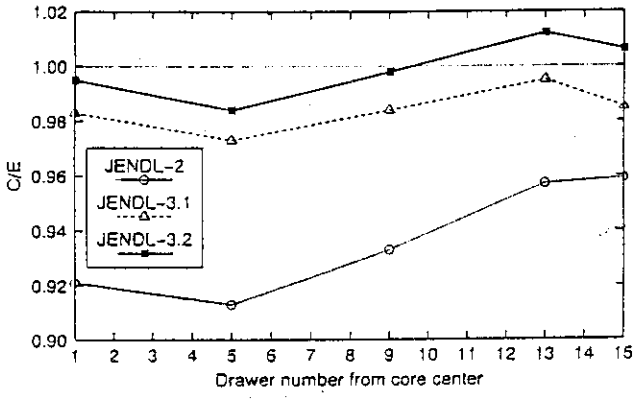

Fig.10 The C/E values of control rod worth in ZPPR-9

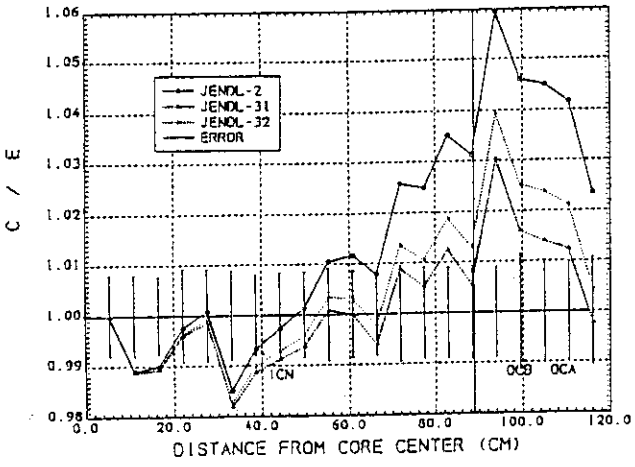

Fig.11 The C/E values of ^{239}Pu fission rate distribution in ZPPR-9

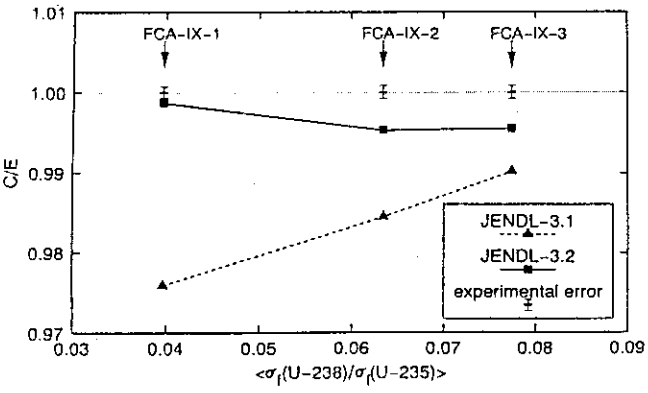

Fig.12 The C/E values of k_{eff} in FCA-IX -1,2 and 3

2.2.2 Measurements and Analyses of ^{238}U Capture to ^{239}Pu Fission Rate Ratio at Fast Critical Assembly

Takeshi SAKURAI, Tatsuo NEMOTO and Susumu IIJIMA
Japan Atomic Energy Research Institute
Tokai-mura, Naka-gun, Ibaraki-ken 319-11

Abstract

A neutron reaction rate ratios of ^{238}U capture to ^{239}Pu fission(C8/F9) were measured at Fast Critical Assembly of Japan Atomic Energy Research Institute in order to evaluate the accuracy of calculation of C8/F9. The measurements were made by a foil activation technique at three assemblies : two assemblies simulating metallic-fueled LMFBR cores and an assembly simulating a Mox-fueled LMFBR core. The analysis of the measurements was made based on JENDL-3.2 nuclear data library. Good agreements between the experiment and the calculation within experimental errors were obtained at all of the mock-up cores.

Introduction

A neutron reaction rate ratio of ^{238}U capture to ^{239}Pu fission(C8/F9) is important as an index of breeding behavior of LMFBR. In the benchmark tests of not only JENDL-2 but also JENDL-3.2, a significant overestimation by about 5% of C8/F9 at ZPPR-9 assembly simulating a large Mox-fueled LMFBR core has been found[1]. The new measurements of C8/F9 have been made at LMFBR mock-up cores providing systematic change in neutron spectrum at Fast Critical Assembly(FCA) of Japan Atomic Energy Research Institute. In this paper, results at two mock-up cores for metallic-fueled LMFBR (assemblies XVI-1 and XVI-2)[2,3] and a mock-up core for Mox-fueled LMFBR (assembly XVII-1)[4] are presented.

LMFBR mock-up cores at FCA

Assembly XVI-1 is a full-scale mock-up core fueled with both plutonium and enriched uranium. Assemblies XVI-2 and XVII-1 are zone-type partial mock-up cores. Each of the assemblies consists of a central test region fueled with plutonium which is surrounded radially by a driver region fueled with plutonium and enriched uranium. Characteristics of these assemblies are summarized in Table 1.

The reaction rates were measured at the core center where a fundamental mode spectrum of each mock-up core was well established. Calculated neutron spectrum and energy components of the ^{238}U capture rates at the present FCA assemblies are given in

figures 1 and 2 respectively. Close similarities on the neutron spectrum and the energy components of the ^{238}U capture rates between FCA assembly XVII-1 and ZPPR-9 assembly are shown in Fig.3. It is indicated from these figures that the present FCA assemblies vary in neutron spectrum from a soft one of a large Mox-fueled core to a hard one of a metallic-fueled core.

Measurement

The reaction rates of ^{239}Pu fission and ^{238}U capture were measured by a foil activation technique with thin metallic depleted uranium foils and plutonium foils covered with aluminum and a high resolution γ -ray spectroscopy system composed of coaxial type Ge detectors and a computer[5]. These foils were placed between plates of core material in a fuel cell during irradiation.

The ^{239}Pu fission rate and the ^{238}U capture rate were determined from the fission product(^{143}Ce, ^{133}I, ^{97}Nb and ^{97}Zr) activities in the plutonium foil and ^{239}Np activity in the depleted uranium foil respectively. Calibration of effective efficiencies of the γ -ray spectroscopy system for the fission rate was made using the plutonium foil irradiated with an absolute fission chamber of ^{239}Pu[6], while a γ -ray source of ^{243}Am-^{239}Np[7] was applied to the calibration for the capture rate. Reliability of the calibration techniques based on the absolute fission chambers and the ^{243}Am-^{239}Np source was confirmed by using a thermal neutron standard field[8].

Cell heterogeneity corrections were applied to the results of the capture rate. The corrections were determined with fine distributions of the capture rate in the fuel cell measured by foil mapping. The corrections were less than 3%.

A small correction of less than 1% was applied to the results of the fission rate at assembly XVII-1 to take account of self shielding of the fission rates in a plutonium fuel plate. This correction was determined by a continuous energy monte-carlo calculation with MVP[9].

Analysis

Analyses of the reaction rate ratios were made by using JFS-3-J32 group constants set[1] based on JENDL-3.2 nuclear data library. Effective cross sections of each core region were calculated by a collision probability method with SLAROM[10] in one dimensional infinite slab geometry. Neutron flux was calculated by a 70-group anisotropic diffusion theory with CITATION-FBR[11] in two dimensional cylindrical geometry.

Results and discussions

A comparison of the measured results of C8/F9 between the FCA assemblies is given in Fig.4. Experimental errors(one σ) were 3.2% at assembly XVI-1 and less than 2.5% at assembly XVI-2 and XVII-1. Components of the errors of the each reaction

rates are summarized in Table 2. More than 20% smaller values of C8/F9 were observed in the metallic-fueled cores than in the Mox-fueled one as shown in Fig.4. These large reductions are caused by a harder neutron spectrum of the metallic-fueled cores than that of the Mox-fueled one as shown in Fig.1.

Calculation to experiment ratios(C/E) of the C8/F9 are summarized in Fig.5. The calculated value agreed well with the experimental one within the experimental error at all of the present mock-up cores where the value of C8/F9 varied considerably.

Conclusion

Measurements of C8/F9 and analyses based on JENDL-3.2 were made at FCA assemblies providing both the soft neutron spectrum of the large Mox-fueled LMFBR and the hard one of the metallic-fueled LMFBR. As a result, no dependence of the C/E value of C8/F9 on neutron spectrum was observed. The calculated values of C8/F9 were in good agreement with the experimental ones within the experimental errors.

The authors are grateful to FCA staffs for their support in the experiments.

References

1) Takano, H., et al. : "BENCHMARK TESTS OF JENDL-3.2 FOR THERMAL AND FAST REACTORS," Proc. Int. Conf. Nuclear Data for Science and Technology, (Gatlinburg, USA, 1994).
2) Iijima, S., et al. : "Benchmark Physics Experiment of Metallic-fueled LMFBR at FCA," JAERI-M 92-196, (1992), (in Japanese).
3) Iijima, S., et al. : "Mock-up Experiments of Metallic-fueled LMFBR in FCA Assembly XVI-2," JAERI-M 93-181, 37, (1993).
4) Iijima, S., et al. : "Mockup Experiments of Mox-fueled LMFBR in FCA Assembly XVII-1," JAERI-Review 94-009, 80, (1994).
5) Nemoto, T. and Ōbu, M. : "Data Processing Code System for Foil Experiments," JAERI-M 84-147, (1984), (in Japanese).
6) Ōbu, M. : "Preparation and Characteristics of Fission Chambers with Actinide Nuclides," JAERI-M 9757, (1981), (in Japanese).
7) Kōno, N., Shinohara, N. : Private communication.
8) Sakurai, T., et al. : "Experimental Comparison of Calibration Methods for Measurement of Reaction Rate by Using Fission Foils," JAERI-M 93-153, (1993), (in Japanese).
9) Mori, T., et al. : "Vectorization of Continuous Energy Monte Carlo Method for Neutron Transport Calculation," J. Nucl. Sci. Technol., 29, 325, (1992).
10) Nakagawa, M. and Tsuchihashi, K. : "SLAROM : A Code for Cell Homogenization of Fast Reactor," JAERI 1294, (1984).
11) Iijima, S. : Private communication.

Table 1 Characteristics of FCA assemblies

Assembly	XVI-1	XVI-2	XVII-1
Fuel	Metallic-fuel	Metallic-fuel	Oxide-fuel
Fuel enrichment	15.4 %*	10.4 %	14.3 %
Dimension of active core			
Height	91.5 cm	91.5 cm	91.5 cm
Radius			
Test-zone	34.3 cm**	34.3 cm	34.3 cm
Driver-zone	45.5 cm***	46.7 cm	47.3 cm

* Pu+^{235}U
** inner core radius
*** outer core radius

Table 2 Components of the experimental errors

^{238}U capture rate		^{239}Pu fission rate	
Intensity of ^{243}Am - ^{239}Np source	0.3%	Deposit mass of a ^{239}Pu fission chamber	0.5%
Counting statistics of a ^{243}Am-^{239}Np source	~0.1%	Counting statistics of a ^{239}Pu fission chamber	~0.3%
Weight of a depleted U foil	0.2%	Corrections of fission chamber count rate *	0.5%~2.0%
Counting statistics of a depleted U foil	0.2%~0.9%	Counting statistics of a Pu foil	0.8%~1.7%
Decay correction (^{239}Np)	0.4%	Counting statistics of a flux level monitor	1.0%~1.5%
γ -ray self attenu -ation correction in a depleted U foil	0.7%	Total	1.5%~3.0%
Cell factor	~0.5%		
Total	1.0%~1.3%		

* Corrections for fission product self attenuation in the deposit and fission counts below bias level

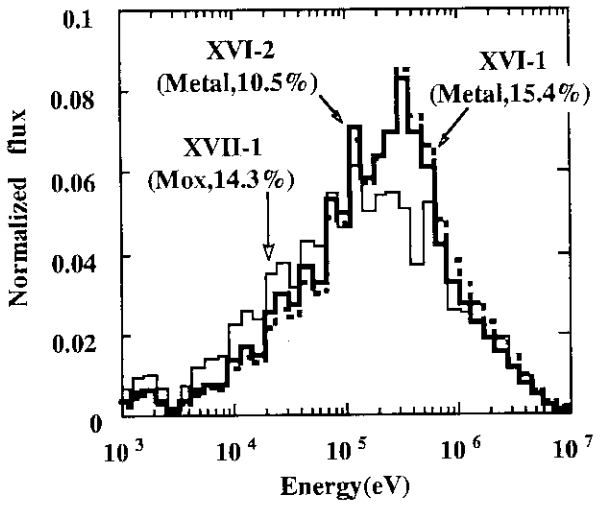

Fig.1 Neutron spectrum at FCA assemblies

( ) : Fuel type and enrichment

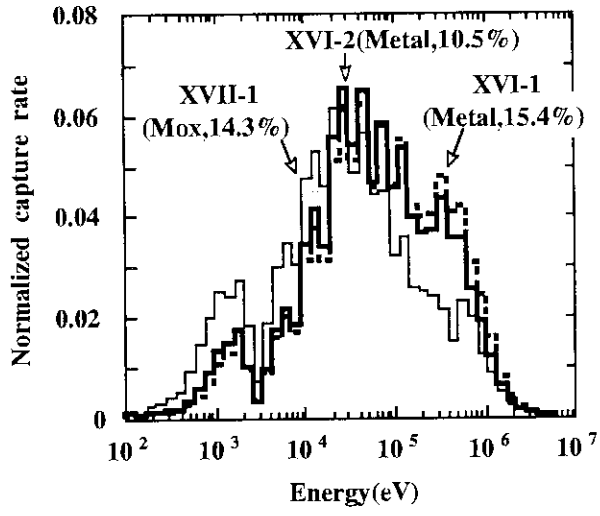

Fig.2 Energy components of U-238 capture rate at FCA assemblies

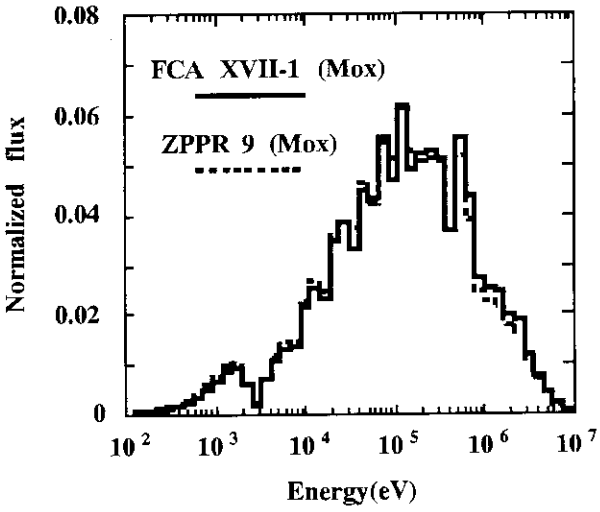

(a) Neutron flux

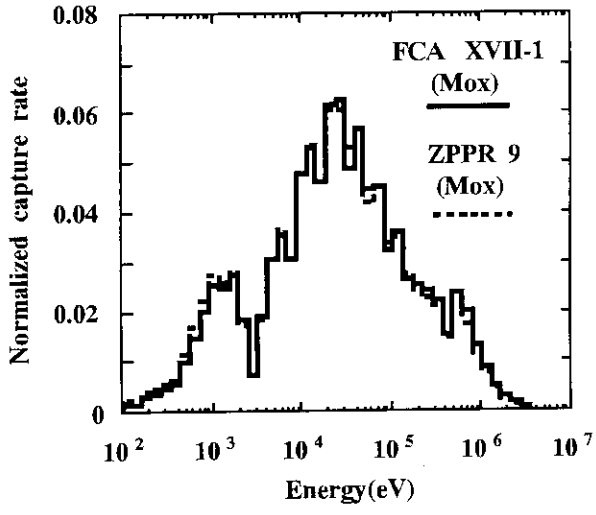

(b) Energy components of U-238 capture rate

Fig.3 Comparison of neutron spectrum and energy components of U-238 capture rate between FCA assembly XVII-1 and ZPPR-9 assembly

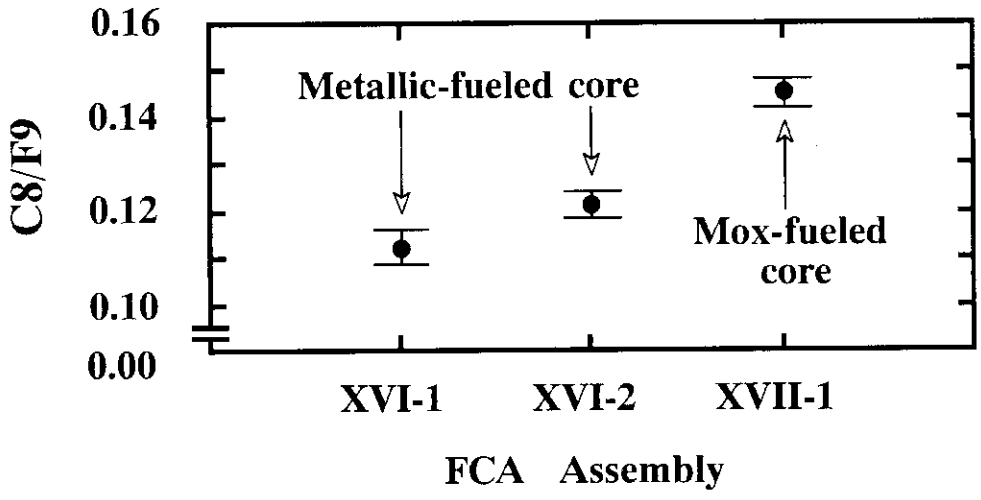

Fig.4 Comparison of the measured C8/F9 between FCA assemblies

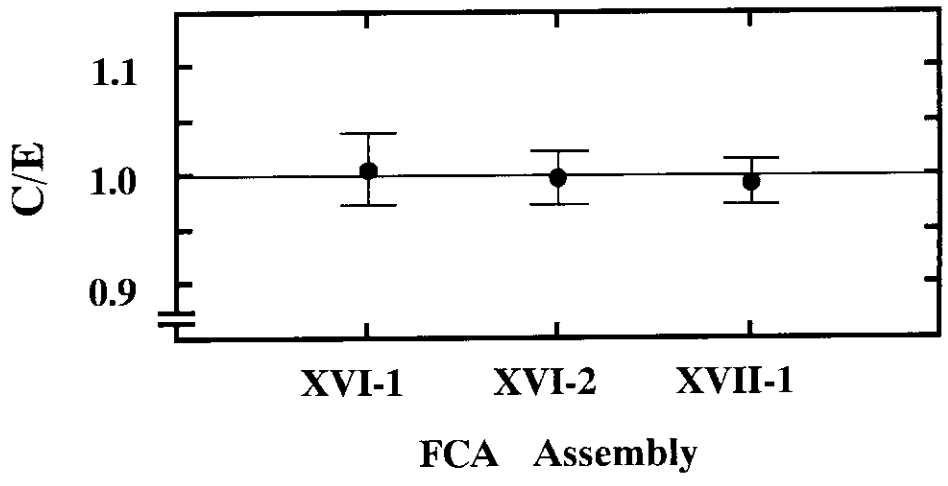

Fig.5 Calculation to experiment ratios(C/E) of the C8/F9 at FCA assemblies

2. 2. 3 Usage of JENDL Dosimetry File for Material Dosimetry in JOYO

Soju SUZUKI

Experimental Reactor Division, O-arai Engineering Center, Power Reactor and Nuclear Fuel Development Corporation, 4002 Narita-cho, O-arai machi, Ibaraki-ken 311-13

Abstract

A cross section set with covariance error matrix for neutron spectrum unfolding has been newly prepared from JENDL-3 dosimetry file and was applied to the dosimetry test in the MK-II core (the irradiation core) of Experimental Fast Reactor "JOYO". The dosimetry results by the new cross section set were compared with the previous ones by ENDF/B-V dosimetry file to evaluate the applicability and accuracy for the fast reactor dosimetry. In this work, it has been concluded that more improvement can be expected for the JOYO dosimetry test by employing JENDL-3 dosimetry file.

1. Introduction

In Experimental Fast Reactor "JOYO" at O-arai Engineering Center of PNC, the reactor material dosimetry by unfolding neutron energy spectrum are carried out to keep the reliability and the accuracy of neutron dose for a number of irradiation tests, in addition to the conventional nuclear calculations. A set of neutron cross section with covariance error matrix is essential to the unfolding and also influences greatly to the final dosimetry results. We have recently prepared a new NEUPAC [1] cross section set based on JENDL-3 dosimetry file [2], which has covariance error data, and have evaluated its applicability to the dosimetry test in the JOYO MK-II core.

2. Outline of Dosimetry Method in JOYO

The neutron dose such as DPA (displacements per atom) and fast fluence are evaluated from the whole neutron spectrum, which is unfolded from reaction rates measured with a set of dosimeters (Fe, Sc, Co, Cu, ^{235}U, ^{238}U, ^{237}Np and others.) [3]. The unfolding computer code, the initial guess spectrum and the cross section sets for the dosimetry test are as follows;

- Spectrum unfolding Code : J1 function code NEUPAC-Jlog
- Initial Guess spectrum : Calculated by DOT3.5 code (21 group or 100 group)
- Cross Section Set : Infinite dilute 103 group with covariance matrix for 10^{-3} eV to 20 MeV

In this work, two different cross section sets [4] have been prepared with NJOY code [5] for unfolding process. One is from ENDF/B-V and another is from JENDL-3 dosimetry file.

3. Results and Discussion

3.1 Unfolded Neutron Spectrum

By using cross section sets based on ENDF/B-V and JENDL-3, two different type of typical fast reactor spectra were unfolded and compared with each other in the fuel region and in the stainless steel reflector region of JOYO. Figure 1 shows the unfolded spectra with its ratio depending on neutron energy by both cross section sets. Tables 1 and 2 summarize the C/E (ratio of calculated value to measured one) for each dosimeter reaction rate before and after spectrum unfolding. Figures 2 and 3 show the sensitivities of the total flux to JENDL-3 and ENDF/B-V in the fuel region, respectively and Figs. 4 and 5 show those in the reflector region.

The result of JENDL-3 in the fuel region is about 10 % smaller at the spectrum peak in the energy range between 0.1 MeV and 1 MeV, and is about 50 % larger around 5×10^{-3} MeV and 2×10^{-4} MeV than that of ENDF/B-V. The main reason for the latter is the strong sensitivity of ^{59}Co (n, γ) ^{60}Co reaction rate as shown in Fig. 2. On the other hand, in the reflector region, there is no clear difference between both integrated fast fluxes of JENDL-3 and ENDF/B-V and the result of JENDL-3 below 0.1 MeV is about 20 % smaller around 5×10^{-3} MeV and about 20 % smaller around 2×10^{-4} MeV than that of ENDF/B-V. The reason for the latter is the sensitivity of ^{59}Co (n, γ) ^{60}Co reaction rate again, as can be seen in Fig. 4.

3.2 Dosimetry Results

Tables 3 and 4 summarize the final evaluated neutron dose in the fuel region and reflector region. The integrated flux of JENDL-3 is about 9 % larger than that of JENDL-3 for the energy range above 0.1 MeV, which is most important for the irradiation effects of core material, and the DPA rate of JENDL-3 for ferritic iron is also about 5 % smaller than that of ENDF/B-V. On the other hand, only a slight difference less than 1 % can be seen in the results for the reflector region, although 1 σ error is approximately twice as large as that of the fuel region.

4. Conclusion

In order to improve the accuracy and reliability of JOYO dosimetry test, a new unfolding cross section set with covariance matrix has been prepared from JENDL-3 dosimetry file and

applied to the dosimetry test in the JOYO MK-II core. As a result of this work, the new cross section set gives about 9 % smaller fast flux above 0.1 MeV and about 5 % smaller DPA of ferritic steel in the fuel region, comparing with those of ENDF/B-V. On the other hand, only a little difference within 1% was found between the present result of JENDL-3 and the previous result of ENDF/B-V in the reflector region. In this work, it has been concluded that JENDL-3 dosimetry file is applicable for use of the JOYO dosimetry test, and an improvement of accuracy and reliability for the irradiation tests can be expected by employing it.

References

1) Sasaki M. and Nakazawa M.: "Production of Analysis Code for "JOYO" Dosimetry Experiment", PNC N941 80-192Tr (1980)

2) Nakazawa M., Kobayashi K., Iwasaki S., Iguchi T., Sakurai K., Ikeda Y., and Nakagawa T.: JAERI 1325 (1991)

3) Chatani K. and Suzuki S.: ISSN 0385-4876 81 (1993) (in Japanese)

4) Chatani K. and Suzuki S.: JAERI-M 94-068, 76 (1994)

5) MacFarlane, R. E., Muir, D. W. and Boicourt, R. M.: LA-9303, Vol.I (ENDF-324) , (1982)

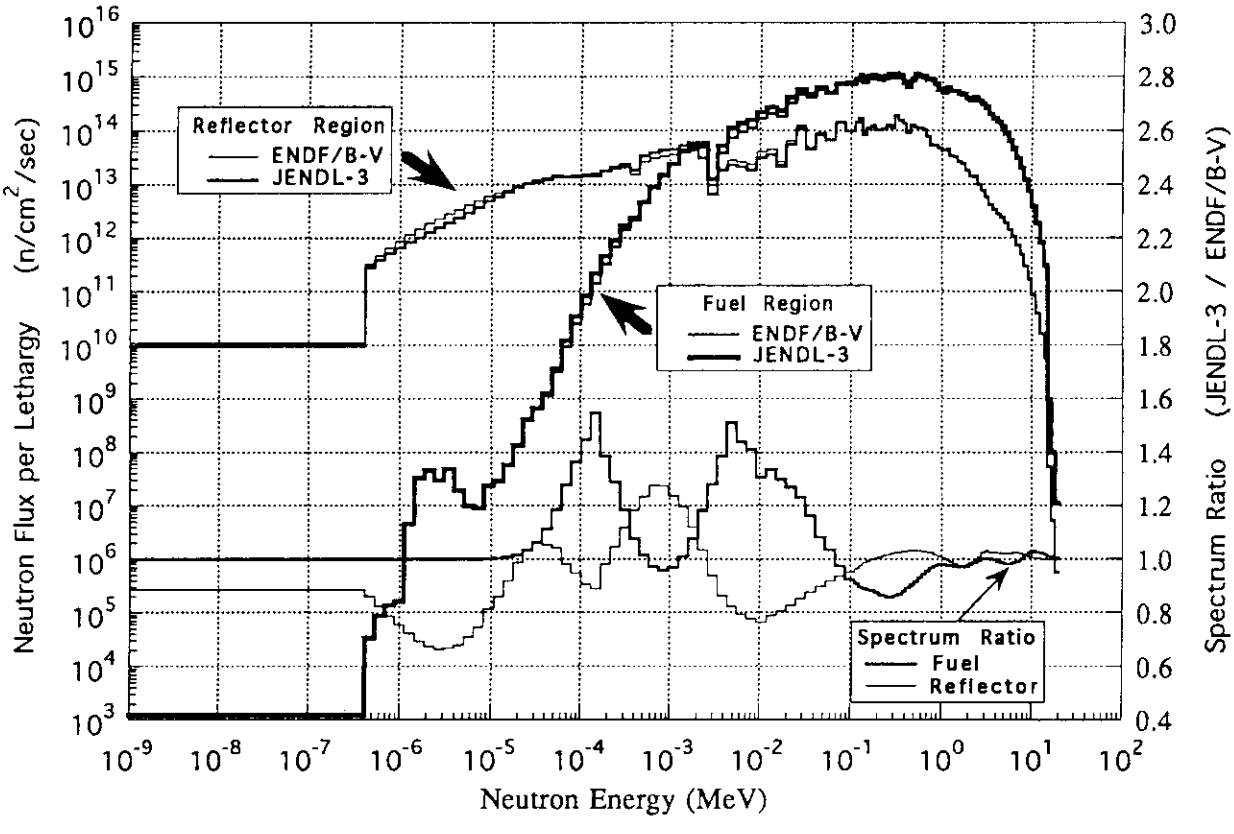

Fig. 1 Unfolded Neutron Spectrum in the MK-II Core

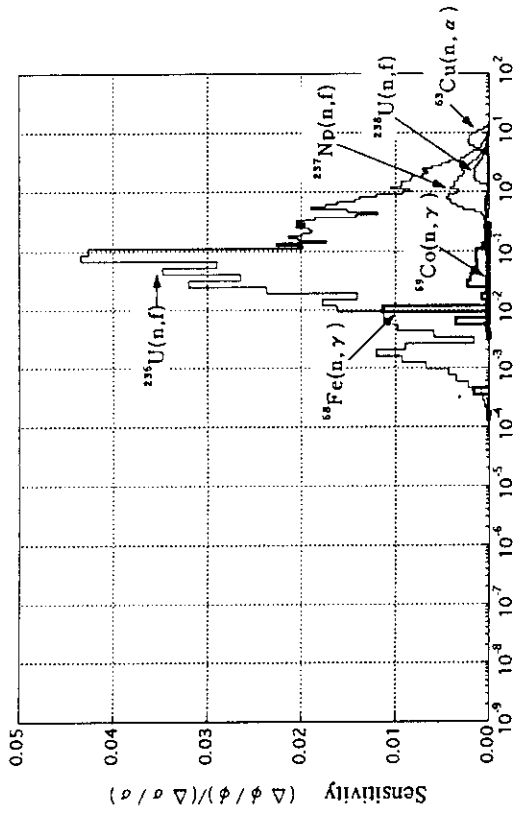

Fig. 3 Sensitivity of Total Flux to ENDF/B-V (Fuel Region)

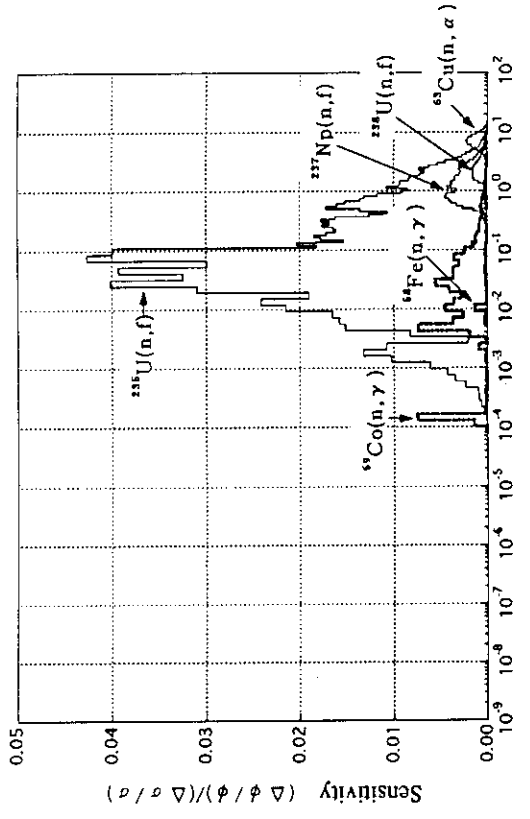

Fig. 2 Sensitivity of Total Flux to JENDL-3 (Fuel Region)

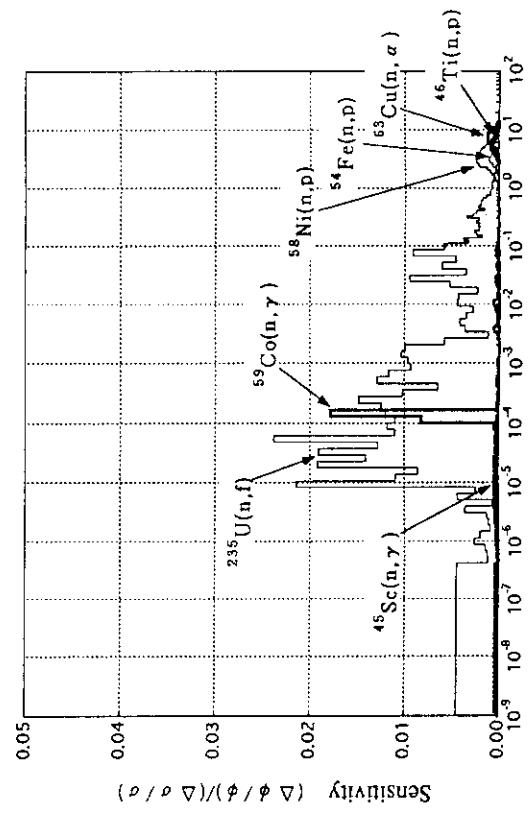

Fig. 5 Sensitivity of Total Flux to ENDF/B-V (Reflector Region)

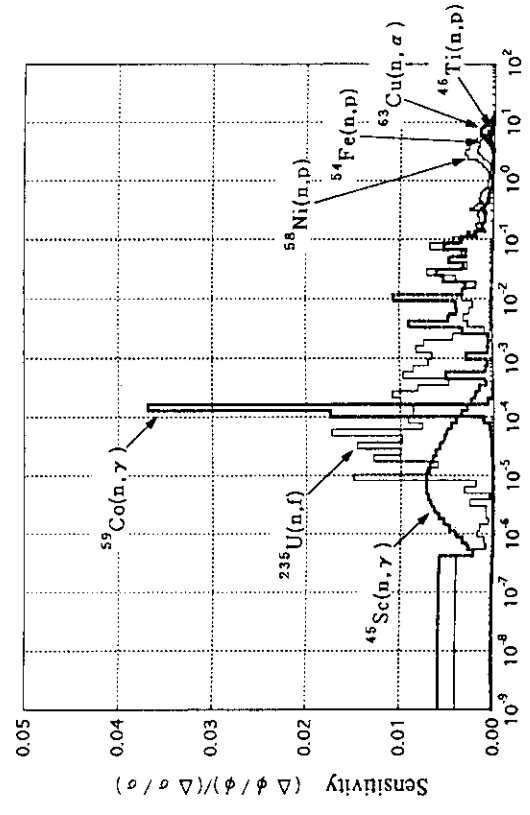

Fig. 4 Sensitivity of Total Flux to JENDL-3 (Reflector Region)

Table 1 C/E of Reaction Rate before and after Spectrum Unfolding (Fuel Region)

by JENDL-3

No.	Reaction Type	before Unfolding		after Unfolding	
		C/E	Error	C/E	Error
1	59Co(n, G)	0.812	0.13	0.927	0.07
2	237Np(n, f)	1.369	0.18	1.019	0.13
3	235U(n, f)	1.079	0.12	1.023	0.06
4	238U(n, f)	1.501	0.19	1.020	0.06
5	46Ti(n, P)	1.530	0.25	1.011	0.15
6	54Fe(n, P)	1.538	0.20	1.021	0.08
7	58Fe(n, G)	1.051	0.18	1.145	0.13
8	58Ni(n, P)	1.515	0.20	1.010	0.10
9	63Cu(n, A)	1.543	0.22	1.041	0.10
	Average	1.326		1.024	

by ENDF/B-V

1	59Co(n, G)	0.840	0.28	0.830	0.26
2	237Np(n, f)	1.396	0.18	1.080	0.13
3	235U(n, f)	1.087	0.12	1.017	0.06
4	238U(n, f)	1.484	0.19	1.025	0.06
5	46Ti(n, P)	1.521	0.25	1.014	0.15
6	54Fe(n, P)	1.564	0.20	1.048	0.08
7	58Fe(n, G)	1.032	0.19	1.026	0.14
8	58Ni(n, P)	1.473	0.20	0.990	0.10
9	63Cu(n, A)	1.525	0.23	1.044	0.10
	Average	1.325		1.008	

Table 2 C/E of Reaction Rate before and after Spectrum Unfolding (Reflector Region)

by JENDL-3

No.	Reaction Type	before Unfolding		after Normalization		after Unfolding	
		C/E	Error	C/E	Error	C/E	Error
1	59Co(n, G)	1.885	0.27	0.962	0.27	1.005	0.06
2	235U(n, f)	1.590	0.12	0.811	0.12	0.948	0.07
3	45Sc(n, G)	2.064	0.11	1.053	0.11	1.050	0.06
4	46Ti(n, P)	1.949	0.25	0.994	0.25	0.994	0.15
5	54Fe(n, P)	2.217	0.20	1.131	0.20	1.031	0.07
6	58Ni(n, P)	2.047	0.19	1.044	0.19	0.960	0.09
7	63Cu(n, A)	1.831	0.22	0.934	0.22	0.982	0.10
	Average	1.940		0.990		0.996	

by ENDF/B-V

1	59Co(n, G)	1.851	0.37	0.944	0.37	1.099	0.32
2	235U(n, f)	1.605	0.12	0.819	0.12	0.964	0.07
3	45Sc(n, G)	2.122	0.29	1.083	0.29	1.224	0.27
4	46Ti(n, P)	1.942	0.25	0.991	0.25	0.970	0.15
5	54Fe(n, P)	2.284	0.20	1.166	0.20	1.041	0.08
6	58Ni(n, P)	1.950	0.20	0.995	0.20	0.901	0.09
7	63Cu(n, A)	1.804	0.23	0.921	0.23	0.977	0.10
	Average	1.937		0.988		1.025	

Table 3 NEUPAC Results in the Fuel Region of the MK-II Core

by JENDL-3

ID No.	Window Function	INITIAL	FINAL	Error (%)	Error Contribution (%) Reaction Rate	Xsec	Initial ϕ	Improvement Ratio
1	ϕ_{total}	4.377×10^{15}	3.986×10^{15}	4.8	49.0	18.2	32.8	2.29
2	$\phi_{>1MeV}$	8.772×10^{14}	6.171×10^{14}	7.4	23.4	15.5	61.2	2.39
3	$\phi_{>0.1MeV}$	3.277×10^{15}	2.648×10^{15}	7.9	18.5	15.0	66.5	1.55
4	DPA/sec	1.642×10^{-6}	1.285×10^{-6}	5.0	40.7	20.7	38.6	2.31

by ENDF/B-V

ID No.	Window Function	INITIAL	FINAL	Error (%)	Error Contribution (%) Reaction Rate	Xsec	Initial ϕ	Improvement Ratio
1	ϕ_{total}	4.377×10^{15}	4.035×10^{15}	4.7	51.9	17.6	30.5	2.33
2	$\phi_{>1MeV}$	8.772×10^{14}	6.298×10^{14}	7.3	24.6	12.1	63.3	2.41
3	$\phi_{>0.1MeV}$	3.277×10^{15}	2.903×10^{15}	7.8	17.5	16.1	66.4	1.58
4	DPA/sec	1.642×10^{-6}	1.349×10^{-6}	5.0	40.8	20.3	38.9	2.31

Table 4 NEUPAC Results in the Reflector Region of the MK-II Core

by JENDL-3

ID No.	Window Function	INITIAL	FINAL	Error (%)	Error Contribution (%) Reaction Rate	Xsec	Initial ϕ	Improvement Ratio
1	ϕ_{total}	5.519×10^{14}	5.820×10^{14}	8.9	5.3	1.0	93.7	1.19
2	$\phi_{>1MeV}$	2.903×10^{13}	2.889×10^{13}	16.0	1.9	10.0	88.1	1.21
3	$\phi_{>0.1MeV}$	2.641×10^{14}	2.793×10^{14}	13.4	0.9	0.5	98.6	1.04
4	DPA/sec	1.066×10^{-7}	1.097×10^{-7}	10.6	2.1	1.6	96.4	1.09

by ENDF/B-V

ID No.	Window Function	INITIAL	FINAL	Error (%)	Error Contribution (%) Reaction Rate	Xsec	Initial ϕ	Improvement Ratio
1	ϕ_{total}	5.521×10^{14}	6.014×10^{14}	9.2	4.2	2.3	93.5	1.16
2	$\phi_{>1MeV}$	2.904×10^{13}	2.906×10^{13}	16.4	1.5	7.3	91.2	1.18
3	$\phi_{>0.1MeV}$	2.642×10^{14}	2.774×10^{14}	13.5	0.7	0.7	98.7	1.04
4	DPA/sec	1.067×10^{-7}	1.113×10^{-7}	10.8	1.6	1.8	96.6	1.08

2.2.4 Integral Data Testing of JENDL-3.2 for Fusion Reactor and Shielding Applications

Yukio Oyama
Japan Atomic Energy Research Institute
Tokai-mura, Naka-gun, Ibaraki-ken 319-11

Abstract

Integral data testing of JENDL-3.2 is being performed in the activities of two working groups of the Japanese Nuclear Data Committee. The continuous and group-wise libraries prepared from JENDL-3.2 are planned to be tested by the working groups. In this paper, the continuos library FSXLIB-J3R2 processed from JENDL-3.2 for MCNP was tested for fission and fusion neutrons using data of integral experiments and compared to the results of JENDL-3.1. The results of integral data testing of JENDL-3.2 for fusion and shielding application are reviewed.

1. Introduction

Integral data testing of JENDL-3.2[1] is extensively being performed as the activities of both Fusion Neutronics Integral Test Working Group and Shielding Integral Test Working Group organized under the Reactor Constant Sub-Committee of the Japanese Nuclear Data Committee. Main contributors in the WGs for integral testing is listed in Table 1. Fusion Neutronics WG focused on fusion application, while Shielding WG rather focused on fission reactor shielding application. Hence, the former WG picked up the recent experiments for a variety of materials with simple geometry using DT accelerator sources, and the latter WG selected shielding materials with rather complicated geometry using a fission reactor. The integral experiments performed mainly in Japanese facilities such as OKTAVIAN and FNS were selected to test for fusion reactor application because there is few new experiment in the world except Japan. On the other hand, experiments to test for reactor shielding were chosen from the foreign experiments such as ORNL, KfK and Winfrith.

The MCNP calculations for those experiments were performed in the same way as the previous benchmark test[2,3] for JENDL-3.1.[4] In this time, integral data testing specially for gamma-ray was newly added with new gamma-ray benchmark experiments for Cu, W, Fe performed after completion of JENDL-3.1. On the other hand, The FENDL activity is conducted by IAEA/NDS coordination for making standard libraries so as to use in the International Tokamak

Experimental Reactor (ITER) design. For this purpose, the FENDL-1[5] transport library is being tested to feed back the results to FENDL-2 compilation. The candidate evaluations for FENDL-2 include JENDL-Fusion File with the file-6 form which was partly evaluated for JENDL-3.2.

Materials included in the selected integral experiments were Li, Be, C, N, O, F, Mn, Al, Si, Ti, Ni, Fe, Cr, Co, Cu, Zr, Nb, Mo, Pb, W for fusion neutronics experiments and Fe, stainless steel and Na for fission shielding experiments. The calculated results compared to the experiments are presented with some key discussions and the status of JENDL-3.2 validation is summarized.

2. Experiments Selected for Integral Testing

The integral experiments for data testing of fusion materials were chosen from the recent fusion integral experiments performed at FNS in JAERI and at OKTAVIAN in Osaka University. Most of those experiments were compiled in the report[6] and the latest compilation was made by IAEA/NDS for FENDL benchmarks[7]. These are of simple geometry and mostly single material to eliminate a modeling uncertainty. One is for leakage spectrum and in-system parameters such as spectrum and reaction rates on slabs, and the other is for leakage spectrum on spheres. Since the latter with a rather thin shell is affected by back-angle scatterings more than the former, the effect by cross section might be appeared in different way. For shielding experiments, the different types of experiments were selected to examine by the different sensitivity of measured response on the selected important materials, i.e., Fe and Na.

For gamma-ray, there also exist two types of experiments, i.e., in-system response on slabs and leakage spectrum from spheres. However, since the latter case was measured by pulse neutron technique to separate neutron contribution, the gamma-ray produced by slowing down neutrons was rejected by time cut-off. This seems to give different information on gamma-ray production cross sections.

3. Processed Library

Because transport calculations require the processed libraries suitable for their computational methods, a nuclear data file has to be converted to the libraries. The continuous pointwise cross section library FSXLIB-J3R2[8] was prepared from JENDL-3.2 nuclear data file for this purpose. The NJOY83.6 was used for the process of 340 nuclides. The multigroup library JSSTDL-3.2 with 195 neutron and 104 gamma-ray groups is also being prepared but not completed yet. Thus the integral data testing was performed for the continuous library, except for special computing codes such as NITRAN and DIAC which used their own libraries processed from JENDL-3.2.

4. Results and Discussion

4.1 Testing for Neutron Data

Cross sections of JENDL-3.2 for most of materials are more or less improved from JENDL-3.1. The results of Li_2O, C, N, O, Ti, Zr, Nb, Mo, W, Na, Fe showed better agreements than the JENDL-3.1 results. Figure 1 shows the example of improvement for neutron emission spectrum in the 0.5-3 MeV energy region of the liquid-nitrogen slab experiment. While some materials, e.g., Al, Si,Cr, Mn, Co, Pb were still similar or worse. Specially for the lead results, the large discrepancy was found in the emission spectrum below 1 MeV. As for Be, the JENDL-3.2 was not revised but new experiments of sphere leakage spectrum were analyzed and tested. The new results showed reverse tendency of discrepancy below 2MeV region to the slab leakage result as shown in Fig. 2. This suggests that the reason can be attributed to angular distribution of (n,2n) reaction.

As for important material, Fe, the extensive analyses were performed by Yamano[9] and Maekawa[10], separately to point out the deficits of Fe data in JENDL-3.1. Yamano pointed out that the Q-value of 1st level of ^{56}Fe and ^{58}Fe (MT=55) was mismatched to that of natural iron from analyses of sphere leakage experiment as shown in Fig. 3 , while Maekawa pointed out cross section of 1st level of ^{57}Fe (MT=51) which is minor abundance 2.2% affected the low energy spectrum in deep penetration. Figure 4 shows the effects of MT=51 and MT=55 improve separately the integrated flux in low energy regions.

4.2 Gamma-ray Data

The gamma-ray emission spectra from sphere were fairly good for most of materials tested,[11] e.g., for CF_2, Al, Si, Co, Mo, Cu. Some materials still need improvements as shown in Fig. 5 for Cr. The overall performance is easily seen in Fig. 6 which indicates the calculated to measured values of the energy integrated spectra for each material of the sphere experiments. The energy information is most important in gamma-ray transport calculation to estimate energy production and nuclear heating. From the figure, it can be seen that the C/Es of the JENDL-3.2 fall within 15%. This assures the good quality of gamma-ray production data of JENDL-3.2 for 14 MeV energy neutrons.

The in-system experiments are sensitive to lower energy neutrons in deep positions of the assmbly. In the benchmark test of JENDL-3.1 by using those experiments, it was pointed out that an energy balance of gamma-ray data to neutron data ahould be carefully kept. This was taken account into the JENDL-3.2 evaluation, so that the large improvement was obtained for gamma-ray heating measurements as shown in Fig. 7 for W. However, the energy balance still should be checked, because the C/E value in the figure is still large by a factor of 2.

5. Summary

The first round test was almost finished for the JENDL-3.2 continuous library. However, for practical use of nuclear data, the multigroup library should also be tested. The results of integral data testing showed improvements for the experiments with most of materials, but some discrepancies were still observed in the low energy emission spectra for heavy materials. For gamma-ray data, the spectrum shape was almost satisfied, however, the integrated value such as gamma-ray heating tends to be overestimated for deep penetration problems including gamma-ray production by lower energy neutrons.

The fusion file is being prepared, because it was pointed out that angular-energy correlation is important in fusion neutron energy region. Thus finally those data should be tested for fusion application. At the same time, the data testing of FENDL-1 is being performed and compared to the JENDL-3.2.

Acknowledgments

The author thanks the member of both Fusion Neutronics Integral Test Working Group and Shielding Integral Test Working Group for providing their test results for this paper.

References

1) Nakagawa T.: " JENDL-3 Revision 2," Proc. 1993 Symposium on Nuclear Data, JAERI-M 94-019, pp68-78 (1994)
2) Eds. Nakajima Y. and Maekawa H.: "Proceedings of the Second Specialist Meeting on Nuclear Data for Fusion Reactors," JAERI-M 91-062 (1991)
3) Kawai M., et al.:"Shielding Benchmark Tests of JENDL-3," JAERI 1330 (1992)
4) Shibata K., et al.: "Japanese Evaluated Nuclear Data Library, Version-3," JAERI 1319 (1990)
5) Ganesan S. and Muir D.W.: " FENDL Multigroup Libraries", IAEA-NDS-129, (1992)
6) "Collection of Experimental Data for Fusion Neutronics Benchmark," Eds. Fusion Reactor Physics Subcommittee, JAERI-M 94-014 (1994)
7) Ganesan S.: "Preparation of Fusion Benchmarks in Electronic Format for Nuclear Data Validation Studies," INDC(NDS)-298 (1994)
8) Kosako K., et al.: " FSXLIB-J3R2: A Continuos Energy Cross Section Library for MCNP based on JENDL-3.2," to be published in JAERI-Data/Code report (1994)
9) Yamano N., et al., "Status on testing of JENDL-3.2 Iron Data with Shielding Benchmarks," Proc. Int. Conf. of Nuclear Data for Sci. & Technol., Gatlinburg, Tennessee, May 9-13, 1994
10) Maekawa F., et.al.: "Measurement of Low Energy neutron Spectrum in Iron Assembly and Verification of Evaluated Nuclear Data," Ann. Mtg. of Atm. Soc. Jap., Mar. 29-31, Tukuba

(1994)

11) Maekawa F. and Oyama Y.: " Benchmark Test of Gamma-ray Production Data in JENDL-3.2 and FENDL-1", IAEA CRP Mtg. on Measurement, Calculation and Evaluation of Photon Production Data, Nov. 14-17, Bologna, Italy, (1994)

Table 1 Integral Experiments and Participants for Testing of JENDL-3.2

Fusion Neutronics Integral Test WG

FNS-Slab		
In-system Experiment	n&γ Fe, Cu, W	Y. Oyama+, F. Maekawa, T. Mori
Leakage Spectrum-TOF	Li_2O, Be, C,...	K. Ueki,
	(Multigroup)	K. Hayashi, K. Maki
OKTAVIAN Pulsed Sphere	n&γ LiF, CF_2, Be,	A. Takahashi, C. Ichihara
	F, Si, Cu, Zr, Pb,...	F. Maekawa(γ-ray)
OBNINSK Pulsed Sphere	Fe,...	K. Ueki
KfK Sphere	Be	K. Hayashi
Library Preparation	FSXLIB-J3R2	K. Kosako

Shielding Integral Test WG

ORNL-TSF	Fe	N. Yamano+, A. Hasegawa
Broomstick Experiments	Na, O, N, SS	A. Hasegawa
ORNL-TSF	Fe	M. Kawai, K. Ueki
JASPER	Fe,γ	T. Mori, A. Ohashi
	Na	M. Kawai
KfK Sphere (Cf-252)	n&γ Fe,	N. Yamano, K. Ueki
FNS Deep Penetration(14MeV)	SS316L,γ	H. Nakashima
RPI	C	Y. Matsumoto

+ working group leader

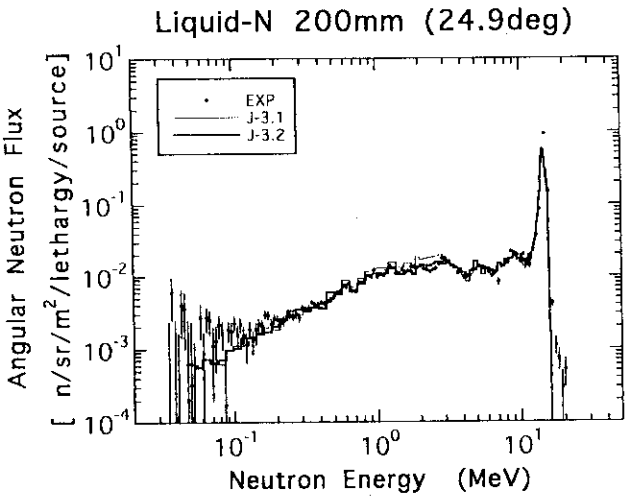

Fig. 1 Neutron emission spatra from the 20 cm-thick liquid nitrogen slab at 24.9 degree.

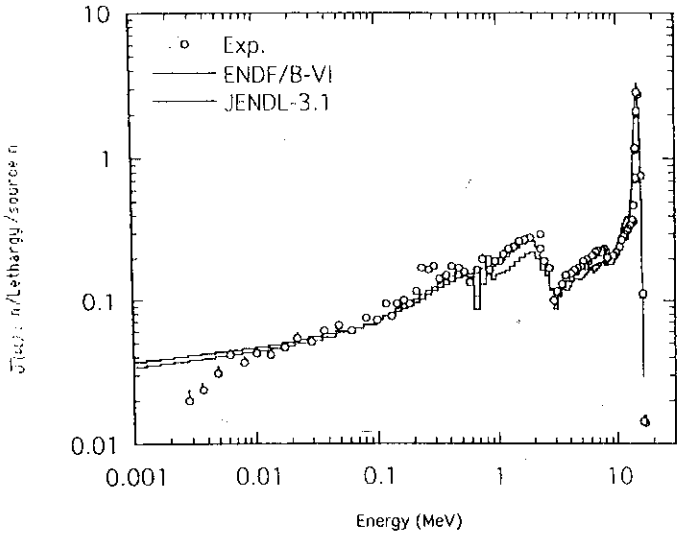

Comparison Plot of Be Sphere Calculated by NITRAN
(Outer Radius=17.35cm, Inner Radius=5.7cm)

Fig. 2 Neutron spectra leaking from Be-sphere with thickness of 5.825 cm calculated by the NITRAN-1D code. The Be data of ENDF/B-IV is the same as that of FENDL-1.

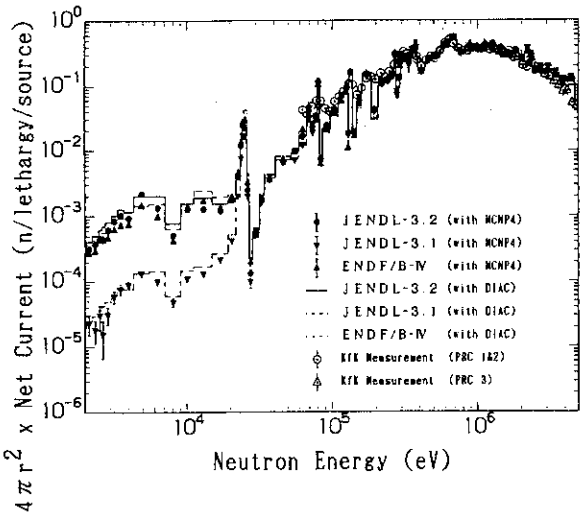

Fig. 3 Calculated results of the KfK sphere leakage experiment on iron showing large difference in the nuclear data for low energy spectrum.

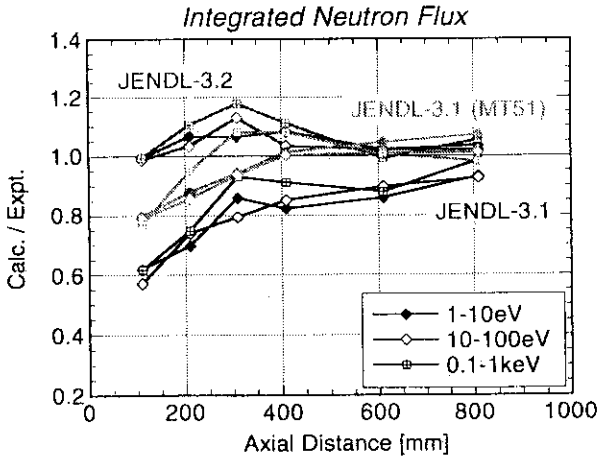

Fig. 4 Effects of 1st level data of iron isotopes. The JENDL-3.2 was changed in cross section of MT=51 and Q-value of MT=55.

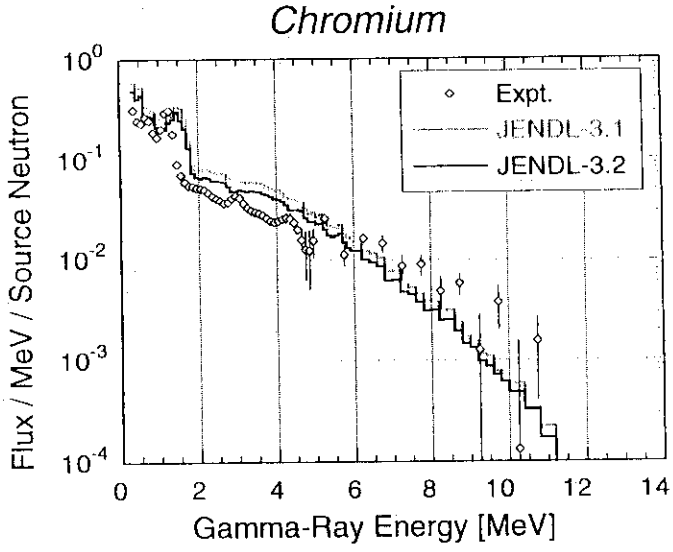

Fig. 5 Gamma-ray emission spectrum from the Cr sphere. The JENDL-3.2 still overestimates the spectrum at 2-5 MeV.

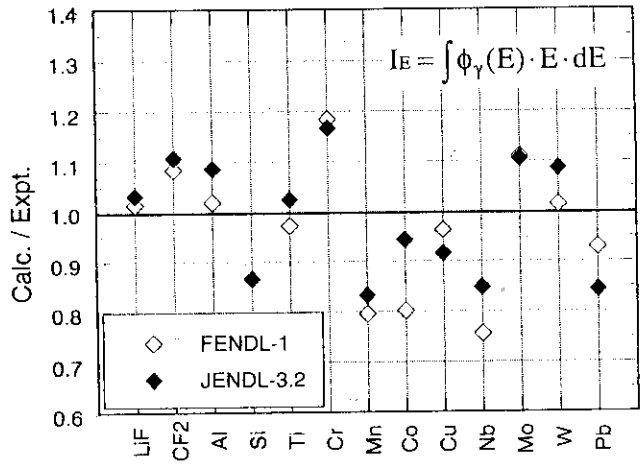

Fig. 6 Overall performance of gamma production data for integral energy release with the 14 MeV neutron sphere experiments.

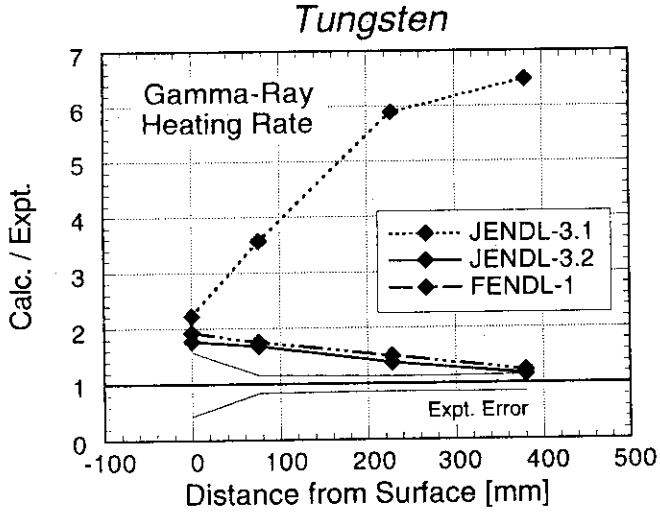

Fig. 7 Incorrect energy balance in JENDL-3.1 enhanced gamma-ray heating in the tungsten slab experiment. In spite of much improvement by JENDL-3.2, the C/E is still large by a factor of 2.

2. 3 Nuclear Reaction Theory

2. 3. 1 Quantum and Statistical Theories of Nuclear Reactions

M. Kawai

Department of Physics, Kyushu University

Abstract Basic concepts and methods in the description of nuclear reactions are briefly reviewed in a historical perspective. Discussed are the discovery and the quantum mechanical and statistical theories of compound nucleus (CN), the discovery of direct processes at intermediate and low energies, optical model, and a theoretical treatment of direct and CN processes. in coexistence.

I. Introduction

The history of nuclear reaction studies dates back to 1909 to 1911 when Rutherford's group discovered the nuclei of Au and Pt atoms through observations of large angle elastic scattering of α particles by thin foils of the metals[1]. The first systematic studies of nuclear reaction mechanisms, however, were carried out in 1932 to 1933 by Fermi et al.[2] They irradiated 38 nuclides ranging from Hydrogen to Uranium with then newly discovered neutrons, and observed the induced radioactivity. Two remarkable features were observed: (a)(n,γ) cross sections were very large, and (b)cross sections at very low energies were very large for some nuclides, but not so much for other nuclides. (a) suggested that the system stayed in a highly excited state in which it emits photon(s) for a very long time. Fermi et al estimated the period to be at least 10^{-16}sec., very much longer than the collision time, of the order of 10^{-22} sec. (b)was later found to be due to resonances at the incident energies.

II. Compound nucleus model and resonance theories

The features of neutron induced reactions mentioned above were explained by N. Bohr, and G. Breit and E. P. Wigner[3] with *compound nucleus model.* The model postulates strong interaction between nucleons that causes immediate dissipation of the energy of the incident nucleon among many nucleons in the target nucleus. As a result, none of the nucleons has enough energy to escape from the compound state and a compound nucleus is formed. It is a quasi-bound state that lasts until the energy re-concentrates onto a small number of nucleon(s) that are then emitted from it. Energy eigen-values of a compound nucleus are, as those of true bound system, discrete. They are, however, complex because of its finite life time

$$W_\lambda = E_\lambda - i\Gamma_\lambda/2 \qquad \text{(I.1)}$$

where Γ_λ is related to the life time , τ_λ , by $\tau_\lambda = \hbar/\Gamma_\lambda$. Reactions only proceed when the incident energy matches one of the resonance energies, E_λ, within the width, Γ_λ, hence resonance. The long life explains the large (n,γ) cross sections. If Γ_λ is a few tens eV, as often observed, τ_λ is indeed of the order of 10^{-16}sec. as estimated by Fermi et al.!

Breit and Wigner derived the famous *Breit-Wigner formula* for cross sections at energies near a resonance by analogy with the atomic resonance fluorescence using Wigner-Weisskopf perturbation theory. The analogy, however, is imperfect since nuclear force is too strong to warrant perturbation theory. Besides, the incident neutron does not disappear in the intermediate state, unlike the photon in resonance fluorescence. A complete quantum mechanical formulation free from such defects was given by Kapur and Peierls [3].

Characteristic features of the Kapur-Peierls formalism, and of the subsequent R-matrix formalism etc., are the use of coordinate space representation. The *internal region*, I, is defined to be where all nucleons are close together and interact with each other by nuclear force. A *channel* γ is where system is partitioned into two particles, say c and C, whose centers of mass are separated by $r_\gamma \geq a_\gamma$ where a_γ,is the *channel radius, which* is beyond the range of nuclear interaction between c and C. The boundary between channel γ, and I is defined by $r_\gamma a_\gamma$. The compound nucleus state wave function, X_λ, .is defined to satisfy the Schrodinger equation in I,

$$HX_\lambda = HX_\lambda \qquad \text{(in I)},$$

where H is the total Hamiltonian and W_λ is the energy eigen-value. The boundary condition for X_λ is given at the boundaries of I with the channels, neglecting its amplitude in the configurations in which the system is separated into more than 3 fragments. Kapur and Peierls assumed the boundary condition of a *decaying state*. If we neglect all angular momenta and charges of the particles for simplicity, it has the form

$$X_\lambda = \sum_\gamma A_{\lambda\gamma} \frac{e^{ik_\gamma r_\gamma}}{r_\gamma} \phi_\gamma(\xi_\gamma) \qquad (r_\gamma = a_\gamma \text{for all } \gamma) \qquad \text{(II.2)}$$

where the summation is over all the channels. $\phi_\gamma(\xi_\gamma)$ is the internal wave function, k_γ is the wave number of relative motion at the experimentally given total energy, E, and $A_{\lambda\gamma}$ is the amplitude of X_λ at the boundary of channel γ. A decaying state is supposed to represent a compound nucleus state long after it is formed: with no incident wave any more, it only decays from all open channels in outgoing waves as in (II.2). Eqs. (II.1) and (II.2) constitute an eigen-value problem of which W_λ is a discrete eigen-value, X_λ is the corresponding eigen-function. They and their time reversed functions, $\tilde{X}_\lambda$, form a complete bi-orthogonal set, $\{X_\lambda, \tilde{X}_\lambda\}$, with $<X_\lambda|X_\lambda> = <\tilde{X}_\lambda|\tilde{X}_\lambda> = 1$, $<\tilde{X}_\lambda|X_{\lambda'}> = N_\lambda \delta_{\lambda\lambda'}$ and $\sum_\lambda |X_\lambda><\tilde{X}_\lambda| / N_\lambda = 1$ in I

where the inner products are taken within I.

The total wave function, $\Psi_\alpha^{(+)}$, which describes a reaction initiated in channel α at energy E, satisfies the Schrodinger equation, $H\Psi_\alpha^{(+)} = E\Psi_\alpha^{(+)}$, and an asymptotic boundary condition:

$$\Psi_\alpha^{(+)} \infty [\frac{e^{-ik_\alpha r_\alpha}}{r_\alpha} - \sum_\beta \sqrt{\frac{v_\alpha}{v_\beta}} S_{\beta\alpha} \frac{e^{ik_\beta r_\beta}}{r_\beta}] \qquad \text{(II.3)}$$

where $S_{\beta\alpha}$ is the S-matrix element of transition $\alpha \rightarrow \beta$, and the v are the relative velocities in the channels. If one expands $\Psi_\alpha^{(+)}$ in $\{ X_\lambda \}$ in I as

$$\Psi_\alpha^{(+)} = \sum_\lambda a_\lambda X_\lambda \qquad \text{(in I)}, \tag{II.4}$$

one can calculate the coefficients, a_λ, using the Schrodinger equations and the boundary conditions for $\Psi_\alpha^{(+)}$ and $\{ X_\lambda \}$. One can then obtain $S_{\beta\alpha}$, if one substitutes (II.2) and (II.3) into (II.4) and compares the amplitudes of the outgoing wave in channel β on both sides of the equation. The result is

$$S_{\beta\alpha} = e^{-2ik_\alpha a_\alpha}\delta_{\beta\alpha} - i\sum_\lambda \frac{g_{\lambda\beta}g_{\lambda\alpha}}{E - W_\lambda} \tag{II.5}$$

where $g_{\lambda\gamma} = \sqrt{\hbar v_\gamma /(2\pi)^3 N_\lambda}\, A_{\lambda\gamma}$ Eq. (II.5) is the *dispersion formula* of the S-matrix element. As one can see, few assumptions, in particular no perturbative approximations, are made in its derivation. The second term on the right hand side of (II.5) causes resonance when E gets close to one of the W_λ, The first term represents a scattering by a hard sphere of radius a_α that occurs only in the elastic channel. It is virtually the only process that occurs if the incident energy is off resonance

The total cross section of the reaction $\alpha \rightarrow \beta$ is given by

$$\sigma_{\beta\alpha} = \frac{\pi}{k_\alpha^{\,2}}\left|\delta_{\beta\alpha} - S_{\beta\alpha}\right|^2 . \tag{II.6}$$

If E is within Γ_λ from E_λ, and all other resonances are so far away that they can be neglected in the S-matrix element, one obtains the *Breit-Wigner one-level formula.*

$$\sigma_{\beta\alpha} \approx \frac{\pi}{k_\alpha^{\,2}} \cdot \frac{\Gamma_{\lambda\beta}\Gamma_{\lambda\alpha}}{(E - E_\lambda)^2 + \Gamma_\lambda^{\,2}/4}, \quad \text{for } \beta \neq \alpha), \tag{II.7}$$

where $\Gamma_{\lambda\gamma} = \left|g_{\lambda\gamma}\right|^2$. Since $g_{\lambda\gamma} \propto A_{\lambda\gamma}$, $\Gamma_{\lambda\gamma}$ is proportional to the probability of X_λ having the internal state ϕ_γ. It therefore reflects the structure of X_λ. It can be shown that for an isolated resonance

$$\Gamma_\lambda = \sum_\gamma \Gamma_{\lambda\gamma} .$$

The total width, Γ_λ, is the total probability of decay of state λ per unit time and γ.-width,. $\Gamma_{\lambda\gamma}$, is that through channel γ.

The definition of the resonance state depends on the boundary condition. The decaying state boundary condition is physically plausible, but not unique. In fact, one can replace (2) by

$$X_\lambda = \sum_\gamma C_{\lambda\gamma} \frac{u_\gamma(r_\gamma)}{r_\lambda} \cdot \phi_\gamma(\xi_\gamma) \tag{II.8}$$

where $u_\gamma(r_\gamma)$ satisfies

$$u_\gamma'(r_\gamma)/u_\gamma(r_\gamma)\Big|_{r_\gamma=a_\gamma} = b_\gamma \qquad \text{(II.9)}$$

where b_γ is a quantity that specifies the boundary condition. For a decaying state, $b_\gamma = ik_\gamma$ is assumed. Since ik_γ is E-dependent, so are all resonance parameters, including W_λ!, although they can be regarded as constants in a narrow energy rangy around the resonance. In the R-matrix theory of Wigner[5] b_γ = real constant is assumed. The resonance parameters are then energy independent. The price for that is that the dispersion formula directly derived is for the R-matrix, and the S-matrix is only obtained by a linear fractional transformation. The result of the transformation, if carried out exactly, can be shown[6] to be term by term identical to the Kapur-Peierls formula. This is, of course, not the case if approximations are made, as is always done in practice, either to the R-matrix or to the transformation. Another choice is $b_\gamma = ik_{\lambda\gamma}$ where $k_{\lambda\gamma}$ is the wave number corresponding to $E = E_\lambda$. Then, W_λ is a pole of the S-matrix[7]. Bloch[8] pointed out that all the boundary conditions mentioned above may be included in the Hamiltonian

$$\mathrm{H}+\sum_\beta \frac{\hbar^2}{2\mu_\beta}\delta(r_\beta - a_\beta)[(\frac{d}{dr_\beta} - b_\beta)r_\beta] \ .$$

In all the formalisms mentioned above make use of the concept of channel radius the choice of which is not unique. Resonance parameters depend on the choice, except for $b_\gamma = ik_{\lambda\gamma}$. The exact S-matrix is, of course, independent of the choice, but approximate ones are not. Normally, it is adjusted so that the approximate S-matrix best reproduces experimental data.

The formalism initiated by Feshbach[9] has no channel radius since it is based on the partition of the Hilbert space of wave functions, rather than the configuration space. The partition is rather flexible. Perhaps the most common one is that into P-space that includes all open channels and the complementary Q-space. A compound nucleus state is defined as an eigen-state of QHQ,

$$QHQ\,\Phi_s = E_s\,\Phi_s \ ,$$

and the resonance energy, W_s is given by

$$W_s = E_s + \left\langle \Phi_s \middle| QHP\frac{1}{E+i\varepsilon - P\overline{H}P}QHP \middle| \Phi_s \right\rangle$$

where P and Q are projection operators onto P and Q spaces respectively. Feshbach's formalism has no ambiguity related to channel radius. It, however, has its own non-uniqueness related to the partition of the Hilbert space. Q- space is often defined as a space in which all nucleons are bound in a single particle potential. This definition naturally depends on the single particle potential.

III.Statistical compound nucleus model

The spacing of compound nucleus levels become narrower and the widths of individual levels wider as the incident energy gets higher. The levels eventually overlap with each other.. At such energies, the energy spread of the incident beam, I, contains many resonance levels, and what is measured is an energy average over I, hereafter denoted by $< >$. The observed total cross section of a reaction $\alpha \to \beta \neq \alpha$, e.g., is given by

$$< \sigma_{\beta\alpha} >= \frac{\pi}{k_\alpha^{\,2}} < \left| \sum_\lambda \frac{g_{\lambda\beta} g_{\lambda\alpha}}{E - E_\lambda + i\Gamma_\lambda / 2} \right|^2 > . \qquad \text{(III.1)}$$

If one neglects all the resonance levels outside I, and assumes that the parameters of the remaining resonances are statistically random, one can neglect the average of the cross terms and obtain

$$< \sigma_{\beta\alpha} >= \frac{\pi}{k_\alpha^{\,2}} < \left| \frac{g_{\lambda\beta} g_{\lambda\alpha}}{E - E_\lambda + i\Gamma_\lambda} \right|^2 > \approx \frac{\pi}{k_\alpha^{\,2}} \sum_{\lambda \in I} \frac{2\pi}{I} \frac{\Gamma_{\lambda\beta}\Gamma_{\lambda\alpha}}{\Gamma_\lambda} \approx \frac{\pi}{k_\alpha^{\,2}} \cdot \frac{2\pi}{< D >} < \frac{\Gamma_{\lambda\beta}\Gamma_{\lambda\alpha}}{\Gamma_\lambda} >$$

where $< D >$ is the average level distance and $< \Gamma_{\lambda\beta}\Gamma_{\lambda\alpha} / \Gamma_\lambda >$ is the average value of the ratio in I . If the Γ' are uncorrelated to each other, $< \Gamma_{\lambda\beta}\Gamma_{\lambda\alpha} / \Gamma_\lambda > \approx \; < \Gamma_{\lambda\beta} >< \Gamma_{\lambda\alpha} > / < \Gamma_\lambda >$, hence

$$< \sigma_{\beta\alpha} >= \frac{\pi}{k_\alpha^{\,2}} \cdot \frac{T_\beta T_\alpha}{\sum_\gamma T_\gamma} \qquad \text{(III.2)}$$

where

$$T_\gamma = 2\pi < \frac{\Gamma_{\lambda\gamma}}{D} >, \qquad \text{(III.3)}$$

under the assumption that D is uncorrelated to the widths. Eq. (III.2) is the well-known *Hauser- Feshbach formula*[13] for a transition to a discrete final state of the residual nucleus . T_γ is called a *transmission coefficient*. The sum of $< \sigma_{\beta\alpha} >$ over all the open channels , β, is the compound nucleus formation cross section through channel α. It is given by

$$\sigma_\alpha^{CN} = \sum_\beta < \sigma_{\beta\alpha} > = \frac{\pi}{k_\alpha^{\,2}} T_\alpha \qquad \text{(III.4)}$$

since the denominator is canceled by the summed numerator. One can rewrite (III.4) as

$$< \sigma_{\beta\alpha} >= \sigma_\alpha^{CN} R_\beta \qquad \text{(III.5)}$$

where $R_\beta = T_\beta / \sum_\gamma T_\gamma$ is the branching ration of the decay from channel β. Eq. (III4') shows the statistical independence of the formation and decay of the compound nucleus since $< \sigma_{\beta\alpha} >$ is given by a product of the probabilities of those processes, The memory of how the compound nucleus is formed is lost by the time of it decays.

If the residual nucleus B is in the continuum, the cross section per unit energy interval of the outgoing particle is given by

$$\frac{\partial \sigma_{\beta\alpha}}{\partial E_\beta} = \sigma_\alpha^{CN} R_\beta(E_\beta) \omega_{\mathrm{B}}(U_B) \qquad \text{(III.6)}$$

where $\omega_B(U_B)$ is the level density of B at excitation energy $U_B = U_{B\max} - E_\beta$, where $U_{B\max}$ is the maximum value of U_B. The energy spectrum is determined by $R_\beta(E_\beta)\omega_B(U_B)=T_\beta\omega_B(U_B)$ since the denominator, $\sum_\gamma T_\gamma$, of, $R_\beta(E_\beta)$ does not depend on E_β. Using ($T_\beta \infty E_\beta \sigma_\beta^{CN}(E_\beta)$,

one gets

$$\frac{\partial\sigma_{\beta\alpha}}{\partial E_\beta} \infty E_\beta \sigma_\beta^{CN}(E_\beta)\omega_B(U_B) . \qquad \text{(III.7)}$$

Thus, the energy spectrum is determined by the cross section of the inverse process, i.e., formation of the compound state through channel β, and the level density of the *residual nucleus, not* the compound nucleus. The level density, $\omega_B(U_B)$, is n exponentially increasing function of U_B. Expanding its logarithm around $U_{B\max}$ and keeping only the first order term, one obtains

$$\omega_B(U_B) = \omega_B(U_{B\max})\exp(-\frac{E_\beta}{T_B}) \qquad \text{(III.8)}$$

where

$$T_B = (\frac{d\omega_B}{dU_B})\Big|^{-1}_{U_B=U_{B\max}} \qquad \text{(III.9)}$$

is called the *temperature* of B. Substituting (III.9) into (III.8), one obtains

$$\frac{\partial\sigma_{\beta\alpha}}{\partial E_\beta} \infty E_\beta \sigma_\beta^{CN}(E_\beta)\exp(-\frac{E_\beta}{T_B}) . \qquad \text{(III.10)}$$

Since $\sigma_\beta^{CN}(E_\beta)$ varies slowly with E_β,, the energy spectrum is mainly determined by $E_\beta \exp(-E_\beta / T_B)$which is called Maxwellian. and is essentially the energy spectrum of molecules evaporated from a liquid. The model is therefore called *evaporation model*[14] It should be noted that the evaporation model is derived straightforwardly from the dispersion formula of the S-matrix under the assumptions of uncorrelated randomness of resonance parameters. No additional assumptions such, as the principle of detailed balance, is made. The underlying statistical assumption on resonance parameters, however, is still questionable, though look plausible. That will be discussed in **VIII.**

IV. Direct reactions at high energies

In the late 1940s, a series of experiments with 90 MeV neutrons and 200 MeV deuterons was done at Berkeley. It was found that much more high energy particles are emitted at forward angles than the prediction of compound nucleus model. R. Serber explained it with a model[15] that at such high energies the first step in the process of a reaction is collisions of the incident particle with individual target nucleons since the collision time is so short that the interaction with the third nucleon can be neglected. Since the nucleon-nucleon scattering cross section is small at high energies, the mean free path of the projectile in the nuclear medium is comparable with the nuclear radius. In many cases, therefore, the

projectile gets out of the nucleus without or after small number of collision(s) with target nucleons. It is emitted at high energies and in forward directions. The struck target nucleons follow similar fate if their energies are high. If the energies of the projectile or the struck nucleons get too low, they are trapped in the nucleus and eventually form a compound nucleus.

Serber's picture was immediately translated into various models of direct reactions, such as optical model[16], intra-nuclear-cascade model[17] stripping and pick-up model of reactions involving deuterons[18], etc.. The picture was given quantum mechanical foundations in *impulse approximation* [19] that was then developed into the multiple scattering theory[20] and the Brueckner theory of nuclear matter.

V. Optical model

Soon after direct reactions were found at high energies, it was also found at low energies. Besides stripping and pick up reactions of deuterons, which were first found, perhaps the most remarkable discovery was the gross structure in the neutron total cross section σ_t at low energies, $E_n = 0 \sim 3MeV$. In his poor resolution measurements of σ_t. as a function of E_n, and the target nucleus mass number, A, H. H. Barshall observed[21] peaks and valleys with spacing and widths of the order of MeV, in contradiction to a monotonous dependence on E_n and A predicted by the compound nucleus model.

Feshbach, Porter and Weisskopf[22] (hereafter abbreviated as FPW) interpreted this as due to the interference between the incident and the elastically scattered waves. The interference is possible only if the scattered wave is emitted at the same time as the incident wave. Compound nucleus process is too slow for that. FPW assumed that the prompt scattering can be described as a scattering by a complex one-body potential,

$$U(\mathbf{r},\sigma) = V(\mathbf{r},\sigma) + iW(\mathbf{r},\sigma),$$

where $\mathbf{r}$ is the relative coordinate between the incident neutron, n, and the target nucleus, A, and σ is the spin of n. The imaginary part, $iW(\mathbf{r},\sigma)$, represents the absorption of the flux of the entrance channel into non-elastic channels. The absorption may be virtual, and the flux may come back to the elastic channel later, after the incident wave has gone. It is important to note that W is not necessarily zero even if no non-elastic channel is open.

FPW succeeded in reproducing Barshall's data with a square-well potential of radius $R = 1.45A^{1/3}$fm and depths,

$$V = 42MeV \text{ and } W = 0.03V.$$

It is remarkable that W is only 3% of V. That shows that in most cases the incident neutron is scattered off by the mean field of the target nucleus.

Compound nucleus *is* formed, however. Resonance peaks do show up in good resolution experiments at the energies of Barshall's experiments. How could this be compatible with the small W that FPW found? They emphasized the fact that optical model

describes a wave function. averaged over the energy interval, I, of the incident beam, and its scattering amplitude, f_{se},, called *shape elastic scattering* amplitude, is an energy-average of the elastic scattering amplitude, f_{el},

$$f_{se} =< f_{el} >. \tag{V.1}$$

Friedman and Weisskopf[23] argued that the energy-averaged wave function was a wave packet of length $\hbar / I$ in time that was of the order of 10^{-22} sec in Barshall's experiment., and optical model only descried what happened in that short time.

How about the total cross section, σ_t, which includes everything, then? It *can* be calculated with optical model because of the optical theorem, $\sigma_t = 4\pi \operatorname{Im} f_{el}(0)/k_n$ where $f_{el}(0)$ is the forward elastic scattering amplitude. Thus,

$$< \sigma_t >= \frac{4\pi}{k_n} \operatorname{Im} < f_{el}(0) >= \frac{4\pi}{k_n} \operatorname{Im} f_{sc}(0) . \tag{V.2}$$

The physical reason for this is simple. When a short wave packet hits the target nucleus, all reaction processes *begin* at once, although slow ones finish much later. The total cross section, which is the sum of the Cross sections of them all, can therefore be calculated from the instantaneous change of the wave packet, i.e., from f_{se}.. Obviously, this argument does not apply to cross sections of individual processes. For example, elastic scattering through compound nucleus formation is not included in f_{se}., but in

$$f_{ce} = f_{el} - f_{se} . \tag{V.3}$$

The corresponding cross section, $\sigma_{ce} = |f_{cs}|^2$ cannot be calculated with optical model. It also contributes to the energy averaged elastic scattering cross section, hence

$$< \sigma_{el} >= \sigma_{se} + \sigma_{ce}.$$

The energy-average of total reaction cross section, σ_r, is $< \sigma_r >=< \sigma_t > - < \sigma_{el} >$ $=< \sigma_t > - < \sigma_{se} > - < \sigma_{ce} >$ Hence,

$$\sigma_c \equiv< \sigma_r > + \sigma_{ce} =< \sigma_t > - \sigma_{se} \tag{V.4}$$

can be calculated with optical model. If all the non-shape-elastic processes are compound nucleus process, σ_c. is the compound nucleus formation cross section. It must then be identical with the compound nucleus formation cross section defined previously. Thus, e.g., for s-wave neutrons,

$$\sigma_c = \sigma_n{}^{CN} = \frac{\pi}{k_n{}^2} T_{n0} = \frac{2\pi^2}{k_n{}^2} < \frac{\Gamma_{n0}}{D} >. \tag{V.5}$$

As we saw in **III**,. $\sigma_n{}^{CN}$ and transmission coefficients are essential ingredients of the statistical compound nucleus model. (V.5) shows that one can calculate them with optical model. Also, the *strength function*, $< \Gamma_{n0} / D >$, is a directly measurable quantity. FPW calculated it with their optical potential for 0 energy neutrons as a function of A and reproduced experimental data very well, except for some cases that could be understood from the structure of the target nuclei.

In the continuum region, f_{el} is a slowly varying function of energy, therefore $f_{el} = < f_{el} > = f_{se}$. One can therefore calculate f_{el} itself and consequently every measurable quantity in the elastic channel with optical model and compare with experimental data. Thus, measurements of not only cross sections, but also various polarization quantities have been made for various combinations of projectiles and target nuclei in wide range of incident energies. Optical potentials have been searched for to reproduce individual experimental data. Global optical potentials have also been found for nucleons, deuteron, and alpha particle in certain regions of incident energies and target nuclei[24]. Optical model is one of the most basic concepts of nuclear reaction studies. today.

VI. Direct reactions at low energies

Success of the optical model shows that direct reactions occur not only at high energies, as Serber's model implied, but also at low energies. In fact, stripping of deuteron[25] was discovered even before the optical mode. Excitation of collective nuclear states was then found in (p,p') and (α,α').[26] The characteristic diffraction-pattern like angular distribution in those reactions was well reproduced by the differential cross section formula

$$d\sigma / d\Omega \infty j_l(qR)^2 \qquad \text{(VI.1)}$$

which can be obtained with simple plane wave Born approximation (PWBA) under the assumption of surface reaction. In (VI.1), q and l are the linear and angular momentum transfer and R is the nuclear radius. j_l is the spherical Bessel function of order l. (VI.1) enable one conversely to determine l from the observed angular distribution. Since l and $(-1)^l$ are the difference between the spins and parities, respectively, of the initial and the final nuclear states, this provides one with a means of determining the spin and parity of one of the states from the other. That was the advent of *the nuclear spectroscopy with direct reactions.*

PWBA reproduced angular distributions well enough to determine l, and often relative magnitude of cross sections, but not their absolute magnitude: Calculated values were off experimental values sometimes by a factor of 1000. DWBA[24, 27] was then introduced as a more reliable method of analysis. For a transition $\alpha \rightarrow \beta$, the wave functions of relative motion, χ_α and χ_β, are , in stead of plane waves, now solutions of

$$(K_\gamma + U_\gamma)\chi_\gamma = E_\gamma \chi_\gamma \qquad (\gamma = \alpha, \beta)$$

with the distorting potential, U_γ . The S-matrix element is given by

$$S_{\beta\alpha}^{DWBA} = C < \chi_\beta^{(-)}\phi_\beta | V_\beta - U_\beta | \chi_\alpha^{(+)}\phi_\alpha > = C < \chi_\beta^{(+)}\phi_\beta | V_\alpha - U_\alpha | \chi_\alpha^{(-)}\phi_\alpha > \qquad \text{(VI.2)}$$

where C is a constant, V_γ, $\gamma = \alpha$ or β, is the potential that causes the transition. The superscript (+) ((-)) on the χ stands for an outgoing (incoming) scattered wave. The first form of $S_{\beta\alpha}^{DWBA}$ in (VI.2) is called *post form* and the second one *prior form.* The post-prior identity may not hold if the expressions are calculated approximately as is done in most calculations.

The U_γ are normally taken to be the optical potentials that describe elastic scattering in the respective channels. Tacit assumptions are that the projectile (ejectile) feels the same mean field as in elastic scattering before (after) the transition takes place. This procedure, however, is theoretically questionable, as Satchler pointed out, because it double-counts V_γ once as the transition potential, and once in the optical potential. Satchler proposed *asymmetric DWBA.*[28] in which the distorting potential is the optical potential minus a term linear in V_γ. This model is a step closer to the method of coupled channels discussed shortly than DWBA, although it is not always easy to implement in practice. since the modified potential cannot be determine from elastic scattering data.[24]

In some cases, direct transition $\alpha \to \beta$ is hindered or forbidden but two step processes. $\alpha \to \gamma_n \to \beta (n = 1,2,...)$ are allowed, but not so strong. Examples are $({}^3He \to \alpha \to t)$, $({}^3He \to d \to t)$, $(p \to d \to t)$ etc.,. In such cases second order DWBA is useful[24, 29, 30]

DWBA should not work for strong transitions. In such cases, multi-step processes are important. The method of coupled channels (CC) is a general theoretical frame work to deal with such reactions. [24, 27] It was first used by S. Yoshida[31] and was extensively developed by T. Tamura[32] for an analyses of inelastic collective excitations. In CC, the total wave function, $\Psi_\alpha^{(+)}$, is expanded as

$$\Psi_\alpha^{(+)} = \sum_s \chi_s(\mathbf{r}_s)\phi_s(\xi_s) \qquad \text{(VI.3)}$$

in the wave functions of those channels, s, which are strongly coupled, either directly or indirectly, to the entrance channel α and/or the exit channel β. Assuming that the internal wave functions, $\phi_s(\xi_s)$, are known, one solves the Schrodinger equation,

$$(E_s - K_s - U_s)\chi_s = \sum_{s' \neq s} < \phi_s | H - E | \phi_t > \chi_t \ , \qquad \text{(VI.4)}$$

for the unknown wave functions of relative motion, $\chi_c(\mathbf{r}_c)$. E_s (K_γ) is the total (kinetic) energy of relative motion, and U_s is the diagonal matrix element of the interaction potential. A basic assumption of CC is that one can replace the U_s for all γ, by phenomenological complex potentials and include in them all the effects of all the eliminated channels. The boundary condition for the $\chi_s(\mathbf{r}_s)$ is that the incident wave is only in χ_α and outgoing waves are in all the χ_γ.

The coupling potentials, $< \phi_s | H - E | \phi_t >$, on the RHS of (VI.4) are local operators in the coordinate space if only inelastic channels are coupled. They are non-local operators if rearrangement channels are coupled[33], and the method is called the method of coupled reaction (rearranged) channels. (CRC). CC wave functions are sometimes used as distorted waves in DWBA calculations to take account of strong coupling of inelastic channel(s) in the entrance and/or exit channels. The approximation is called CCBA.

If the projectile or ejectile is weakly bound, they can easily break up, really or virtually, in the course of the reaction. The break-up channels couple strongly with the elastic channel and with each other. Since the break-up states are in the continuum, there are continuously infinite numbers of coupled channels. The method of Continuum Discretized Coupled Channel (CDCC)[34] is designed to deal with this problem, with truncation and discretization of the linear and angular momenta of the weakly bound sub-system. The model space then contains only a finite number. of channels. CDCC has been highly successful as a method of analysis of reactions involving weakly bound systems, in particular deuteron, ^{6,7}Li, and ^{12}C.

The method of coupled channels has been highly successful in reproducing variety of experimental data on multi-step direct reactions in light and light heavy ions leading to discrete states of the residual nucleus. It is a standard theoretical frame for theories of direct nuclear reaction with discrete final nuclear states. .

VII Direct and compound nucleus processes

Coexistence of direct and compound nucleus processes poses a serious problem to the basic assumption of the statistical compound nucleus model described in **III** that the resonance parameters are statistically uncorrelated. Separation of the shape elastic scattering, a direct process, from the compound nucleus process discussed in **V** can naturally be extended to a general reaction, $\alpha \to \beta$, $(\alpha \neq \beta.)$: A direct process is described by an energy averaged S-matrix element,

$$S_{\beta\alpha}{}^{dir} = < S_{\beta\alpha} >, \qquad \text{(VII.1)}$$

and the slow processes by fluctuation part of the S-matrix element,

$$S_{\beta\alpha}^{fl} = S_{\beta\alpha} - S_{\beta\alpha}^{dir} . \qquad \text{(VII.2)}$$

The cross section is given by

$$\sigma_{\beta\alpha} = \sigma_{\beta\alpha}^{dir} + \sigma_{\beta\alpha}^{fl}$$

where

$$\sigma_{\beta\alpha}^{dir} = \frac{\pi}{k_\alpha{}^2}\left|S_{\beta\alpha}^{dir}\right|^2 \quad \text{and} \quad \sigma_{\beta\alpha}^{fl} = \frac{\pi}{k_\alpha{}^2}\left|S_{\beta\alpha}^{fl}\right|^2 . \qquad \text{(VII.3)}$$

Question now is how this separation be related to the dispersion formula of the S-matrix? Suppose one takes energy average of (II.5),

$$S_{\beta\alpha}^{dir} = < S_{\beta\alpha} > = < -i\sum_\lambda \frac{g_{\lambda\beta} g_{\lambda\alpha}}{E - W_\lambda} > . \qquad \text{(VII.4)}$$

If the $g_{\lambda\gamma}$ are statistically uncorrelated as assumed in **III**, the RHS of (VII.4) would be 0. Since $S_{\beta\alpha}^{dir}$ is not 0 in reality , $g_{\lambda\gamma}$ must be correlated, no matter how complicated and random the compound nucleus levels may be. The resonance terms implicitly contain *non-resonant* $S_{\beta\alpha}^{dir}$. How can then the statistical compound nucleus model be derived from the dispersion formula?

It has been shown[35] that the dispersion formula can be rewritten in the form,

$$S_{\beta\alpha}^{dir} - i\sum_{\lambda}\frac{\tilde{g}_{\lambda\beta}\tilde{g}_{\lambda\alpha}}{E-\tilde{W}_{\lambda}}\ , \qquad \text{(VII.5)}$$

so that

$$<\sum_{\lambda}\frac{\tilde{g}_{\lambda\beta}\tilde{g}_{\lambda\alpha}}{E-\tilde{W}_{\lambda}}> =0, \qquad \text{(VII.6)}$$

i.e., the modified resonance terms no longer contain non-resonant $S_{\beta\alpha}^{dir}$. The modified resonance parameters in (VII.6), denoted with tilde, depend on the interval of energy averaging, I, as does $S_{\beta\alpha}^{dir}$. Thus, what are included in the direct and resonance components of the S-matrix depend on I. The gross structure of neutron total cross sections at very low energies can be seen only when I is several hundreds keV, containing many compound nucleus resonances. . The fine structure can seen only if I is less than the distances of compound nucleus levels. If I is between those two extremes, $S_{\beta\alpha}^{dir}$ contains intermediate structures such as *door way state* resonances. A door way state is a bound state imbedded in the continuum, like a compound nucleus state, but with excitation of only one degree of freedom[9]. The smaller I is, the finer is the structure included in $S_{\beta\alpha}^{dir}$, although it may not be experimentally observable.

The fluctuation cross section is defined by

$$\sigma_{\beta\alpha}^{fl} = \frac{\pi}{k_{\alpha}^{2}} < \left|\sum_{\lambda}\frac{\tilde{g}_{\lambda\beta}\tilde{g}_{\lambda\alpha}}{E-\tilde{W}_{\lambda}}\right|^{2} > , \qquad \text{(VII.7)}$$

just as the compound elastic scattering cross section. It again depends on I. One can only calculate it under some statistical assumptions[35]. It should be noted that the $\tilde{g}_{\lambda\gamma}$ are in general still correlated to each other which may result in modifications of the Hauser-Feshbach formula, even its product form of probabilities of the compound nucleus formation and decay, depending on the assumptions on the statistical distribution of the $\tilde{g}_{\lambda\gamma}$.

VIII Summary and Discussions

Developments of some basic concepts of nuclear reaction theories is surveyed in a historical perspective. Many of the more recent important developments which are still in progress are left out. In particular, pre-equilibrium processes in light and heavy ion reactions have been the subjects of great t interest in recent years,[36] and much relevant to the present symposium. Intensive studies, both experimental and theoretical are being made[37]. Hopefully in the near future, they will be understood as well as direct and compound nucleus processes, and a unified picture of nuclear reactions will emerge that quantitatively describe all stages of nuclear reactions from shape elastic scattering to compound nucleus decay.

References

1. H. Geiger, J. Harling and E. Madsen, Proc. Roy Soc. **A82** (1909) 495; E. Rutherford, Phil. Mag. ser.6, **21** (1911) 669
2. Fermi, D'Agostin, Rasetti,and Segre, Proc. Roy. Soc. Ser A **146** (1934) 483
3. N. Bohr, Nature **137** (1936) 344; G..Breit and E. P. Wigner, Phys. Rev. **49** (1936) 519
4. P. L. Kapur and R. E. Peierls, Proc. Roy. Soc. **A166** (1938) 277
5. E. P. Wigner and L. Eisenbud, Phys. rev. **72** (1947) 29; see also A. M. Lane and R. G. Thomas, Rev. Mod. Phys. **98** (1955) 693
6. M. Kawai and M. Nagasaki, Prog Theor. Phys. **19** (1958) 77
7. J/ Humblet and L. Rosenfeld, Nucl. Phys. **26** (1961) 529
8. C. Bloch, Nucl. Phys. **4** (1957) 503
9 H. Feshbach, Ann. Phys. (N.Y.) **5** (1958) 357, **19** (1962) 287
10. E. P. Wigner, Gatlinberg Conference on Neutron Physics by Time of Flight, ORNL 2309, (1957) 59
11. H. Feshbach, *Theoretical Nuclear Physics, Nuclear Reactions,* John Wiley & Sons Inc., 1992
12. C.E. Porter and R. G. Thomas, Phys. Rev. **104** (1956) 483
13. W. Hauser and H. Feshbach, Phys. Rev. **87** (1952) 366
14. V. F. Weisskopf and D. H. Ewing, Phys. Rev. **57** (1940) 472
15. R. Serber, Phys. Rev. **72** (1947) 1114
16. S. Fernbach, R. Serber and T. B. Taylor, Phys. Rev. **75** (1949) 1352
17 M. L. Goldberger, Phys. Rev. **74** (1948) 1269; R. Metropolis et al., Phys. Rev. **110** (1958) 185
18 S. M. Dancoff, Phys. Rev. **72** (1947) 1017; G. F. Chew and M. L. Goldberger, Phys. Rev. **77** (1950) 470;
19 G. F. Chew and M. L. Goldberger, **87** (1952) 778;G. F. Chew and G. C. Wick, Phys. Rev. **83** (1952) 636
20. A. K. Kerman, H. McManus and R. Thaler, Ann. Phys. (N. Y.)**8** (1959) 551
21. H. H. Barshall, Pys/ Rev. **86**(1952) 436
22. H. Feshbach, C. E. Porter and V. F. Weisskopf, Phys. Rev. **96** (1954) 448,
23. F. L. Friedman and V. F. Weisskopf, in *Nield Bohr and the Development of Physics,* W. Pauli, Ed., Pergamon, London, 1955
24. G. R. Satchler, *Direct Nuclear Reactions,* Clarendon Press, Oxford, 1983
25. S. T. Butler, Phys. Rev. **80** (1950) 1095, Proc. Roy. Soc. **A208** (1951) 559
26. S.Hayakawa and S. Yoshida, Prog. Theor. Phys. **14** (1955) 1: D. M.Brink, Proc. Phys.. Soc. **A68** (1955) 994
27 N. Austern, *Direct Nuclear Reaction Theories*, John Wiley & Sons, Inc., 1976

28. G. R. Satchler, Lectures in theoretical physics Vol. VIII-C (eds. P. D. Kunz, D. A. Lind and W. E. Brittin) Univ. Of Colorado, Boulder, 1966
29. M. Toyama, Phys. Letts. **38B** (1972) 147; R. Schaeffer and G. F. Bertsch, ibid. 159
30. P. D. Kunz and E. Rost, Phys. Letts. **47B** (1973) 136
31. S. Yoshida, Proc. Phys. Soc. **69** (1956) 668
32. T. Tamura, Rev. Mod. Phys. **377** (1965) 679; Phys. Rep.**14** (1974) 60
33. T. Ohmura, B. Imanishi, M. Ichimura and M. Kawai, Prog. Theor. Phys. **41** (1970) 391, **43** (1970) 347; T. Udagawa, H. H. Wolter abd W. R. Coker, Phys. Rev. Lett. **31** (1973) 1507
34. M. Kamimura, M. Yahiro, Y. Iseri, Y. Sakuragi, H.Kameyama and M. Kawai, Prog. Theor. Phys Suppl. **89** (1986); N. Austern, Y. Iseri, H. Kameyama, M. Kamimura, M. Kawai, G. H. Rawitscher and M. Yahiro, Physics Reports, **154** (1987) 125
35. M. Kawai, A. K. Kerman and K. W. McVoy, Ann. Phys. **75** (1973) 156; see also Ref. 11
36. E.Gadioli and P. E. Hodgson, *Pre-equilibrium Nuclear reactions,* Clarendon Press, Oxford, 1992
37. See the relevant papers tpresented to this symposium.

2. 3. 2 Analysis of the Nucleon-nucleus Reactions by the Quantum Molecular Dynamics

Satoshi Chiba, Koji Niita, Toshiki Maruyama, Tokio Fukahori, Hiroshi Takada and Akira Iwamoto

Japan Atomic Energy Research Institute

Abstract

The quantum molecular dynamics + statistical decay model has been applied to analyze the nucleon-induced nuclear reactions in the energy range from 50 to 3 GeV in order to verify its applicability to light-ion induced nuclear reactions. It was found that the present approach could give a quantitative description of various cross sections such as (p,p'), (p,n), (n,p) reactions from a wide range of targets and also target-like isotope production cross sections from p+Fe reaction, showing its basic ability as a tool for the study of intermediate energy nuclear reactions and nuclear data evaluation.

1. Introduction

The nucleon-induced nuclear reactions in the intermediate to high energy region (projectile energy greater than several tens MeV) have been understood mainly in terms of the cascade model, which is an attempt to describe the nuclear reactions as a superposition of nucleon(N)-nucleon collisions. This model is recognized to be applicable in the energy region where the de Broglie wavelength is considerably shorter than the inter-nucleon spacing in the nucleus (~2 fm). Some prescriptions have been introduced to incorporate the effects of the (fixed) mean-field potential in which the nucleons travel[1], which are important at low energy region. However, most of the cascade codes available for nuclear data evaluation are not fully microscopic in nature, i.e., degree of freedom of every nucleons is not considered explicitly. This fact inevitably results in an introduction of phenomenological parameters which may depend on the target mass and projectile energy. Furthermore, there is an essential limitation that the mean-field introduced in the cascade model does not change in the sequence of the intra-nuclear cascade which may significantly change the potential in the target nucleus due to creation of considerable number of excitons. Although it is well known that the cascade model is a powerful way to predict various quantities in the intermediate energy region, another approach based on different (and hopefully more realistic) assumptions is strongly desired as an alternative/supplementary way of the conventionally used cascade model from both basic and applied purposes.

In late 80', a model, called Quantum Molecular Dynamics (QMD), has been proposed to describe various quantities of the heavy-ion nuclear reactions in a microscopic way[2]. All the input information required in this model is thus related to the nucleon-nucleon (N-N) interaction, not to the nucleon-nucleus reaction, which feature helps to avoid the phenomenological parameters. The QMD takes account of the effects of the mean field and N-N collisions automatically, although in quite different ways. These two ingredients, i.e., the mean field and N-N collision, correspond to a microscopic description and origin of the real and imaginary parts of the optical model potential respectively, which are the most important quantities in understanding nuclear reactions. Thanks to the work of Kyoto university group who has developed a method to obtain stable ground states in the same framework, QMD has been applicable from quite low projectile energy (around 10MeV/nucleon)[3].

In spite of the basic potential of the QMD, it was not applied to study the nucleon-induced nuclear reactions intensively except for the work of Peilert et al[4] who had analyzed the (p,n) reaction cross sections of several targets in the intermediate energy range. His analysis, however, did not take account of the statistical decay of the hot fragments produced from the QMD calculation, thus covering only a restricted range of the available phase-space. The purpose of the present work is to continue our effort[5] to validate the applicability of QMD + statistical decay model to the nucleon-induced nuclear reactions, and also to obtain information on the reaction mechanisms.

2. The Quantum Molecular Dynamics

In QMD, each nucleon (denoted by a subscript α) is expressed by a Gaussian wave function of the form:

$$\phi_\alpha(r_\alpha) = \frac{1}{(2\pi L)^{3/4}}\exp\left[-\frac{(r_\alpha - R_\alpha)^2}{4L} + \frac{i}{\hbar}P_\alpha r_\alpha\right] \tag{1}$$

where L is a parameter which represents the spacial spread of a nucleon, R_α and P_α corresponding to the position of the center of a nucleon in the coordinate and momentum space. The total wave function ϕ is taken to be a direct product of these single-particle wave functions. The equation of motion of R_α and P_α is determined by the time-dependent variational principle:

$$\dot{R}_\alpha = \frac{\partial\langle\phi|H|\phi\rangle}{\partial P_\alpha}, \qquad \dot{P}_\alpha = -\frac{\partial\langle\phi|H|\phi\rangle}{\partial R_\alpha} \tag{2}$$

and the stochastic N-N collision term which satisfies the Pauli blocking. The Hamiltonian H consists of the relativistic kinetic+mass energy and the effective N-N interaction U:

$$H = \sum_\alpha \sqrt{P_\alpha^2 + m_\alpha^2} + \sum_{\alpha>\gamma} U(r_\alpha - r_\gamma) \tag{3}$$

where the effective interaction was assumed to consist of the two-body and density-dependent parts of the Skyrme interaction[6] + Coulomb + symmetry energy term. This assumption leads to the following form of $\langle\phi|H|\phi\rangle$:

$$\begin{aligned}\langle\phi|H|\phi\rangle = {} & \sum_\alpha \sqrt{P_\alpha^2 + m_\alpha^2} + \frac{1}{2}\frac{A}{\rho_0}\sum_\alpha \langle\rho_\alpha\rangle + \frac{1}{1+\tau}\frac{B}{\rho_0^\tau}\sum_\alpha \langle\rho\rangle^\tau \\ & + \frac{1}{2}\sum_{\alpha\gamma} c_\alpha c_\gamma \frac{e^2}{|R_\alpha - R_\gamma|}\,erf\left(|R_\alpha - R_\gamma|/\sqrt{4L}\right) + \frac{C_s}{2\rho_0}\sum_{\alpha\gamma}(1 - 2|c_\alpha - c_\gamma|)\rho_{\alpha\gamma}\end{aligned} \tag{4}$$

where

$$\begin{aligned}\langle\rho_\alpha\rangle &\equiv \sum_\gamma \rho_{\alpha\gamma} = \sum_\gamma (4\pi L)^{-3/2}\exp\left(-|R_\alpha - R_\gamma|^2/4L\right) \\ c_\alpha &\equiv \frac{1}{2} - (t_z)_\alpha = \begin{cases} 1 : \textit{proton} \\ 0 : \textit{neutron} \end{cases}\end{aligned} \tag{5}$$

and "*erf*" denotes the error function. The t_z represents the z-component of the isospin. The symmetry energy parameter C_s was taken to be 25 MeV. The saturation density ρ_0, Skyrme parameters A, B and τ were taken to be 0.165 fm^{-3}, -124 MeV, 70.5 MeV and 1⅓, respectively. These values give, in a limit of nuclear matter, a binding energy/nucleon of 16 MeV and the soft equation of state. The width parameter L was fixed to be a value of 2 fm^2 which was selected to give stable ground states in a wide mass range. Fixing those values, there is no additional parameter in the QMD calculation. The relative distance of two particles, $|R_\alpha - R_\gamma|$, was actually replaced by the following quantity:

$$\begin{aligned}(\tilde{R}_{\alpha\gamma})^2 &\equiv (R_\alpha - R_\gamma)^2 + \frac{1}{1-\beta_{\alpha\gamma}^2}\left[(R_\alpha - R_\gamma)\cdot\beta_{\alpha\gamma}\right]^2 \\ \beta_{\alpha\gamma} &= \frac{P_\alpha + P_\gamma}{\sqrt{m_\alpha^2 + P_\alpha^2} + \sqrt{m_\gamma^2 + P_\gamma^2}}\end{aligned} \tag{6}$$

This quantity is equal to the relative distance of the particles α and γ in the center-of-mass of these particles, and defines a Lorentz scaler.

The stochastic nucleon-nucleon collision is taken into consideration as similar to the cascade

model: When the impact parameter of two nucleons, defined as a Lorentz invariant, is smaller than a certain value determined from the energy-dependent N-N cross section, it is assumed that a collision takes place. We have been considering 1) elastic scattering[7,8] between baryons (nucleon, Δ and N*(1440)), 2) production of Δ and N* from N-N collision (inelastic scattering) and their inverse reactions, 3) decay of Δ and N* by emission of π-meson and their inverse processes. We basically follow the prescription of Wolf et al.[9] However, re-parametrization of the elastic and inelastic scattering cross sections[10] has been carried out to extend the applicable energy region up to 3 GeV. Population probabiity of each process and their angular distributions were selected by the Monte-Carlo method. The Pauli blocking of the final phase-space is checked. If it is occupied by other nucleons, the collision is prohibited.

The ground state of the target nucleus was generated by packing $\boldsymbol{R}_\alpha$ and $\boldsymbol{P}_\alpha$ randomly based on the Woods-Saxon type distribution in the coordinate space and corresponding local Thomas-Fermi approximation in the momentum space, with a restriction that the binding energy must be close enough to that of the liquid-drop model prediction.

3. Calculation Flow

Calculation of the cross sections proceeds in the following way;

1) The ground state of target nucleus is generated.
2) Select the impact parameter randomly in a given range.
3) Locate the projectile and the target according to the selected impact parameter.
4) Boost the projectile and the target on the coulomb trajectory according to the projectile energy.
5) The QMD calculation is performed up to a certain time.
6) The remaining cluster is identified based on the distance of the centroids of particles.
7) Excitation energy of the cluster is calculated as a difference of the internal energy of the cluster ($\langle\phi|H|\phi\rangle$ where ϕ is the direct product of the single-particle wave functions belonging to the cluster) and the liquid-drop binding energy. The sums in the Hamiltonian is taken for the corresponding particles.
8) Statistical decay of the cluster is considered. Emission of n, p, d, t, ^{3}He and α is taken into account by a simple evaporation model.
9) Processes 1) to 8) is repeated, typically 50,000 times, and finally statistical average is performed.

4. Results and Discussion

In **Figs. 1** and **2**, the presently calculated values of ^{56}Fe(p,xn) reaction cross sections at 113 and 800 MeV are compared with the experimental data[11,12] and prediction of the cascade + evaporation code Nucleus[13]. At 113 MeV, Nucleus code underestimates the backward cross sections, which fact has been interpreted as an evidence of lack of the pre-equilibrium process in the cascade model. The present calculation, on the contrary, reproduces the cross section at 113 MeV from the forward to the backward angles. In other words, the QMD calculation automatically includes the reaction mechanism known as the pre-equilibrium process without assuming any of such models. The same degree of agreement is also achieved at 800 MeV. At both energies, however, the present calculation underestimates the high-energy tail of the forward angle cross sections. The reason of this underestimation is not clear yet. One possible explanation is that we have been neglecting the momentum dependence in the effective N-N interaction U which is known to change its sign at a few hundred MeV, and is definitely repulsive at 800 MeV.

In **Figs. 3** and **4**, the ^{56}Fe(p,2p+n)^{54}Mn and (p,6p+4n)^{47}Sc production cross sections are shown. In both cases, the QMD + statistical decay calculation gives reasonable descriptions of the measured data without adjusting any parameter. In spite of the good agreement between the QMD and cascade model predictions in the (p,xn) cross sections as shown in **Figs. 1** and **2**, surprisingly huge difference was observed between these two methods in this kind of target-like fragment production cross sections.

Distribution of particle multiplicity from the p+^{12}C reaction at several incident energies are displayed in **Fig. 5**. Here, the multiplicity was counted as a number of fragments at the time 4.5 to 6.0×10^{-22} second after the QMD calculation has been started. This time corresponds to just after the step 6) at Section 3; at this time, the QMD calculation was terminated and connected to the statistical decay model. The word "fragment" in this case includes both the clusters and nucleon. Multiplicity 1 therefore denotes an event where there is only one "fragment". In other words, the projectile was absorbed by the target nucleus and there is only a compound nucleus left. The following conclusions may be drawin from **Fig. 5**;

1) At the lowest incident energy, the event with multiplicity 1 is dominant, showing that production of the compound nucleus and its decay is the most dominant reaction mechanism at low energy end.
2) At 20 to 50 MeV, those events with multiplicity 2 and 3 become more and more dominant. These multiplicities correspond to that of typical pre-equilibrium reactions where the (p,p'), (p,n), (p,2p), (p,np), (p,2n)... reaction occur in a short time as a result of the subsequent two-body N-N interactions. It will be worthwhile to note that the QMD calculation includes automaticallily emission of more than one particle from the pre-equilibrium stage, i.e., the multiple pre-equilibrium emission is included in QMD.
3) At higher energies, the multiplicity distribution becomes more and more flat, showing a typical feature of the spallation reaction.

This figure therefore shows the fact that QMD calculation can describe the change of the reaction mechanisms of the nucleon-induced nuclear reaction from 1) compound nuclear reaction at low energy, 2) pre-equilibrium process at the intermediation energy, and 3) spallation reaction at high energy region. Notice that no parameter was adjusted to describe this change of the reaction mechanisms. This will be an essential difference from other theories such as Feshbach, Kerman and Koonin theory where the multistep direct reaction cross section must be normalized to the experimental data in terms of the V_0 parameter which is dependent on both the target mass and projectile energy. It was verified that the QMD includes, in this way, the major reaction mechanisms of the nucleon-induced nuclear reaction in a unified manner without adjusting any parameter.

5. Summary

The Quantum Molecular Dynamics + statistical decay model have been applied to analyze the nucleon-induced nuclear reactions. The (p,n) and fragment production cross sections of p+Fe reactions have been calculated and compared with experimental data and predictions of the well-known cascade model. It was confirmed that the present approach could give a quantitative description of these cross sections and thus could be a tool for the study and evaluation of intermediate energy nucleon-nucleus reactions. It was also verified that the QMD calculation contained the major reaction mechanisms of the nucleon-nuclear reactions in a unified manner; the compound nuclear reaction, pre-equilibrium (including multiple processes) reaction and spallation.

References

1) Bertini, H.W., "MONTE CARLO CALCULATIONS ON INTRANUCLEAR CASCADES", ORNL-3383, Oak Ridge National Laboratory (1963).
2) Aichelin, J., Peilert, G., Bohnet, A., Rosenhauser, A., Stöcker, H. and Greiner W., Phys. Rev. C37, 2451(1988).
3) Maruyama, T., Ohnishi, A. and Horiuchi, H., Phys. Rev. C45, 2355(1992).
4) Peilert, G., Konopka, J., Stöcker, H., Greiner, W., Blann, M. and Mustafa, M.G., Phys. Rev. C46, 1457(1992).
5) Chiba, S., Fukahori, T., Takada, H., Maruyama, T., Niita, K. and Iwamoto, A., "APPLICABILITY OF THE QUANTUM MOLECULAR DYNAMICS TO NUCLEON-NUCLEUS COLLISIONS", submitted to Int. Conf. on Nucl. Data for Science and Tech., Gatlinburg, Tennesseee, U.S.A. 1994.
6) Skyrme, T.H.R., Nucl. Phys. 9, 615(1959).
7) Cougnon, J., Mizutani, T. and Vandermeule, J., Nucl. Phys. A352, 505(1981).
8) Bertch, G.F. and Gupta, S.D., Phys. Rep. 160, 189(1988).
9) Wolf, G., Batko, G., Cassing, W., Mosel, U., Niita, K. and Schäfer, M., Nucl. Phys. A517, 615(1990).
10) VerWest, B.J. and Arndt, R.A., Phys. Rev. C25, 1979(1982).
11) Meier, M.M., Clark, D.A., Goulding, C.A., McClelland, J.B., Morgan, G.L., Moss, C.E. and Amian, W.B., Nucl. Sci. Eng. 102, 310(1989).
12) Amian, W.B., Byrd, R.C., Goulding, C.A., Meier, M.M., Morgan, G.L., Moss, C.E. and Clark, D.A., Nucl. Sci. Eng. 112, 78(1992).
13) Nishida, T., Nakahara, Y. and Tsutsui, T., "Developement of Nuclear Spallation Simulation Code and Calculation of Primary Spallation Products", JAERI-M 86-116 (1986).

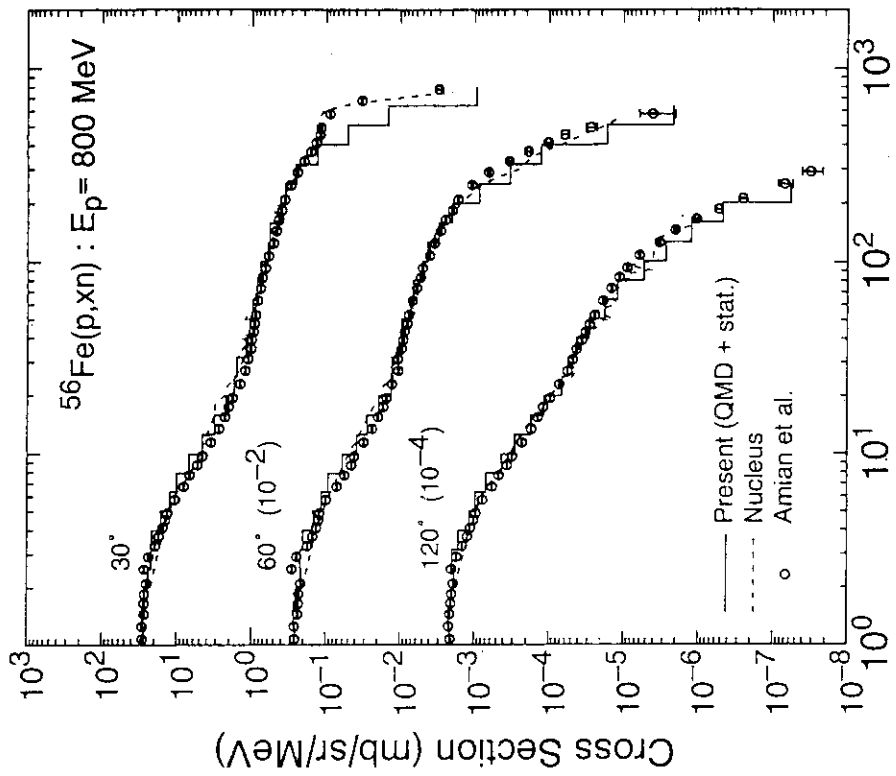

Fig. 2 Double-differential ^{56}Fe(p,xn) reaction cross section at 800 MeV

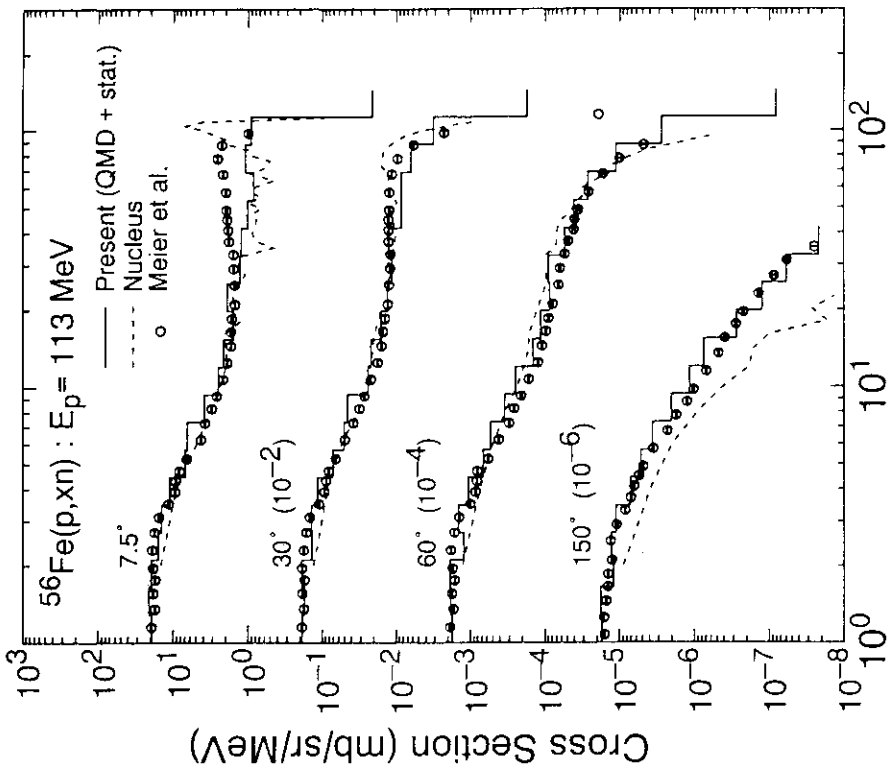

Fig. 1 Double-differential ^{56}Fe(p,xn) reaction cross section at 113 MeV

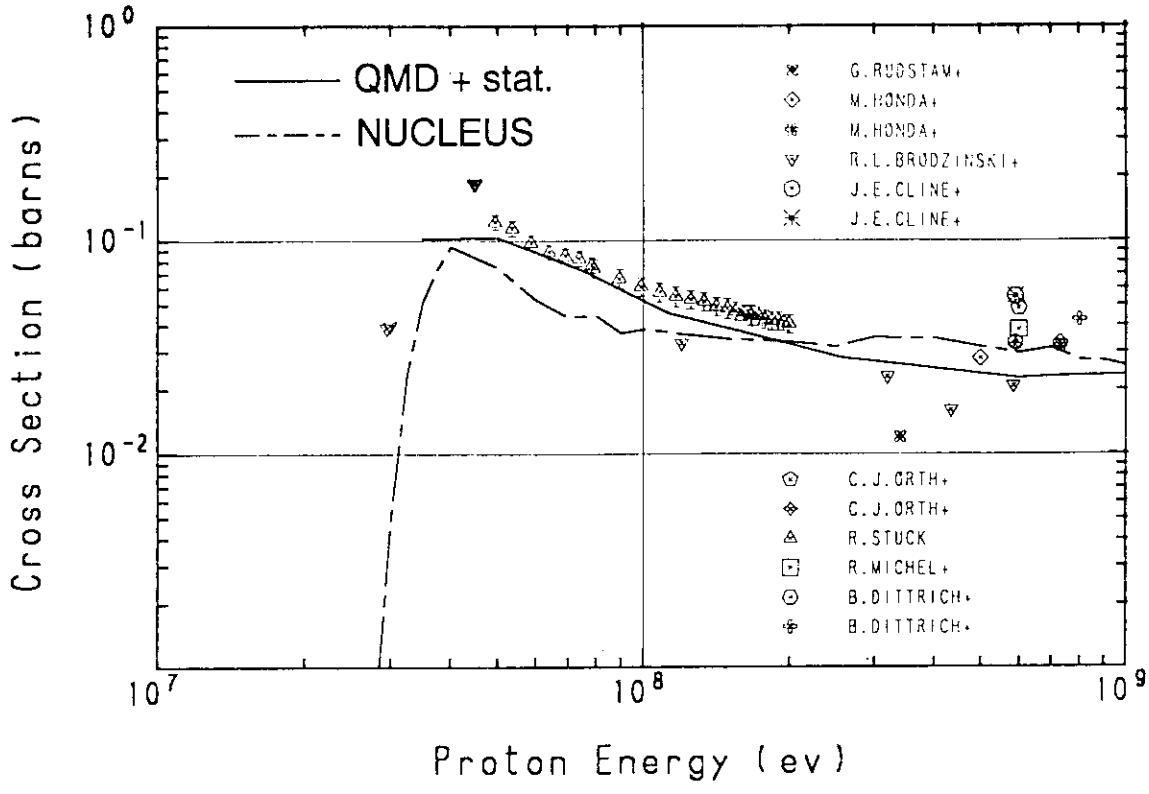

Fig. 3 Excitation function of the $^{56}Fe(p,2p+n)^{54}Mn$ reaction

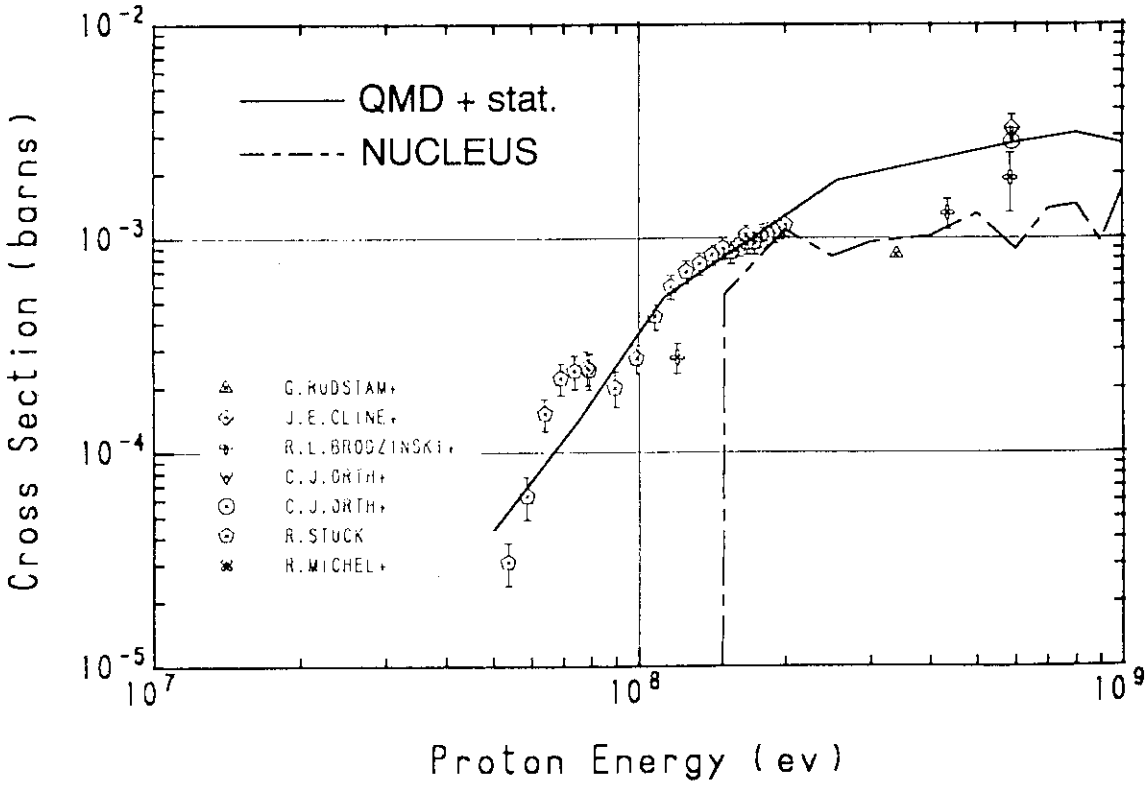

Fig. 4 Excitation function of the $^{56}Fe(p,6p+4n)^{47}Sc$ reaction

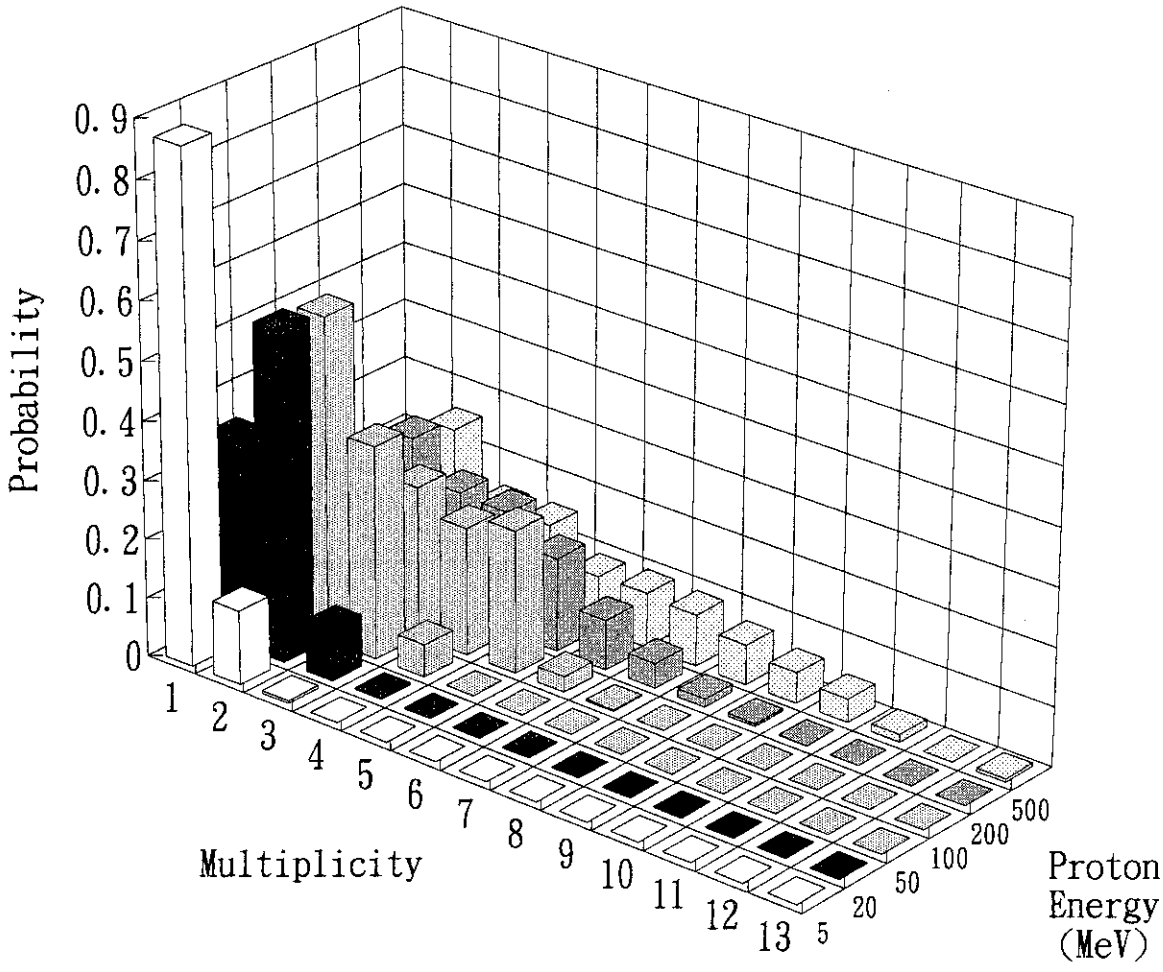

Fig. 5 Particle multiplicity distribution from p+^{12}C reaction predicted by the QMD calculation (before the statistical decay is considered)

2. 4 Measurement

2. 4. 1 Measurement of $\nu(m^*)$ for Thermal Neutron Induced Fission of ^{239}Pu

Katsuhisa NISHIO[1], Yoshihiro NAKAGOME[2], Ikuo KANNO[1] and Itsuro KIMURA[1]

1. Department of Nuclear Engineering, Kyoto University
Yoshida, Sakyo-ku, Kyoto 606-01, Japan
2. Research Reactor Institute, Kyoto University
Kumatori-cho, Sennan-gun, Osaka 590-04, Japan

Abstract

Average number of prompt neutrons as a function of fragment mass $\bar{\nu}(m^*)$ was measured for the thermal neutron induced fission of ^{239}Pu. By measuring the velocities and energies of two fission fragments simultaneously (2V2E measurement), both of the pre-neutron emission fragment mass m^* and the post-neutron mass m were obtained. The neutron emission number ν was deduced by subtracting m from m^*. Our result of $\bar{\nu}(m^*)$ agreed with that of Apalin *et al.*, in whole mass region and that of Fraser *et al.* in the light fragment group. This curve was compared with a calculation using the Brosa *et al.* model, and it was shown that their model represents the experimental data well. In this experiment, neutron emission probability from a given mass, $P_{m^*}(\nu)$, was also investigated as well as the fragment kinetic energy distribution, $P_{m^*}(E)$. The results of the fragment mass dependency of these distributions showed that the fluctuations of kinetic and excitation energy of the fragment were close to each other in the light fragment group but discrepant in the heavy region.

1. Introduction

The energy equivalent to the Q-value of a nuclear fission reaction is converted into kinetic and excitation energies of two fission fragments, and most of the latter is subsequently dissipated by the emission of prompt neutrons. For a thermal neutron induced fission, usually one to three neutrons are emitted from a fully accelerated fragment. The mean excitation energy carried away per neutron is equal to the sum of the neutron binding energy and the mean neutron emission energy in the fragment center-of-mass system, and is estimated to be about 8 MeV. So, we can evaluate the excitation energy from $\bar{\nu}(m^*)$.

The measurements of $\bar{\nu}(m^*)$ for $^{239}Pu(n_{th},f)$ are scarce. In the middle of 60's, Apalin *et al.*[1] and Fraser *et al.* [2] measured this value by detecting the neutrons with a liquid scintillator, but their results are discrepant with each other. So, we have measured this value by the 2V2E method.

In this experiment, not only the mean values of the prompt neutron numbers and the kinetic energy but also the probability distributions of these values with respect to the fragment mass, ($P_{m^*}(\nu)$ and $P_{m^*}(E)$), have been observed.

2. Principle of 2V2E measurement

In the fission process, the mass and the momentum of the fission fragments are conserved as

$$m_1^* + m_2^* = A_{cn} \quad , \tag{1}$$

$$m_1^* V_1^* = m_2^* V_2^* \quad , \tag{2}$$

where the asterisk means the quantities of the pre-neutron emission fragments, and m_i^* and V_i^* $(i = 1,2)$ are the mass and the velocity of the initial fragments, respectively. A_{cn} is the mass of the fissioning nucleus. We cannot measure V_i^*, but the velocity of the post-neutron emission velocity, V_i . If it is assumed that the neutrons are emitted isotropically in the fragment center-of-mass system, the average velocity does not change before and after the neutron emission, namely

$$\overline{V_i}^* = \overline{V_i} \quad . \tag{3}$$

Therefore, from Eqs. (1), (2) and (3), the initial fragment mass is given by

$$m_i^* = \frac{\overline{V_j}^*}{\overline{V_i}^* + \overline{V_j}^*} A, \quad (i = 1,2,\ j = 3 - i) \quad . \tag{4}$$

The fragment kinetic energy E^* and total kinetic energy $TKE(m^*)$ are calculated by

$$E^* = \frac{1}{2} m^* V^{*2} \quad , \tag{5}$$

$$TKE(m^*) = E_1^* + E_2^* \quad . \tag{6}$$

If SSBD is used to measure the fragment kinetic energy of the post-neutron emission fragment, the kinetic energy after neutron evaporation, E, is represented according to the Schmitt's energy calibration formula [3].

$$E = \frac{1}{2} m V^2 = (a + a'm)X + b + b'm \quad , \tag{7}$$

where X is the pulse height, and a, a', b and b' are the energy calibration constants.

The post-neutron emission mass is obtained using Eq. (7) as

$$m = \frac{aX + b}{V^2/2 - a'X - b'} \quad . \tag{8}$$

Finally, the neutron multiplicity is determined by subtracting Eq.(8) from Eq.(4),

$$\nu(m^*) = m^* - m \quad . \tag{9}$$

3. Experiment

3.1. Apparatus

The 2V2E measurement of fission fragments for $^{239}Pu(n_{th},f)$ was carried out at the super mirror neutron guide tube facility of the Kyoto University Reactor (KUR). The experimental arrangement is shown in Fig.1. The slow neutron flux at the exit of the guide tube was about 5×10^7 n/cm^2/s. A vacuum fission chamber with a ^{239}Pu target and detectors was placed at this position.

The ^{239}Pu target which was positioned at the center of the chamber was prepared by the lacquer method [4] and its thickness was about 5 μg-Pu/cm^2. The contents of ^{239}Pu and ^{240}Pu were 92 % and about 8 %, respectively. Other impurities were removed by an ion exchange method.

The velocities, V_i , of both fragments were measured by the TOF method with a flight path length of 28.9 cm, for which the thin film detectors (TFDs) made of NE102 were used to get the start signals. Typical thickness of the TFD was 30 μg/cm^2. SSBDs (ORTEC F-series detector, 900 mm^2), which were mounted at the end of the flight tubes, were used to pick up the stop signals of the TOF measurement and to measure the fission fragment energies.

Four signals, i.e. energies and flight times of two fragments, were digitized and stored by a personal computer by a list mode to analysis them off-line.

3.2. Calibrations and corrections

Energy calibration of the SSBD follows the well-known Schmitt scheme, as described in section 2. The four calibration constants including in Eq.(7) could be calculated using the experimentally obtained peak channels of the pulse height spectrum [4] [5].

The relation between the flight time t and the channel number T is,

$$t = uT + w \quad , \qquad (10)$$

where u is the slope of the time calibration line, and was estimated using a time calibrator (ORTEC Model-462). For the estimation of w in Eq. (10), we used the experimentally obtained peak channel of the light fragment group $\overline{T_L}$ of the TOF spectrum. This channel corresponds to the mean flight time $\bar{t}_L$ of this group, which was calculated to be 20.67 ns using the available mean velocity of 1.398 cm/ns [6]. The value of w was obtained from these values.

For the data analysis the following two corrections were carried out; (a) energy loss of the fission fragments in the TFD and (b) plasma delay in the SSBD.

4. Results and discussion

4.1 Mean values of fragment kinetic energy and neutron multiplicity

The obtained mass yield distribution for ^{239}Pu(n_{th},f) is represented in Fig.2 by solid circle. In this figure, the data by Neiler *et al.*[5] are also represented by solid curve. It is seen that present result shows good agreement with their data except in the symmetric mass region.

The fragment mass dependent mean kinetic energy $\overline{E}(m^*)$ and total kinetic energy $\overline{TKE}(m^*)$ are shown in Fig.3 by solid circle and solid square, respectively. For comparison, the result by Wagemans *et al.* [7] is also represented in this figure. The kinetic energy of the fission fragment m^* distributes around the mean value. By normalization of this curve, which makes total yield to be 100 %, the probability distribution of the kinetic energy of a mass, $P_{m*}(E)$, can be obtained. The vertical bars in Fig.3 depicts the square root of the variance of $P_{m*}(E)$.

The Mean value of neutron multiplicity for one fragment $\overline{\nu}(m^*)$ and the total neutron multiplicity for both fragments $\overline{\nu}_T(m^*)$ are represented in Fig.4. The results of Apalin *et al.*[2] and Fraser *et al.*[3], both of which were obtained by the direct neutron detection method, are also

shown. Our result agrees with their values in the light fragment group and with that of Apalin *et al.*'s in the heavy fragment group. Vertical bars shown in Fig.7 represents the square root of the neutron emission probability distribution, $P_{m*}(\nu)$, which will be discussed later. The average value of total neutron number has become 3.2 $\pm$0.1, which is about 10 % larger than the evaluated value of JENDL-3 [8].

4.2 Calculation with the Brosa model

Brosa *et al.* proposed a model which provided a theoretical interpretation for the distribution of neutron multiplicity [9]. This model is described by a combination of multichannel fission path and a random neck rupture process. There are two asymmetric fission paths named as standard 1 and standard 2, and the existence of these two channels appears explicitly in the mass yield curve as shown in Fig.2 by dotted and dashed Gaussian curves. Combination of this branch ratio and the random neck rupture model produces the distribution of $\bar{\nu}(m^*)$, and the calculated result is shown in Fig.4 by open circle. Their model represents the experimental data well, especially about the shoulder like structure in the light fragment group and the linear increment in the heavy group.

4.3 Distributions of kinetic energy and neutron emission probability of a fragment m^*

In Fig.5, $P_{m*}(E)$ and $P_{m*}(\nu)$ are shown when a mass number is 100 and/or 140. From this figure it is seen that the variance of $P_{m*}(E)$ of heavy fragment is smaller than that of light fragment, whereas that of $P_{m*}(\nu)$ of heavy fragment is larger. As the neutron number reflects the excitation energy of the initial fragment, by assuming the excitation energy carried away per neutron be 8 MeV, the standard deviation of excitation energy σ_{ex} can be estimated from that of neutron number σ_ν as,

$$\sigma_{ex} = 8 \cdot \sigma_\nu \quad . \tag{11}$$

We have examined the standard deviations of kinetic and excitation energy as a function of fragment mass, and this result is shown in Fig.6. From this figure it is found that the energy fluctuations of kinetic and excitation energies of light fragment are close with each other, but in the heavy region these two variances deviate significantly. It may be considered that the motion of the initial fragment at the scission point is the origin of these fluctuations.

5. Conclusions

Fragment mass dependence of the mean neutron multiplicity for ^{239}Pu(n_{th},f) was measured by the 2V2E measurement. The present value of $\bar{\nu}(m^*)$ agrees well with that of Apalin *et al.*'s in the whole mass region and that of Fraser *et al.*'s in the light fragment group. We also confirmed from the calculation that the Brosa *et al.* model can represent this curve well.

We have investigated two probability distribution of a mass, i.e. $P_{m*}(\nu)$ and $P_{m*}(E)$. The variance of the excitation energy was evaluated systematically and was compared with the fluctuations of the kinetic energy. In the result, it was shown that the fluctuations of these energies were close with each other in light fragment group, but discrepant in heavy region.

REFERENCES

(1) Apalin, V.F. *et al.*, Nucl. Phys., **55**, 249 (1964).
(2) Fraser, J.F. and Milton, J.C.D., Annu. Rev. Nucl. Sci., **16**, 379 (1966).
(3) Schmitt, H.W. *et al.*, Proc. Symp. Physics and Chemistry of Fission, Vol. I , p.531, IAEA (1965).
(4) Parker, W. *et al.* : Nucl. Instrum. Meth., 7, 22 (1960).
(5) Neiler, J.L. *et al.*, Phys. Rev., **149**, 894 (1966).
(6) Milton, J.C., and Fraser, J.S., Can. J. Phys., **40**, 1626 (1962).
(7) Wagemans, C., *et al.*, Phys. Rev., **C30**, 218 (1984).
(8) Shibata, K., *et al.*, JENDL-3, JAERI 1319 (1990).
(9) Brosa, U. *et al.*, Phys. Report, **197**, 167 (1990).

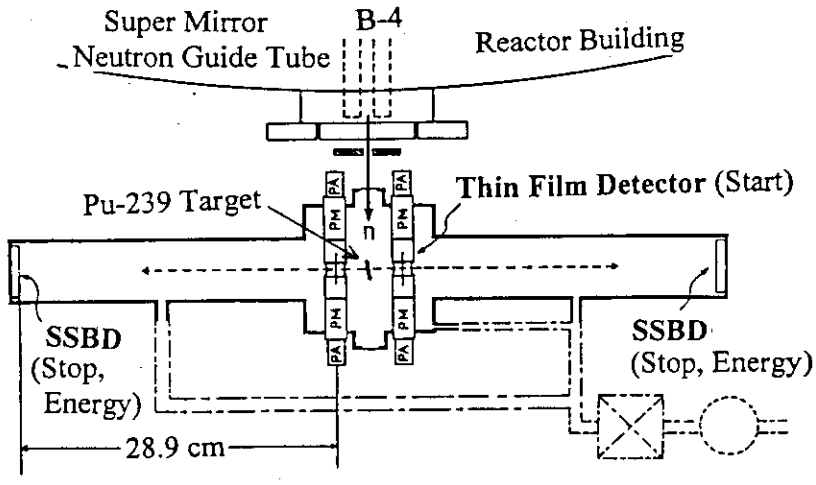

Fig.1 Experimental set up at the KUR nuetron guide tube

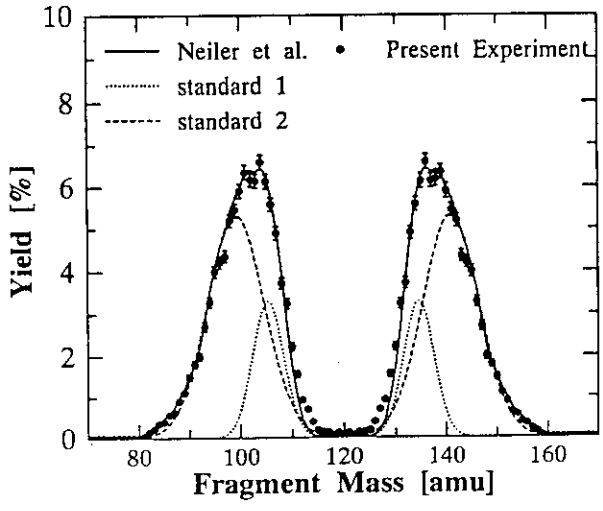

Fig.2 Mass yield curve for $^{239}Pu(n_{th},f)$

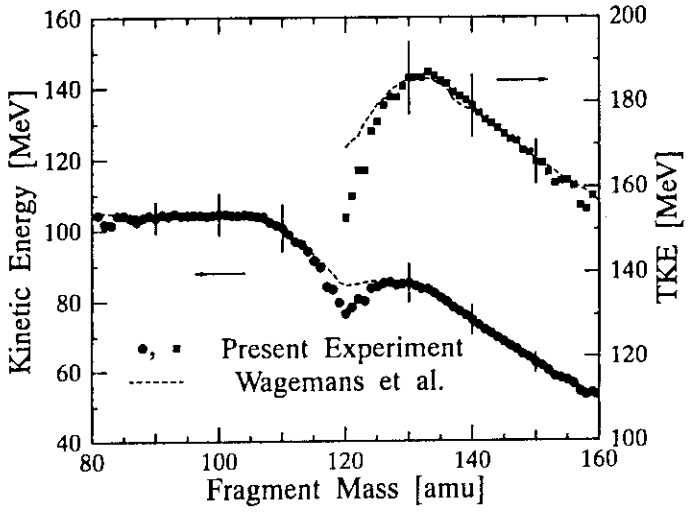

Fig.3 Distribution of average kinetic energy

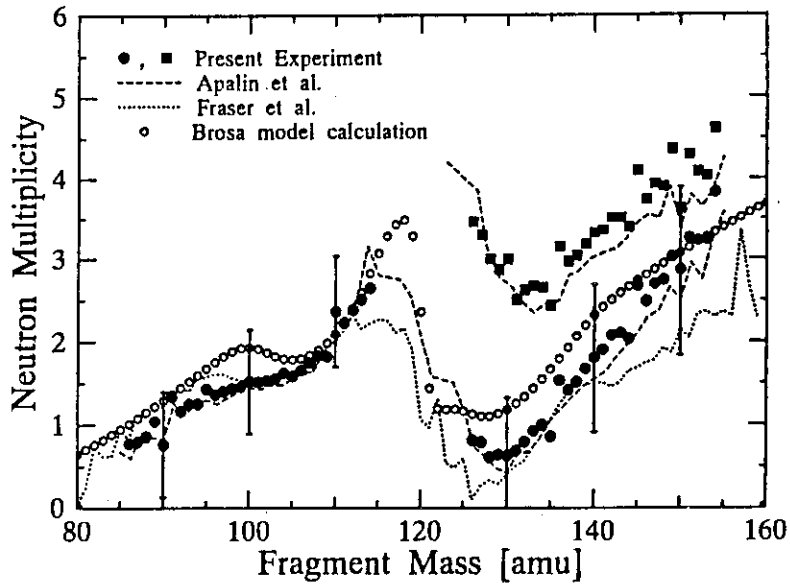

Fig.4 Mean value of neutronn multiplicity for $^{239}Pu(n_{th},f)$

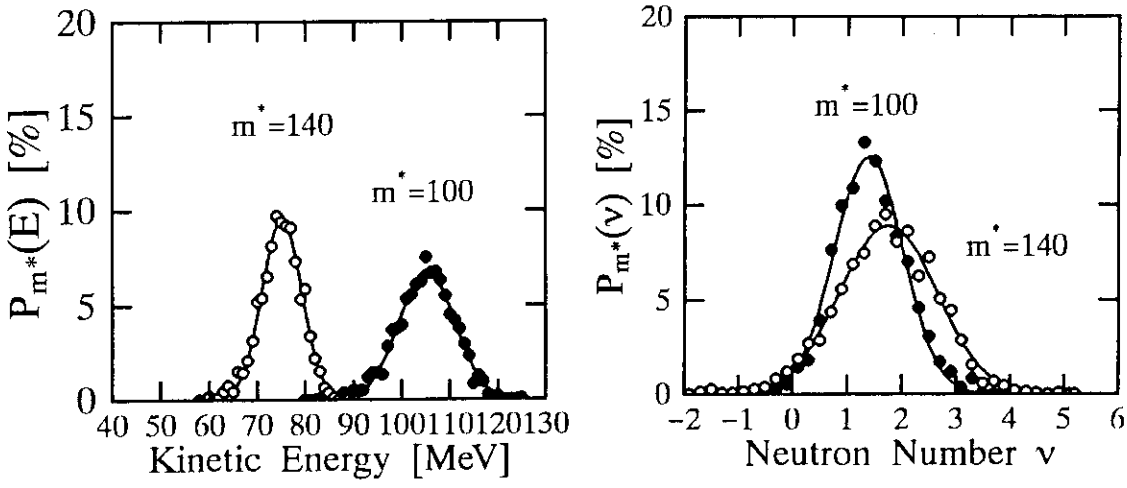

Fig.5 Distributions of kinetic energy and neutron emission probability of a given mass (100 u and 140 u)

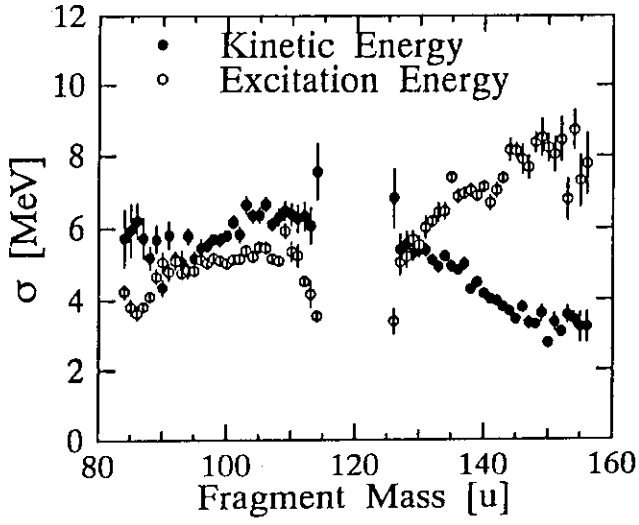

Fig.6 Standard deviations of kinetic and excitation energies

2.5 Nuclear Data Needs from Non-energetic Fields (Material Science Research)

2.5.1 Cold Neutron Production and its Application

Michihiro FURUSAKA
BSF, National Laboratory for High Energy Physics
Tsukuba 305

Neutrons are a very powerful probe similar but complimentary to electrons or photons, because neutron has mass one and spin 1/2, but has no charge. Two typical examples of scientific researches done by neutron scattering are described. One is a study of the structure of SiC fibers, and the other is the vibration modes in a one dimensional magnetic system $CsVCl_3$.

The future project of next generation pulsed spallation neutron source in Japan, Japan Hadron Project is also described in conjunction with other future projects in the world.

1. Introduction

The neutron scattering method can be applied to very wide scientific fields such as, materials science, condensed matter physics, chemistry, polymer, colloids, biology, fundamental physics and so on. Brockhouse and Shull were awarded a Nobel prize of physics this year, who have done pioneering work in a neutron scattering field. This is one of the evidences of the usefulness of the neutron scattering technique for the condensed matter research.

Neutron as a probe has unique characteristics among other methods: i) since neutron has mass one, typical length and energy scale both match simultaneously to those of typical condensed matters, ii) neutron has no charge, therefore well penetrate into bulk samples, iii) neutron scattering cross sections independent of mass numbers, iv) since isotopes have different cross sections, neutron scattering contrast can be changed considerably by the isotope substitution method, v) neutron has spin 1/2, therefore it is a unique probe for magnetic materials.

2. Production of slow neutrons

There are currently two kinds of methods to produce slow neutrons for neutron scattering experiments. One is to use a research reactor and the

other is a spallation neutron source driven by a proton accelerator. Table 1 shows a brief list of such sources in Japan as well as in the world. There are a few tens of research reactors mainly in Europe and in USA, but only a few pulsed spallation sources exist in UK, USA and also in Japan.

In the case of research reactors, fission neutrons from uranium fuel elements are moderated by either light or heavy water to get thermal neutrons. In the case of a spallation source, usually, heavy element target like uranium, tungsten or tantalum is used. When protons from a pulsed proton accelerator hit the target, spallation process takes place and fast neutrons are produced. They are then cooled by water to get thermal neutrons, or by liquid hydrogen or solid methane for cold neutrons.

Reactor based facilities are often called "steady state", because they produce time independent flux, and spallation sources are called "pulsed", because they normally produce very sharp pulsed neutron flux. Although the basic techniques used for both sources are the same as mentioned in the introduction, they require somewhat different instrumentation and analysis. Instruments at steady sources provide information analogous to microscopes: they are good at investigating very narrow space precisely, and pulsed sources analogous to panorama-camera: they are very good at getting overviews.

2. Applications to condensed materials

Because of the space limitation, only two examples are shown here. One is an elastic scattering case, *i.e.*, to get structural information, and the other is an inelastic scattering case, *i.e.*, to analyze momentum transfer Q dependent vibration modes.

One of the unique instruments at KENS is a Small/Medium-angle Neutron Diffractometer WINK, which is shown in Fig. 1. This instrument provides not only atomic scale, but also larger scale information up to nanoscopic length scales. In other words, it utilizes incident neutrons of the wide wavelength range (λ=1-16A) to get the very wide momentum transfer range ($Q=0.015\text{-}15A^{-1}$). Therefore, WINK is suitable for studying complex structures in actual materials, which can not be solved with conventional instruments.

Structure determination study of SiC fibers is a typical example of showing the capabilities of WINK. SiC fibers are one of the new materials which have very high tensile strength even at very high temperatures.

Scattering profiles obtained by WINK and a X-ray small-angle scattering instrument (SAXS) is shown in Fig. 2. The detailed study revealed that the differences between them were due to the differences in scattering length density contrasts between constituent materials. From the small-angle neutron scattering (SANS) study, residual hydrogen contents which contributed to a flat incoherent scattering were determined. A shoulder at around 0.2-0.3 A^{-1} in SANS was attributed to scattering from very small voids in the fibers. It turned out that with WINK, we can determine the size of the voids as small as a few A in radius, i.e., the voids which have a scale comparable to only a few atoms in diameter. The size of the β-SiC crystallites was determined from both SANS and SAXS, as well as from the width of a Bragg-peak in powder diffraction. From lower momentum transfer range ($<0.03A^{-1}$), orientation dependent scattering was observed due to the orientation of the fibers. The evidence of glassy carbons, vitreous silica was also found from powder diffraction patterns.

Another important application which neutron scattering techniques are indispensable is inelastic magnetic scattering. As is stated in the introduction, neutron scattering can simultaneously determine both energy and momentum transfer ranges appropriate to condensed matter science. Triple axis spectrometers are very popular for such studies for relatively low energy transfer range, therefore almost all the reactors have a few of them. For higher energy transfer range (50-2,000 meV), chopper spectrometers are the almost only useful ones. Multi Angle Rotor Instrument (MARI) installed at ISIS at Darsbury Rutherford Appleton Laboratory (DRAL) in UK is one of the most powerful one in the world. MARI is a fruit of the Japan-UK collaboration. Fig. 3. shows a neutron scattering intensity map in energy versus Q space in $CsVCl_3$ which is a one dimensional Heisenberg antiferromagnet. Magnetic systems which have spin 1/2 behave as quantum spin systems and the systems with spin 5/2 and higher as classical systems. $CsVCl_3$ has spin 3/2, in between them, therefore very suitable system to study crossover phenomena from a classical to a quantum spin system. As shown in Fig. 3, the system has dispersion relation similar to the classical spin wave, but has linewidth considerably broader than expected by classical theory of spin wave.

3. Future Projects

Since available number of neutron facilities and instruments are rather limited and effective neutron fluxes are much lower compared with X-ray from synchrotron radiation facilities, there are continuing efforts to build new powerful sources. ANS in USA is a 350 MW reactor project aiming at the facility that has neutron flux of five times the HFR reactor at ILL. ESS proposed by EU is a 5 MW pulsed spallation neutron source project that will have average neutron flux similar to HFR, but will have much higher efficiency by using the sharp pulse structure. Russia and Austria have similar but some what smaller projects to build spallation neutron sources. In the USA, similar high power spallation sources are proposed at three different sites, namely, Argonne, Los Alamos and Brookhaven National Laboratories. One of the laboratories will eventually be selected for the actual building site.

Thus megawatt class pulsed spallation sources would become popular in the world in 10-20 years from now on. KENS becomes too small to maintain the scientific activities in the neutron scattering field in Japan. We certainly need to build a new facility comparable to the megawatt class sources mentioned above. The JHP project is one of such projects, proposed by Institute for Nuclear Study, University of Tokyo (INS) and KEK. The original plan was to build a spallation source based on a 1 GeV proton (H^-) linac and a proton compressor ring (0.2 MW: 1 GeV, 200 μA), but we are reconsidering the parameters and seeking the possibility of building a 1 MW class source. Fig. 4 shows a draft of the layout of the neutron scattering experimental hall (N-arena) for the JHP project.

There is also a proposal by JAERI, which is based on a huge proton accelerator for nuclear transmutation. Their plan is to accelerate H^- beam (~1.5 MW: 1.5 GeV, ~1 mA) simultaneously with the proton beam, and use it for basic science, like neutron scattering, muon and so on.

Since both projects at INS (KEK) and JAERI are based on similar accelerators, there are continuing efforts to join the two projects to build a better facility.

4. Research and Development

Power of the proton accelerator is merely a source term. To get maximum output, for example good scientific papers, from a neutron scattering facility, total optimizations among various components are necessary. We

are doing extensive research and developments for a target, moderator and reflector assembly for the JHP project.

One of the best performance gain we obtained so far is a development of a coupled hydrogen moderator with pre-moderator for a cold neutron source. The gain over a decoupled liquid hydrogen moderator, which is widely used in the world, is nearly 6. The pulse width is about 1.5 times wider, but peak height is still 3 times higher than the decoupled one. We are still seeking for the higher performance system.

Table 1. Typical neutron scattering facilities in the world

Facility	Laboratory (Country)	Type of the source	Power or Energy, Current, repetition rate
KENS	KEK (Japan)	Pulsed Spallation	500 MeV, 5 PμA, 20 Hz
JRR-3M	JAERI (Japan)	Reactor	20 MW
KUR	Kyoto Univ. (Japan)	Reactor	5 MW
ISIS	DRAL (UK)	Pulsed Spallation	750 MeV, 200 μA, 50 Hz
LANSCE	Los Alamos (USA)	Pulsed Spallation	800 MeV, 60 μA, 10 Hz
IPNS	ANL (USA)	Pulsed Spallation	800 MeV, 12 μA, 50 Hz
HFR	ILL (EU, France)	Reactor	57 MW
HFBR	BNL (USA)	Reactor	60 MW
HFIR	Oak Ridge (USA)	Reactor	85 MW

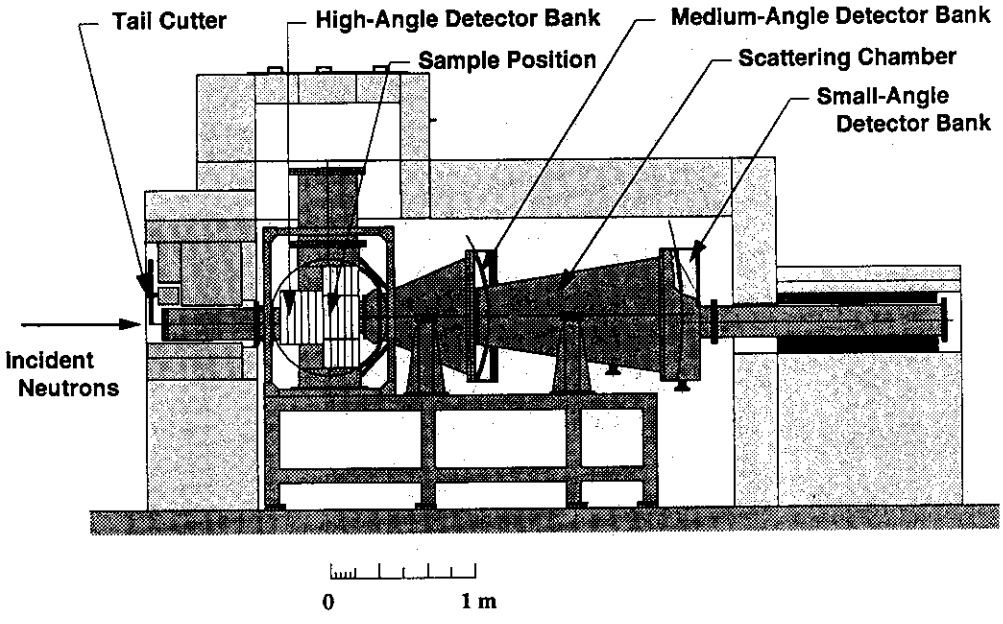

Fig. 1. Side view of the Small/Medium-angle diffractometer WINK.

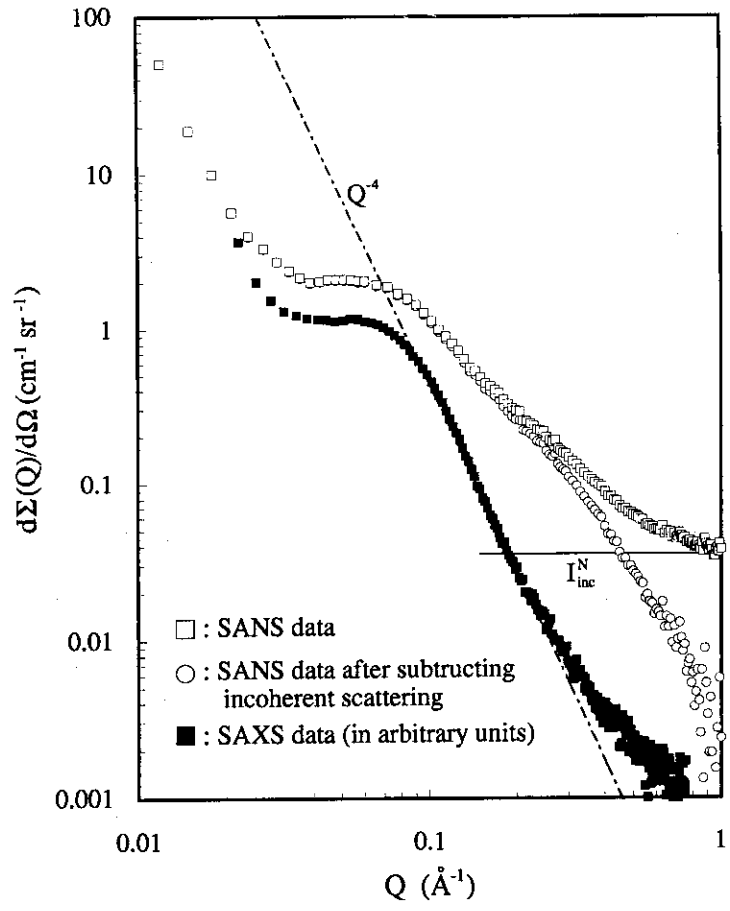

Fig. 2. Neutron and X-ray small-angle neutron scattering intensities in SiC fibers.

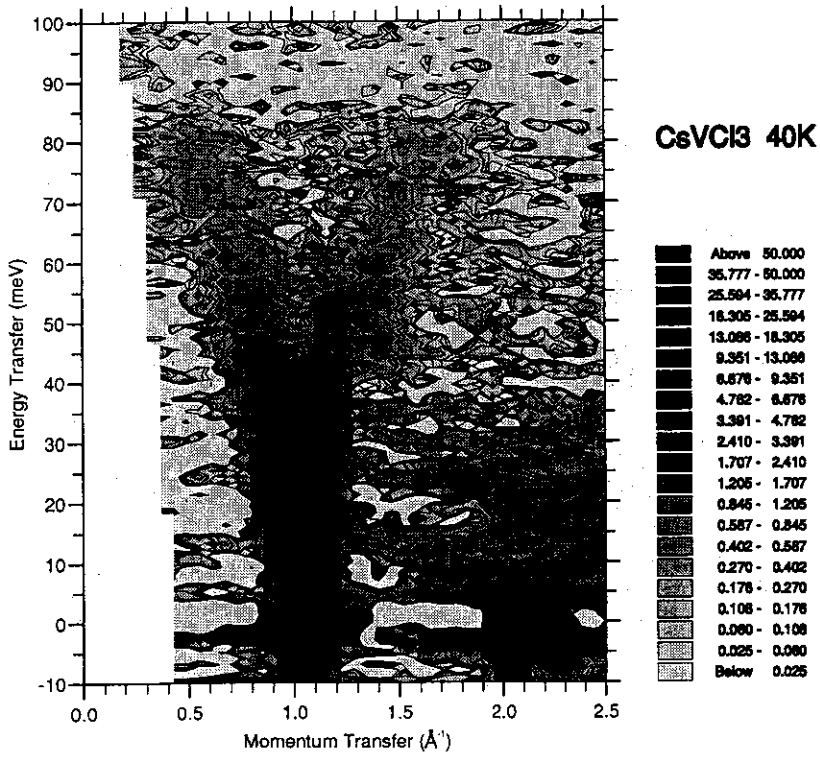

Fig. 3 Intensity map obtained by MARI spectrometer in one dimensional Heisenberg antiferromagnet system $CsVCl_3$.

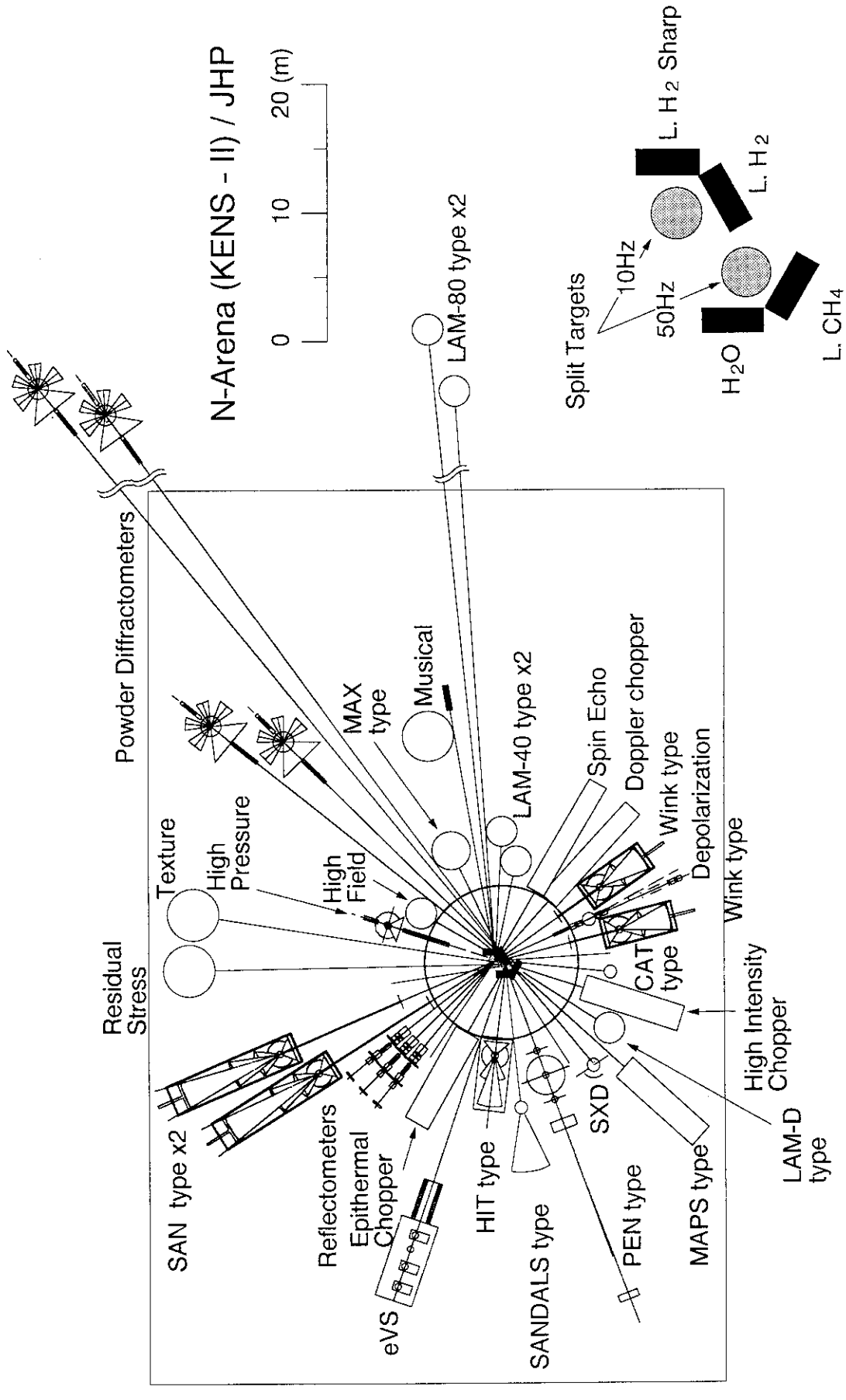

Fig. 4 Layout of the neutron scattering experimental hall for the JHP project.

2. 5. 2 Radiation Damage in Materials

- Primary Knock-on Atom Energy Analyses of Cascade Damage -

Naoto SEKIMURA
Departmentof Quantum Engineering and Systems Science
Faculty of Engineering, University of Tokyo
Hongo, Bunkyo-ku, Tokyo 113

To understand cascade damage formation as a function of primary recoil energy, thin foils of gold were irradiated with 20 - 400 keV self-ions to 1.0 x 10^{14} ions/m^2 at 300 K. Yield of groups of vacancy clusters saturated at ion energy higher than 100 keV. Number of clusters in a group had variation even from the same energy ions. Size distribution of the clusters was not strongly dependent on number of clusters in a group and ion energy. Density of vacancy clusters in a group formed near the specimen surface was calibrated to estimate vacancy cluster formation in neutron-irradiated material. A model was proposed to predict distribution of defect clusters in the irradiated materials based on a primary recoil spectrum. Examples of recomposed distribution of vacancy clusters in a group in irradiated gold were compared with the measured data.

1. Introduction

Cascade displacement damage initiated from a high energy PKA (primary knock-on atom) is one of the major problems in estimating microstructural evolution and property changes in fusion materials under 14 MeV neutron irradiation. The structure of cascade damage in materials irradiated with high energy particles is strongly dependent on the energy of PKA, so that correlation of the material response under various irradiation environments should be established based on a PKA energy spectrum[1,2]. Kiritani and their co-authors tried to analyze cascade damage formation in thin foil specimens under 14 MeV neutron irradiation[2-4]. They fitted the observed size of defect cluster groups and number of defect clusters in a group to the PKA energy spectrum simply assuming that larger clusters were formed by higher energy PKA.

The PKA energy spectrum in the materials irradiated with 14 MeV neutrons extends typically to several hundred keV. Heavy ion irradiations of these energy range have been used to study cascade damage formation or "collapse" of cascade region into vacancy clusters[5-10].

The present authors have been studying cascade damage formation and interactions in thin foil specimens by an "in-situ" observation facility which combines a 400 kV heavy ion accelerator and a 200 kV electron microscope[11-18].

In the present study, thin foils of gold were irradiated with self-ions up to 400 keV to examine PKA energy dependence of cascade damage structure and vacancy cluster formation. In thin foil experiments, point-defects released from a cascade are expected to escape to the foil surface without any interaction. Cascade collisional sequences by these self-ions, which lose most of their energy in the foil, are considered to be identical to the monoenergy PKA damage. A model to predict cascade damage formation based on the PKA energy spectrum under neutron and high energy ion irradiation is proposed.

2. Experimental

Thin foils of 99.99% pure gold were prepared by electro-polishing after annealing at 973 K for 3.6 ks. Irradiation experiments were performed using a 400 kV Cockcroft accelerator in the University of Tokyo, Tokai site. Specimens were irradiated with 20, 50, 100, 200, 300, 400 keV Au^+ ions at 300 K. Ion fluence was fixed at 1.0×10^{14} ions/m^2 for all the specimens to avoid cascade overlapping and "impact effect" from other cascades[2]. In-situ observation of defect clusters in gold under 400 keV Xe^+ ion irradiation showed that areal density of clusters increased linearly with ion fluence around this fluence range[16]. Irradiated thin foil specimens were observed by a 200 keV transmission electron microscope (TEM). Typical foil thickness for TEM observation was 60 nm to include almost all the damage formation depth.

3. Results

Defect clusters are observed in the TEM foils of gold irradiated with self-ions to 1.0×10^{14} ions/m^2. Majority of the clusters are of vacancy type in the shape of stacking fault tetrahedra (SFT). Ion flux is not found to affect formation of defect clusters. Some vacancy clusters are formed within small regions forming cluster groups. Figure 1 shows distributions of number of vacancy clusters in a group which are considered to be formed by a single incident ion. Fraction of the groups which contain larger number of vacancy clusters is found to increase with ion energy. It should be noted that number of vacancy clusters in a group has variation even by the irradiation with same energy self-ions which are considered to be mono-energetic PKAs.

Total density of vacancy clusters increases with ion energy, and almost all the irradiated ions higher than 100 keV produce cluster groups. Figure 2 shows ion energy dependence of vacancy cluster yield and group yield which are defined by areal density of clusters and cluster groups divided by ion fluence, respectively. The cluster yield increases more than 1.0 at about 70 keV, which agreed with the previous report by Merkle et al[5]. At 400 keV, depth distribution of defect production extends over 60 nm from the surface resulting in the slight decrease of measured group yield. Size distributions of the clusters are also measured for each number of clusters in a group. Size of individual vacancy cluster is not found to be strongly affected by ion energy and also by the number of clusters in a group.

4. Discussion

The cluster yield does not show linear relationship with ion energy especially at 100 keV and higher energy, because of the overlapping of subcascades within a cascade in gold in which separation between subcascades is not so wide as the size of clusters[2]. The interaction between subcascades decreases the number of vacancy clusters from a PKA and the single cluster are most frequently observed even at 400 keV.

As formation of vacancy clusters by self-ions is limited within the thin layer of the specimen surface, large clusters cannot be formed near the surface. Defect production depth by lower energy self-ions is comparable to the size of defect clusters[19], and vacancy rich regions in the core of cascades may easily escape to the surface resulting in no defect clusters. To estimate defect cluster formation as a function of PKA energy in neutron-irradiated materials from the present self-ion irradiation data, we should calibrate the yield of vacancy clusters and cluster groups based on the measured cluster size distribution for each number of clusters in a group. Calibrated density of defect cluster of size l, $D'(l)$, is calculated by the following equation;

$$D'(l)=D(l)\int_0^{\infty} f(x)\mathrm{d}x \;/\; \int_l^{\infty} f(x)\mathrm{d}x$$

where $D(l)$ is measured cluster density of size l and $f(x)$ is calculated production probability of defects at the depth x from the ion incident surface. Calibrated cluster yield and group yield are also shown in figure 1 as dotted lines.

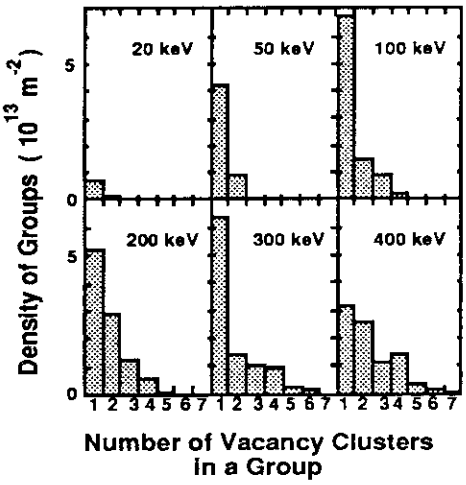

Fig. 1 Number of defect clusters in the group in gold irradiated with self ions.

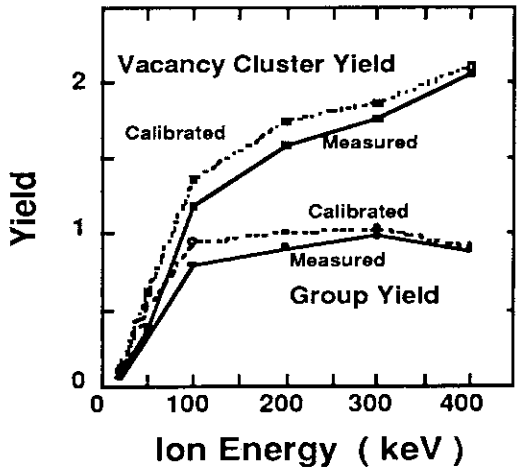

Fig. 2 Yield of defect clusters and groups of defect clusters in gold as a function of irradiated ion energy. Dotted lines show the calibrated results from the size and depth distributions of defect clusters.

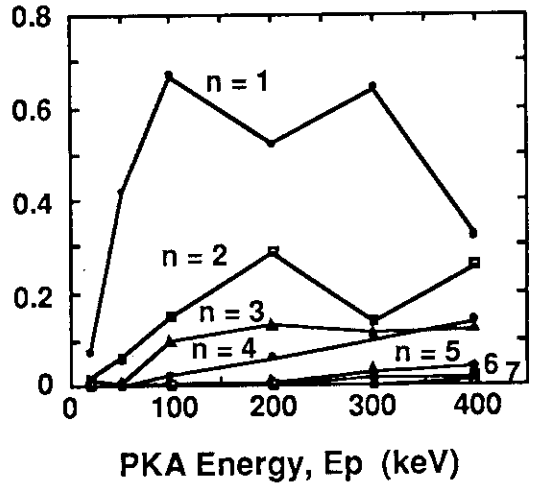

Fig. 3 Fraction of defect groups which contain n clusters as a function of PKA energy determined by 20 - 400 keV self-ion irradiation, $P(n,Ep)$

Next step is to recompose these data to fit the PKA energy spectrum under fusion or high energy particle irradiation conditions. We can estimate the probability of formation of the cluster groups which consist of n clusters as a function of PKA energy, Ep. Figure 3 shows this function, $P(n,Ep)$, from the calibrated results. Using this function and the PKA energy spectrum, $W(Ep)$, distribution of defect clusters under the high energy particle irradiation conditions can be evaluated by the following formula;

$$\int_0^{\infty} W(Ep)\, P(n,Ep)\, dEp \quad (n = 1,2,3, \cdots\cdots)$$

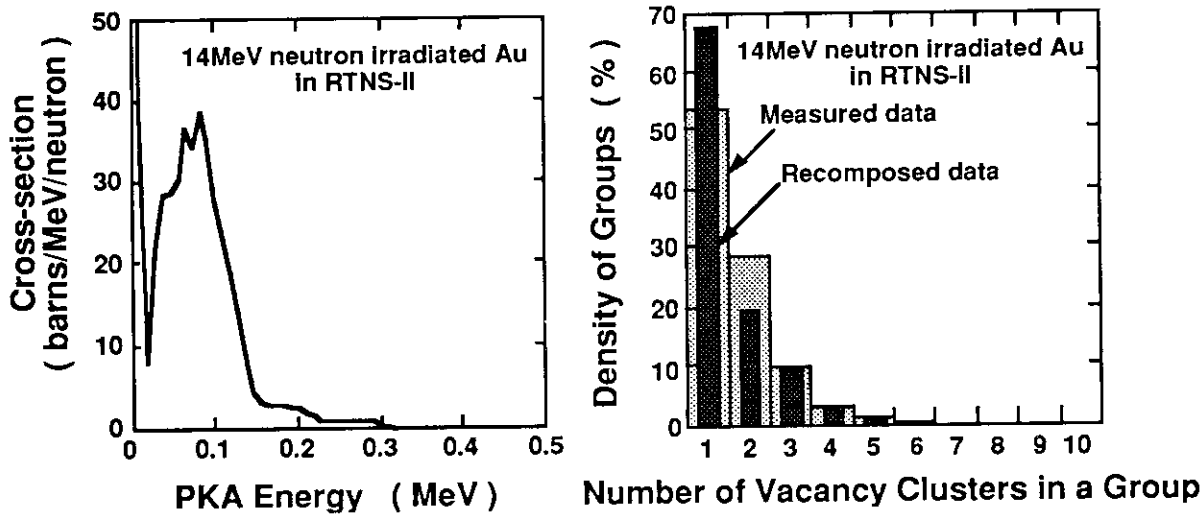

Fig. 4 Calculated PKA energy spectrum in gold irradiated with 14 MeV neutrons by the SPECTER code (left), and comparison of estimated and measured distribution of number of defect clusters in a group in a thin foil of gold irradiated with 14 MeV neutrons (right). Neutron fluence of the measured data is 1.2×10^{20} m^{-2}.

This model postulates no interaction between cascades. Kiritani et al reported defect cluster formation in thin foils of gold irradiated with 14 MeV neutrons by RTNS-II. They found that distributions of vacancy clusters in a group changed with irradiation dose, and that density of the clusters in gold did not increase monotonically with irradiation dose[2]. They called these phenomena as an "impact effect" and estimated effective zone of the impact effect as 40 nm in diameter for gold under 14 MeV neutron irradiation. As the average distance between cascades in the present ion irradiation study is 100 nm, it can be said that the present results do not contain the "impact effect".

Figure 4 compares the recomposed distribution of number of vacancy clusters from the present ion irradiation experiments using the calculated PKA energy spectrum by the SPECTER code 20), and measured results from 14 MeV neutron irradiation to 1.2 x 10^{20} n/m^2 [2], where density of vacancy clusters was found to increase linearly with fluence. The present model based on the self-ion irradiation up to 400 keV shows very good correlation with the measured results, as maximum PKA energy spectrum of 14 MeV neutron irradiation is about 300 keV.

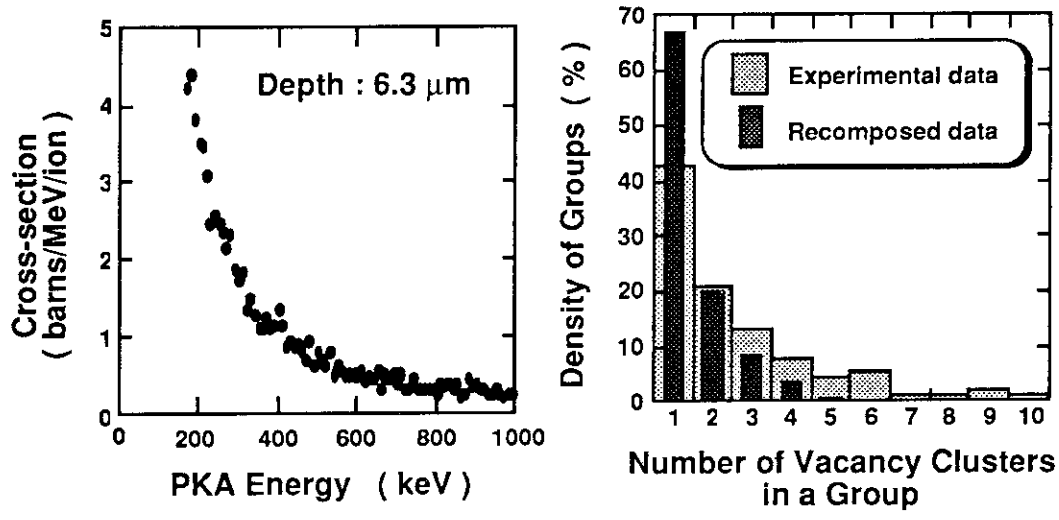

Fig. 5 Calculated PKA energy spectrum in gold irradiated with 170 MeV self-ions by the TRIM code (left). Comparison of estimated and measured distribution of number of defect clusters in a group in a thin TEM foil of gold (right). In front of the TEM specimens, a gold foil of 6.3 μ m in thickness was placed and irradiated with 170 MeV self-ions to 1.0 x 10^{14} ions/m^2.

To evaluate effects of PKA higher than 400 keV, thin foils of gold were irradiated with 170 MeV self-ions to 1.0 x 10^{14} ions/m^2. Irradiations were carried out at room temperature using a 20 MV tandem accelerator at the Japan Atomic Energy Research Institute. By placing gold foils of 1.1, 3.0, 4.3, 6.3 and 7.2 μ m in thickness in front of the TEM specimens, we can change the PKA energy spectrum in the specimens. Details of the experimental procedures and results are reported in a separate paper[21]. Figure 5 (a) shows the calculated PKA energy spectrum by the TRIM 89 code in the case of thickness of gold foil of 6.3 μ m. Measured and

predicted distribution of number of clusters in a group are compared in figure 5 (b). From these results, it is shown that small fraction of high energy component of PKA affects the distribution of cluster groups which have large number of vacancy clusters. A model to extrapolate defect cluster formation by PKA over 400 keV is discussed in a separate paper [21].

5. Conclusion

Vacancy cluster formation by self-ion irradiation up to 400 keV was evaluated to understand cascade damage as a function of primary recoil energy, and a model was proposed to predict distribution of vacancy cluster formation based on primary knock-on energy spectrum assuming no interaction between cascades. Estimated results by this model agreed the measured distribution of number of vacancy clusters in a group in gold irradiated with 14 MeV neutrons to relatively low dose before the cascade-cascade interactions become effective. Modeling of cascade damage formation and microstructural evolution by the self-ion irradiation data is considered to potentially be the best way to establish correlations between variety of irradiation environments in fission reactors, charged particles experiments, intense neutron source and fusion reactors.

References

1) S. Ishino and N. Sekimura, Annales de Chemie, Science des Materiaux, 16 (1991) 341.
2) M. Kiritani, T. Yoshiie, S. Kojima and Y. Satoh, Radiation Effects and Defects in Solids 113 (1990) 75.
3) M. Kiritani, Mater Sci. Forum 15-18 (1987) 1023.
4) M. Kiritani, J. Nucl. Mater 155-157 (1988) 113.
5) K. L. Merkle, L. R. Singer and J. R. Wrobel, Appl. Phys. Lett. 17 (1970) 6.
6) A. Y. Stathopoulos, Phil. Mag. A44 (1981) 285.
7) A. Y. Stathopoulos and C. A. English, J. Nucl. Mater 108&109 (1985) 69.
8) C. A. English and M. L. Jenkins, Mater Sci. Forum 15-18 (1987) 1003.
9) T. Muroga, K. Hirooka and S. Ishino, ASTM-STP 870 (1985) 407.
10) M. Kiritani, H. Kato, M. Hoshino, H. Matsui and N. Matsunami, J. Nucl. Mater 191-194 (1992) 1128.
11) S. Ishino, N. Sekimura, K. Hirooka and T. Muroga, J. Nucl. Mater 141-143 (1986) 776.
12) S. Ishino, N. Sekimura and T. Muroga, Mater Sci. Forum 15-18 (1987) 1105.
13) N. Sekimura and S. Ishino, J. Nucl. Mater 155-157 (1988) 1217.
14) N. Sekimura, Y. Yamanaka and S. Ishino, ASTM STP 1046 (1989) 596.
15) H. Sakaida, N. Sekimura and S. Ishino, J. Nucl. Mater 179-181 (1991) 928.
16) Y. Kanzaki, N. Sekimura and S. Ishino, J. Nucl. Mater191-194 (1992) 1119.
17) N. Sekimura and S. Ishino, Rad. Eff. and Defects in Solids 124 (1992) 109.
18) S. Ishino, N. Sekimura, H. Sakaida and H. Kanzaki, MaterSci.Forum 97-99 (1992) 165.
19) J. P. Biersack et al, Nucl. Instr. and Meth. 174 (1980) 257.
20) L. R. Greenwood and R. K. Smither, ANL/FPP/TM-197.
21) N. Sekimura, Y. Kanzaki, M. Okada, T. Masuda, S. Ishino, T. Iwata and A. Iwase, to be published.

2. 6 International Activities

2. 6. 1 International Fusion Materials Irradiation Facility (IFMIF) Program

Kenji Noda

Japan Atomic Energy Research Institute, Tokai-mura, Naka-gun, Ibaraki-ken

319-11, Japan

Energy Selective Neutron Irradiation Test facility (ESNIT) was conceived at Japan Atomic Energy Research Institute (JAERI) as a domestic high energy neutron irradiation means for R&D of materials in nuclear applications, especially for nuclear fusion applications. ESNIT is a d-Li stripping type neutron irradiation facility with additional functions of neutron energy selectivity and post irradiation examination. A series of technical evaluation of ESNIT concept has been carried out since 1989, and a d-Li stripping type neutron source with neutron energy selectivity was evaluated to be technically feasible and suitable for fusion materials testing.

An international assessment on several neutron source concepts as candidates of the International Fusion Materials Irradiation Facility (IFMIF) was done during 1989 to 1992. The d-Li stripping type neutron source concept with neutron energy selectivity was chosen as an appropriate IFMIF concept. Recently, IEA Fusion Power Coordination Committee (FPCC) recommended to initiate preparation for Conceptual Design Activity (CDA) of IFMIF, and the CDA plan is being discussed in the preparatory activity for the CDA. The CDA is expected to be initiated after approval of the CDA plan at FPCC meeting at the beginning of 1995.

1. Introduction

The D-T fusion reactor environment for materials is featured by severe irradiation of high energy neutrons with energies up to 14 MeV. Energetic neutrons displace primary knock-on atoms (PKA), which form cascade damage, and produce nuclear transmutation products. The PKA energy and cross sections of producing the nuclear transmutation products strongly depend on neutron energy. Microstructure and properties changes of neutron-irradiated materials are taken place as synergistic effects of displacement damage and introduction of nuclear transmutation products. Fusion neutrons produce PKA with high energies introducing much displacement damage and a large amount of nuclear transmutation products such as helium and hydrogens, comparing with those in fission reactors. Consequently, materials properties degradation in fusion reactor environments are quite different from that in fission reactors.

Development of materials tolerable to severe high energy neutron irradiation is necessary to realize fusion reactors beyond ITER. It is a consensus that a high energy intense neutron irradiation facility which can provide neutron irradiation fields suitable for fusion materials testing is indispensable for such materials development. From this standpoint, technical development of a d-Li stripping type accelerator based neutron source was carried out in the United States from 1978 to 1985 in the Fusion Materials Irradiation Test Facility (FMIT) project [1,2]. However, the project was canceled just before the construction.

Energy Selective Neutron Irradiation Test facility (ESNIT) was conceived at Japan Atomic Energy Research Institute (JAERI) as an advance irradiation tool for materials in nuclear applications, especially for fusion application [2-10]. ESNIT is a small version of the FMIT with additional functions of neutron energy

selectivity and post irradiation examination. A series of technical evaluation of ESNIT concept has been done since 1989. At international advisory meeting on ESNIT at the beginning of 1993, ESNIT, i.e., a d-Li stripping type neutron source with neutron energy selectivity, was evaluated to be technically feasible in very near future and very suitable for generic nuclear materials studies, especially for fusion materials R&D [10]. On the other hand, the IEA fusion materials community carried out an international assessment on several neutron source concepts as candidates of the International Fusion Materials Irradiation Facility (IFMIF) during 1989 to 1992 in terms of technical feasibility and suitability for fusion materials testing [11-16]. A d-Li stripping type neutron source with neutron energy selectivity was chosen as an appropriate IFMIF concept, which was eventually a close reflection of the outcomes of the FMIT and ESNIT program. Recently, IEA Fusion Power Coordination Committee (FPCC) recommended to initiate preparation for Conceptional Design Activity (CDA) of IFMIF to make detailed IFMIF-CDA plan. The CDA is expected to be initiated as an international collaborative activity after approval of the detailed CDA plan at FPCC meeting at the beginning of 1995.

In this paper, status of ESNIT and IFMIF programs as a domestic and an international high energy neutron irradiation facilities is described, respectively.

2. Status of ESNIT program

2.1. Concept of ESNIT

ESNIT consists of a deuteron linear accelerator system, a liquid Li target system and an experimental system. Characteristics of the ESNIT are summarized as follows [3-10].

(1) Neutron spectra: The d-Li neutron spectra have a peaking character and the peak energy can be selected at least three steps (e.g., 5, 10, 14 MeV) by changing the deuteron energy in the range 10 to 40 MeV.

(2) Neutron flux and test volume: With the maximum current of 50 mA, a neutron flux higher than $1.5X10^{14}$ n/cm^2s (10 dpa/y for stainless steels) can be attained for the volume of about 5X5X5 cm^3 for beam diameter of 40 mm and flat current distribution. Such test volume was estimated to be adequate for performing various types of in-situ tests and irradiation tests of a significant number of small test specimens. An annual neutron fluence corresponding to 30 dpa/y for stainless steels can be attained by limiting test volume to about 10 cm^3.

(3) Controllability of neutron flux/energy: The neutron flux and the peak energy of the spectra can be independently changed.

(4) Time structure of neutron beam: To avoid the influence of pulse irradiation, beam pose period should be shorter than 10^{-6} s from consideration of lifetimes of point defects. The accelerator is expected to be operated with 120 MHz in CW(continuous wave) mode, so that materials irradiation tests can be carried out without the pulse irradiation effects.

(5) Test cells: At least two irradiation test cells are provided for high availability of the neutron generation system. Better accessibility to the test cells relative to the conventional research reactors enables various in-situ experiments and precise irradiation condition control.

(6) Post-irradiation examination facility: Post-irradiation examination hot cells especially for the small specimens tests are coupled close to the test cells.

2.2. Status of technology for ESNIT

2.2.1. Accelerator technology

Basic layout of the accelerator system consists of the following components: (1) ion sources and an ion extraction system for d^+ ions of 60 mA at the energy of 75 KeV, (2)low energy beam transport (LEBT), (3)Radio Frequency Quadrapole linac (RFQ) with the exit energy of 2 MeV which is driven in CW (continuous wave) mode at 120 MHz, (4) Drift Tube Linac (DTL) driven in CW mode at 120 MHz, which consists of separated multiple tanks to accelerate the d^+ ions at 10, 15, 20, 25, 30, 35, 40 MeV, (5)high energy beam transport (HEBT), (6) target interface section consisting of multipole magnet system to change the beam size and current density distribution on the lithium target, (7) RF source, etc. [6,7,10].

At the international advisory meeting on ESNIT, it was evaluated that the present status of the accelerator technology for ESNIT had few critical issues in physics sense and that the construction of ESNIT was able to proceed with confidence, with proper concern for engineering and prototype models. Careful engineering R&D, fabrication of prototype models and R&D using them should result in a reliable factory-grade neutron irradiation facility for materials testing. According to the above-mentioned recommendation, the further technical evaluation for accelerator system of ESNIT is in progress.

2.2.2. Target technology

The target system consists of flowing Li targets and a Li circulation system including cooling and purification systems [6,8,10]. The concept of the target system is the similar to that of FMIT [1,2]. The Li target is directly connected to the accelerator system without a vacuum boundary to inject d^+ ions with the desired energies to the flowing Li target. Boiling of Li due to beam heating is suppressed by centrifugal force which is generated by flowing liquid Li along the target backwall with a appropriate curvature. Many kinds of R&D for the target technology were successfully carried out in the FMIT project [1,2]. In the technical evaluation for the Li target of ESNIT, the effort has been mainly focused on thermo-hydraulic behavior of Li flowing target to define the boiling conditions. From such evaluation, it was found that the region of the most severe condition for the boiling was the free surface of flowing Li in the case of the lower deuteron energy [8]. At the international advisory meeting on ESNIT, it was pointed out that improvement of thermal-hydraulic evaluation, prototype model tests for flowing behavior, evaluation of back streaming of Li vapor, beam-on target tests, etc. were necessary [10]. At this moment, evaluation of thermal-hydraulic evaluation using an advanced calculation code and preparation of experimental evaluation of Li vaporization behavior are being carried out.

2.2.3. Experimental system technology

Uncollided and collided neutron spectra (for Fe and Al_2O_3) and flux distribution in the irradiation field of ESNIT were calculated for various deuteron energies, various beam size and various beam profile using a proper source model [6,10]. Although the neutron spectra extend to 40 MeV, nuclear data only for neutron energies up to 20 MeV are available. So, the nuclear data in the range 20 to 50 MeV have been evaluated for common

elements of materials in fusion reactors and ESNIT itself [6,10]. Calculation of damage parameters is important to make test matrices and research plans. Computer codes to calculate damage parameters, especially for amount of nuclear transmutation products are being developed [6,10]. Materials researches to be performed using ESNIT were defined for fusion materials R&D and fundamental materials irradiation researches. In addition, it was evaluated that the neutron energy selectivity was very useful for irradiation tests of various fusion materials, since energy levels of neutron spectra could be decreased to the level at which effects of the high energy tail was negligibly small, in the case that the effects of the high energy tail were large. At the international advisory meeting on ESNIT, most of activities on experimental system technology were evaluated to be appropriate with some recommendations such as further evaluation of nuclear data for low activation materials and development of PKA calculation code for neutron energy range up to 50 MeV, etc.

3. Status of IFMIF program

3.1. Criteria of suitability for IFMIF

International evaluation on the suitability and technical feasibility of several candidates of IFMIF concepts was initiated in 1989 as one of activities in IEA Implementing Agreement for Fusion Materials R&D. Criteria of suitability for IFMIF from the standpoints of fusion materials testing in international use are as follows [11,14].

(1) The neutron spectrum should be as close as possible to that at the first wall of fusion reactors. The energy distribution for other components in the fusion reactor should be obtained by spectral tailoring. (2) The source should allow experiments in a neutron flux corresponding to a neutron wall load of $2MW/m^2$ ($6X10^{-7}$ dpa/s) anticipated for a DEMO fusion reactor. DEMO relevant lifetime fluence (i.e., 100 dpa) must be attained for a period of several years. (3) A volume of 1 liter is required at an uncollided neutron flux corresponding to $2MW/m^2$ or greater. (0.4 liter for a collided neutron flux corresponding to $2MW/m^2$ or greater) (4) Collided neutron flux gradient must be lower than 10%/cm for limitation of miniaturization of various tests and homogeneity of radiation damage within the test section. (5) Accessibility to the irradiation field should be good. (6) In respect of time structure of neutron beam, a quasi-continuous operation is mandatory. The repetition time of pulses should be shorter than annealing time of point defects.

3.2. Selection of IFMIF candidate concepts

Several candidate concepts for IFMIF were proposed, i.e., (1) accelerator based neutron sources; d-Li neutron source, spallation neutron source and T-H neutron source, (2) plasma based neutron source; beam plasma (Mirror type) neutron source, Reverse Field Pinch (RFP) fusion neutron source, High Density Z-Pinch (HDZP) neutron source. In the candidate concepts, RFP and HDZP were evaluated to be out of scope of IFMIF from the standpoint of technical feasibility and the criteria of suitability for IFMIF. The d-Li, the spallation, the T-H and the beam plasma neutron sources were further evaluated through activity of IFMIF technical working group in the framework of IEA Implementing Agreement for Fusion Materials R&D from 1990 to 1992. Evaluation results by the working group are mentioned below.

(1) d-Li neutron source:

The d-Li neutron source is considered to meet the suitability criteria for IFMIF. The neutron spectra, however, have the region of which energies exceed 14 MeV, i.e., so-called "high energy tail" extending to 30 to 40 MeV. Influences of the high energy tail on the materials testing must be checked. The PKA spectra and amount of transmutation products were calculated for various elements [13,16]. It was found in such calculation that the high energy tail for the deuteron energy in the range 35 to 40 MeV had almost no influence on materials testing for elements of metallic materials from the standpoint of simulation of neutronic environment of fusion reactors while some influences for low Z elements such as carbon. The influences for low Z elements can be avoided by decreasing the deuteron energy to 30 MeV [16]. The technical feasibility of d-Li neutron source was evaluated to be the highest among the IFMIF candidate concepts, since many R&D issues have been already solved in the FMIT project [9,11,14].

(2) Spallation neutron source:

The neutron spectra of the spallation neutron source are very broad and the high energy tail extends to 100 MeV. However, the effective energy range of neutron spectra in which neutron flux is large enough to carry out materials testing is almost the same as that of fission reactors. It was, therefore, evaluated that the neutron spectra of the spallation neutron source were too soft (i.e., too low in neutron energy) to carry out fusion materials testing. The spallation neutron source requires a high energy (600 to 1000MeV) proton accelerator in CW mode operation and liquid Pb or Pb-Bi targets. The technical feasibility was evaluated to be lower than that of d-Li neutron source, but higher than that of beam plasma neutron source [11,12].

(3) T-H neutron source:

The T-H neutron source consists of 21 MeV tritium accelerator system and a flowing water target system [14,16]. The neutrons with cut-off energy of about 14 MeV are generated by $H(T,n)^3He$ reactions. Although the neutron spectra have no high energy tail, the spectra are somewhat too soft for fusion simulation [16]. Furthermore, it is very difficult to obtain sufficient test volume in this type of neutron source [16]. The technical feasibility was evaluated to be low, because of difficulty of an intense tritium accelerator system and water jet target technology [16].

(4) Beam plasma neutron source

The neutron spectra of the beam plasma neutron source are very similar to those at the first wall of fusion reactors, since the neutron source generates 14MeV neutrons [13]. Concerning the technical feasibility, the beam plasma neutron source was evaluated to need many R&D, in comparison with the d-Li and the spallation neutron sources [12].

Based on the above-mentioned evaluation of IFMIF candidate concepts, the d-Li neutron source concept with neutron energy selectivity by changing deuteron energy in the range 30 to 40 MeV was chosen as an agreed IFMIF concept from the standpoint of suitability for fusion materials testing and technical feasibility by the executive committee of IEA Implementing Agreement for Fusion Materials R&D in 1992.

3.3. Status of IFMIF activity

By the executive committee mentioned above, it was recommended that the IFMIF (i.e., d-Li neutron source) should be constructed and operated by 2000 to proceed development of DEMO fusion reactors and that

the design activity for the IFMIF should be initiated as early as possible. Such recommendation was reported at IEA Fusion Power Coordination Committee (FPCC). The FPCC at the beginning of 1994 recommended to initiate preparation of the Conceptual Design Activity (CDA) of IFMIF. According to the recommendation, the preparatory activity for IFMIF-CDA was carried out in 1994. Two planning meeting on IFMIF-CDA in administrative and technical aspects were held in Tokai (June, 1994) and in Karlsruhe (September, 1994). The objectives of the CDA, organization for implementing the CDA, technical issues, basic design concept, milestone, time schedule and requirements for irradiation field of IFMIF from standpoint of user, etc. were discussed in the abovementioned meetings. On the basis of the discussion, proposal of IFMIF-CDA is being prepared. After approval of the CDA plan by FPCC at the beginning of February, 1995, IFMIF-CDA is expected to be initiated and carried out for two years to make an agreed conceptual design for an optimized d-Li neutron source as IFMIF.

References

[1] A. L. Trego et al., Nucl. Technol./Fusion 4 (1983) 675.

[2] R. J. Burke and J. J. Holmes, J. Nucl. Mater. 133&134 (1985) 869.

[3] T. Kondo, H. Ohno, M. Mizumoto and M. Odera, J. Fusion Energy 8 (1989) 229.

[4] K. Noda, Y. Oyama, S. Yamaguchi, H. Maekawa and A. Hishinuma, J. Nucl. Mater. 174 (1991) 319.

[5] K. Noda, H. Matsuo, K. Watanabe, M. Sugimoto, Y. Kato, H. Sakai, T. Kikuchi, Y. Oyama, H. Ohno and T. Kondo, J. Nucl. Mater. 179-181 (1991) 1147.

[6] K. Noda, M. Sugimoto, Y. Kato, H. Matsuo, K. Watanabe, T, Kikuchi, H. Usui, Y. Oyama, H. Ohno and T. Kondo, J. Nucl. Mater. 191-194 (1992) 1367.

[7] M. Sugimoto, K. Noda, H. Ohno and T. Kondo, J. Nucl. Mater. 191-194 (1992) 1432.

[8] Y. Kato, K. Watanabe and T. Kondo, J. Nucl. Mater. 191-194 (1992) 1428.

[9] T. Kondo, H. Ohno, R. A. Jameson and J. A. Hassberger, Fusion Eng. Design 22 (1993) 117.

[10] K. Noda, H. Ohno, M. Sugimoto, Y. Kato, H. Matsuo, K. Watanabe, T. Kikuchi, T. Sawai, T. Usui, Y. Oyama and T. Kondo, J. Nucl. Mater. in press.

[11] D. G. Doran and J. K. Leiss, J. Fusion Energy 8 (1989) 137.

[12] Proc. on International Fusion Materials Irradiation Facility (IFMIF) Workshop, Feb. 14-17, 1989 (San Diego)

[13] D. G. Doran, F. M. Mann and L. R. Greenwood, J. Nucl. Mater. 174 (1990) 125.

[14] T. Kondo, D. G. Doran, K. Ehrlich and F. W. Wiffen, J. Nucl. Mater. 191-194 (1992) 100.

[15] D. G. Doran et al., IEA Neutron Source Working Group Report (May 1993).

[16] D. G. Doran and S. Cierjacks et al., IEA Neutron Source Working Group Report (July 1993).

2.6.2 Japanese Activity on Nuclear Structure Data Evaluation

K.Kitao
Data Engineering, Inc.
8-10, Mitsuwadai-2, Wakaba-ku, Chiba 264,

A brief review of evaluation works on nuclear structure data in Japanese through 1965 is given chronologically. Main activities in Japan are as follows: (1) contribution to ENSDF through 1979 by the JNDC-ENSDF working group, (2) evaluation of the decay data for estimation of decay heat of the shutdown nuclear reactor, and (3) Prediction of band-structure in excited state of non-rotational nuclei.

Introduction

Good and enough experimental data on nuclear structure bring good evaluation. Best compilation of experimental data is the Evaluated Nuclear Structure Data File (ENSDF)* at present. Unfortunately, experimental information on nuclei has its limit, because available accelerating particles, targets and detectors have some limitations. As the results, experimental data have many missing parts. On the other side, there are many users of evaluated data whose does request completeness for any data. Work as filling up missing parts of experimental results is based on extrapolation and/or interpolation on properties of nuclei. Of course, systematics on nuclear properties through several mass region also are used as means. But each nuclide is a considerably individual one and method of systematics is not success at any time. However, the method is correctly attractive one to study of nuclear properties.

* Evaluated Nuclear Structure Data File, a computer file of evaluated experimental nuclear structure data maintained by the National Nuclear Data Center, BNL, USA.

Data accumulation

The first edition of Table of Isotopes, a data book on decay properties of nuclides, was published on the Journal "Review of Modern Physics" in 1940, and it contained only 17 pages. Subsequent nuclear experiments have accumulated abundant and more accurate results for nuclear properties with advent of particle accelerators as well as NaI(*Tl*) and Germanium detectors. Then, its 7th edition published in 1978 occupies almost 1500 pages. The number of pages in the next edition of the book may be over 3000. K.Way and E.P. Wigner[1] had calculated decay heat of the shutdown reactor and compared with experimental results in 1948. In later year, Way came to edit a journal devoted to compilations and evaluations of experimental and theoretical results in nuclear physics. It is sure that she had been quite

conscious of needs for data compilations through works on decay heat calculation. Way published the first issue of Nuclear Data A (former to Atomic and Nuclear Data Tables) in 1965 and Nuclear Data B (former to Nuclear Data Sheets) in 1966. We could find the name of R. Nakasima (Hosei Univ.) and M. Yamada (Waseda U.) in members of the board of editors of Nuclear Data B. H.Ikegami (Osaka Univ.) was also listed as one of those in Nuclear Data A. It connotes that our Japanese researchers have concerned with compilation and evaluation of nuclear data through the beginning the data work.

Decay data evaluation

In 1965, the Japan Atomic Energy Research Institute (JAERI) was established. Japanese Nuclear Data Committee (JNDC), operated jointly by JAERI and Atomic Enrage Society of Japan, has started its activities in 1963. M.Yamada (Waseda Univ.) and his collaborators proposed the gross theory[2] of the beta decay in 1969 and calculated beta-strength function. They[3] also predicted the half-lives of beta emitted nuclides including those far from the beta stable line by the theory. It is obvious that the theory base on the compilation of decay data. In 1974, JNDC has organized a working group for evaluation of decay heat from the shutdown reactor. The group built up a first file of the decay data on fission products from ENSDF in 1981. This file, so called the JNDC FP decay file, included also beta-ray intensities[4] evaluated with the aid of the gross theory. Then, the group has proposed the recommended values of decay heat calculated using with the file in 1989. The final report of the group was published with some corrections and additions from direct measurements in 1990[5].

In 1976, IAEA Nuclear Data Section has established an international network supporting ENSDF and related works. This work is called mass chain evaluation. By the way, evaluation based on systematics is called horizontal one. The JNDC-ENSDF group has participated to the network through 1977 and done share of evaluation and entry of data in mass region A=118-129. The journal "Nuclear Data Sheets" had published the first evaluation work by our group on the issue of 1979 [6].

A. Hashizume (RIKEN) published the first Japanese nuclear wall chart in 1970, and the first edition [7] of JAERI's wall chart compiled by Y. Yoshizawa, et al. (Univ. Hiroshima) was published in 1976. The later has been published for each four year. Its "sales point" is that nuclides are classified with half-life, and that calculated values for unmeasured half-lives of nuclides far from the beta stable line are given using with the Yamada's gross theory.

Horizontal evaluation

In a sense, the calculation of beta-decay half-lives by Yamada et. al. can be regarded as evaluation. A large accumulation of data does stimulate some bird-view of data, and enable to reveal common properties in nuclides in some mass region, i.e., syatematics of properties. By

discover of systematics we can expect to light up some hidden nuclear properties. In 1967, M.Sakai (INS, Univ. Tokyo) [8] predicted the existing of rotational band-like structure (so called quasi- band) in vibrational nuclei as well as spherical nuclei. He said the idea of the quasi-band created in staying at BNL, USA. His works are clear to base on abundant accumulated data, i.e., ENSDF. M.Yamada[9], together with Gove, studied systematics on separation energy of neutron and proton in 1968.

Concluding remarks

Basic work on data evaluation is comprehensive collection of experimental data first of all. Recent works in experimental nuclear physics have shifted to in-beam spectroscopy with heavy ion, and studies for static nuclear decay are very few. This is undesirable situation for data compilation on nuclear structure. Data entered in ENSDF is still not sufficient. Precision of data, for example that of intensities for ground-state beta-radiations from the radioactive decay, is also not enough. We expect many young researchers to commit studying such problem, although these are not most topical and academic objects. Activity of our old evaluator comes gradually to decay. we welcome young generation to participate the work on evaluation and compilation of nuclear structure data.

References

1) K.Way and E.P.Wigner: Phys. Rev. **73**, 1318 (1948).
2) K. Takahashi and M. Yamada: Progr. Theo. Phys. **41**, 1470 (1969).
3) T. Takahashi et. al.: At. Data Nucl. Data Table **12**, 101 (1973).
4) T. Yoshida and N. Nakasima: J. Nucl. Sci. Technol. **18**, 393 (1981).
5) K. Tasaka et al.: JNDC Nuclear Data Library of Fission Products (2nd Version), JAERI Report, JAERI 1320 (1990).
6) T. Tamura et al.: Nuclear Data Sheets **26**, 385 (1979).
7) Present version is T. Horiguchi et al.: Chart of the Nuclides (1992).
8) M. Sakai: Nucl. Phys. **A104**, 301 (1967). This is the first paper by the author on this theme.
9) N.B.Gove and M.Yamada: Nuclear Data **A4**, 237 (1968)

2.7 Summary Talk

A. Takahashi (Osaka University)

First, we review briefly the situation of nuclear data activity in the world. Recently, i.e. after the Cold War, nuclear data activity is drastically going down especially in the former leading countries like USA and CIS (former USSR). The declining trend is obvious in experiments (nuclear data measurements) due to shut-down of many previous key-facilities. However, considerable activities in experiments are being kept here in Japan, and new activities are growing up in some countries in Asia, e. g., China. New motive forces in nuclear science and engineering, which can promote near-future nuclear data activity, are foreseen in the OMEGA & Proton Engineering Center Project and the IFMIF project of JAERI for which conceptual design activities are started or to be started. Needs of nuclear data in "higher" neutron energy, i. e. more than 20 MeV which is the upper end energy of latest world evaluated files like ENDF/B-VI and JENDL3, will be the coming trend for experimental and evaluation efforts. Such orientation has already been seen since the last Symposium on Nuclear Data in November 1993.

The completion and release of JENDL3.2 has initiated a new series of benchmark studies on applications to fission and fusion reactors. Many results of JENDL3.2 benchmarking are presented in this Symposium. The benchmark studies on fission reactor application have shown that C/E values are much converged to 1.0, compared with the cases of JENDL3.1, for most cases of different reactor types. It seems that general improvement is attained by JENDL3.2. It was impressive that the vectorized Monte Carlo code MVP developed recently in JAERI was powerfully used in the benchmark calculations. The benchmark studies on fusion reactor application have also shown that we can see many improvements for many nuclides: JENDL3.2 and JENDL-Fusion-File are expected to be included in the newly selected FENDL2 library of IAEA.

Progresses of experiments, i.e. measurements of nuclear data, are reflected in 18 presentations in Poster Session. About 9 presentations of 18 are related to fusion application, 5 of 18 to fission and 3 of 18 to "higher" energy applications. In fusion neutronics benchmarks, integral experiments on neutron and gamma-ray spectra with spherical and slab assemblies done in Japan have very efficiently been utilized to be compared with JENDL.3.1, JENDL3.2, ENDF/B-VI and

FENDL1. The new measurement of C8/F9 ratio done at FCA of JAERI has resolved the "historical" C/E discrepancy for the ZPPR9 data.

Prof. Kawai gave the audiences an excellent lecture on the history of nuclear reaction theory. It was good education to point out that many break-throughs in nuclear theory were done by criticizing and reconstructing the "golden rule" which we had believed in. The application of QMD (Quantum Molecular Dynamics) theory to nuclear reactions in the "higher" energy has appealed very exciting because of the excellent agreements of its calculations with measured secondary particle spectra and also due to the demonstartion on screen using beautiful animation of time-evolving reaction procedures. Such a new tool of theoretical analysis must attract Young People who will join the nuclear data community.

Did we have much discussions in the Symposium ? There were seen many hot discussions going on in many places in front of posters. Therefore the poster session was successful and fruitful. Did we see good indication of growing Young Activity ? Well there were seen several new faces and rather-young researchers doing good works like QMD and FKK theories, but still "ultra-young" (or retired) power remains more and we should wait it for future. We could welcome foreign speakers from Bangladesh and CIS countries in the Symposium. To extend the internationality of the N. D. Symposium is one of issues for future. Also the role of JAERI Nuclear Data Center in future may be important to establish "Asian Nuclear Data Center" as said by some people in this Symposium. English was used in the Foreign Session of this Symposium, and may be considered as common coference language in future "Asian" N.D. Symposiums.

3. Papers Presented at Poster Session

3. 1 Precise Measurement of Neutron Total Cross Section of Pb-208 and Pb-nat

Katsuhei Kobayashi, Shuji Yamamoto, Yoshiaki Fujita
Research Reactor Institute, Kyoto University
Kumatori-cho, Sennan-gun, Osaka 590-04, Japan
and
Oleg A. Shcherbakov, Alexander B. Laptev
Petersburg Nuclear Physics Institute
188 350 Gatchina, Russia

Neutron total cross sections of ^{208}Pb (97.65%) and natural lead (^{nat}Pb) have been measured with the experimental uncertainties less than 1 % by the time-of-flight method using 46 MeV electron linear accelerator. In the present work, three types of neutron transmission measurements have been made (1) in the energy range from 4 to 180 eV, (2) in the expanded energy region from 2 eV to 2 keV, and (3) at 24, 55 and 145 keV with Fe- and Si-filtered neutrons, respectively.

Although the shape of the energy dependent cross sections for ^{208}Pb and ^{nat}Pb in ENDF/B-VI is similar to the present measurements, the absolute values for both cross sections are lower by about 1.5 % than the present values in the relevant energy region. The evaluated cross section of ^{nat}Pb in JENDL-3 is in good agreement with the measured data, although the evaluated data of ^{208}Pb are lower by 2 % than the measured ones. The present results are in good agreement with recent data measured by Schmiedmayer et al.(for ^{208}Pb), Alexandrov et al.(for ^{208}Pb), and Granada et al.(for ^{nat}Pb).

1. Introduction

Recently, three transmission measurements for ^{208}Pb or ^{nat}Pb have been reported.[1-3] Alexandrov et al. measured the neutron total cross section of ^{208}Pb in the energy region from 1 eV to 10 keV at GNEIS.[1] Transmission measurements for ^{208}Pb were also made by Schmiedmayer et al. at ORELA with a good time-of-flight (TOF) resolution from 50 eV to 40 keV.[2] The neutron total cross section of ^{nat}Pb was measured by Granada et al. at energies between 1 and 900 eV using a linear accelerator (linac).[3]

In the present work, neutron transmission measurements of ^{208}Pb and ^{nat}Pb are made (1) in the energy region from 4 to 180 eV by a resonance capture detector[4] with Ta and Sb samples, (2) in the continuous energy range from 2 eV to 2 keV, and (3) at 24, 55 and 145 keV with Fe- and Si-filtered neutrons[6] by a ^{10}B capture detector, making use of 46 MeV linac at the Research Reactor Institute, Kyoto University (KURRI). The measured results are compared with the recent evaluated data in JENDL-3[6] and ENDF/B-VI[7]. The present results are also compared with

---

A part of this study was performed under the support of Japan Society for the Promotion of Science (JSPS/EP1/931S).

the recent data measured by Alexandrov et al.[1], Schmiedmayer et al.[2], and Granada et al.[3]

2. Experimental Method

2.1. Transmission Samples

The transmission sample of ^{208}Pb has high enrichment of 97.65 %, and other isotopic compositions are 0.87 % of ^{206}Pb and 1.48 % of ^{207}Pb, with impurities less than 0.003 %. The ^{208}Pb sample was 3.6 cm in total thickness (0.12169 $\pm$ 0.000041 atoms/b), which was composed of 3 pieces of cylindrical plates (15, and 11 mm thick, 25 mm diameter, and 10 mm thick, 50 mm diameter). The ^{nat}Pb sample was made of 4 metallic plates (0.13108 $\pm$ 0.000044 atoms/b) (each plate : 1 cm thick, 3x3 $cm^{(2)}$), and the purity was 99.9993 %.

2.2. Pulsed Neutron Source

The transmission measurements were made by the neutron TOF method using the 46 MeV linac at KURRI. Bursts of fast neutrons were produced by the water-cooled photoneutron target of Ta, which was set at the center of an octagonal water tank, 10 cm thick and 30 cm diameter, to moderate fast neutrons. A Pb block, 5x5 cm square and 20 cm long, was placed in front of the Ta target to reduce the γ-flash by the electron burst. In the TOF measurements, the KURRI linac was operated at the repetition rate of 250 Hz, with the pulse width of 68 ns, the electron peak current 2 A and the energy 30 MeV. A Cd filter of 0.5 mm in thickness was placed in the TOF neutron beam to suppress overlap of thermal neutrons from the previous pulses.

2.3. Experimental Arrangement

The experimental geometry is shown in Fig. 1. The neutron detector was located at 12.7 m distant from the Ta target. The transmission samples, which were put on an automatic sample changer, were placed at a position of about 10 m from the Ta target. For the experiments with Fe- and Si-filtered neutrons, the filtering materials were put at the entrance, middle and exit points of the flight tube. Total thickness of the filters was 27 cm for Fe and about 100 cm for Si, respectively. The neutron beam intensity during the experiment was monitored with a BF_3 proportional counter, which was inserted into the TOF neutron beam.

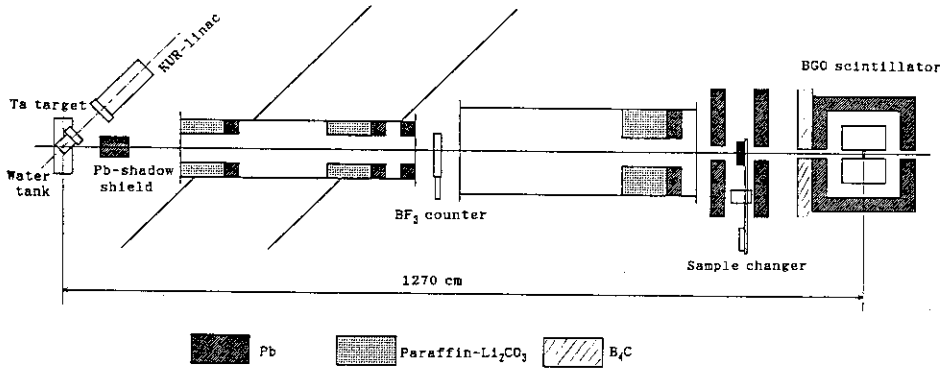

Fig. 1 Experimental arrangement for the transmission measurement.

2.4. Neutron Detectors

As a neutron detector for the TOF measurement from 4 to 180 eV, we have used a resonance capture detector[5], which is composed of 12 pieces of $Bi_4Ge_3O_{12}$(BGO) crystals and capture samples of Ta (1 mm thick plate, 1.8x1.8 cm^2) and Sb (1.13 g/cm^2, 1.8x1.8 cm^2). This detector gives quite high counts at the resonance energies of Ta and Sb in the linac TOF spectrum.[5] Coincidence measurement between any two segments of the 12 BGO crystals was useful to achieve a better signal-to-noise ratio. For the background measurement, the same materials as the capture samples were put into the TOF neutron beam. Additional filters of Mn and Co were useful for determination of the background level.

For the cross section measurements by the continuous white neutron spectrum and the filtered neutron beams, we have applied a ^{10}B capture sample (1.10 g/cm^2, 1.8x1.8 cm^2) to the above resonance capture detector instead of the Ta and Sb samples. Background levels were determined by fitting the saturated data-values of Sb, Ta, Co and Mn resonances.

3. Data Taking and Reduction

The signals from the BGO detection system were led into a time analyzer, which was initiated by the KURRI linac burst, and the TOF data were stored in a data acquisition system. The TOF analyzer was operated as four 2048-channel analyzers which corresponded to each sample "in" and "out" position (#1 for open, #2 for ^{208}Pb, #3 for open, and #4 for ^{nat}Pb). The automatic sample changer was cycled for the period of 6 minutes per one cycle, and the cycle time was allocated to each sample so as to minimize the statistical error in the cross section obtained. Another four 2048-channel analyzers were used as neutron monitors for each sample measurement.

We have prepared Fortran programs for the data processing. After the dead time correction was performed, the counts measured with the resonance capture detector were taken from the resonance peak region at full width at half maximum in the TOF spectrum[5], and the TOF channel data by the ^{10}B capture detector were summed in an appropriate energy interval to give the total cross section.

4. Results and Discussion

The neutron total cross sections of ^{208}Pb and ^{nat}Pb have been measured from 4 to 180 eV with the resonance capture detector by the linac TOF method. Making use of a ^{10}B capture detector, the cross sections have been also measured from 2 eV up to 2 keV with a continuous white neutron spectrum and at 24, 55 and 145 keV with Fe- and Si-filtered neutrons, respectively. The measured data show good agreement with each other in the overlap energy region. The uncertainties are mainly due to (1) statistical counts, (2) number of the sample atoms, and (3) corrections for air absorption in the transmission samples and for the sample impurities or ^{206}Pb and ^{207}Pb contributions in ^{208}Pb. The experimental uncertainties for the ^{208}Pb measurements are nearly the same as those for the ^{nat}Pb, and the total amount of their uncertainties are 0.17-0.65 % from 4 to 180 eV, 0.13-0.66 % from 2 eV to 2 keV, 0.55-0.62 % at 24 keV, about 0.42 % at 145 keV, and about 1.3 % at 55 keV, respectively.

The present results of ^{208}Pb and ^{nat}Pb are shown in Fig. 2 and compared with the evaluated

data in both files, JENDL-3[6] and ENDF/B-VI[7]. From the figure, it can be seen that both results are almost constant below 2 keV and the ^{208}Pb data are larger by about 0.25 b than the ^{nat}Pb values. Although the shape of both energy dependent cross sections in ENDF/B-VI is similar to the present measurements, the absolute values for both cross sections are lower by about 1.5 % than the present values in the relevant energy region. The evaluated cross section of ^{nat}Pb in JENDL-3 is in good agreement with the measured data, although the evaluated data of ^{208}Pb are lower by 2 % than the measured ones. At tens of keV energies with filtered neutrons, the JENDL-3 data are much lower than the present measurements.

The present data of ^{208}Pb show very good agreement with the recent results by Alexandrov et al.[1] and Schmiedmayer et al.[2] with each other. Very recent data of ^{nat}Pb measured by Granada et al.[3] are also in good agreement with the present values.

References :

(1) Y. A. Alexandrov, et al., "Measurement of the neutron Total Cross Sections for Bi and Pb: Estimate of the Electric Polarizability of the Neutron," *Proc. Int'l Conf. on Nucl. Data for Sci.*, Springer-Verlag, p.160, 1992.
(2) J. Schmiedmayer, et al., "Electric properties of the neutron from Precision Cross Section Measurements," *ibid.*, p.163, 1992.
(3) J. G. Granada, et al., *Physica* **B 190**, 259 (1993).
(4) K. Kobayashi, et al., *Nucl. Instr. Neth.*, **A 287**, 570 (1990).
(5) K. Kobayashi, et al., "Measurement of Capture cross Sections for ^{238}U and Sb," *Proc. Int'l Conf. on Nucl. Data for Sci.*, Springer-Verlag, p.65, 1992.
(6) K. Shibata, et al., "*Japanese Evaluated Nuclear Data Library, Version-3, JENDL-3*," JAERI 1319, JAERI, 1990.
(7) R. F. Rose (Ed.), "*ENDF/B Summary Documentation*," BNL-NCS-17541, 4th Ed. (ENDF/B-VI) 1991.

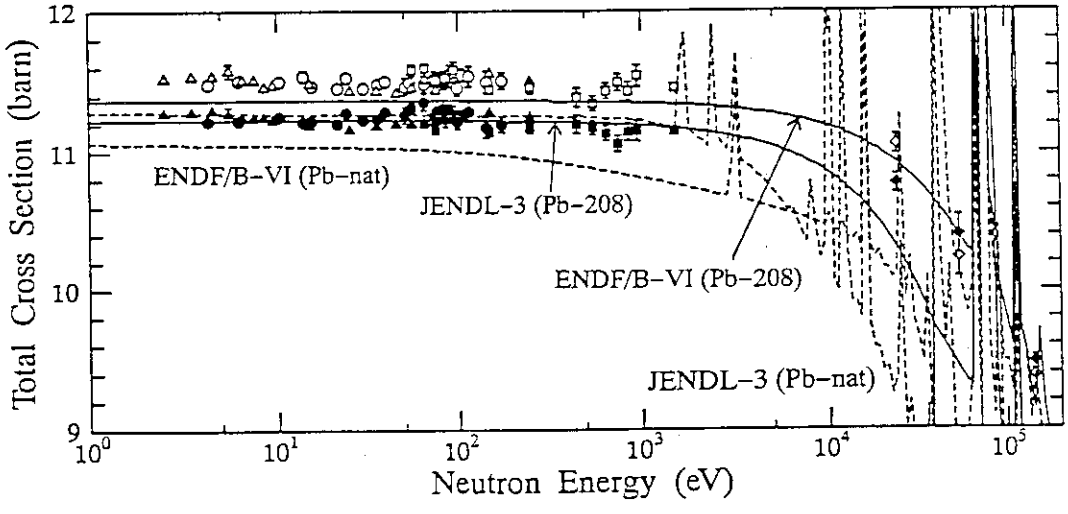

Fig. 2 Comparison of the measured neutron total cross sections of Pb-208 and Pb-nat with the evaluated data in JENDL-3 and ENDF/B-VI.

3. 2 Measurements of keV-neutron Capture γ Rays of Fission Products

Masayuki IGASHIRA

Research Laboratory for Nuclear Reactors, Tokyo Institute of Technology

2-12-1 O-okayama, Meguro-ku, Tokyo 152, Japan

γ rays from the keV-neutron capture reactions by ^{148,149,152,154}Sm and ^{161,162,163}Dy have been measured in a neutron energy region of 10 to 100 keV, using a large anti-Compton NaI(Tl) spectrometer. The preliminary results about the capture cross sections and γ-ray spectra of those nuclides are presented and discussed.

1. Introduction

Accurate keV-neutron capture cross section data of fission products are necessary for the development of innovative nuclear reactors, and capture γ-ray spectra of largely deformed nuclei would provide important information on nuclear excitation modes such as the M1 scissors mode[1]. Therefore, we started measurements of keV-neutron capture γ rays of fission products to obtain those nuclear data. A series of measurements has been finished in a neutron energy region of 10-100 keV. In the present paper, the preliminary results about ^{148,149,152,154}Sm and ^{161,162,163}Dy are presented and discussed.

2. Experimental Procedure and Data Processing

The experimental procedure and data processing method have been described in detail elsewhere[2,3], and so are summarized briefly in the present paper.

Pulsed keV neutrons were produced from the ^{7}Li(p,n)^{7}Be reaction by bombarding a Li-evaporated copper disk with the 1.5-ns bunched proton beam from the 3-MV Pelletron accelerator of the Research Laboratory for Nuclear Reactors at the Tokyo Institute of Technology.

Each capture sample was 1 g of highly enriched (95-100%) oxide powder contained in a case made of graphite whose inner size was 2 cm in diameter and 0.25 to 0.75 cm in thickness. Each sample was located 11.8 cm away from the neutron source at an angle of 0° with respect to the proton beam direction. A Au sample was used as a standard to determine the absolute number of neutrons incident on each capture sample.

Capture γ rays were detected with a large anti-Compton NaI(Tl) spectrometer[4], employing a time-of-flight (TOF) method. The spectrometer was placed in a heavy shield. The distance between the sample and the spectrometer was 86 cm. Capture γ rays were observed at a angle of 125° with respect to the proton beam direction. Capture events detected by the spectrometer were stored in a workstation as two-dimensional data on TOF and pulse height (PH). The measurement with each sample and the measurements with and without the standard Au sample were made cyclically to average out changes in experimental conditions such as the incident neutron spectrum.

A PH weighting technique[5] was applied to the net PH spectra of Sm and Dy isotopes and Au to obtain the capture yields. The capture yields of Au and the standard capture cross section of Au[6] were used to determine the absolute number of neutrons incident on

each sample. Furthermore, the net PH spectra of Sm and Dy isotopes were unfolded by using a computer program FERDOR[7] to obtain the corresponding capture γ-ray spectra.

Corrections were made for the self-shielding and multiple-scattering of neutrons in the sample, for the absorption of capture γ rays in the sample, and for the dependence of γ-ray detection efficiency on the position in the sample. Powder samples are generally hygroscopic. However, we have not yet performed the analysis of the water in the samples, and so the correction for the water has not yet been made.

3. Results and Discussion

The preliminary results for the capture cross sections of ^{148,149,152,154}Sm and ^{161,162,163}Dy are compared with other measurements[8–18] and evaluations[19,20] in Figs. 1-7, respectively. The present results of ^{148,149,152}Sm are in good agreement with the recent measurements by Wisshak et al.[8], although the present results tend to become larger than theirs at lower neutron energies. Here, it should be noted that we adopted the ENDF/B-VI evaluations[6] as the standard capture cross section of Au which are about 5 % larger than those adopted by Wisshak et al.[8] in the present neutron energy region, and that the JENDL-3.2 evaluation[19] of ^{148,149,152}Sm was based on their data. The present results of ^{154}Sm are smaller than other measurements[11,13–16], but in considerable agreement with the JENDL-3.2 evaluations[19] at higher neutron energies. The present results of ^{161,163}Dy are in good agreement with those of Kononov et al.[18], but somewhat smaller than those of Beer et al.[17]. The results of ^{162}Dy are much larger than those of Kononov et al.[18], but in considerable agreement with the ENDF/B-VI evaluations[20].

The unfolded capture γ-ray spectra of ^{148,149,152,154}Sm and ^{161,162,163}Dy are shown in Figs. 8 and 9, respectively. A bump or shoulder is observed around 3 MeV in each spectrum of the Sm and Dy isotopes. The energy position of the bump or shoulder is consistent with the systematics obtained from our early work[2]. The bump was attributed only to a resonance structure of the E1 γ-ray strength function in the work, but the origin of the bump should be investigated also from different aspects such as the excitation of nuclear M1 scissors mode[1].

References

1) N. Lo Iudice and F. Palumbo, Phys. Rev. Lett. **41** (1978) 1532.
2) M. Igashira, H. Kitazawa, M. Shimizu, H. Komano and N. Yamamuro, Nucl. Phys. **A457** (1986) 301.
3) S. Raman, M. Igashira, Y. Dozono, H. Kitazawa, M. Mizumoto and J. E. Lynn, Phys. Rev. **C41** (1990) 458.
4) M. Igashira, K. Tanaka and K. Masuda, Proc. the 8th Int. Symp. on Capture Gamma-Ray Spectroscopy and Related Topics, Fribourg, Switzerland, 1993, edited by J. Kern (World Scientific, Singapore, 1994) p.992.
5) R. L. Macklin and J.H. Gibons, Phys. Rev. **159** (1967) 1007.
6) ENDF/B-VI data file for ^{197}Au (MAT=7925), evaluated by P. G. Young (1984).
7) H. Kendrick and S. M. Sperling, GA-**9882** (1970).
8) K. Wisshak, K. Guber, F. Voss, F. Kappeler and G. Reffo, Phys. Rev. **C48** (1993) 1401.
9) B. J. Allen, J. H. Gibbons and R. L. Macklin, Adv. Nucl. Phys. **4** (1970) 205.
10) V. Benzi, R. D'Orazi and G. Reffo, Nuovo Ciment, **13** (1973) 226.
11) R. L. Macklin, N. H. Lazar and W. S. Lyon, Phys. Rev. **107** (1957) 504.
12) M. Mizumoto, Nucl. Phys. **A357** (1981) 90.
13) R. L. Macklin, J. H. Gibbons and T. Inada, Nature, **197** (1963) 369.
14) A. K. Chaubey and M. L. Sehgal, Phys. Rev. **152** (1966) 1055.
15) V. N. Kononov, B. D. Yurlov, E. D. Poletaev and V. M. Timokhov, Sov. J. Nucl. Phys. **27** (1978) 5.

16) K. Shiddappa, M. Sriramachandra Murty and J. Rama Rao, Annals Phys. **83** (1974) 355.
17) H. Beer, G. Walter, R. L. Macklin and P. J. Patchett, Phys. Rev. **C30** (1984) 464.
18) V. N. Kononov, E. D. Poletaev, B. D. Yurlov, M. V. Bokhovko, L. E. Kazakov and V. M. Timokhov, Proc. the 4th Int. Symp. on Neutron Capture Gamma-Ray Spectroscopy and Related Topics, Grenoble, France, IOP Conf. Series No. **62** (Institute of Physics and Physical Society, London, 1982) p.518.
19) M. Kawai, S. Chiba, H. Matsunobu, T. Nakagawa, Y. Nakajima, T. Sugi, T. Watanabe and A. Zukeran, Proc. Int. Conf. on Nuclear Data for Science and Technology, Gatlinburg, USA, 1994.
20) ENDF/B-VI data file for ^{161}Dy (MAT=6640), ^{162}Dy (MAT=6643) and ^{163}Dy (MAT=6646), evaluated by R. E. Schenter and F. Schmittroth (1974).

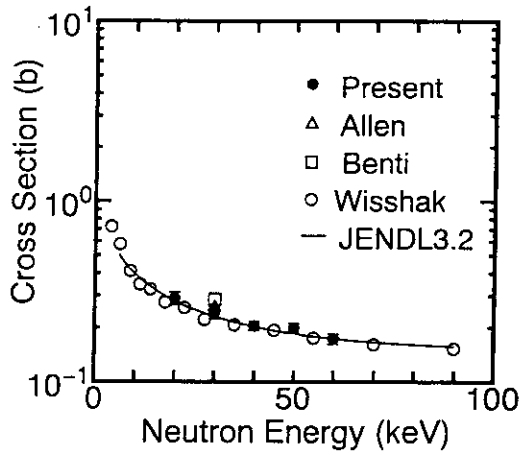

Fig.1. Capture cross sections of ^{148}Sm.

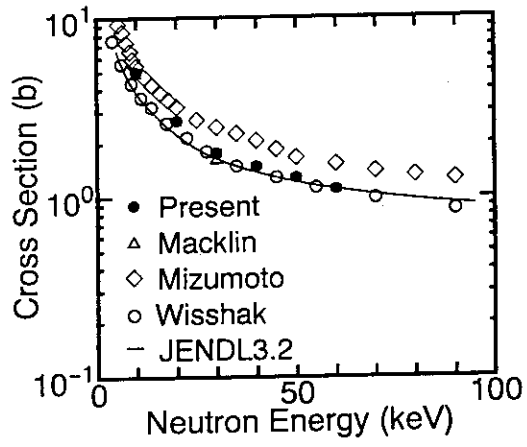

Fig.2. Capture cross sections of ^{149}Sm.

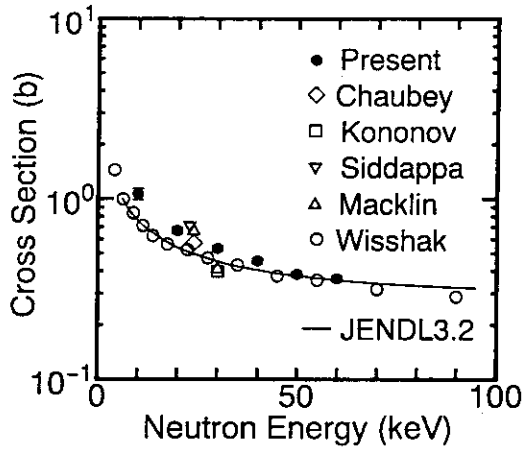

Fig.3. Capture cross sections of ^{152}Sm.

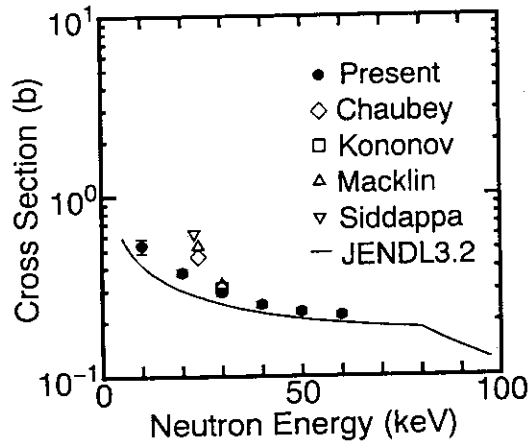

Fig.4. Capture cross sections of ^{154}Sm.

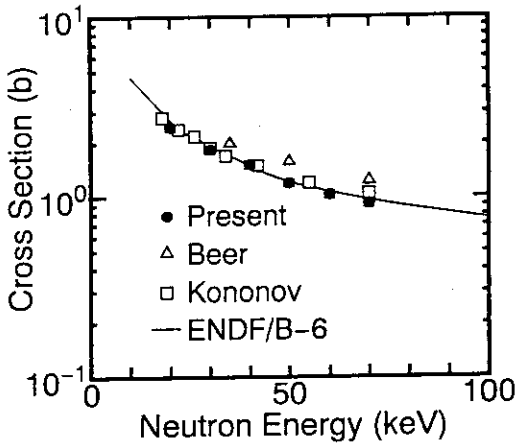

Fig.5. Capture cross sections of ^{161}Dy.

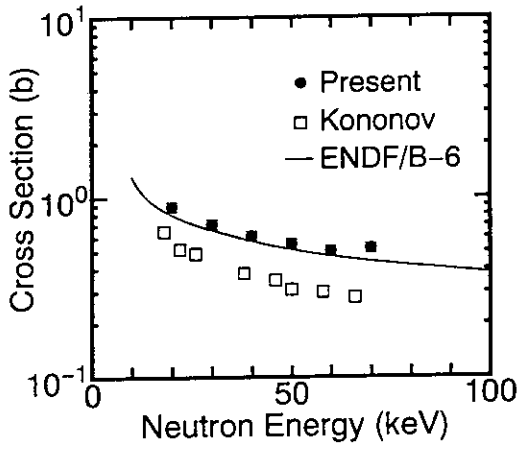

Fig.6. Capture cross sections of ^{162}Dy.

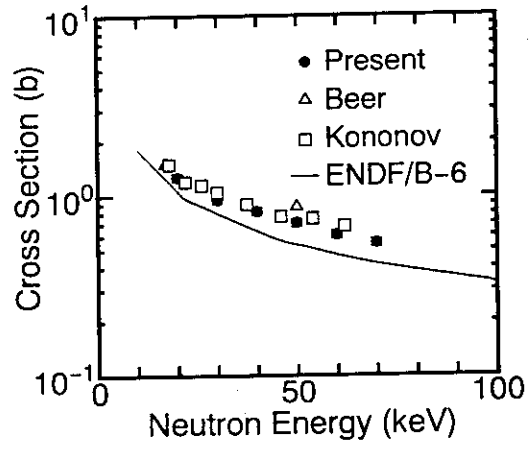

Fig.7. Capture cross sections of ^{163}Dy.

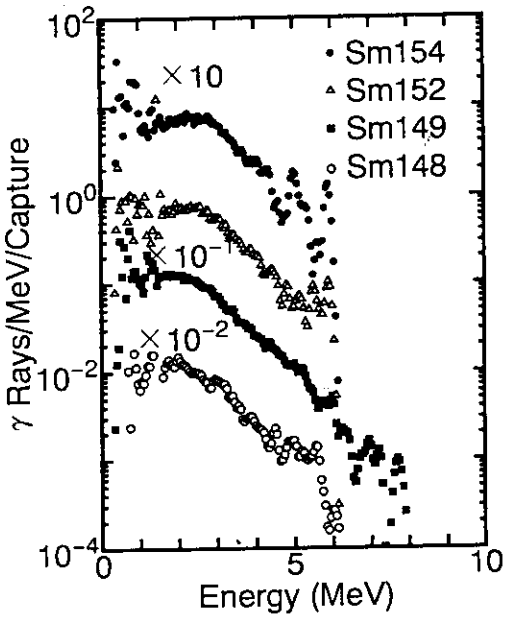

Fig.8. Capture γ-ray spectra of ^{148,149,152,154}Sm at an average neutron energy of 30 keV.

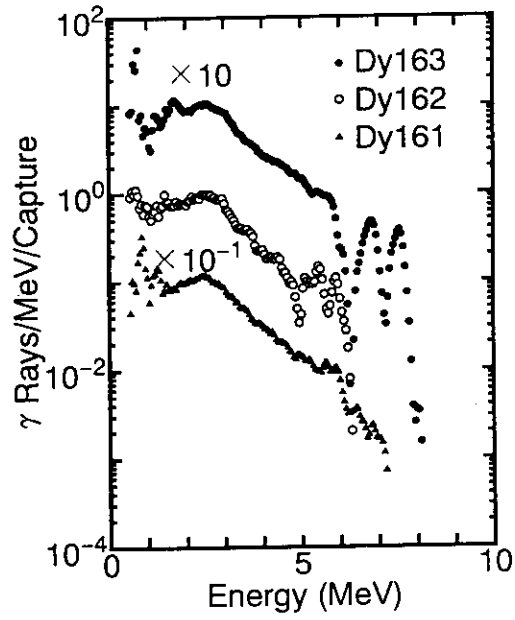

Fig.9. Capture γ-ray spectra of ^{161,162,163}Dy at an average neutron energy of 30 keV.

3. 3 Sensitivity Analysis of JENDL-3.2 in Fast Reactor

Toshikazu TAKEDA and Takanori KITADA
Osaka University, Depart.Nuclear Engineering
Yamadaoka 2-1, Suita, Osaka, 565

The effect of the difference between JENDL-3.1 and 3.2 libraries upon the neutronic performance parameters of the fast critical assembly ZPPR-9 has been evaluated based on sensitivity analysis. It is seen that k_{eff} is reduced by 0.9% for JENDL-3.2 compared to JENDL-3.1, and the main contributions are the fission cross section of ^{239}Pu, the fission spectrum of ^{239}Pu, the scattering cross sections of ^{238}U, Fe, Na, and O. The sensitivity analysis is also carried out for reaction rate ratio, control rod worth and reaction rate distribution.

1. Introduction

A sensitivity analysis is performed to investigate the difference between JENDL-3.1 and JENDL-3.2 libraries for the fast critical assembly ZPPR-9[1], which represents a typical homogeneous fast reactor of about 650MWe. For the sensitivity analysis, the sensitivity coefficients are calculated using the SAGEP code[2] based on the generalized perturbation theory in the RZ geometry. The calculation is done in 16 energy groups with the 70 group cross section set JFS3J3[3] obtained from JENDL-3.1. Two sets of 16 group cross sections are calculated for JENDL-3.1 and 3.2 with the fast reactor cell calculation code CASUP[4]. Multiplying the cross section difference by the sensitivity coefficient, the effect of each cross section on core performance parameters of ZPPR-9 is evaluated. As the core performance parameters we consider k_{eff}, reaction rate ratio of ^{238}U capture to ^{239}Pu fission(^{28}C/^{49}F), ^{239}Pu fission rate distribution and control rod worth. The sum of individual contributions calculated by the sensitivity analysis is compared with direct subtraction calculations.

2. Sensitivity Analysis

Results of the direct subtraction calculations of k_{eff}, reaction rate ratio, reaction rate distribution and control rod worth for JENDL-3.1 and 3.2 are shown in Table 1.

1) k_{eff}

JENDL-3.2 produces ~0.9% lower k_{eff} than JENDL-3.1 as shown in Table 1. Table 2 shows the contribution of each cross section to the 0.9% difference. The ^{239}Pu of JENDL-3.2 decreases k_{eff} by about 0.3% compared to JENDL-3.1. The fission cross section has an effect of -0.13% and the fission spectrum has an effect of -0.18%. Figure 1 and 2 show the energy-wise contribution of the ^{239}Pu(n,f) cross section and the ^{238}U(n, γ) cross section to the k_{eff} difference. For ^{239}Pu the contribution is negative around 1KeV, and is positive below 1KeV. The scattering cross sections of ^{238}U, Fe, Na and O have large effects of -0.62% in total as shown in Table 2. Thus the main contributions to the 0.9% difference is the scattering cross sections of these nuclides, the fission cross section and the fission spectrum of ^{239}Pu. The direct subtraction calculation yields the 0.91%Δk difference, and this is in good agreement to the sum(0.84%Δk) of the results from the sensitivity analysis.

2) Reaction Rate Ratio ($^{28}C/^{49}F$)

The difference of the $^{28}C/^{49}F$ values between JENDL-3.1 and 3.2 is small(0.9%) as shown in Table 1. Table 3 shows that ^{239}Pu yields a positive contribution of 0.40% in which the fission cross section has an effect of 0.26%. The ^{238}U yields a negative contribution of -0.52% in which the capture cross section has a largest effect of -0.34%. Figure 3 shows the energy-wise contribution of the ^{238}U capture cross section to $^{28}C/^{49}F$ value. The contribution has a positive and negative effect depending energy regions. The scattering cross sections of Fe, Na and O have large effects of 0.85%. Thus the main contributions to the difference is the scattering cross sections of these nuclides and the fission cross section of ^{239}Pu and the capture cross section of ^{238}U. The direct subtraction calculation yields the 0.86% difference and the results of the sensitivity analysis yields the result of 0.74%.

3) ^{239}Pu Fission Rate Distribution

Although ^{239}Pu fission rate distribution C/E calculated by JENDL-3.1 has 2% spatial dependence, that dependence becomes small(1%) for JENDL-3.2. This is caused by the fact that ^{239}Pu fission rate is enlarged especially for the outer region by using JENDL-3.2 compared to JENDL-3.1.

4) Control Rod Worth(center)

Table 1 shows that JENDL-3.2 produces 1.10%(center) and 2.34%(core edge) higher control rod worth than JENDL-3.1. This eliminates the spatial dependence of the C/E values for control rod worth. Table 4 shows the contribution of each cross section to the 1.10% difference for central control rod worth. The ^{238}U yields a positive contribution of 1.37% in which the scattering cross section has the main contribution of 0.85%, and the energy-wise contribution of ^{238}U transport cross section to control rod worth change is shown in Figure 4. Figure 4 shows that the energy regions around 50~60 KeV have the positive contribution to control rod worth change. The scattering cross sections of Na and O yield negative contribution of -0.33% and -0.31%, respectively. Thus the main contributions for control rod worth change is the scattering cross sections of these nuclides and the transport and scattering cross sections of ^{238}U.

3. Conclusions

The difference between k_{eff}, reaction rate ratio, reaction rate distribution and control rod worth calculated by JENDL-3.1 and 3.2 was evaluated based on the sensitivity analysis for ZPPR-9. The C/E values obtained by JENDL-3.2 approach 1.0 compared to JENDL-3.1 except for the reaction rate ratio of ^{238}U fission to ^{239}Pu fission and the ratio of ^{238}U capture to ^{239}Pu fission. In general, scattering cross sections of ^{238}U, Fe, Na and O have large effect on the difference.

References

(1) H.Takano, et al," Institution of Two Dimensional Benchmark Problems and Production of Group Constants," JAERI-memo 58-110 (1983).

(2) A. Hara, T Takeda, and Y Kikuchi," SAGEP : Two-Dimensional Sensitivity Analysis Code Based Generalized Perturbation Theory," JAERI-M 84-027 (1984).

(3) T. Asami, et al," Japanese evaluated nuclear data library Version 3(JENDL-3)," J. At. Energy Soc. Jpn., (in Japanese). 31, 6 (1983).

(4) S. Ono, et al," CASUP : Cell Calculation Code for Fast Reactor Analysis," Techol. Rep. Osaka Univ., 33, 1708 (1983).

Table 1 C/E Values of Neutronic Characteristics Calculated by JENDL-3.1 and JENDL-3.2

Neutronic Characteristics		C/E values		Relative difference(%)
		JENDL-3.1	JENDL-3.2	
k-effective	k_{eff}	1.0059	0.9967	-0.91
Central reaction rate ratio	$^{28}F/^{49}F$	1.009	0.957	-5.15
	$^{28}C/^{49}F$	1.046	1.055	0.86
	$^{25}C/^{49}F$	0.994	1.002	0.80
^{239}Pu reaction rate	Inner core middle	0.987	0.988	0.10
	Inner core edge	0.980	0.982	0.20
	Outer core middle	0.969	0.979	1.03
Control rod worth	Center	0.996	1.007	1.10
	Core edge	0.984	1.007	2.34

Table 2 Nuclide-wise contribution to k_{eff}

Cross section		Alternation(%)
Pu-239	Capture	0.03
	Fission	-0.13
	ν -value	-0.01
	Transport	0.00
	Scattering	0.00
	Fission spectrum	-0.18
U-238	Capture	0.10
	Fission	-0.02
	ν -value	0.00
	Transport	-0.05
	Scattering	-0.12
U-235	Capture	0.01
	Fission	0.00
	ν -value	0.00
	Transport	0.00
	Scattering	0.00
Iron	Capture	0.00
	Transport	0.01
	Scattering	-0.24
Sodium	Capture	0.00
	Transport	0.02
	Scattering	-0.11
Oxygen	Capture	0.00
	Transport	0.00
	Scattering	-0.15
Total(%)		-0.84
Relative difference(%)		-0.91

Table 3 Nuclide-wise contribution to $^{28}C/^{49}F$

Cross section		Alternation(%)
Pu-239	Capture	0.03
	Fission	0.26
	ν -value	0.00
	Transport	0.00
	Scattering	0.01
	Fission spectrum	0.10
U-238	Capture	-0.34
	Fission	0.00
	ν -value	0.00
	Transport	-0.02
	Scattering	-0.16
U-235	Capture	0.01
	Fission	0.00
	ν -value	0.00
	Transport	0.00
	Scattering	0.00
Iron	Capture	0.00
	Transport	0.00
	Scattering	0.30
Sodium	Capture	0.00
	Transport	0.00
	Scattering	0.20
Oxygen	Capture	0.00
	Transport	0.00
	Scattering	0.35
Total(%)		0.74
Relative difference(%)		0.86

Table 4 Nuclide-wise contribution to control rod worth at core center

Cross section		Alternation(%)
Pu-239	Capture	0.03
	Fission	-0.02
	ν -value	0.03
	Transport	-0.01
	Scattering	-0.02
	Fission spectrum	0.25
U-238	Capture	0.05
	Fission	0.02
	ν -value	0.01
	Transport	0.44
	Scattering	0.85
U-235	Capture	0.04
	Fission	0.00
	ν -value	0.00
	Transport	-0.01
	Scattering	0.00
Iron	Capture	0.01
	Transport	-0.10
	Scattering	-0.10
Sodium	Capture	0.00
	Transport	-0.09
	Scattering	-0.33
Oxygen	Capture	0.00
	Transport	-0.01
	Scattering	-0.31
Total(%)		0.70
Relative difference(%)		1.10

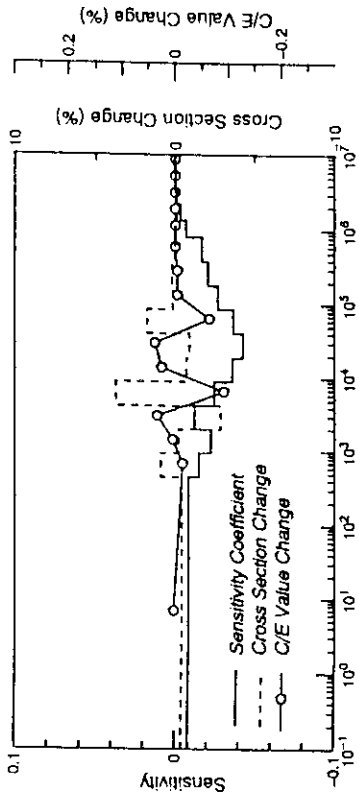

Fig.1 Energy wise contribution of $^{239}Pu(n,f)$ to k_{eff} difference

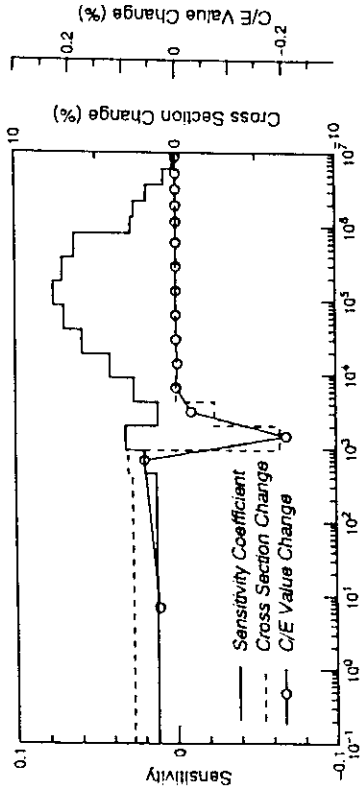

Fig.2 Energy wise contribution of $^{238}U(n,\gamma)$ to k_{eff} difference

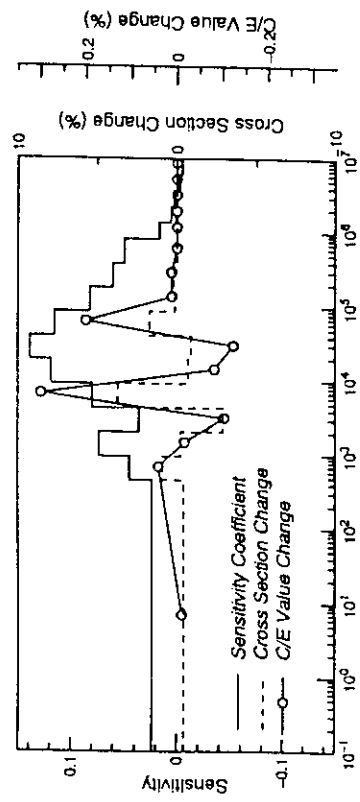

Fig.3 Energy wise contribution of $^{238}U(n,\gamma)$ to $^{28}C/^{49}F$ difference

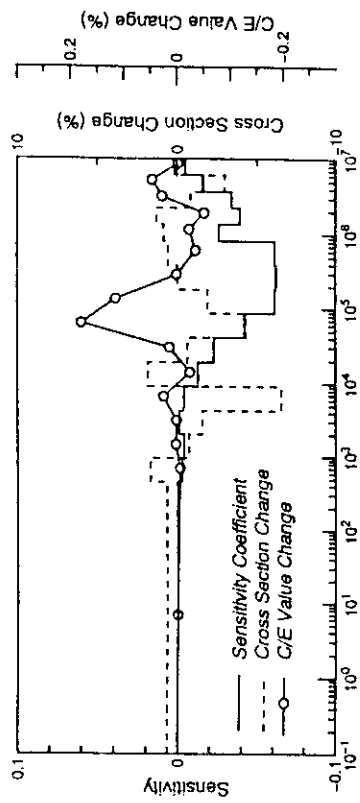

Fig.4 Energy wise contribution of $^{238}U_{tr}$ to CRW(center) difference

3. 4 Analysis of Reaction Rate Ratio, ^{238}U Capture/Total Fission, Using the JENDL-3.2 Library

Ken NAKAJIMA
Japan Atomic Energy Research Institute
Tokai-mura, Naka-gun, Ibaraki-ken 319-11, JAPAN

To investigate the accuracy of the neutronic calculation in various neutron spectra, the ratios of ^{238}U capture rate to total fission rate (*C8/F*) of light-water moderated UO_2 fuel lattices have been analyzed using the Japanese Evaluated Nuclear Data Library version 3.2, JENDL-3.2. The calculation of *C8/F* ratio has been carried out by the MVP continuous energy Monte Carlo code employing the JENDL-3.2. The calculated results showed good agreement with the experiment for the lattices having large V_m/V_f ratios. However, for smaller values of V_m/V_f, they over estimated the experimental results.

I. INTRODUCTION

The reaction rate ratios, such as the conversion ratio, are widely used as benchmark data for the neutronic calculation methods. In previous works, Nakajima et al[1-2] had measured the reaction rate ratios of ^{238}U captures to total fission, *C8/F*, in a series of light-water moderated UO_2 lattices. The objective of these studies was to investigate the accuracy of neutronic calculations. In this work, the *C8/F* ratios are calculated using the Japanese Evaluated Nuclear Data Library, JENDL-3.2 (latest version) and compared with the *C8/F* ratios obtained experimentally.[1-2]

II. MEASUREMENT

The *C8/F* ratios were measured by the γ-ray spectrometry of irradiated fuel rod in light-water moderated lattices.[1-3] In the measurements, following experimental cores were constructed at the Tank-Type Critical Assembly, TCA.

1. One region UO_2 cores

   Four cores were constructed. Each one composed of 2.6 wt% enriched UO_2 fuel rods, of which the moderator to fuel volume ratio (V_m/V_f) was 1.50, 1.83, 2.42, and 3.00, respectively. These cores are denoted as 1.50U, 1.83U, 2.42U, and 3.00U, respectively.
2. Two region tight lattice cores

   Two cores, having a central test region surrounded by a driver region, were constructed.

The test region composed of 3.2 wt% enriched UO_2 fuel rods, and the driver region composed of 2.6 wt% enriched UO_2 fuel rods. The V_m/V_f ratio of the test region was 0.564 and 1.42, respectively. For the driver region, this ratio was fixed at 1.44. These cores are denoted as 0.56S and 1.42S, respectively.

III. ANALYSIS

The *C8/F* ratios have been calculated using the MVP continuous energy Monte Carlo code employing the JENDL-3.2 library. Calculations using the JENDL-3.1 library were also conducted for the purpose of comparisons. Two types of calculation models were employed. One was a cell model, composed of one fuel rod and water-moderator. The horizontal boundary condition was mirror reflection. The cell height was determined to maintain the system criticality. The other model was a full-core model including all the core regions and the water-reflector. The latter model gives the effective neutron multiplication factor as well as the *C8/F* ratios.

IV. RESULTS AND DISCUSSION

The *C8/F* ratios calculated are shown in Table 1 and 2. For the purpose of comparisons, experimental values are also shown in these tables. The calculated results for the two models agree with each other to within a standard deviation of the Monte Carlo calculation. These ratios show good agreement with the experimental values for the lattices having large V_m/V_f ratios. However, for smaller values of V_m/V_f, they over estimated the experimental results as shown in Fig. 1. Comparisons with the calculated results employing the JENDL-3.1 showed that the *C8/F* ratio had no significant difference from the JENDL-3.2, although the effective neutron multiplication factors, which is shown in Fig. 2, with the JENDL-3.2 were approximately 1% larger than those with the JENDL-3.1.

IV. SUMMARY

The accuracy of the neutronic calculation in various neutron spectra was investigated. The MVP continuous energy Monte Carlo code employing the JENDL-3.2 library has been used to obtain the *C8/F* ratios of light-water moderated UO_2 fuel lattices. For large V_m/V_f ratios, the calculated results showed good agreement with the experimental values, however, for smaller values of V_m/V_f, they over estimated the experimental results.

The calculated *C8/F* ratios generated by the JENDL-3.1 and the JENDL-3.2 libraries

showed no significant differences, although the effective neutron multiplication factors with the JENDL-3.2 were approximately 1% larger than those with the JENDL-3.1.

REFERENCES

1) K. NAKAJIMA et al.,: *Nucl. Sci. Eng.*, **116**, 138 (1994).
2) K. NAKAJIMA et al.,: submitted to Nucl. Technol.
3) K. NAKAJIMA et al.,: *Nucl. Sci. Eng.*, to be published.

Table 1. Results of *C8/F* ratios using the cell model

Core	Experiment[a]	JENDL-3.1[b]	C/E[c]	JENDL-3.2[b]	C/E
0.56S	0.728(0.021)	0.76540(0.0013)	1.051	0.76552(0.0012)	1.052
1.42S	0.461(0.013)	0.46955(0.0007)	1.019	0.46927(0.0007)	1.018
1.50U	0.477(0.014)	0.48437(0.0007)	1.015	0.48339(0.0008)	1.015
1.83U	0.434(0.013)	0.44150(0.0007)	1.017	0.44209(0.0007)	1.019
2.48U	0.383(0.011)	0.38507(0.0006)	1.005	0.38592(0.0006)	1.008
3.00U	0.356(0.011)	0.35589(0.0006)	1.00	0.35707(0.0006)	1.003

[a] With an experimental error in parenthesis.
[b] Calculated value with a standard deviation of the Monte Carlo calculation in parenthesis.
[c] Calculation-to-experiment ratio.

Table 2. Results of *C8/F* ratios using the full-core model

Core	Experiment	JENDL-3.1	C/E	JENDL-3.2	C/E
0.56S	0.728(0.021)	0.76435(0.0095)	1.050	0.77796(0.0091)	1.069
1.42S	0.461(0.013)	0.47219(0.0039)	1.024	0.46768(0.0047)	1.014
1.50U	0.477(0.014)	0.48007(0.0052)	1.006	0.48446(0.0050)	1.016
1.83U	0.434(0.013)	0.43936(0.0050)	1.012	0.43636(0.0047)	1.005
2.48U	0.383(0.011)	0.37988(0.0036)	0.992	0.38424(0.0033)	1.003
3.00U	0.356(0.011)	0.35329(0.0040)	0.992	0.35510(0.0044)	0.997

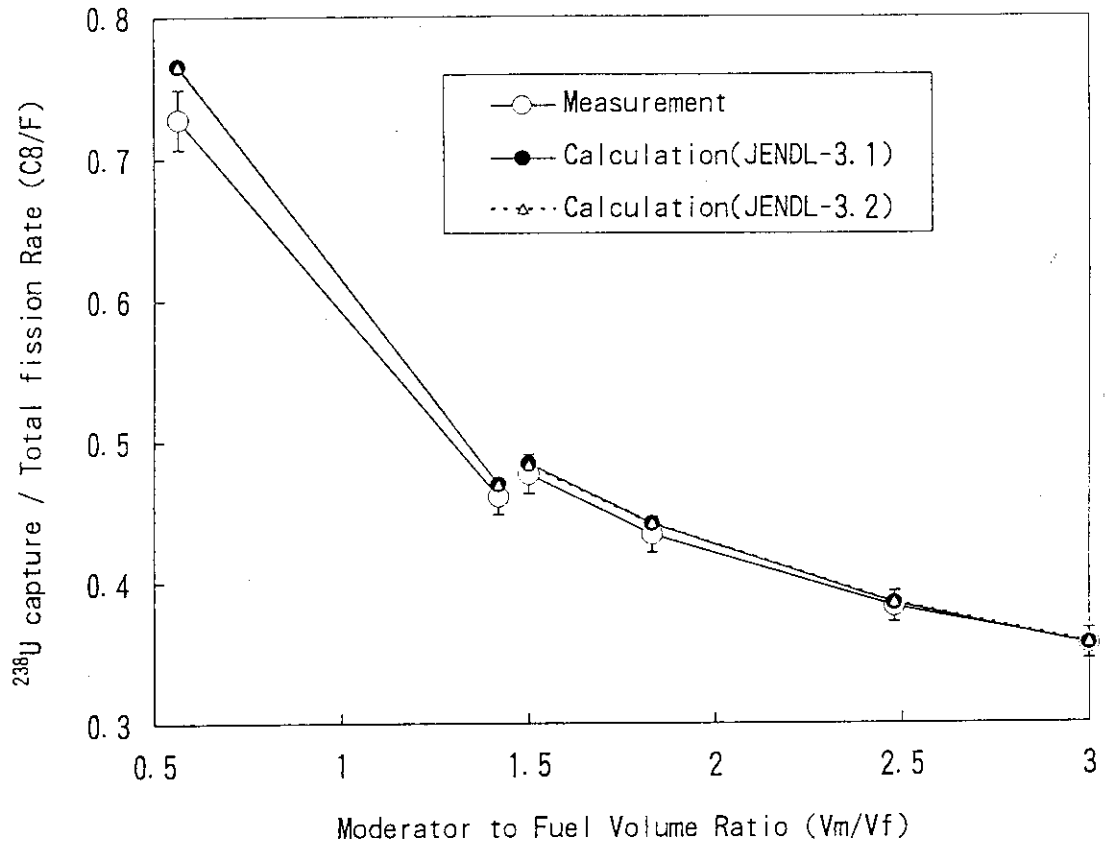

Fig. 1. Comparisons of experimental *C8/F* ratios with calculation using the cell model.

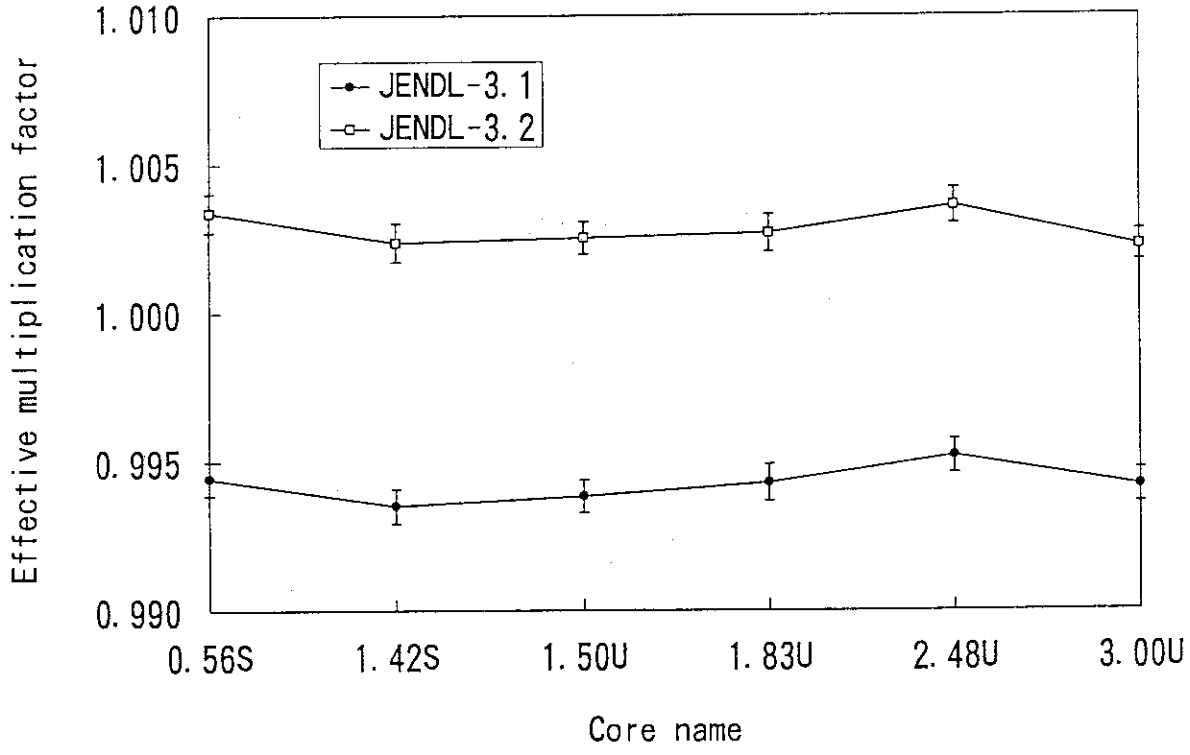

Fig. 2. Calculated effective neutron multiplication factors.

3. 5 Evaluation of Prompt Neutron Spectra for Actinides

Takaaki Ohsawa
Atomic Energy Research Institute, Kinki University
3-4-1 Kowakae, Higashi-osaka, Osaka 577, Japan

Abstract : The prompt neutron spectra for major actinides of U-233, -235, -238 and Pu-239 and for minor actinides were evaluated for JENDL-3.2. Some improvements in the method of calculation were made over the evaluation for JENDL-3.1 which was based on the constant inverse-cross section version of the Madland-Nix model.

I. Introduction

It has become evident from benchmark calculations that the fission neutron spectra for major actinides in JENDL-3.1 need to be reviewed. On the other hand, studies of nuclear transmutation of long-lived actinides require better knowledge of nuclear data for fission neutrons. The author has developed a methodology of calculation of the fission neutron spectra which provides better evaluations and can be used to estimate the spectra for minor actinides.

2. Methodology

Six improvements over JENDL-3.1 evaluation have been done in the method of calculation. The improvements and their effects are briefly described below.

(1) Energy-dependence of the inverse cross section

The energy-dependence of the inverse cross setions was considered in the present calculation of the emitted neutron spectra on the basis of the Madland-Nix formalism [1], in stead of the constant inverse cross section assumption adopted in JENDL-3.1 evaluation. The inverse cross section for the average light and heavy fragments were calculated using the Becchetti-Grennlees optical potential [2]. **Figure 1(a)** shows the inverse (compound-formation) cross section for the two average fragments of U-233 and **Fig.1(b)** compares the results of spectra calculated with and without the energy dependence. It can be seen that inclusion of the energy dependence considerably softens the fission neutron spectra.

(2) Level density parameters

The level density parameters (LDPs) for the light and heavy fragments were calculated employing the Ignatyuk model [3] taking into account the shell effects of the fission fragments. Compared with the conventional method based on the linear approximation of the form $a = A/C$ (C : an adjustable parameter ranging from 8 to 11), the Ignatyuk model provided a smaller value for the LDP for the average *heavy* fragment, because of the shell effects which are stronger than for light fragments.

(3) Multiple-chance fission

Multiple-chance fissions were taken into consideration for incident neutron energies above ~6 MeV. In the evaluation for JENDL-3.1, it was asumed that fission proceeded via (n,f) reaction even at energies where multiple-chance fissions could occur. This simplification resulted in harder fission neutron spectra, because of ignorance of cooling down of the fissioning nucleus by emission of prefission neutrons.

In the present calculation, the total fission probability was decomposed into (n,f), (n,n'f), (n,2nf), (n,3nf) and (n,4nf) reaction componemts by using empirical values of fisssion probabilities from (d,pf) and (t,pf) reactions. An example of analysis of the fission probability is shown in **Fig.2.**

(4) Non-equal nuclear temperatures

The constraint of the equality of the nuclear temperatures for the two fragments, assumed in the original Madland-Nix model, was relaxed in order to allow for different deformation energies for the two fragments at the scission point.

(5) Systematics of fragment mass distribution

Systematics for the fragment mass distribution were adopted to estimate the average fission fragment nuclides at a given incident energy if no experimental data were available. Nagy's systematics [4] was used for the fission of U-238, and Moriyama-Ohnishi's systematics [5] was adopted for minor actinides.

(6) Energy-dependence of the TKE

The incident-energy dependence of the total kinetic energy was considered. We obtained a least-squared fit line to the available experimental data, and the line was extrapolated up to 20 MeV.

3. Results

3.1 Some Examples of Evaluation

(a) **U-238**, E_n =2 MeV

As can be seen in **Fig.3**, the new evaluation is considerably softer than the JENDL-3.1 evaluation, but agrees fairly well with the measurement of Baba *et al* [6]. The JENDL-3.1 evaluation reproduces the experimental data of Boikov [7] for E_n=2.9 MeV; this seems to imply that the older evaluation was too hard.

(b) **U-233**, E_n =0 MeV

Figure 4 shows that two distinct features are observed in the new evaluation in comparison with the tentative evaluation done by the compilation group for JENDL-3.2 (labeled as JENDL- 3.2T) : ① the peak of the spectrum is shifted to low-energy side, and at the same time, ② the high energy component above 6 MeV is enhanced and shows better agreement with the data of Strostov [8] in this region. The effect ① is a result of the energy-dependence of the inverse cross section, and the effect ② is due to Ignatyuk's LDP for the average heavy fragment.

(c) **Np-237**, E_n =6 MeV

The fission spectrum of ^{237}Np is shown in **Fig.5** for E_n=6 MeV. At this ebergy, though the dominant contribution comes from the first-chance fission, there is about 12% of

contribution from the second−chance fission. The calculated total spectrum reproduces the experimental data of Trufanov [9].

(d) **Am−241,** E_n =20 MeV

Figure 6 shows the fission spectrum and its components of ^{241}Am for E_n =20 MeV. It can be observed that the slope of the high energy portion of the component spectra gets increasingly steeper as we go from first− to fourth−chance fission. This is an indication of the cooling down of the fissioning nucleus due to emission of prefission neutrons.

3.2 Systematic Trend of Fission Spectra for Actinides

The hardness of the fission neutron spectra is determined by the total excitation energy $<E^*>$ of the fission fragments, which is given by $<E^*>=<E_R>+B_n+E_n-TKE$, where $<E_R>$ is the total energy release of fission, B_n the neutron binding energy, E_n the incident neutron energy. The quqntity for 16 actinides ranging from U to Bk were calculated based on the fragment mass distributions predicted by the Moriyama−Ohnishi model [5]. Least−squares fitting to the calculated values yielded the following equation: $<E_R>=0.2197Z^2/A^{1/3}-114.368$ (MeV). On the other hand, the systematic dependence of the TKE on the Coulomb parameter was found [10] to be expressed as $TKE=(0.1189\pm0.0011)Z^2/A^{1/3}+7.3$ ($\pm$1.5) (MeV). These two equations are plotted in **Fig. 7.** It can readily be seen the the difference $<E_R>-TKE$ increases with $Z^2/A^{1/3}$. This explains the familiar knowledge that the average fission neutron energy increases with fissility parameter. [11]

4. Concluding Remarks

It was found that the experimental data of the fission neutron spectra as well as of the reactor benchmark experiments were in better consistency with the new evaluation. The method was also applied to evaluate the fission neutron spectra for minor actinides; a general trend was found that the the spectra tended to be harder with increasing Coulomb parameter $Z^2/A^{1/3}$ of the compound nucleus.

References

1) D.G.Madland and J.R.Nix, Nucl. Sci. Eng. **81**, 213 (1982)
2) F.D.Becchetti, Jr. and G.W.Greenlees, Phys. Rev. **182**, 1190 (1969)
3) A.V.Ignatyuk, Sov. J. Nucl. Phys. **29**, 450 (1979)
4) S.Nagy *et al.*, Nucl. Sci. Eng. **88**, 154 (1984)
5) H.Moriyama and T.Ohnishi, Technical Reports of the Institute of Atomic Energy, Kyoto University, No.**166** (1974)
6) M.Baba *et al.*, JAERI−M 89−143 (1989)
7) G.S.Boikov *et al.*, Sov. J. Nucl. Phys. **53**, (1991)
8) B.I.Starostov *et al.*, Proc. All−Union Conf. on Neutron Physic, Kiev, 1983, Vol.2, p.290
9) A.M.Trufanov, A.Ruben *et al.*, Proc. IAEA/Consultants' Meeting on Nuclear Data for Neutron Emission in the Fission Process, Vienna, 1990, INDC(NDS)−251, IAEA (1991), p.105
10) V.E.Viola, K.Kwiatkowski and M.Walker, Phys. Rev. **31**, 1550 (1985)
11) A.B.Smith *et al.*, ANL/NDM−50 (1979)

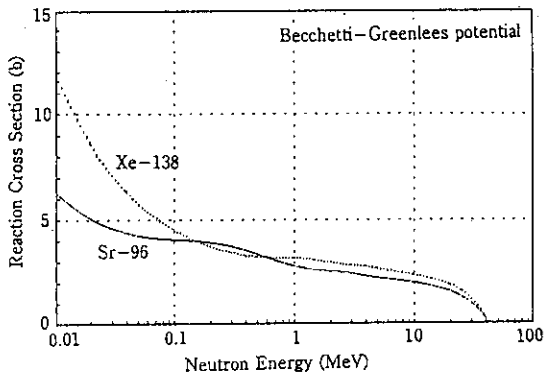

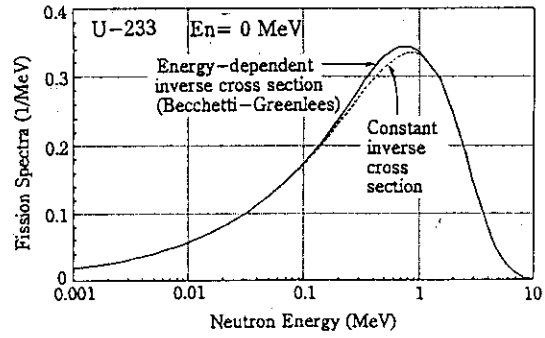

Fig.1 (a) Inverse cross sections for avarage fission fragments of ^{233}U calculated with the Becchetti-Greenlees potential. (b) Comparison of fission neutron spectra calculated using constant and energy-dependent inverse cross sections.

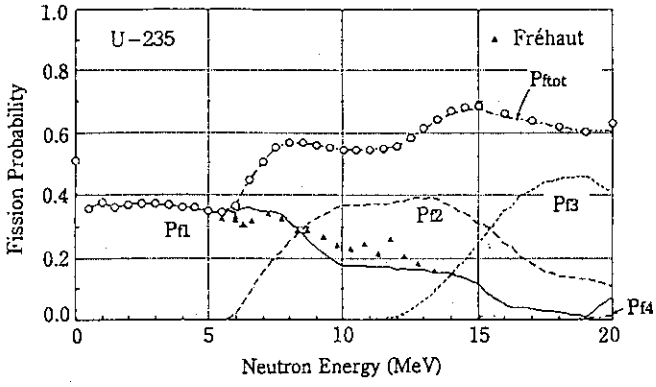

Fig.2 Analysis of the fission probability for ^{235}U.

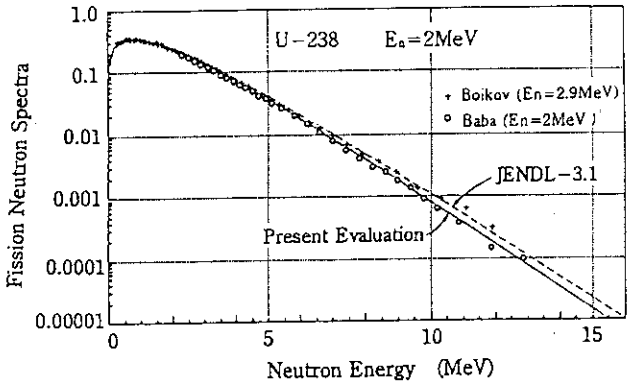

Fig.3 Fission neutron spectra of ^{238}U for En=2 MeV.

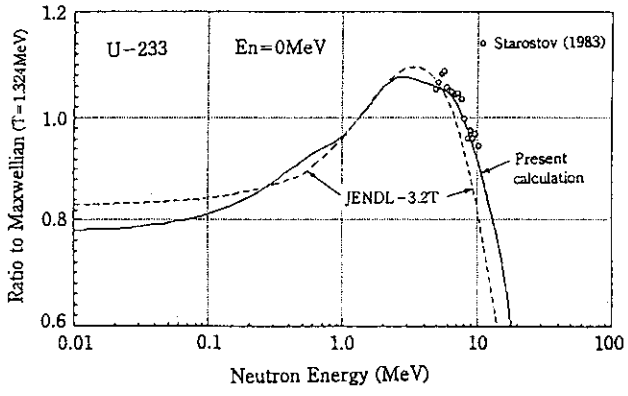

Fig.4 Fission neutron spectra of ^{233}U for En=0 MeV.

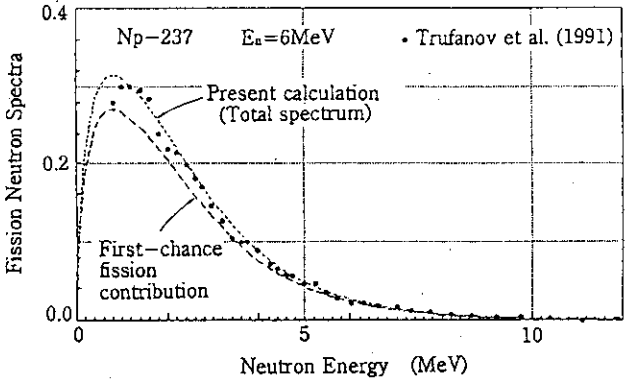

Fig.5 Fission neutron spectra of ^{237}Np for En=6 MeV.

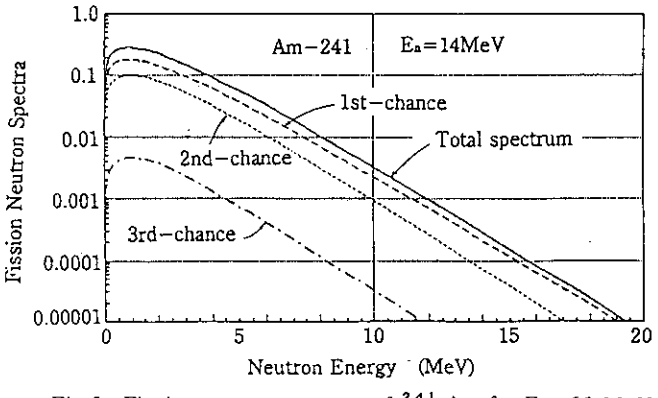

Fig.6 Fission neutron spectra of ^{241}Am for En=20 MeV.

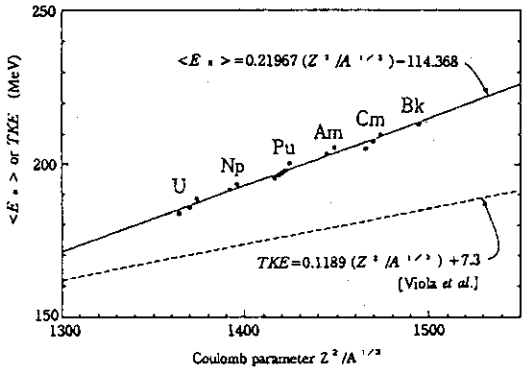

Fig.7 Total energy release of fission and average TKE as a function of the Coulomb parameter.

3.6 Semi Classical Model of the Neutron Resonance Compound Nucleus

Makio OHKUBO
Department of Reactor Engineering, Tokai
Japan Atomic Energy Research Institute

Abstract

A Semi-classical model of compound nucleus is developed, where time evolution and recurrence for many degrees of freedom(oscillators) excited simultaneously is explicitly considered. The effective number of oscillators play role in the compound nucleus, and the nuclear temperatures are derived, which are in good agreement with the traditional values. Time structures of the compound nucleus at resonance is considered, from which equidistant level series with an envelope of strength function of giant resonance nature is obtained. S-matrix formulation for fine structure resonance is derived.

1. Introduction

In observed neutron resonance levels, equidistant level series are found frequently than the prediction of the statistical distributions based on GOE [1, 2, 3, 4]. These facts suggest that a diametrically different phenomena might be embedded in the neutron resonance compound nucleus, which are ordinarily believed to be a typical quantum chaos. As a step to understand these facts, a semi-classical model of neutron resonance compound nucleus is developed where time evolution with recurrence is considered explicitely. In this article, a brief description of the results is made because of limited space.

2. Oscillator Number and Nuclear Temperature

In the neutron resonance compound nucleus, many degrees of freedom are excited simultaneously and may be coupled with each other. By the analogy of resonance in classical physics, these degrees of freedom must recur to the initial phase repeatedly [5]. We assume that the amplitude of the compound nucleus is a product of independent M normal modes(oscillators) which play roles in the compound nucleus. At a resonance, i-th normal mode depicts a closed orbit with a recurrence time τ_i. The recurrence time of the compound nucleus, τ is the least common multiple (LCM) of τ_i ($i=1, 2, \ldots, M$). As a recurrence criterion, we assume an angular tolerance of 1 radian for these oscillators [6]. Then, the average value of τ is described by the number of oscillators M, and the total excitation energy E_X(6-8MeV) as $\tau = h(2\pi)^{M-1}/E_X$, where h is Plank's constant. Combining a quantum mechanical relation $\tau = h/D$, where

D is an average resonance level spacing, we can derive the oscillator number M as

$$M = 1 + \ln(E_X/D)/\ln(2\pi). \quad \cdots\cdots\cdots\cdots\cdots\cdots\cdots\cdots \quad (1)$$

In eq. (1), h is not included. Using E_X and D from the neutron resonances data, M can be obtained for many nuclei, and are shown in Fig. 1.

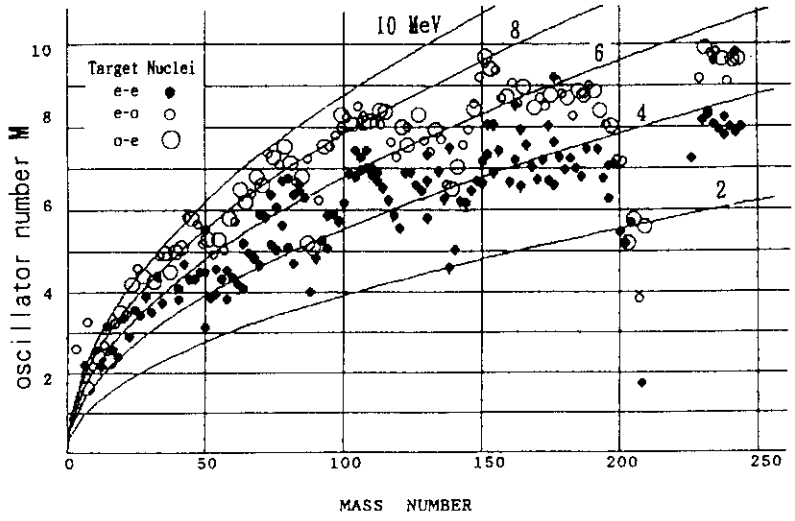

← Fig. 1
Oscillator number M versus target mass number. The curves are exciton number n_{ex} for E_x =2~10 MeV.

↓ Fig. 2
Ratio M/n_{ex} versus target mass number.

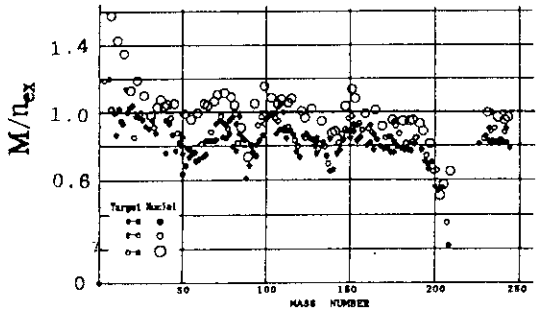

On the other hand, by the Fermi-gas model [7] the exciton number n_{ex} of compound nucleus is given by $n_{ex} \sim (g_0 E_X)^{1/2}$, where $g_0(\sim A/13)$ is single particle level density at Fermi energy. The ratios of M/n_{ex} vs mass number is shown in Fig. 2. It is stressed that M are nearly the same values to n_{ex}.

Nuclear temperature T is derived assuming that M is proportional to E_X ;

$$T = \left(-\frac{1}{D}\frac{\partial D}{\partial E_X}\right)^{-1} = \frac{E_X}{M \ln(2\pi) - 1}. \quad \cdots\cdots\cdots\cdots \quad (2)$$

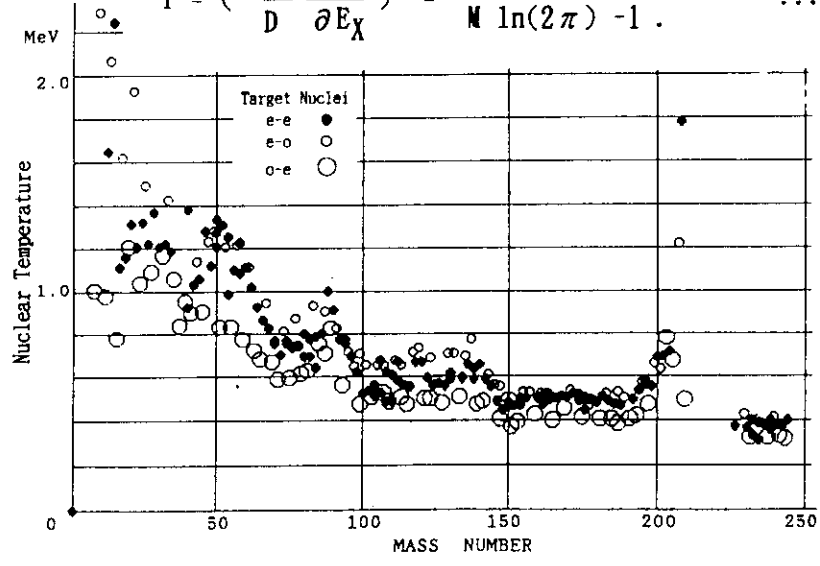

Fig. 3
Nuclear Temperature T by eq. (2) versus target mass number.

Nuclear temperature T by eq.(2) are shown in Fig.3 for many nuclei. No correction is made on E_X and D. These T are in good agreement with the traditional values [8] except for the light nuclei and for the nuclei near the closed shell.

3. Reaction Mechanism, Time Structures and S-matrix

The neutron wave has a frequency of $\omega = 2\pi E_k/h$, and a wave length of p/h, where E_k is kinetic energy and p is neutron momentum. Also the wave packet length of a incident neutron is at least 10^{-8}m, which is very long compared to the nuclear radius. On a target nucleus, incident neutron wave is divided into 1) pass-by component, and 2) absorbed component. The 2nd component excites M oscillators in the compound nucleus, where the average energy of the oscillators is $E_x/M \sim 1$ MeV. An ensemble of oscillators is selectively excited, if the recurrence frequency of the ensemble is equal or integer ratios to the incident neutron frequency. We define the initial phase as 'coalescent phase', where the neutron density is high on the surface of the compound nucleus. The duration P of the coalescent phase is about 10^{-21}s, which is equal to the transit time of neutron through the nuclear potential. Also P is nearly equal to the passing time for an oscillator of energy $E_x/M \sim 1$ MeV, through the angle of 1 radian.

A density distribution of coalescent phase, or a nuclear response function is shown schematically in Fig.4. There are two components [9]. The first one is a δ-function like single peak responsible for the direct reaction, and the second one is a pulse array responsible for the resonance reactions, with an envelope of exponential decay of resonance life time λ. The coalescent phases reappear at every recurrence time, and keep coherent interaction with pass-by component, during passing of the wave packet. Energy spectrum of coalescent phase is shown in Fig.5. It consists of equidistant resonaces with a spacimg of D, with a level width of Γ, and with an envelope function of width W. Here, there are three-fold uncertainty relations; $\Gamma \sim h/\lambda$, $D \sim h/\tau$, and $W \sim h/P$. S-matrix is derived by the Fourier transform of the response function [10]. We tentatively adopt a S function as

$$S(E) = \exp(-2ikR)\left\{1 - \frac{(1-r)A(E)}{1 - r\exp(2\pi iE\tau/h)}\right\}, \quad \cdots\cdots\cdots\cdots (3)$$

where $r = \exp(-\tau/\lambda) \leqq 1$, and A(E) is a Fourier transform of the coalescent phase, with a limit of $0<A(E)<2$. For large resonances at low energy region, $A(E) \sim 2$, and in higher energy A(E) gradually decreases to 0 above ~ 1 MeV. S(E) in eq.(3) has poles in lower half plane of complex E at $E=n(h/\tau) - i(h/(2\pi\lambda))$, where n is integer.

Eq.(3) gives equidistant resonance cross sections(Fig.6) with an envelope A(E). In

high energy region, A(E) becomes 0, and S(E) tends to 1 with no resonance structure.

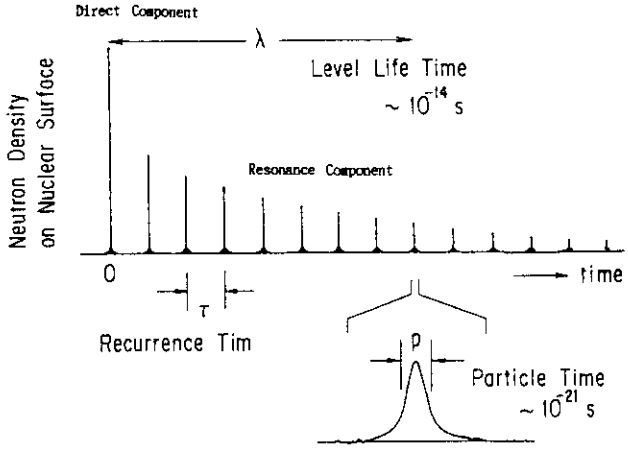

Fig. 4 Time Structure of the coalescent phase

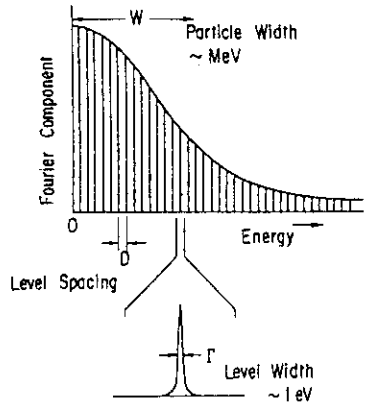

Fig. 5 Energy Spectrum

It must be noted that many ensembles of oscillators are possible to be excited in the same energy region, which have different recurrence times. They overlap in the same energy region, and the statistical distributions of the observed resonances may show similalities to the predictions of the GOE.

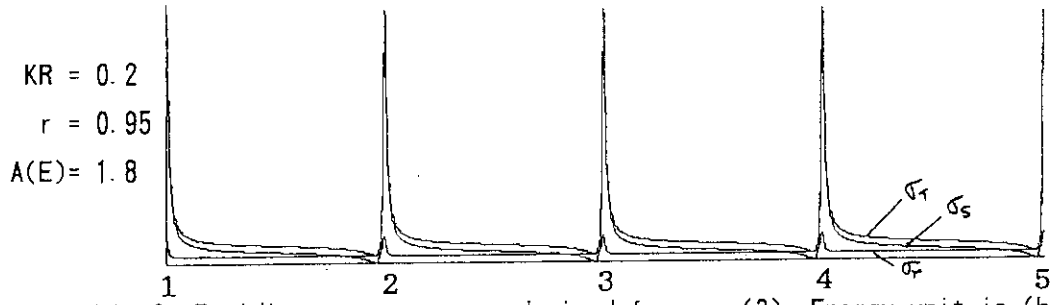

Fig. 6 Equidistant resonances derived from eq. (3). Energy unit is (h/τ).

References

[1] K. Ideno M. Ohkubo; J. Phys. Soc. Japan **30**, 620(1971),
K. Ideno; ibid. **37**, 581(1974)

[2] S. I. Sukhoruchkin; Sov. J. Nucl. Phys. **10**, 285(1970)

[3] N. F. Belyaef and S. P. Borovlev; Yad. Fiz **27**, 289(1978)

[4] C. Coceva et al. Proc. Int. Conf. on Statistical Properties of Nuclei,
Prenum Press, NY, 1972 p447

[5] M. C. Gutzwiller; "Chaos in Classical and Quantum Mechanics"
Springer Verlag 1990

[6] M. Ohkubo ; Proc. Int. Sem. JAERI-M-93-228 (1993) p744

[7] A. Bohr and B. Motterson; Nuclear Structure, Vol 1, Benjamin, London 1968

[8] A. Gilbert and A. Cameron; Canad. J. Phys. **43**, 1446(1965)

[9] K. W. McVoy; Ann. Phys. **43**, 91(1967)

[10] A. G. Sitenko; "Lecture in Scattering Theory", Pregamon press 1971

3. 7 Measurements of Double Differential Charged Particle Emission Cross Sections by Incident D-T Neutrons

Takehiro Kondoh , Akito Takahashi , Hiroshi Nishizawa*

Department of Nuclear Engineering , Faculity of Engineering , Osaka University

Yamadaoka 2-1 , Suita , Osaka , 565 , Japan

**Mitsubishi Electric Corporation , Amagasaki , Hyogo , Japan*

Double differential cross sections for ^{nat}Ni(n,xα) and ^{nat}Cu(n,xα) reactions with 14.1MeV incident neutrons were measured based on the E-TOF two dimensional analysis. Measured data were compared with the other experimental data reported by N.Ito et al. and by S.M.Grimes et al, evaluated data of the ENDF/B-VI and SINCROS-II calculation. Concerning to the ^{nat}Ni(n,xα) reaction, it was observed in this experiment the angular distributions of α-particle emission showed forward-peaked tendency except for the low energy region.

1.Introduction

Energy spectral data for 14.1MeV-neutron-induced secondary charged particles are basic nuclear data for the estimation of the damage and nuclear heating of materials in the D-T neutron field. In general, the measurement of secondary charged particle spectrum is difficult, and experimental data are therefore scarce. We have made experiments based on the E-TOF two dimensional analysis, to measure double differential charged particle emission cross sections for candidate elements of fusion reactors.

2.Experimental procedure

The present experiment is based on the E(energy)-TOF(time of flight) two dimensional analysis method. The relation between E and TOF emitted particles is presented by the following eqation,

$$E = M_0 c^2 \left(\frac{1}{\sqrt{1-(L/cT)^2}} - 1 \right) \qquad (1)$$

where c is light velocity, and M_0, L, and T are the mass, the flight pass length, and the time of flight of emitted particle, respectively. Using the method, it isn't only possible to separate types of particles according to their differences in masses, but also we can identify the signals of marked particle if the signals are on one of the contours caluculated by eqation (1).

The α-particle spectra were obtained by integrating proper counts within the alpha particle contour. For calibrating absolute values of double differential cross sections (DDX), we adopted differential recoil proton cross sections of H(n,p) given in ENDF/B-VI. Details of experiments are presented in Ref.1.

3.Results

Measured DDX for the ^{nat}Ni(n,xα) reaction at 30, 45, 65, 90, 110, 135 degree in the LAB system are shown in Figs.1a through 1c, and for the ^{nat}Cu(n,xα) reaction at 30, 60, 90, 120 degree in Figs.2a through 2b. In the figures are given also the comparisons with evaluated data of the ENDF/B-VI. Energy differential cross section for the ^{nat}Ni(n,xα) reaction is shown in Fig.3, and for the ^{nat}Cu(n,xα) reaction is shown in Figs.4. The comparison with the ENDF/B-VI data, the data reported by S.M.Grimes et al. and the SINCROS-II calculation are also given in these figures.

Concerning to the ^{nat}Ni(n,xα) reaction, it is apparent that the measured α-particle spectra agree with the ENDF/B-VI data except for high energy region at backward angles. The ENDF/B-VI data are evaluated by assuming the forward-backward symmetry. On the other hand, the present data show us that the angular distributions are forward peaked in the energy region except low energy. It tells us that angular distributions tend to be varying with angle and that the amount of the forward-backward asymmetry strongly increases with increment of α-particle energy. In addition to the comparison with the ENDF/B-VI data, the comparison with the data reported by N.Ito et al. is shown in Figs.5a through 5b. We see good agreements, within statistical errors, among these data. Concerning to the energy differential cross section, it is apparent that the data reported by Grimes give excellent agreement with the ENDF/B-VI data and the SINCROS-II calculation, and that the present results don't show good agreement with three other data.

Concerning to the ^{nat}Cu(n,xα) reaction, it is apparent that the measured α-particle spectra agree with the ENDF/B-VI data except for 90 degree.Concerning to the energy differential cross section, it is obvious that data reported by Grimes show good agreement with the SINCROS-II calculation, and while the present data show good agreement with the ENDF/B-VI data except for low energy region. The present data in the low energy region are larger than the SINCROS-II calculation and the data by Grimes, and are smaller in the high energy region.

4.Conclusion

Double differential cross sections for ^{nat}Ni(n,xα) and ^{nat}Cu(n,xα) reactions were measured. Concerning to the ^{nat}Ni(n,xα) reaction, angular distributions tended to be varying with angle and that the amount of the forward-backward asymmetry strongly increases with increment of α-particle energy. Concerning to the ^{nat}Cu(n,xα) reaction, the measured α-particle spectra agreed with the ENDF/B-VI data except for 90 degree.

References

[1] S.Ogino et al., *OKTAVIAN Rep.*, 91-01(1991)

[2] S.M.Grimes et al., *Phys.Rev.C19*, 2127(1979)

[3] N.Ito et al., *JAERI-M*, 92-027(1992)

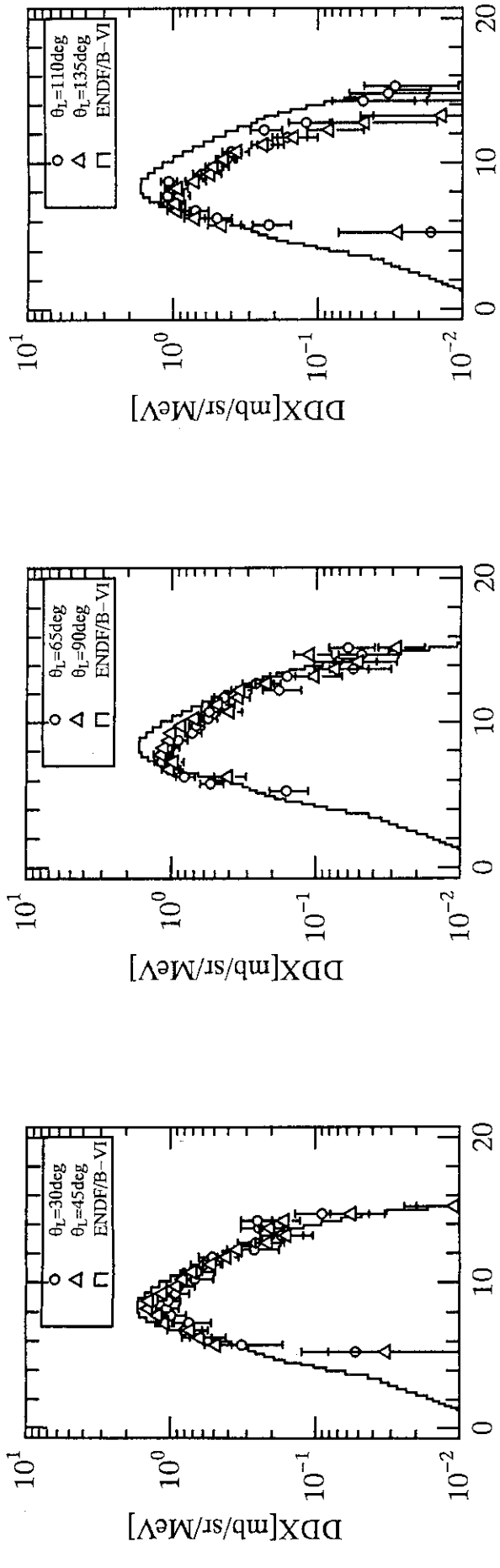

Fig.1a DDX for ^{nat}Ni(n,xα) at 30 deg and at 45 deg

Fig.1b DDX for ^{nat}Ni(n,xα) at 65 deg and at 90 deg

Fig.1c DDX for ^{nat}Ni(n,xα) at 110 deg and at 135 deg

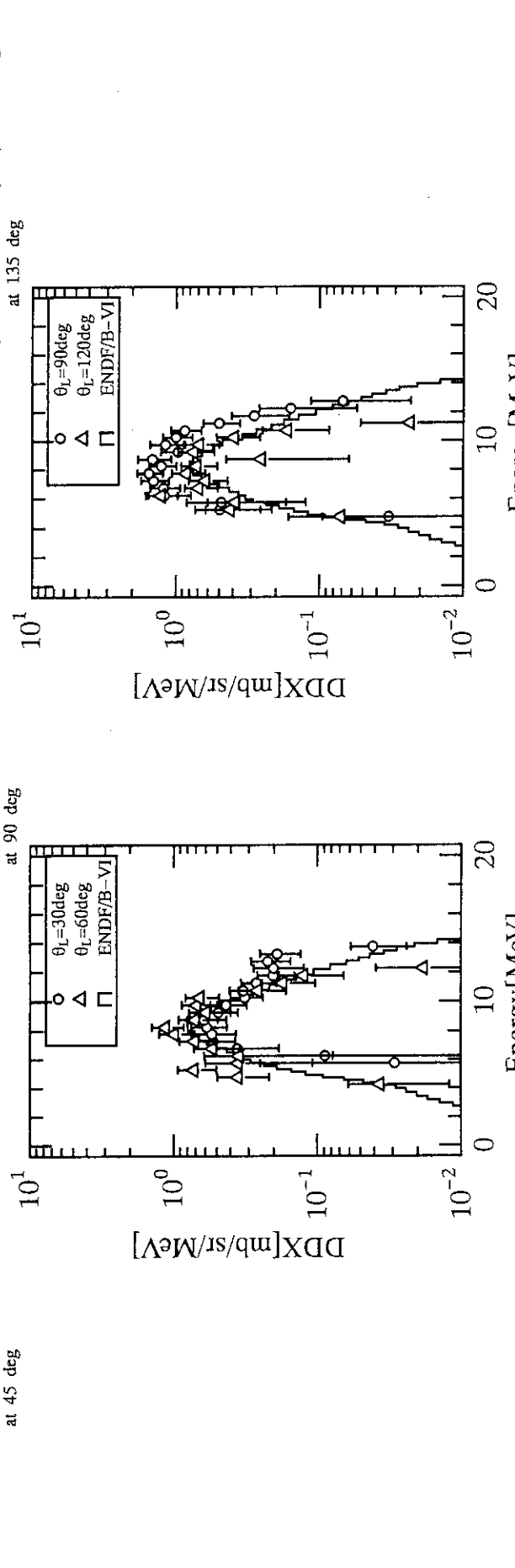

Fig.2a DDX for ^{nat}Cu(n,xα) at 30 deg and at 60 deg

Fig.2b DDX for ^{nat}Cu(n,xα) at 90 deg and 120 deg

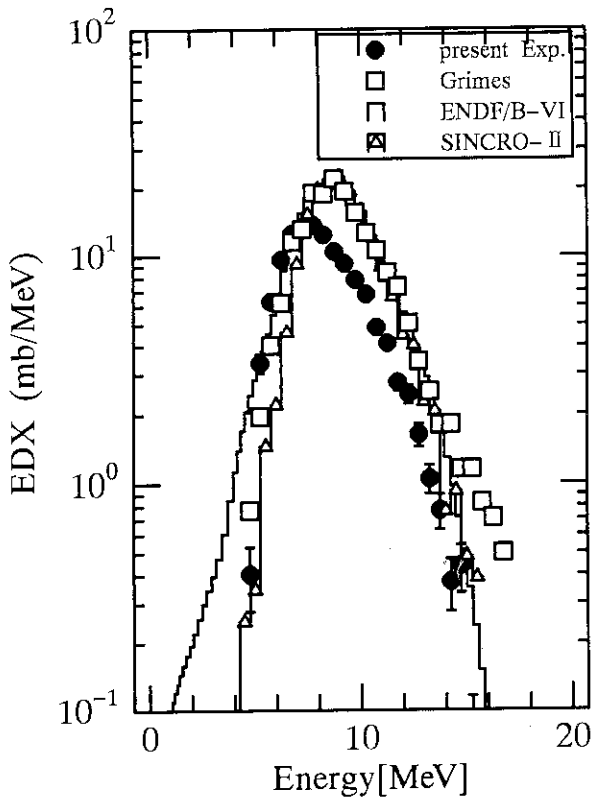

Fig.3 Angle integrated cross section for $^{nat}Ni(n,x\alpha)$

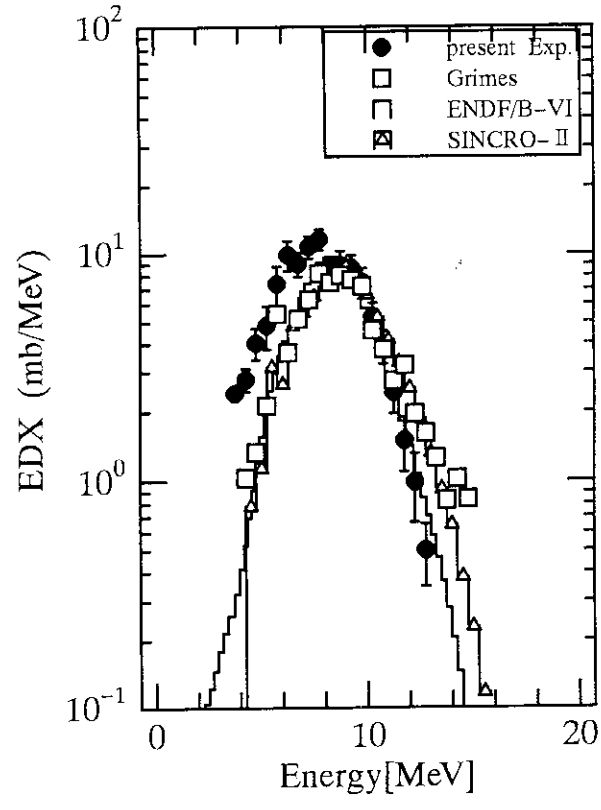

Fig.4 Angle integrated cross section for $^{nat}Cu(n,x\alpha)$

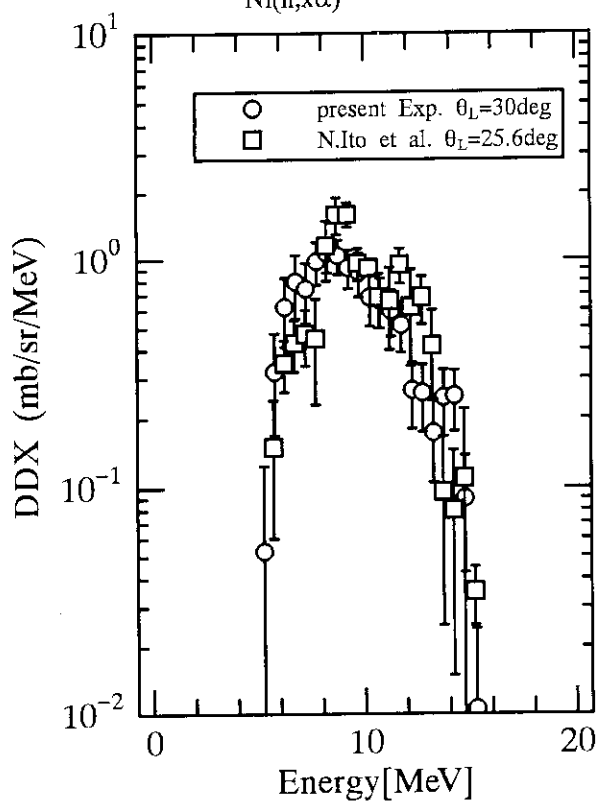

Fig.5a The comparison between present Exp. and N.Ito et al. for $^{nat}Ni(n,x\alpha)$

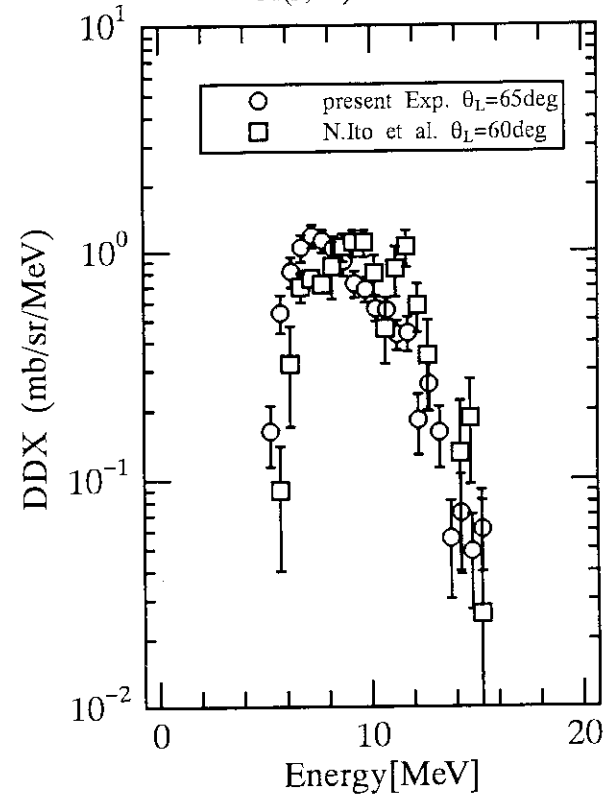

Fig.5b The comparison between present Exp. and N.Ito et al. for $^{nat}Ni(n,x\alpha)$

3. 8 Measurement of Neutron-induced Charged-particle Emission Cross Sections

M.Baba, I.Matsuyama[1], T.Sanami, S.Matsuyama, T.Kiyosumi, Y.Nauchi, N.Hirakawa
Department of Nuclear Engineering, Tohoku University, Sendai 980-77

Experiments have been carried out on 1)double-differential $^{50}Cr(n,x\alpha)$ cross sections between 5.1 and 14.1 MeV, 2)high-resolution $^{58}Ni(n,\alpha)$ emission spectrum between 4.8 and 5.8 MeV, and on 3)$^{14}N(n,p)^{14}C$ cross section for quasi-Maxwellian neutrons with kT≈25 keV, using a high efficiency gridded-ionization chamber.

1. Introduction

Differential cross sections for neutron-induced charged-particle emission reactions are of great importance in various applied and basic fields. We have been conducting measurements of (n,α) and (n,p) cross sections using a high efficiency gridded-ionization chamber (GIC)[1-4]. Recently, we carried out experiments on the followings using Tohoku University Dynamitron accelerator for neutron generation; 1)double-differential $^{50}Cr(n,x\alpha)$ cross sections between 5.1 and 14 MeV, 2)high resolution α-particle spectra for the $^{58}Ni(n,\alpha)$ reaction between 4.8 and 5.8 MeV, and 3)$^{14}N(n,p)^{14}C$ cross section for the "Maxwellian" spectrum of kT≈25 keV.

The experiments 1) and 2) were done as a part of IAEA Coordinated Research Program (CRP) on $(n,x\alpha)$ cross sections to provide differential $(n,x\alpha)$ data of structural elements, Cr and Ni, which are of great importance for estimation of radiation damage and nuclear heating in fusion reactors. The second experiments was motivated by discrepancies between our previous results[3,4] and recent data by Goverdovski et al.[5] obtained through high resolution measurements both in incident and outgoing channels.

The $^{14}N(n,p)^{14}C$ reaction cross section is one of key-parameters in astrophysics, since the reaction plays an important role in S-process nucleo-synthesis. Münster/KfK group reported the experimental cross section data for quasi-Maxwellian neutrons with kT≈25 keV[6] which are about two-times as small as that expected from the inverse reaction, $^{14}C(p,n)^{14}N$. The present experiment employed an equivalent neutron spectrum but an improved experimental method adopting GIC for measurements of proton yield and neutron flux.

2. Double-differential $^{50}Cr(n,x\alpha)$ Cross Section Measurement

Details of experiment and data analysis are described in Refs.1 and 2. Source neutrons were produced *via* the D(d,n), $^{14}N(d,n)$ (En=7.6 MeV)[2], $^{15}N(d,n)$ (En=11.5 MeV)[2], and the T(d,n) (En=14.1 MeV) reactions. The energy spreads were 0.1 to 0.4 MeV.

The schematic view of GIC is shown in Fig.1. The sample was a metallic ^{50}Cr foil (90% ^{50}Cr, electro-deposited on a gold backing), 2.12 mg/cm^2 thick and 25-mm-diam. The ^{50}Cr foil and a W foil for background measurement were mounted on a sample-changer of GIC, and bombarded by a collimated neutron beam. α-particles from the sample were detected in an almost 4π geometry. The counting gas was Kr mixed with a few % CH_4 or CO_2. Three signals from the common cathode (Pc) and two anodes (Pa) were accumulated as two sets of two-dimensional data. α-particles were selected by adjusting the gas pressure and making two-parameter data analysis to eliminate proton events[1].

Background-subtracted two-dimensional data for Pa *vs* Pc were transformed into DDX according to the following equations[1]:

---

[1] Present address: Japan Atomic Power Co-Ltd

$$Pa = E\ (1-\sigma(\bar{x}/d)\cos\theta) \approx E, \qquad Pc = E\ (1-(\bar{x}/d)\cos\theta),$$

where, E is the α-particle energy, d the cathode-grid distance (2.7 cm), θ the emission angle, σ the grid inefficiency (5.9%), and $\bar{x}$ is the distance from the cathode to the center-of-gravity of the ionization trace. Neutron flux on the sample was measured using a proton-recoil counter telescope within about ±4 %[2]. The DDX data were corrected further for 1)geometrical efficiency of GIC[1], 2)backgrounds due to parasitic source neutrons[2], and for 3)energy loss within the sample. Backgrounds by (n,d), (n,t) and (n,^{3}He) reactions could be ignored[1]. Angle-integrated spectra and production cross sections of α-particles were also deduced from DDX. Experimental errors were evaluated considering counting statistics (3~30 %), absolute normalization (3~6%), extrapolation of α-yields (3~6%), and background correction (1~3%)[1,2].

Figure 2 illustrates a typical angle-integrated α-spectrum and the excitation function of the ^{50}Cr(n,xα) reaction in comparison with other experiments, evaluated data and calculation using EXIFON[7]. The present (n,xα) cross section at 14 MeV is in agreement with other data[8,9] in the error range although three data are in large differences. The present α-emission spectrum and excitation function are largely different from ENDF/B-VI and closer to EXIFON in magnitude. In Fig.3, shown are calculations by Yamamuro using the code system EGNASH[10]. The calculations reproduce the present data both in spectrum shape and cross section much better than ENDF/B-VI and EXIFON owing to well-examined optical potential and level density parameters.

3. High Resolution Measurement of ^{58}Ni(n,xα) Emission Spectrum

In this experiment, we employed a Ni sample foil thin enough (≈300 μg/cm^2) and a neutron beam with small energy spread (≈100 keV). By this arrangement, as shown in Fig.4, α-particles for each state of residual nucleus, ^{55}Fe, are clearly separated each other. In this energy region, contribution of ^{60}Ni(n,α) should be ignored. The center-of-mass angular distribution for each α-channel is almost isotropic with slight forward-rise. The present excitation function, as shown in Fig.4, reproduces our previous experiment[3,4] using a thicker sample and a neutron beam with larger energy spread, and higher than Goverdovski et al.'s data[5]. Besides, it goes up almost monotonously with neutron energy without structure reported in Ref.5.

4. ^{14}N(n,p)^{14}C Cross Section Measurement

Source neutrons with a quasi-Maxwellian spectrum were produced by bombarding a thick lithium target with proton beam of 1.912 MeV[6]. These neutrons are emitted in a cone of ≈60°[6]. Therefore, GIC was converted into 2π geometry to permit all source neutrons entering the sample (Fig.5, left). The ^{14}N sample was a thin melamine film (≈150 μg/cm^2) prepared by vacuum evaporation on an aluminum foil. Neutron flux on the sample was measured by detecting tritons from the ^{6}Li(n,t)α reaction. The melamine and a ^{6}LiF sample for flux measurement were attached on the sample changer of GIC. By this arrangement, protons and tritons from the ^{14}N(n,p)^{14}C and ^{6}Li(n,t) reactions, respectively, could be measured in the same geometrical condition which reduced uncertainty in absolute normalization. The proton beam energy was calibrated using a threshold technique for the ^{7}Li(p,n) reaction, and confirmed by TOF measurement using a ^{6}Li glass detector. This detector was used to monitor the neutron flux at 0°-line.

The proton spectrum is shown in Fig.5. The data could be obtained by a short running time (≈3 hours) with 4 μA beam current owing to very large geometrical efficiency of GIC. Signal-to-background ratio is very good despite of the low Q-value of the reaction (Q = 624 keV). Proton yield was deduced by considering the geometrical efficiency of GIC and by extrapolating to zero energy using an integral yield curve *vs* channel number. The effect of proton self-absorption could be ignored. The triton yield was obtained by the procedure described in Ref.1. Number of sample atoms was determined by weighing.

The average cross section, $\langle\sigma_i\rangle$ (i = p, t) and the mean neutron energy $\langle E_n\rangle$ for the "Maxwellian" spectrum, M(E), were deduced as follows assuming the 1/v rule for both reactions:

$$\langle\sigma_i\rangle = \int \sigma_i(E)\cdot M(E)dE / \int M(E)dE, \qquad \langle E_n\rangle = \int E_n \cdot M(E)dE / \int M(E)dE$$

The Maxwellian averaged cross section of the ^{14}N(n,p) reaction $\langle\sigma_p\rangle$ is 1.7 mb (±0.08) for $\langle E_n\rangle$ = 32.3 keV. This is much larger than the Münster/KfK data (0.81±0.05)[6], but very close to that expected from the inverse reaction, and consistent with recent data by LANL[11] (2.15±0.06 mb) and Dubna[12] (2.02±0.03 mb) groups for 25 keV neutrons. Furthermore, the present result is consistent with thermal cross section (1780 mb) if 1/*v* extrapolation is applied.

The authors wish to thank Prof. H.Vonach for providing them with the ^{50}Cr sample. They appreciate Dr. N.Yamamuro for providing theoretical results using EGNASH prior to publication. This work was partly supported by Japan Atomic Energy Research Institute (JAERI).

References:

1. N.Ito, et al: *Nucl.Instr.Methods* **A337**, 474 (1994),
2. I.Matsuyama et al.: *JAERI-M* 94-019 (1994) p.191
3. M.Baba et al.: *J.Nucl.Sci.Technol.*, **31**[7] 745 (1994)
4. M.Baba et al.: *Proc.Int.Conf. on Nucl.Data for Sci. Technol.*,(1994 Gatlinburg), to be published
5. A.Goverdovski et al.: *ibid.*,
6. K.Brehm et al.: *Z.Phys* **A330** 167 (1988)
7. H.Kalka, M.Torjiman, D.Seeliger; *Phys. Rev.*, **C40(4)**, 1619 (1989)
8. S.M.Grimes et al.: *Phys.Rev.*, **C19**, 2127 (1979)
9. C.Derndorfer et al.: *Z.Phys.*, **A301** 327 (1981)
10. N.Yamamuro: Private communication (1994)
11. P.E.Koehler et al.: *Phys.Rev.*, **C39** 1655 (1989)
12. Yu.M.Gledenov et al.: Proc.8th Symp.Capture Gamma-ray Spectroscopy (1993 Fribourg) p.584

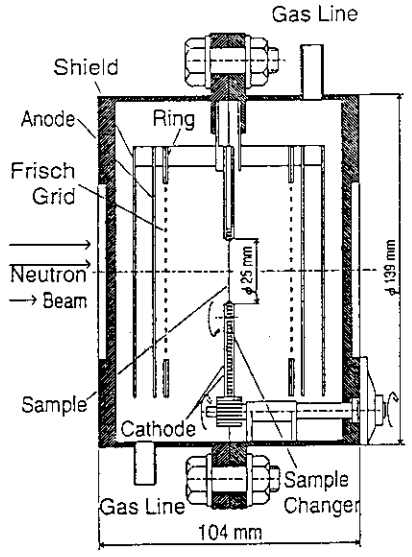

Fig.1: Schematic view of GIC.

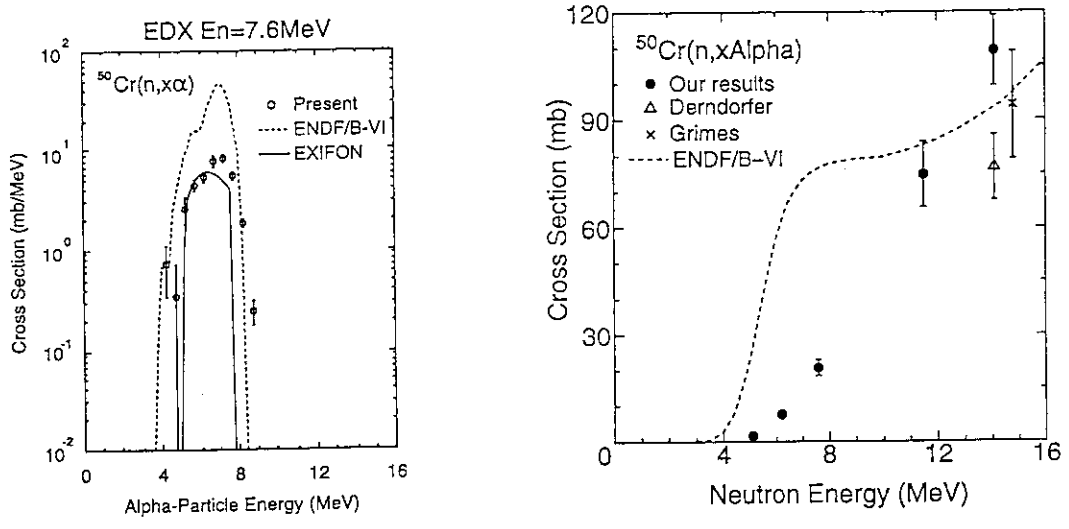

Fig.2: Angle-integrated α-spectrum (left) and excitation function (right) of the ^{50}Cr(n,xα) reaction.

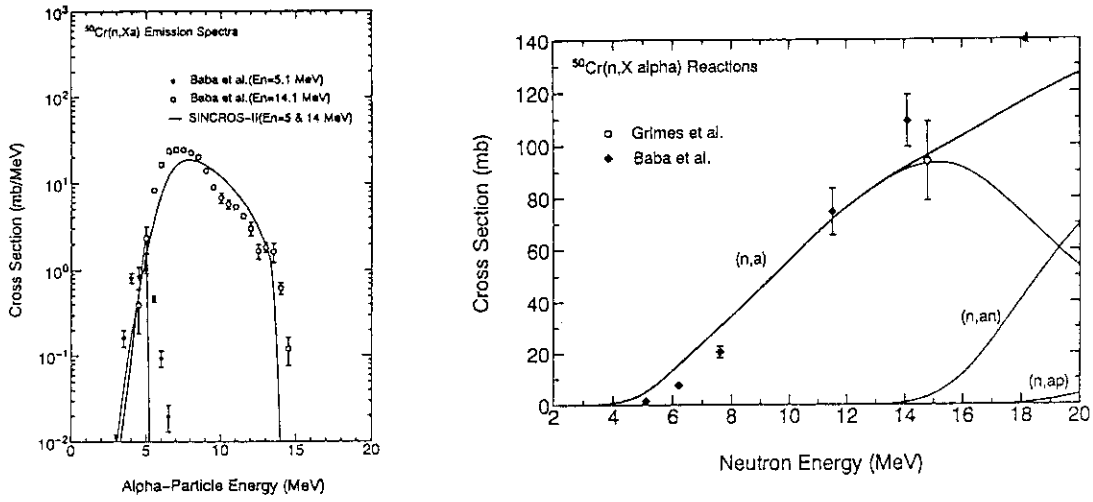

Fig.3: Same as Fig.2; the present data (baba) are compared with calculations by Yamamuro.

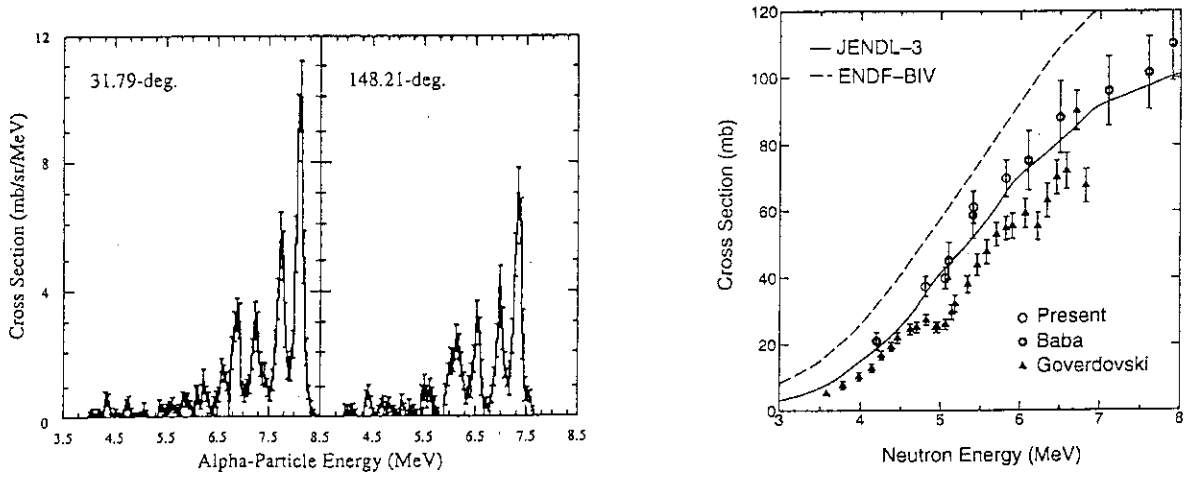

Fig.4: DDX (left) and excitation function (right) by high resolution ^{58}Ni(n,α) measurement.

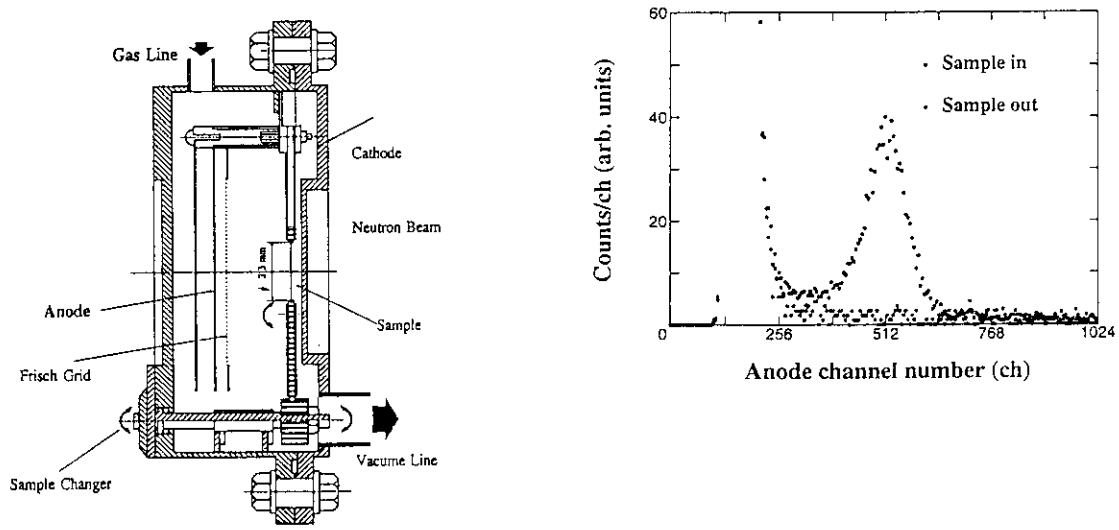

Fig.5: GIC setup (left) and proton spectrum (right) for the ^{14}N(n,p)^{14}C reaction.

3. 9 Measurements of Double-differential Neutron Emission Cross Sections of Fe and Nb for 11.5 MeV Neutrons

Shigeo Matsuyama, Daisuke Soda, Mamoru Baba, Masanobu Ibaraki,
Yasushi Nauchi, Shin Iwasaki, and Naohiro Hirakawa
Department of Nuclear Engineering, Tohoku University,
Aramaki-Aza-Aoba, Aoba-Ku, Sendai, 980-77, Japan

Double-differential neutron emission cross sections (DDXs) for 11.5 MeV neutrons have been measured using the $^{15}N(d,n)^{16}O$ neutron source at the Tohoku University 4.5 MV Dynamitron facility. In this study, DDXs of Fe and Nb for En' > 6 MeV were measured by the conventional single time-of-flight method without distortion by background neutrons associated in the $^{15}N(d,n)^{16}O$ neutron source. Further, for Fe, secondary neutron energy range was extended down to 2 MeV adopting the double time-of-flight method.

1. Introduction

Double-differential neutron emission cross sections (DDXs) for 7-13 MeV incident neutron energies are very important for the neutronics design of fusion and fast reactors. However, DDX data for the 7-13 MeV region are still lacking because of the lack of monoenergetic neutron source and facility. Recently, we employed the $^{15}N(d,n)^{16}O$ reaction for ~ 11 MeV neutron source. The neutron from the $^{15}N(d,n)^{16}O$ reaction is not monoenergetic because of the neutron from several excited states of residual ^{16}O. Nevertheless, the first excited state of ^{16}O is separated enough (6.06 MeV) from the ground state, which allows us to study neutron scattering up to ~6 MeV excitation energy using a single time-of-flight (S-TOF) method [1,2]. For the secondary neutron energy region lower than ~6 MeV where the spectrum measured by the S-TOF method is distorted by background neutrons, we adopted a double-TOF (D-TOF) method that was similar to that employed at China Institute of Atomic Energy (CIAE) [3] and obtained the data eliminating distortion by background neutrons.

2. Experiments and Data Reductions

Experiments were carried out using the Tohoku University 4.5 MV Dynamitron pulsed neutron generator [1,2,4]. The S-TOF and D-TOF methods were employed to get the spectra for En' > 6 MeV and for En' < 6 MeV, respectively.

The S-TOF experimental method was almost the same as that in previous studies [1,2,4]. The neutron target was a gas cell containing enriched $^{15}N_2$ (99.9%) and bombarded by ~2.5 MeV deuteron beams. The source neutron energy spectrum is shown in fig.1. In addition to the 11.5 MeV neutron, several neutron groups corresponding to the excited states of ^{16}O are also observed. There are no appreciable backgrounds in the region higher than 6 MeV. Therefore, time-

consuming "gas-out measurements" were not needed.

The scattering samples were cylinders of elemental iron and niobium (3 cm $\phi \times 5$ cm) which were suspended vertically at a distance of 12 cm from the neutron target. A high efficiency large volume liquid scintillation detector (LLSD) was used as a secondary neutron detector to compensate low intensity of the neutron source. Special data acquisition and reduction systems were employed [2].

In the S-TOF measurement, the flight path length was 6 m. The neutron emission spectra were measured at 12 angles between 20° and 150°. Absolute cross section was determined referring the elastic scattering cross section of the H(n,n) reaction.

The D-TOF method adopts a longer target-sample distance and shorter sample-detector distance than those of the S-TOF method. Figure 2 shows the experimental set up of the D-TOF method. The target-sample distance and sample-detector distance were 3 m and 75 cm, respectively. The neutron target was shielded with water, iron and concrete to reduce sample independent backgrounds. Secondary neutrons were detected by a 14 cm $\phi \times 10$ cm NE213 scintillation detector. Long target-sample distance and short sample-detector distance make the flight time of secondary neutrons induced by 11.5 MeV neutrons shorter than that of background neutrons. Therefore, the secondary neutron group by 11.5 MeV neutrons can be separated from background events in TOF spectrum. Figure 3 shows a TOF spectrum for Fe at 90° together with that for sample-out background. The secondary neutrons by 11.5 MeV neutrons are separated from those by background neutrons. Data were derived for Fe at 90°. Absolute cross section was determined by normalizing to the S-TOF data considering the resolution function.

The experimental TOF spectra were converted in energy spectra considering detection efficiency and the effects of sample-out backgrounds. Then, the energy spectra were corrected for the effects of finite sample-size.

3. Results.

Figure 4 and 5 show typical DDX of Fe and Nb derived by the S-TOF method in comparison with the data derived from JENDL-3.1 and ENDF/B-VI. There are large discrepancies between the experimental data and the evaluated data in forward angles for Fe and in backward angles for Nb.

Figure 6 shows DDX of Fe at 90°. The data for En' > 6 MeV were derived from the S-TOF data and the data for En' < 6 MeV derived from the D-TOF data. By combining the S-TOF and D-TOF method, we can get entire DDX data for 11.5 MeV neutrons.

Therefore, a combination of the $^{15}N(d,n)^{16}O$ neutron source, S-TOF and D-TOF methods will be a powerful means for DDX measurements in 11 MeV region.

References

1) S.Matsuyama et al., Proc. Int. Conf. on Nucl. Data for Sci. and Technol., Gatlinburg, 1994, to be published

2) S.Matsuyama et al., JAERI-M 94-019 (1994) p.210

3) Q. Bujia et al., Proc. Int. Conf. on Nucl. Data for Sci. and Technol., Jülich, 1991, p.436

4) M.Baba et al., J. Nucl. Sci. Technol., **31(8)**, 757 (1994)

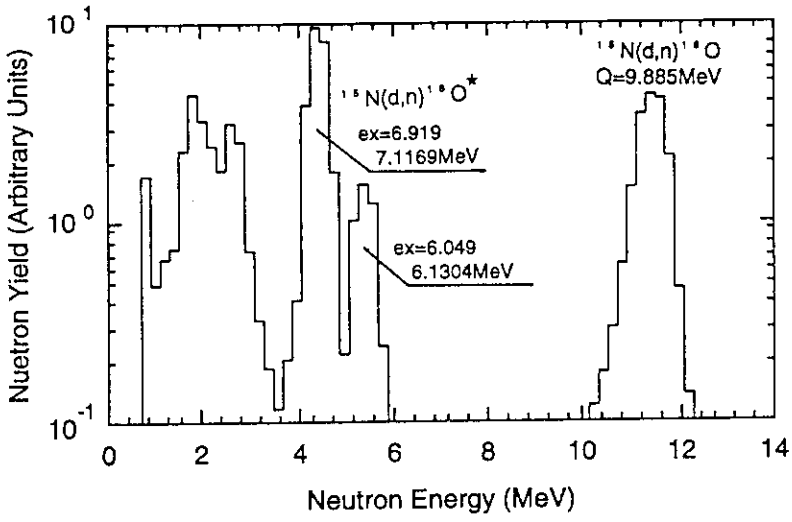

Fig.1. Energy spectrum of the ^{15}N(d,n) neutron source.

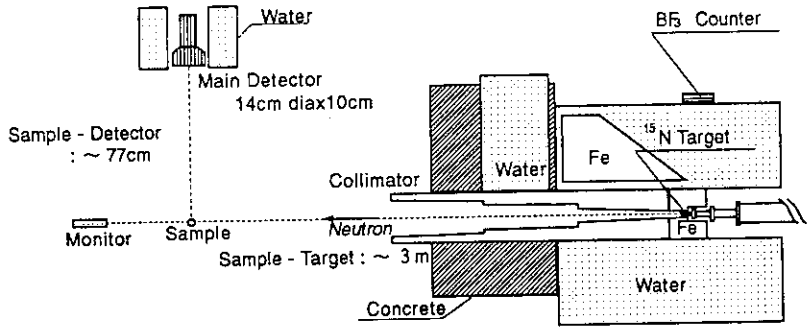

Fig.2. Experimental geometry of D-TOF method.

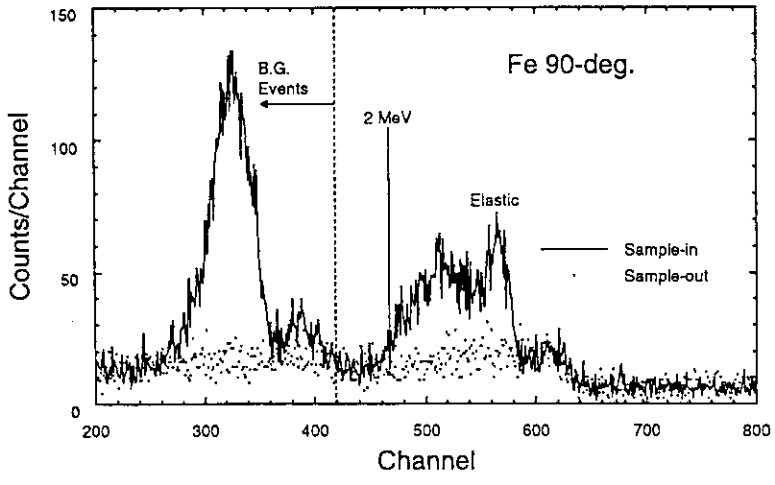

Fig.3. TOF spectrum of Fe at 90° by D-TOF method.

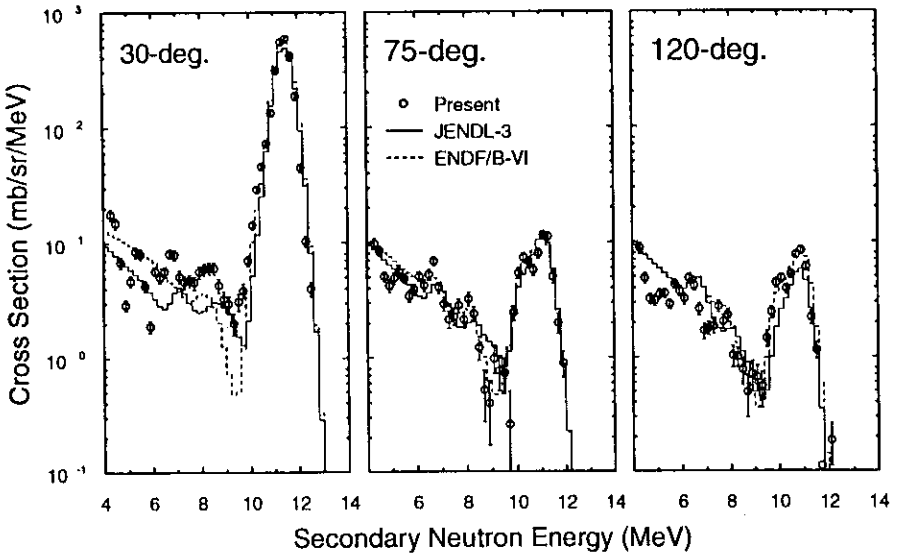

Fig.4. Double-differential neutron emission cross section of Fe.

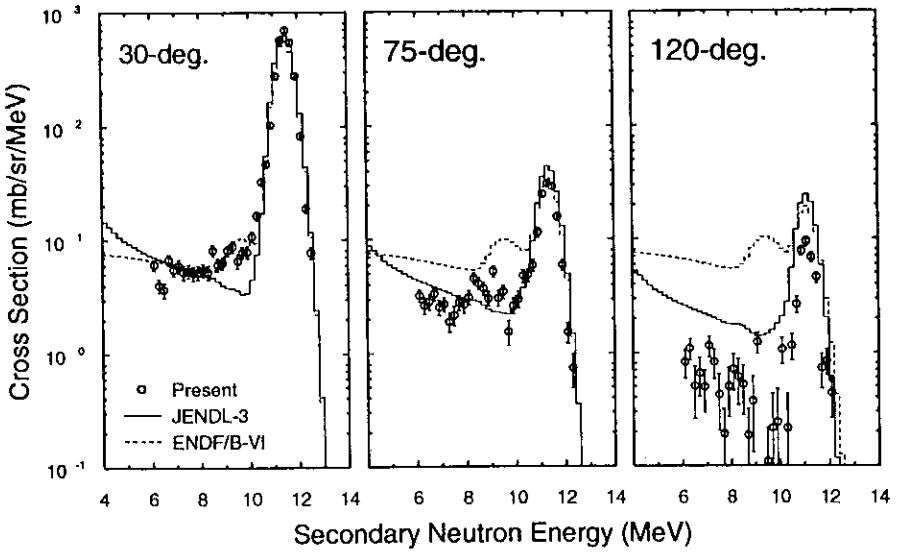

Fig.5. Double-differential neutron emission cross section of Nb.

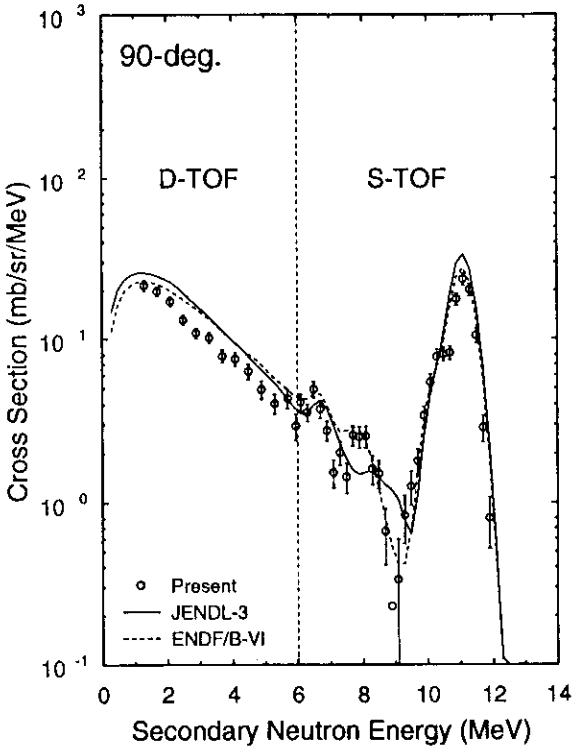

Fig.6. Double-differential neutron emission cross section of Fe at 90-degree.

3.10 Measurement of Helium Production Cross Sections by Helium Accumulation Method

Yoshiyuki TAKAO, Yukinori KANDA, Katuhiro YAMAGUCHI,
Tamotu YONEMOTO, Hiroshi ETOH, Masako MIWA
Department of Energy Conversion Engineering,
Kyushu University, Kasuga, Fukuoka 816, Japan

Abstract

Helium production cross sections for aluminum at proton energies up to 17.5MeV have been measured. Helium accumulation method has been applied to determine these cross sections. The method is a direct measurement of helium production cross sections, because the cross sections are determined by the number of helium atoms produced by proton irradiation in samples. An aluminum sample consists of an aluminum foil (chemical purity 99.999%, size $12\times9\times0.095mm^3$) put between two gold foils (chemical purity 99.97%, size $10\times8\times0.050mm^3$). Ten aluminum samples were irradiated by protons of the energy range from 8.9 to 17.5MeV with a tandem accelerator. The helium atoms were measured by the helium atoms measurement system based on an ultra high vacuum technique. The results of this work: proton-induced helium production cross sections of aluminum, agree with the other experimental data within the error.

1. Introduction

The purpose of this work is to measure the helium production cross sections of aluminum by proton induced reactions. It is important to collect the experimental data of helium production cross sections for the selection of the materials for many kinds of apparatuses, because produced helium causes severe damages, such as embrittlement of structural materials, and blisters and flakes on the surfaces of walls. Though helium production cross sections for many kinds of elements and incident particles have been demanded, there are few available experimental data.

In this work, ten Al samples were irradiated by protons with incident energies from 8.9 to 17.5MeV using a tandem accelerator. The helium atoms produced in the samples were measured by the helium atoms measurement system (HAMS). The procedure of the helium atoms measurement by HAMS is the following. A sample is evaporated in a vacuums chamber; the helium gas released from the sample is analyzed by a mass spectrometer. The helium production cross sections are then determined by the thickness of samples, the number of measured helium atoms and the total electric charge of protons.

2. Experimental procedures

The experiment includes three consecutive stages: sample preparation, irradiation of protons and measurements of the number of helium atoms contained in samples.

2.1 Sample preparation

An Al sample consists of an Al foil (chemical purity 99.999%, size $12\times9\times0.095mm^3$) put between two gold foils (chemical purity 99.97%, size $10\times8\times0.050mm^3$); ten Al samples were prepared. Those foils were cleaned in a acetone bath ultrasonically. Al foils were then baked at a temperature of 673K for an hour in a vacuum of $\leqq7\times10^{-4}$Pa to remove helium atoms contained through its manufacturing process. Au foils were also baked at 1073K. These Au foils were to balance the outgoing energetic α-particles from the Al sample surface due to the kinetic energy of the (p,xα) reactions. A schematic diagram of the Al sample is shown in Fig. 1. We measured the produced helium atoms in both of the Al foil and the Au foils. Au foils collect all emitted helium atoms from the Al foil, since Au foils are thicker than the range of emitted α-particles in Au [1]. Moreover, the helium production cross section of Au is much smaller than that of Al.

2.2 Irradiation of protons

The Al samples were irradiated by protons up to 17.5MeV at Kyushu University Tandem Accelerator Laboratory. Each sample was set in a sample holder with Faraday cup, which was put on a sample table so as to coincide a perpendicular to the Al sample and one of proton beam. Fig. 2 shows a schematic diagram of the sample holder and the sample table. The sample table was set in a vacuum chamber. The vacuum chamber with a diameter of 100cm and a depth of 50cm has a revolving table, which can move around the center of the vacuum chamber. The sample table was set on the revolving table which allows to change samples easily. The vacuum chamber was evacuated by pumping by a turbo-molecular pump to a pressure of $\leqq3\times10^{-4}$Pa. The sample table was then cooled by liquid nitrogen which prevents the release of produced helium atoms due to the diffusion. Temperatures of the sample table and a sample holder were measured by thermocouples and were below 223K during sample irradiation.

The samples were irradiated at a proton current of 0.1μA to reach a positive charge of 178μC measured by using a current integrator; the number of irradiated protons was obtained from this value.

2.3 Measurement of the number of helium atoms

The number of helium atoms produced by proton irradiation in the samples was measured by HAMS. The following is the procedure of helium atoms measurement. The irradiated sample is set on the tantalum boat as a heater in the furnace and is evacuated to a pressure of $\leqq2\times10^{-7}$Pa and is heated electrically at a temperature of more than a melting point of the sample. The released gas containing helium from the sample is purified by the trap of Ti-getter pump. The sample gas is then admitted into a quadrupole mass spectrometer (QMS). The measured mass spectrum is displayed on a CRT of the personal computer and the number of helium atoms is calculated from the integration of the mass 4 peak in the spectrum.

The measuring efficiency of the released helium gas of HAMS is calibrated by a series of measurements of standard helium: known amount of helium gases prepared by using the standard helium supply.

3. RESULTS AND DISCUSSION

The results of this work are shown in Fig. 3 together with cross sections measured in an available experiment. The plots as the helium production cross sections of Al are average cross sections for each proton energy range. The proton energy range for each Al foil was calculated from the energy decrement in the Al sample[2] and is also plotted in Fig. 3.

The error in the measurement of a positive charge of protons was $\pm 0.5\%$. The error in helium atoms measurement was $\pm 4.1\%$ from the fluctuation of mass 4 background and the HAMS absolute calibration. The error in the sample thickness was $\pm 1.0\%$. Consequently, the error in the measured helium production cross section was $\pm 4.2\%$. The largest uncertainty source of our measurement was HAMS absolute calibration caused by the production of a standard helium gas.

Al(p,xα) cross sections measured in this work agree with the other experimental data of Nitoh et al.[3] within the error. The experimental data are cross sections for production of stable magnesium isotopes by proton induced reactions in Al, measured by mass spectrometry. Though these data are cross sections for Al(p,α) reaction at proton energies up to 15MeV, we can compare our results with the data. Because, the main reaction producing helium atoms in the energy range is Al(p,α) reaction.

References

(1) Ziegler, J.F. : *"Helium: Stopping Powers and Ranges in all Elemental Matter"*, (1977), Pergamon Press, New York.

(2) Andersen, H.H., Ziegler, J.F. : *"Hydrogen Stopping Powers and Ranges in all Elements"*, (1977), Pergamon Press, New York.

(3) Nitoh, O., Honda, M.,Gensho, R. : Mass Spectrometry, 24[3], 237(1976), [in Japanese].

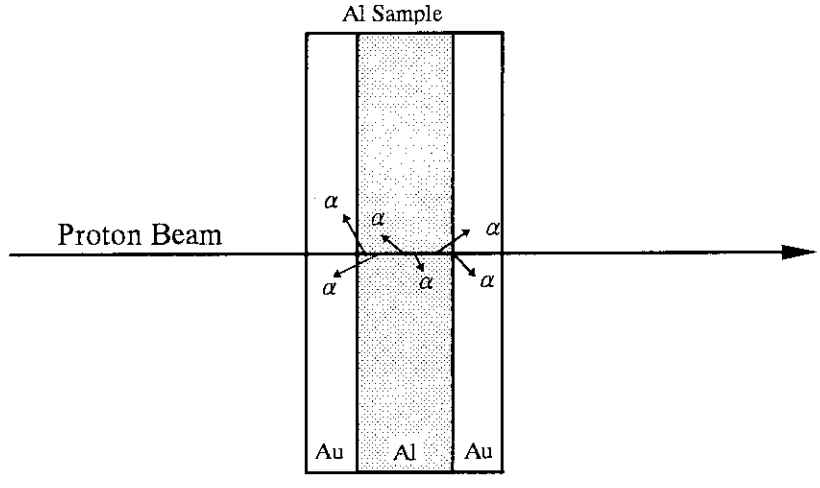

Fig. 1 An Al sample consists of an aluminum foil put between gold foils. The helium atoms released from the Al foil are trapped in Au foils.

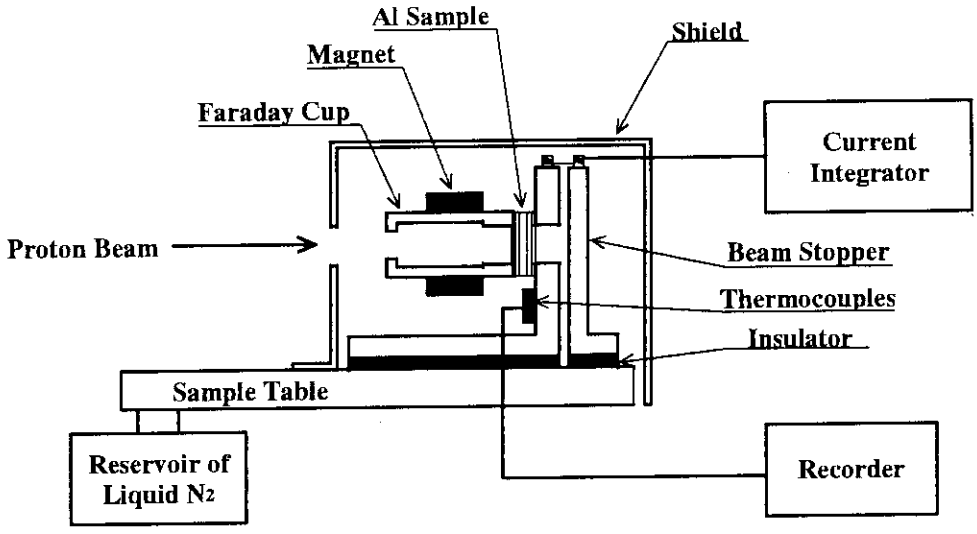

Fig. 2 Schematic diagram of the sample holder and the sample table

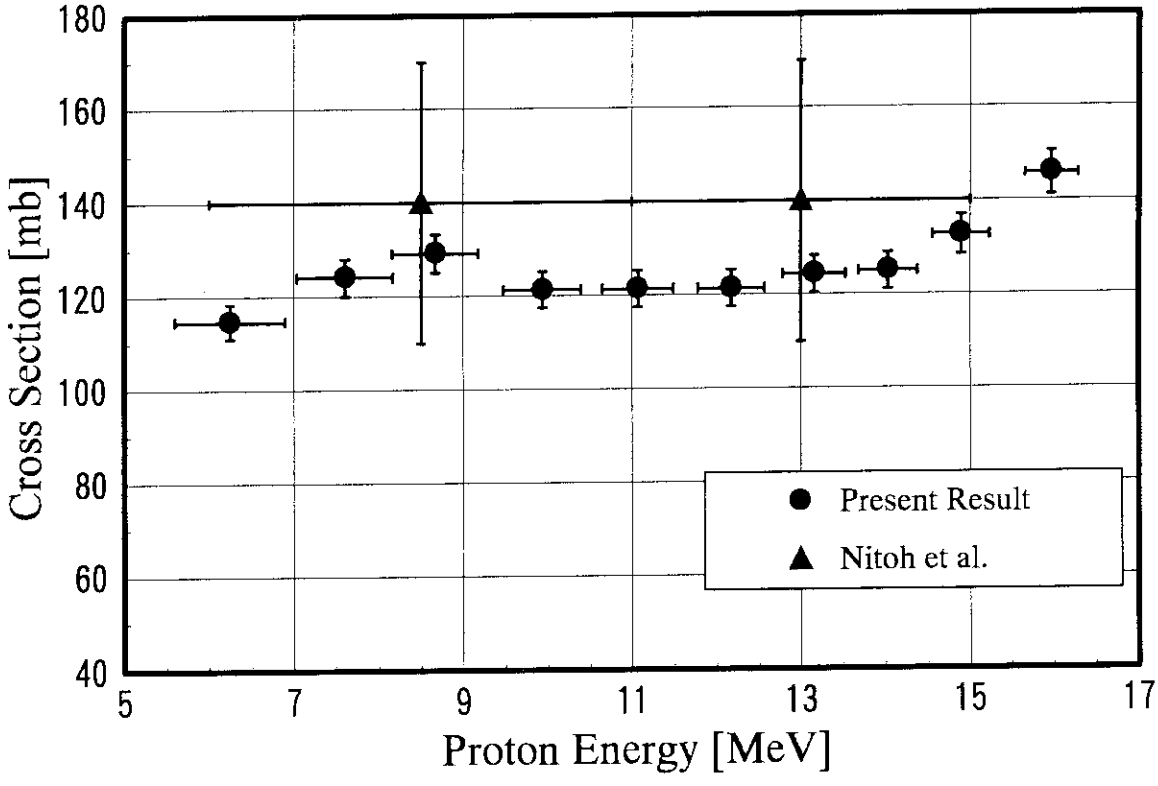

Fig. 3 Al(p,xα) cross sections measured by the helium accumulation method

3.11 Measurement of Neutron Activation Cross-sections for Elements Co, Ni, Y, Nb, Tm and Au between 12 and 20 MeV

S. Iwasaki, S. Matsuyama, T. Ohkubo, H. Fukuda, M. Sakuma, M. Kitamura
and N.Odano*

Department of Nuclear Engineering,Tohoku University
Aramaki-Aza-Aoba, Aobaku, Sendai 980-77, Japan Email: iwa@mine1.nucle.tohoku.ac.jp
*Tokai Branch, Ship Research Institute
Tokai, Nakagun, Ibaraki 319-11

Neutron activation cross-sections for cobalt, nickel, yttrium, niobium, thulium and gold have been measured in the neutron energies from 12 to 20 MeV with the reference cross section of NEA $^{93}Nb(n,2n)^{92m}Nb$ at Tohoku Dynamitron Facility.

1. INTRODUCTION

Precise cross sections above 12 MeV are still sparse except for the energy of 14 MeV although these are important for the high energy dosimetry, and estimation of damage rates and/or activation level of structural materials tested or used in the proposed high energy accelerator based neutron fields.[1] Such cross sections also provide indispensable information to establish the nuclear model for high energy cross sections.[2] Several activation cross sections for cobalt, nickel, yttrium, niobium, thulium and gold have been measured between 12 and 20 MeV.

2. EXPERIMENTAL

Source neutrons were produced via the $T(d,n)^4He$ reaction by bombarding a 2.9-MeV deuteron beam from the Dynamitron accelerator at Tohoku University. Eight packages of high or ultra-high purity metal foils were set around the neutron source at 5 cm from the target in the angular range from 0 to 140 deg. covering the incident neutron energies from 20 down to 12 MeV. Experimental arrangement and technique were almost the same as the previous experiments.[3,4] Neutron flux at each foil was determined from the activation rates of two niobium foils which sandwiched each sample foil in between; the reference cross section for the $^{93}Nb(n,2n)^{92m}Nb$ reaction was taken from the 1991 NEANDC/INDC standard file.[5]

3. RESULTS

The measured cross sections are described here, and those data are compared with the previous data and cross section file data in Fig. 1 (a) through (h).

3.1. $^{59}Co(n,2n)^{58}Co$ cross section

This reaction is important for dosimetry application, especially in the high energy neutron

field[2]. Also, the evaluated cross section for IRDF-90[6] by IRK group was adopted as the secondary standard[7] by NEA besides the $^{93}Nb(n,2n)^{92m}Nb$ cross section. However, the above 14 MeV the evaluated data taken from three dosimetry files :JENDL DOSIMETRY FILE (JDF),[8] IRDF-90 and ENDF/B-VI[9] are still not consistent with each other, reflecting the status of experimental data base of this energy region which each evaluation was based upon. The present result shows the cross section curve located between the above dosimetry file's data.

3.2. $^{58}Ni(n,2n)^{57}Ni$ cross section

This reaction is suitable to apply to the high threshold dosimetry of short term. Previously measured data are deviated tremendously above 15MeV; there are two major data groups with additional minor data sets in between as discussed in Ref.10. The old dosimetry data took the low major group, while the recent evaluations adopted the higher group. Present measurement data do not belong to both two major groups, as indicated by the previous result of our group[4].

3.3. $^{58}Ni(n,np)^{57}Co$ cross section

Although this reaction is suitable as the high threshold dosimeter with relatively long lasting period (year), the status of the data base of this reaction is rather poor except for the energy region around 14 MeV. The present data show consistency with the previous measurement,[4] also with the ENDF/B-VI evaluation above 15 MeV, whereas not with JENDL-3.[11]

3.4. $^{58}Ni(n,p\alpha)^{54}Mn$ cross section

This reaction was first observed in the previous experiment.[4] In the present measurement, one possibility of the ^{54}Mn activity due to the impurities in the sample foils in the previous experiment was completely denied because of use of the ultra-high purity nickel foils. Theoretical model calculation[4] by SINCROS-II[12] estimated the appreciable cross section of about 20mb at 20MeV. The present data are almost double of this estimation. This suggest that the proper selection of charged-particle decay channels in the model calculation for the high energy reactions should be made in order to estimate accurately the helium-gas production rates, or activation rate for the medium weight nuclei of the structural materials.

3.5. $^{89}Y(n,2n)\ ^{89}Y$ cross section

This reaction is supposed to be included in the update version of JDF because of the large cross section with flat energy dependence above 15 MeV having relatively long life time. Present data support the evaluated data of JENDL-3.

3.6. $^{169}Tm(n,2n)^{168}Tm$

This reaction is also supposed to be included in the update version of JDF due to the same reason as the yttrium. The status of the experimental data including the present data is moderately good. The cross-section curve of JENDL Activation File[13] in the figure is slightly lower than the trend of the experimental data between 11 and 16 MeV.

3.7. $^{197}Au(n,2n)^{196}Au$

This reaction has been used some time as a reference one in the activation cross section measurement. Up to date, a large number of experimental data have been reported and the status

of the data is almost sufficient below 20MeV. The present measurement again support the IRDF-90 evaluation.

3.8. $^{197}Au(n,3n)^{195}Au$

In the high energy dosimetry for the advance neutron sources based on the Li+d reaction[1] or spallation reactions, gold is attractive as a single-element dosimeter besides cobalt because of their multiple reactions. This reaction serves as the good dosimeter in the energy range from around 17MeV to 40MeV except for the drawback of the emission of low energy photons which necessitate to use of very thin sample foils. Present data reproduced the previous data of our group,[4] and are lower than other previous measurements.

Experimental details and final numerical data for all observed cross sections are in preparation, and will be presented elsewhere. This work was financially supported by JAERI in 1993. The authors are grateful to Messrs. R.Sakamoto, and M. Fujisawa of the Dynamitron Facility.

REFERENCES

1. M. Sugimoto, K. Noda, Y. Kato, H. Ohno and T. Kondo: JAERI-M 92-027 p.58, (1992).
2. S. Iwasaki and N.Odano, to be published in the Proceedings of the International Conference on Nuclear Data for Science and Technology, Gatlinburg, Tenn., USA, May 9-13, 1994.
3. M. Sakuma , S. Iwasaki, H. Shimada, N. Odano, K. Suda, J.R. Dumais and K. Sugiyama: JAERI-M 92-027, p.278 (1992).
4. S. Iwasaki, M. Sakuma, K. Sugiyama and N. Odano: JAERI-M 93-046, p.257, JAERI (1993).
5. H. Vonach: *Nuclear standards for Nuclear Measurements*', NEANDC-311"U", INDC(SEC)-101, NEA/OECD, p80,(1992).
6. N.P. Kocherov and P.K. McLaughlin: IAEA-NDS-141 (1990).
7. H. Vonach: *Nuclear Standards for Nuclear Measurements*', NEANDC-311 "U", INDC(SEC)-101, NEA/OECD (1992), pp.78-79.
8. M. Nakazawa, et al.: "*JENDL Dosimetry File*", JAERI 1325 (1991).
9. D.E. Cullen, et al.: IAEA-NDS-41/R, rev.0 (1982).
10. S. Iwasaki: JAERI-M 93-046, p.211, (1993).
11. K. Shibata , et al.:"*Japanese Evaluated Nuclear Data Library, Version-3 -JENDL-3-*" JAERI 1319, (1990).
12. N. Yamamuro: JAERI-M 90-006, (1990).
13. Y. Nakajima and T.Nakagawa: private communication.

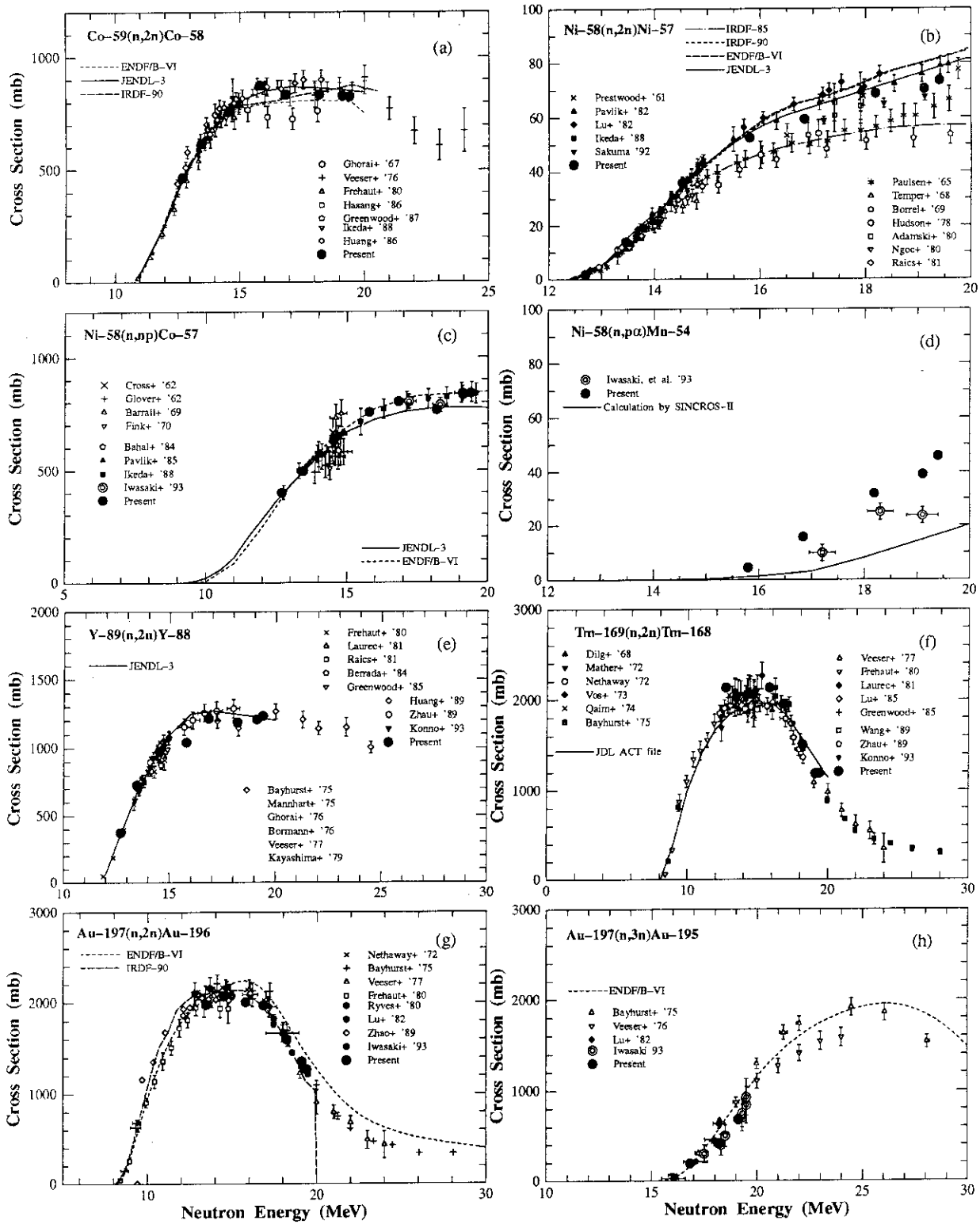

Fig. 1 Comparison of the present experimental data with those of the previous ones and of some evaluated files for the reactions: $^{59}Co(n,2n)^{58}Co$ (a), $^{58}Ni(n,2n)^{57}Ni$ (b), $^{58}Ni(n,np)^{57}Co$ (c), $^{58}Ni(n,p\alpha)^{54}Mn$ (d), $^{89}Y(n,2n)^{89}Y$ (e), $^{169}Tm(n,2n)^{168}Tm$ (f), $^{197}Au(n,2n)^{196}Au$ (g), and $^{197}Au(n,3n)^{195}Au$ (h), respectively.

3.12 Measurement of (p, p') Spectra from Boron Isotopes

N. Koori, K. Ichiba, Y. Watanabe+, H. Shinohara+, T. Michibata+, H. Ijiri+,
K. Sagara++, H. Nakamura++, K. Maeda++, and T. Nakashima++

Faculty of Integrated Arts and Sciences, The University of Tokushima, Tokushima 770
+ Department of Energy Conversion Engineering, Kyushu University, Kasuga 816
++ Department of Physics, Kyushu University, Fukuoka 812

1. Introduction

We have been studying experimentally and theoretically the mechanism of (p,p') scattering from light and medium-heavy nuclei[1-4]. In our studies of polarized proton experiments covering the energy range 12-16 MeV, several data on elastic and inelastic proton scattering have also been accumulated for the 1p-shell nuclei. Double differential cross sections (DDX) or energy spectra of (p,p'x) reactions are required for estimation of neutron data, which are used for calculation of neutron transport and kerma factors. Parameters of the optical potentials for light nuclei are also indispensable as fundamental data in order to understand the reaction mechanism.

In the present work, we have measured ^{nat}B(p,p'x) energy spectra at 14 MeV, then extracted differential cross sections and analyzing powers from the spectra for the elastic and inelastic scattering. The elastic scattering data for ^{10}B and ^{11}B have been analyzed with the spherical optical model (SOM).

2. Measurement and analysis

We have measured double differential cross sections (DDX) from a natural boron target (180 μg/cm^2 thick, and the isotopic abundance of 80.1% of ^{11}B and 19.9% of ^{10}B) by using a 14-MeV polarized proton beam from the tandem Van de Graaff accelerator in Kyushu University. The detection system was almost the same as those reported previously [1]. A ΔE-E counter telescope consisting of three silicon surface barrier detectors (E1: 20μm, E2: 75μm, E3: 2000μm) was employed for detection of protons.

Beam polarization was monitored using a polarimeter consisting of ^{4}He gas target and two ΔE-E silicon detectors at the down stream of a scattering chamber. The beam polarization obtained was 70-80% for the spin-up beam, and 45-55% for the spin-down beam.

An example of the measured DDX including ^{11}B(p,p'x) and ^{10}B(p,p'x) reactions is shown for the laboratory angle of 90° in Fig.1. All the measured DDX spectra for the setting angles from 20° to 160° will be available elsewhere. Contribution from contaminated elements in the target and the edge scattering at the slit in front of the counter telescope are not corrected in the spectrum. The elastic peaks of ^{11}B and ^{10}B were separated by using a peak fitting program "FOGRAS", so that the counting yields and asymmetries are consistent over the

measured angle region. However, in forward angles of 20° and 30°, the separation was not so good.

The extracted differential cross sections and analyzing powers for elastic scattering from ^{10}B and ^{11}B are shown in Fig.2. Errors are smaller than the sizes of indicated points. The data for inelastic scattering are presented elsewhere. In order to consider the optical potential for these isotopes, the SOM fitting by means of the ECIS88 code was carried out for the present data. In the fitting calculation the data points of 20° for ^{11}B and of 20° and 30° for ^{10}B were not taken into account, because of their ambiguity in the peak separation. The parameter sets of Dave and Gould[5] were used as the initial parameter set of the search in the code, after correction to the Coulomb force. As similarly to Woye et al.[6], the search have been done finally for the parameters including the imaginary part of the spin-orbit term W_{SO}. The final result of the parameter sets is given in Table I. As compared in the figure, the results of SOM fits well reproduce the angular distributions of cross sections and analyzing powers. In the figure, dotted lines (Set 3) indicate the result without the imaginary part of the spin-orbit term. The fit is improved by taking into account the imaginary part.

3. Discussion and summary

It is interesting that W_{SO} were obtained to be a negative small value. Brieva and Rook[7] have estimated theoretically the ratio W_{SO} / V_{SO} is to be - 0.05, if the real and imaginary spin-orbit terms are taken into account in the optical model. The presently obtained values for the ratio are similar (- 0.03 for ^{11}B and - 0.06 for ^{10}B) to the proposed one. Since the optical potential for the 1p-shell nuclei is very important for the nuclear data calculation and evaluation, consistent SOM fit calculations are necessary for our data of $^{6,7}Li$, $^{10,11}B$, ^{12}C, ^{14}N, and ^{16}O. Further measurements will be also needed with enriched targets of ^{9}Be, $^{10,11}B$, and ^{13}C etc. for the study of optical potentials for light nuclei.

References

[1] N. Koori et al., JAERI-M 89-167 (1989), JAERI-M 91-009 (1991), JAERI-M 92-029 (1992), JAERI-M 94-011 (1994).
[2] Y. Watanabe et al., Proc. 1990 Symp. on Nuclear Data, JAERI-M 91-032 (1991) p.336.
[3] Y. Watanabe et al., Proc. Int. Conf. on Nuclear Data for Science and Technology p.1002 (1991).
[4] Y. Watanabe et al., Proc. XXth Int. Symp. on Nuclear Physics, Nuclear Reaction Mechanism, p.151 (1990).
[5] J.H. Dave and C.R. Gould, Phys. Rev. C **28**, 2212 (1983).
[6] E. Woye et al. Nucl. Phys. **A394**, 139 (1983).
[7] F.A.Brieva and J.R. Rook, Nucl. Phys. **A307**, 493 (1978).

Table I. Optical potential parameters for ^{11}B and ^{10}B at 14 MeV.

	V_R (MeV)	r_R (fm)	a_R (fm)	W_D (MeV)	r_I (fm)	a_I (fm)	V_{SO} (MeV)	W_{SO} (MeV)	r_{SO} (fm)	a_{SO} (fm)
^{11}B	63.44	1.046	0.642	8.41	1.478	0.360	9.63	-0.28	0.828	0.551
^{10}B	57.54	1.193	0.679	16.85	1.384	0.176	3.63	-0.23	1.172	0.478

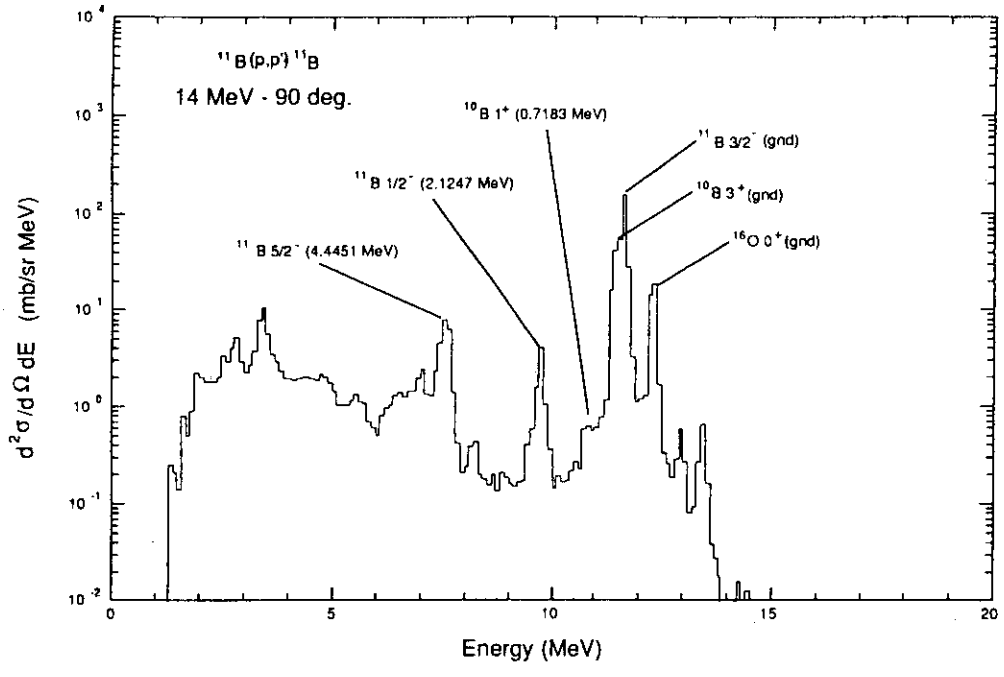

Fig.1. An example of DDX (energy spectrum) of $^{nat}B(p,p'x)$ reaction at 14 MeV. Marked peaks with lines are considered to be analyzes.

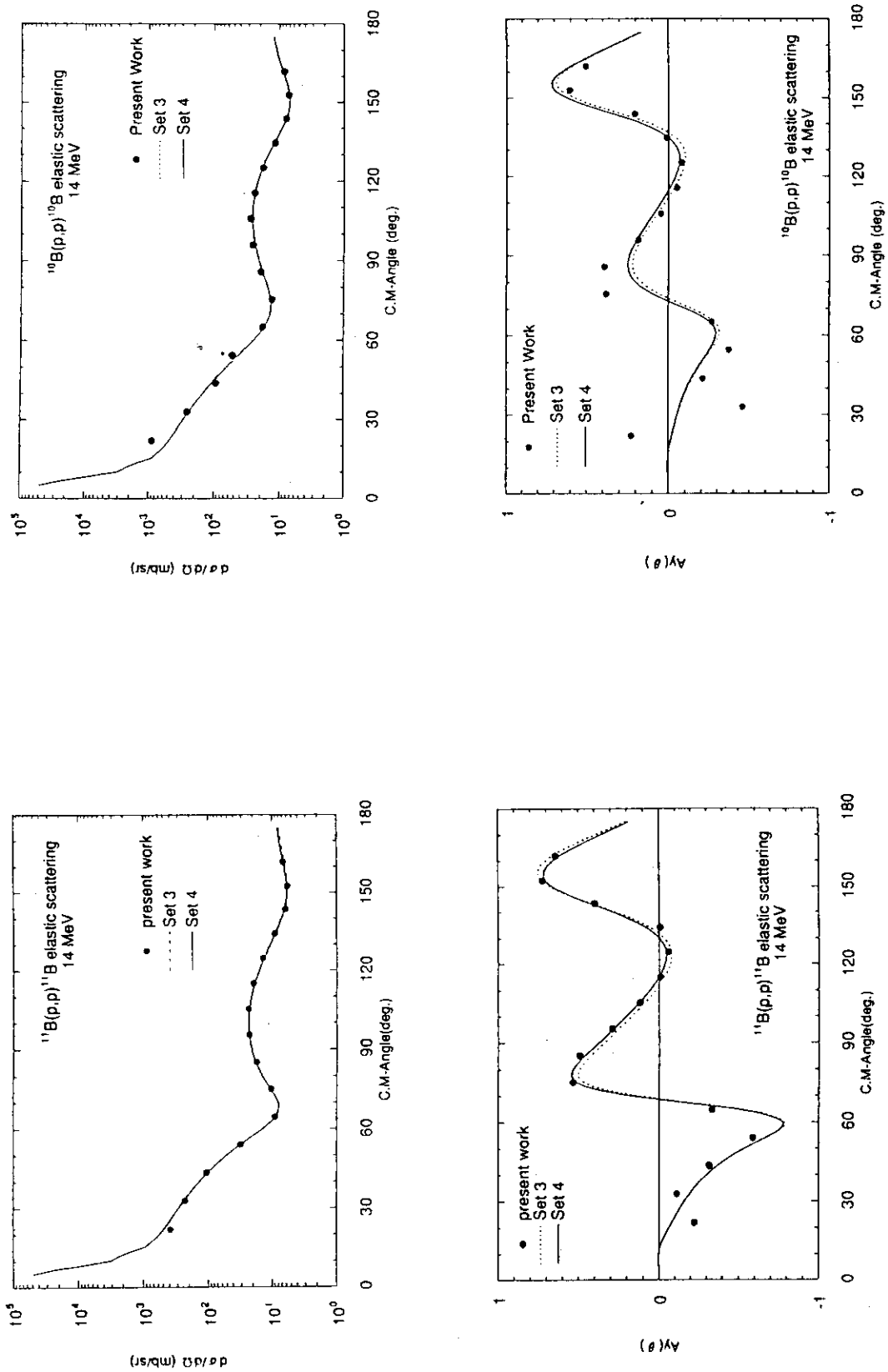

Fig.2. Comparison of experimental differential cross sections and analyzing powers of the ^{11}B(p,p) and ^{10}B(p,p) elastic scattering at 14 MeV with the SOM fits. Solid lines (Set 4) show the result calculated by the parameters given in Table I. See text.

3.13 Benchmark Test of JENDL-3.2 with Pulsed Sphere Experiment using OKTAVIAN

Chihiro ICHIHARA[1], Shu A. HAYASHI[2], Junji YAMAMOTO[3], Itsuro KIMURA[4] and Akito TAKAHASHI[5]

[1]Research Reactor Institute, Kyoto University, Kumatori, Sennan-gun, Osaka 590-04, [2] Institute for Atomic Energy, Rikkyo University, Nagasaka, Yokosuka 240-01, [3] Dep. Engineering, Setsunan University, Neyagawa 572, [4] Dep. Nuclear Engineering, Kyoto University, Yoshida, Kyoto 606-1, [5] Dep. Nuclear Energy., Osaka University, Suita 565

Leakage spectra from sphere piles of 11 elements with incident 14 MeV neutrons were calculated as a benchmark test of newly released JENDL-3.2 nuclear data. The calculation was performed with MCNP Monte Carlo code and was compared with the experimental data taken by using the intense 14 MeV neutron facility, OKTAVIAN. For 10 elements out of 11, JENDL-3.2 prediction gave almost satisfying or preferable result to JENDL-3.1. However, the calculation for W and Co is still far from the experimental spectrum.

Table I Characteristic parameters of the sample piles

Pile	Diam.(cm)	Sample thickness(cm)
Al	40	9.8
Si	60	20.0
Ti	40	9.8
Cr	40	9.8
Mn	61	27.5
Co	40	9.8
Cu	61	27.5
Zr	61	27.5
Nb	28	11.2
Mo	61	27.5
W	40	9.8

Introduction

JENDL-3.2[1], the revised version of JENDL-3[2] was published after few years usage including variety of benchmark test and the design activity for fusion reactors. The present version also needs to be validated by benchmark study using integral experiment. In this paper, we present the compilation of the calculation using MCNP[3] code and FSXLJ3R2[4], the continuous energy library processed from JENDL-3.2. The result was compared with the integral experiment[5] which we had performed using intense neutron facility, OKTAVIAN[6].

1. Experiment

The experiment was performed using an intense 14 MeV neutron facility, OKTAVIAN at Osaka university. Neutron leakage spectra from various sphere piles were measured by means of Time-of-flight method. The neutron measurement was done with an NE-218 liquid scintillator, 12.5 cm in diameter and 5 cm long. The

detector was located 11 m from the tritium target. A polyethylene-iron collimator was put between the tritium target and the neutron detector to reduce the backbround neutrons. In the **Table-1,** measured sample piles are listed.

2. Calculation

The calculation of the leakage neutron spectra was performed except for As and Se as both data are absent in JENDL-3.2. A continuous energy Monte Carlo code MCNP and FSXLJ3R2[5] library processed from JENDL-3.2 were used for the calculation. The **Fig.1** shows their result. It also includes the calculation using FSXLIB-J3 library processed from JENDL-3.1 for the comparison.

3. Result

Out of 11 elements, the JENDL-3.2 calculation for Si, Cr, Mn, Cu, Zr, Nb and Mo gave almost satisfying result. For Al and Ti, JENDL-3.2 gave more or less better prediction than the JENDL-3.1 calculation. For Co and W, however, there exists large discrepancy between the JENDL-3.2 calculation and the experiment.

References

1) Y.Kikuchi: *JENDL-3 rev.2 -JENDL-3.2-*: Proc. International meeting on Nuclear Data for Science and Technology at Gatlinberg (1994) (to be published)
2) K.Shibata et al.: "*Japanese Evaluated Nuclear Data Library, version-3 - JENDL-3 -*", JAERI 1319 (**1990**)
3) J.F.Briesmeister, ed.: *MCNP-A General Monte Carlo Code for Neutron and Photon Transport version 3A*: LA-7396-M, rev.2
4) K.Kosako et al.: (to be published in JAERI-M)
5) C.Ichihara et al. (Edited by the *Sub Working Group of Fusion Reactor Physics Subcommittee*): *Collection of Experimental Data for Fusion Neutronics Benchmark*: JAERI-M 94-014 (**1994**)
6) K.Sumita et al.: *Proc. 12th SOFT*, Vol. 1 (**1982**)
4) K.Kosako et al.: *"FSXLIB-J3: MCNP Continuous Energy Cross Section Library Based on JENDL-3*", JAERI-M 91-187 (**1991**)

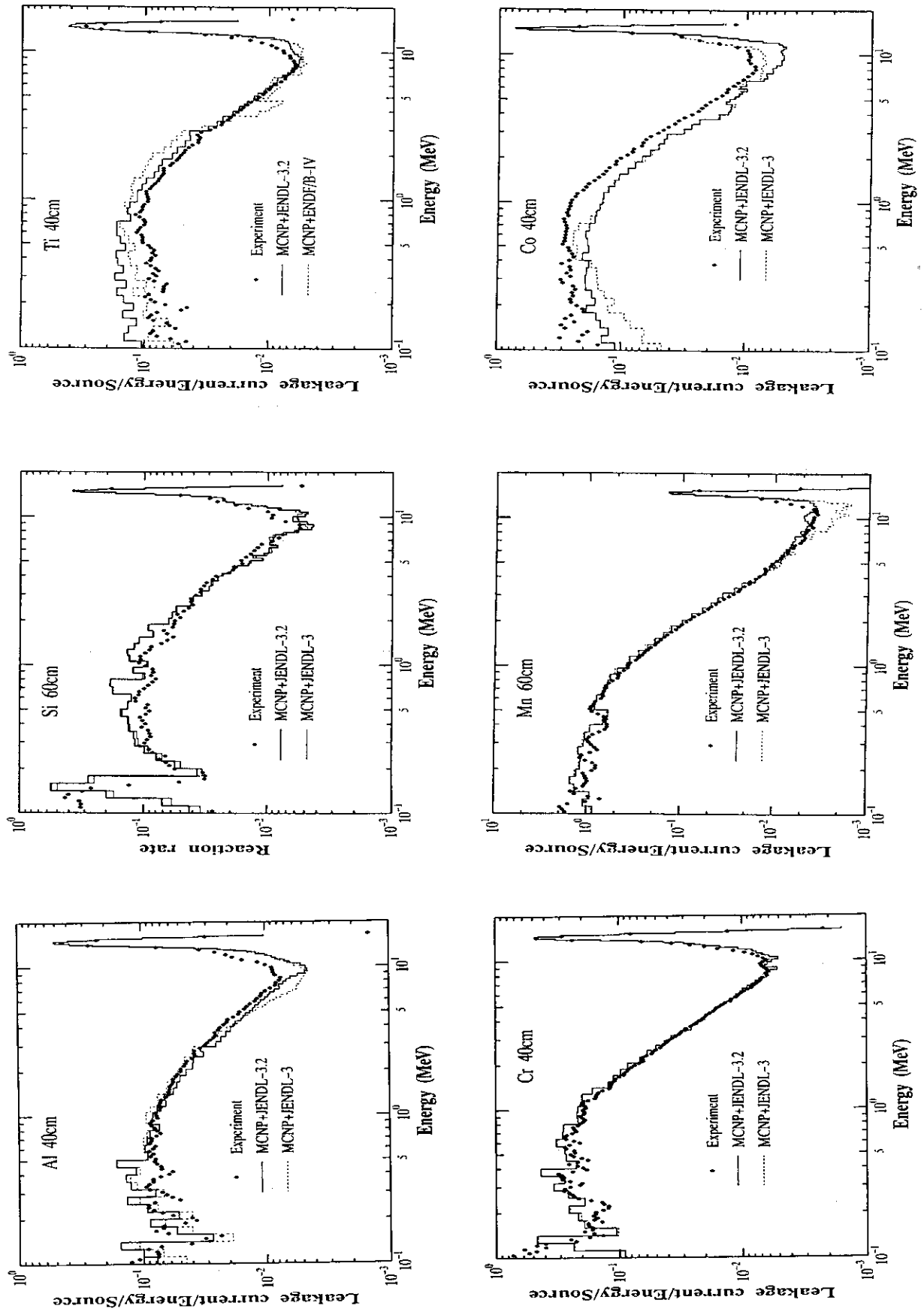

Fig.1(a) Calculated and measured spectra for Al, Si, Ti, Cr, Mn and Co

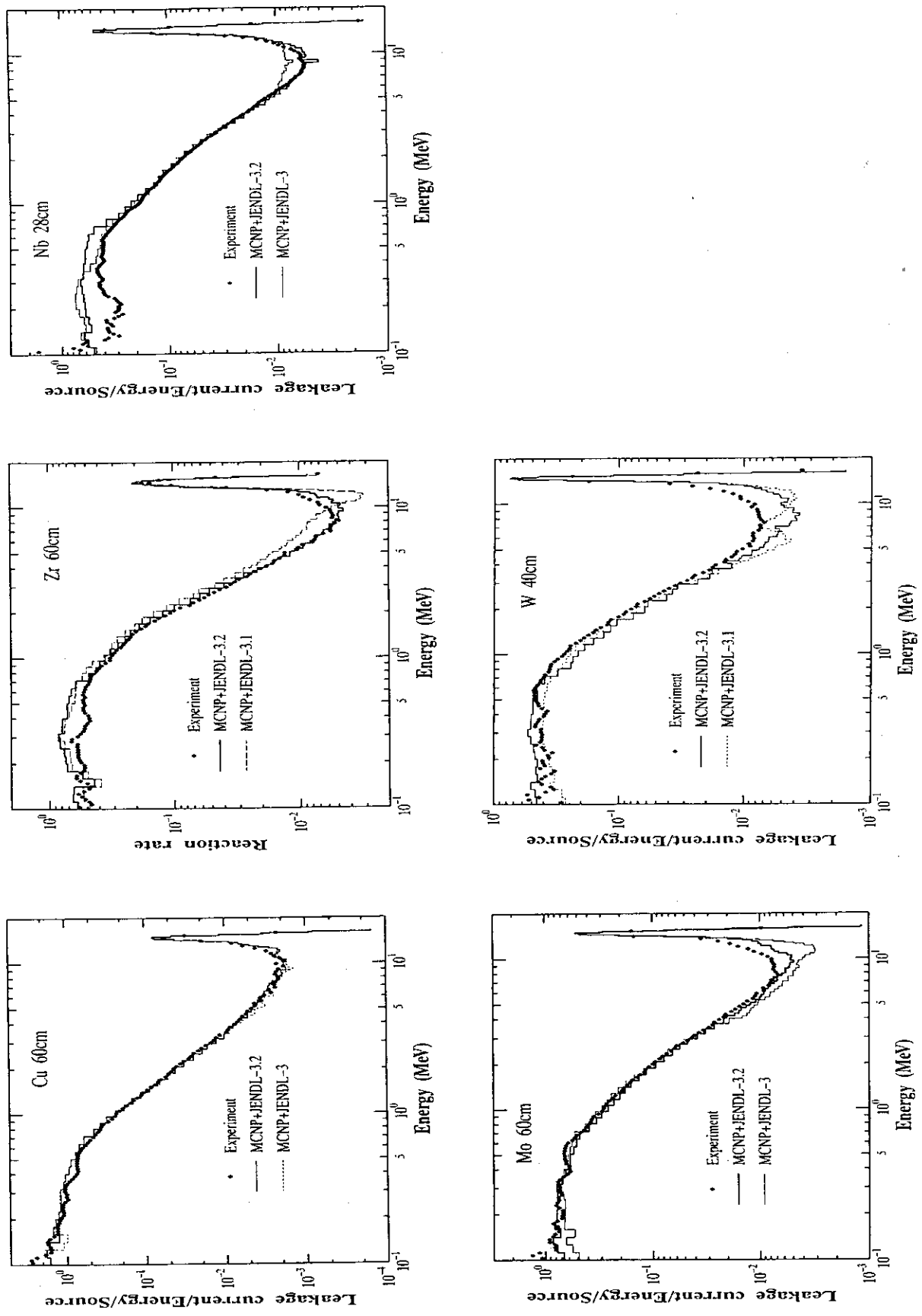

Fig.1(b) Calculated and measured spectra for Cu, Zr, Nb, Mo and W

3.14 Suprathermal Fusion Reactions in Laser-imploded D-T Pellets: Applicability to Pellet Diagnosis and Necessity of Nuclear Data

Y.Tabaru[1], Y.Nakao[1], H.Nakashima[2], K.Kudo[1]
[1]*Department of Nuclear Engineering, Kyushu University, Hakozaki, Fukuoka 812, Japan*
[2]*Department of Energy Conversion Engineering, Kyushu University, Kasuga, Fukuoka 816, Japan*

Abstract

The suprathermal fusion reaction is examined on the basis of coupled transport/hydrodynamic calculation. We also calculate the energy spectrum of neutrons bursting from DT pellet. Because of suprathermal fusion and rapid pellet expansion, these neutrons contain fast components whose maximum energy reachs about 40MeV. The pellet ρR diagnosis by the detection of suprathermal fusion neutrons is discussed.

1.Introduction

In inertial confinement fusion (ICF) plasmas, fusion-born neutrons interact to some extent with the plasma and create new energetic ions by recoil. Some of the recoil ions can undergo fusion during slowing down(*i.e.*, suprathermal fusion) with the background ions (B.G. ions). The neutrons emitted from the suprathermal fusions contain high energy components (11MeV $\leqq E_n \leqq$ 30MeV), because the recoil ions introduce thier kinetic energy into these reactions.

Welch, *et al.* [1] showed that the ratio of "suprathermal" to "primary" fusion neutrons, *i.e.*, the suprathermal fusion probability, gives the information about the fuel density-radius products (ρR) of pellets. Therefore, they pointed out that the detection of high energy neutrons from the pellets is useful for fuel ρR diagnosis. In actual ICF pellets, however, the energy spectrum of burst neutrons becomes more broadened, because the fusion reactions occur during rapid expansion of imploded DT pellets. For the purpose of obtaining useful data for pellet ρR diagnosis, we must take into account the effect of medium expansion.

In this paper, we examine the suprathermal fusion reactions in laser-imploded DT pellets and calculate the realistic enegy spectrum of burst neutrons from the pellets, on the basis of coupled transport/hydrodynamic calculation. We also discuss the realtion between the high energy components of neutron energy spectrum and the pellet ρR.

2.Method of Calculation

2.1 Transport calculation

We use the simultaneous neutron/recoil-ion transport model formulated by Nakao, *et al* [2]. In this model, transport equations are described in the modified Eulerian coordinate[3], *i.e.*, the energy and angular variables are defined in terms of the velocity relative to the medium.

The transport equation for neutrons is the Boltzmann equation; the source neutrons come not only from thermal fusions but also from suprathermal ones. Neutron interactions we

consider are elastic scattering and D break-up reaction. The cross-sections for these processes are given by Seagrave, *et al* [4]. The fundermental equation to describe the transport of recoil ions and alpha particls is the Boltzmann-Fokker-Planck equation. Coulomb scattering and DT suprathermal fusion are taken into acount as the interactions between recoil ions and B.G. ions. The cross section for DT fusion reaction is taken from Duane [5] and is averaged over the velocity distribution of B.G. ions.

We coupled these transport routines for neutrons and charged particles to one-dimensional hydrodynamic code, MEDUSA [6].

2.2 Implosion-burn simulation

For analysis of the suprathermal fusion, we use a reactor-grade pellet model taken from conceptual ICF reactor design, KOYO [7]. **Figure 1** illustrates the configuration and composition of the pellet. This pellet is irradiated by tailored pulse, *i.e.*, a prepulse and a following main pulse; the wave length of laser is taken as 0.35 μ m.

At first, we carry out the implosion simulation for this pellet, using the one-dimensional hydrodynamics code ILESTA-1D [8]. In the implosion simulation, neutron interactions are neglected. The temperature, density and hydrodynamic velocity distributions of the medium obtained around the final stage of implosion are used as the imput of the initial state for the burn simulation carried out with the MEDUSA code.

Examination is also given on the ρR dependence of suprathermal fusion resctions for the various values of laser energy E_L (E_L=2.35～3.35MJ).

3.Results and Discussion

The ρR value of burning DT pellet changs momentarily. Therefore, we use two values representing the ρR. One is the maximum ρR attained (ρR_{max}), and the other is the burn-averaged ρR ($<\rho R>$) definited as follows:

$$<\rho R> \equiv \frac{\int_0^\tau \rho R(t)\, R_F(t)\, dt}{\int_0^\tau R_F(t) dt}$$

where R_F is the rate of fusion reactions in the pellet and τ is the implosion-bum time.

Figure 2 shows the suprathermal fusion probability as a function of the ρR of pellets. In the reactor-grade pellet such as KOYO model, the probability is 1～2%. We can observe a linear dependence of the probability on the $<\rho R>$ of pellets. On the other hand, the dependence of probability on the ρR_{max} of pellets is not linear. Therefore, the detection of suprathermal fusion neutrons is useful for $<\rho R>$ diagnosis and not useful for ρR_{max} one.

Figure 3 represents time-integrated energy spectrum of neutrons bursting from burning DT pellet imploded by 3.35-MJ laser. The energy variable is now written in terms of the neutron velocity in the rest frame. The burst neutrons contain the high energy components whose maximum energy exceeds 40MeV. These high-energy neutrons are produced, when the

suprathermal fusion reactions occur during rapid expansion of DT pellet and emit neutrons in the same direction as the medium expansion velocity. On the other hand, the maximum energy of neutrons emitted from thermal fusions is about 21MeV. Therefore, it is possible to detect high-energy neutrons emitted only from the suprathermal fusions, if we use a neutron activation reaction whose threshold energy is above 21MeV.

Here, we propose to detect the high energy neutrons as above by the following activation reaction,

$$^{23}\mathrm{Na} \xrightarrow[E_n \geqq 23.5\mathrm{MeV}]{(n,3n)} {}^{21}\mathrm{Na} \xrightarrow[t^{1/2}=22.5\mathrm{s}]{\beta\text{-decay}} {}^{21}\mathrm{Ne}\,.$$

The relations between the ratio of the number of high-energy neutrons, $N(E_n \geqq 23.5MeV)$, to the number of total neutrons, N_t, and pellet ρR are estimated and plotted in **Fig.4**. This figure shows that it may be possible to know the pellet $<\rho R>$ by the detection of β-decay of ^{21}Na and by the estimation of the ratio $N(E_n \geqq 23.5MeV) / N_t$. For example, if the ratio is 0.0002, $<\rho R>$ could be estimated to be 2.15 g/cm^2.

4.Concluding Remarks

We have examined the suprathermal fusion reactions in laser-imploded DT pellet, on the basis of transport/hydrodynamic calculation. The energy spectrum of neutrons bursting from DT pellet is fairly broadened and contains the high energy components whose energy reachs about 40MeV. We have also shown that it may be possible to know the pellet $<\rho R>$ using the ^{23}Na foil activated by the suprathermal fusion neutrons.

In the pellet currently adopted for implosion or ignition experiment, however, it is expected that the neutron yield is not so sufficient as to activate the ^{23}Na foil. Therefore, in such a pellet, we have to detect the suprathermal fusion neutrons by the activation reaction whose threshold energy is lower, for example, than that of ^{23}Na. The determination of the most suitable method for each pellet to detect suprathermal fusion neutrons needs calculations for various-sized pellets and the cross-sections for activation reactions (*e.g.* ^{23}Na$(n,3n)$).

References

[1] D.R.Welch, *et al.*, *Rev.Sci.Instrum.*, **59**(1988)610.

[2] Y.Nakao, *et al.*, *J.Nucl.Sci.Technol.*, **30**[1](1993)18.

[3] B.R.Wienke, *Phys. Fluids.*, **17**(1974)1135.

[4] J.D.Seagrave, *et al.*, *Ann. Phys.*, **74**(1972)250.

[5] B.H.Duane, BNWL-1685, Richmond, WA(1972).

[6] J.P.Christiansen, *et al.*, MEDUSA; A one-dimensional laser fusion code, *Comput. Phys.Commun.*, **7**(1974)271.

[7] H.Takabe, *et al.*, : *Emerging Nuclear Energy Systems 1993 (Proc. 7th Int. Conf. Chiba, 1993)*, 76(1994), World Scientific, Singapore.

[8] H.Takabe, *et al.*, : *ILE Research Report, ILE*−8713(1987).

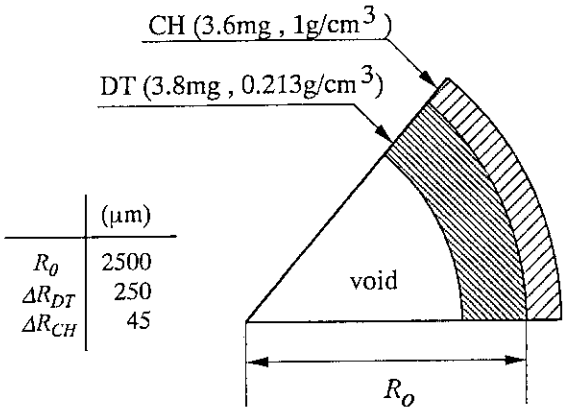

Fig. 1 Initial configuration of pellet for the implosion simulation

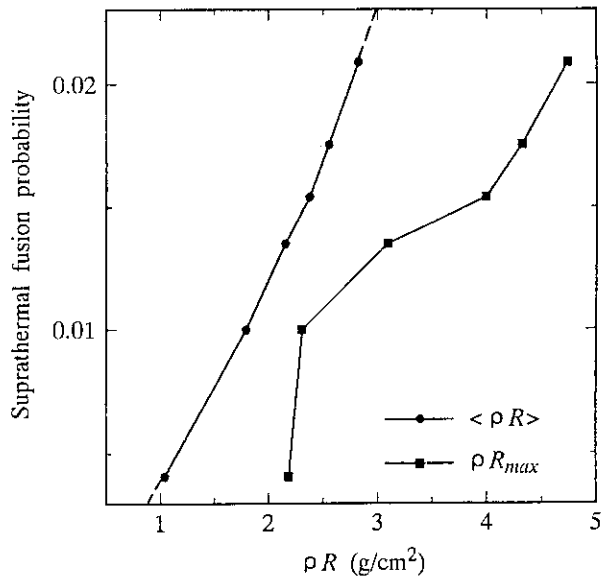

Fig.2 The suprathermal fusion probability as a function of pellet ρR

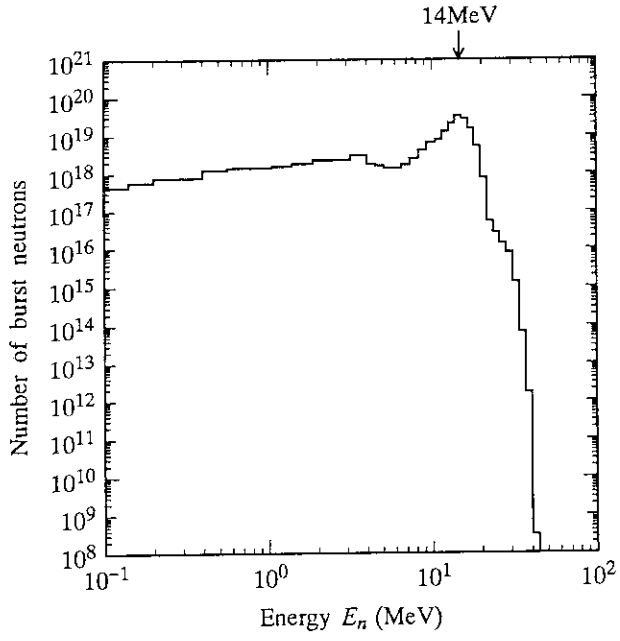

Fig. 3 Time-integrated energy spectrum of neutrons bursting from a laser-imploded DT pellet (E_L=3.35MJ)

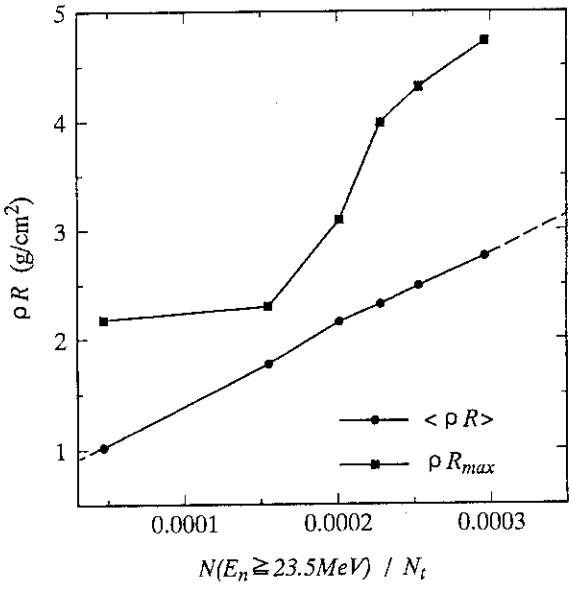

Fig. 4 The relation between the fraction of high energy neutrons and pellet ρR

3.15 Systematics of Activation Cross Sections for 13.4 - 15.0 MeV Neutrons

Y. Kasugai, Y. Ikeda*, H. Yamamoto**, and K. Kawade**

Department of Nuclear Engineering, Nagoya University
**Department of Reactor Engineering, Japan Atomic Energy Research Institute*
***Department of Energy Engineering and Science, Nagoya University*

The cross sections at 14.0 MeV and the relative slopes for the (n, p) and (n, α) reactions were expressed by simple formulae. We could reproduce the excitation functions for the (n, p) and (n, α) reactions in the energy range between 13.4 to 15.0 MeV within the accuracy of ±25% and ±30%, respectively. The present formulae are also useful for check of the decay data.

1. Introduction

The systematics of the cross sections of the (n, p) and (n, α) reactions at around 14 MeV has been studied, and some empirical formulae describing the systematics have been proposed. However there have been a few empirical formula which are available in low mass region (A<40) and no empirical formula to describe the excitation functions. We propose a new empirical formula describing the gross trend of the excitation functions for the (n, p) and (n, α) reactions at 13.4–15.0 MeV.

2. Systematics

We use the data set obtained with the unified activation method using the intense neutron sources of OKTAVIAN (Osaka University) and FNS (JAERI)[1]-[8]. The cross section data were fitted to linear functions as $\sigma=m(E_n-14.0)+\sigma_{14}$, where σ is the cross section in mb, E_n is the neutron energy in MeV, m is the slope of the excitation functions and σ_{14} is the cross section at 14.0 MeV. We express the relative slopes ($m_r=m/\sigma_{14}\times100$) and the cross sections at 14.0 MeV (σ_{14}) by simple formulae.

The relative slopes (m_r) for the (n, p) reactions are plotted as a function of $s=(N-Z)/A$, where A, Z and N are mass number, atomic number and neutron number, respectively, in Fig. 1. The values of m_r strongly depends on the asymmetry parameters(s). The best fitting function is expressed as

$$m_r(\%/MeV)=-19.1+137.8s+1207s^2 \qquad (1)$$

and is shown in Fig. 1 with the solid line. The empirical formula of σ_{14} which is available in the wide mass region (A=19–187) is expressed as

$$\sigma_{14}(mb)=1830(N-Z+1)\exp(-50.7(N-Z+1)/A). \qquad (2)$$

The values of $\sigma_{14}/(N-Z+1)$ are plotted as a function of $(N-Z+1)/A$ in Fig. 2, and the fitted line is also shown with the solid line.

Similarly the empirical formulae of the m_r and the σ_{14} for (n, α) reactions are obtained as follows;

$$m_r(\%/MeV)=-17.86+275.1s \quad (3)$$

and

$$\sigma_{14}(mb)=409.1\exp(-33.0s). \quad (4)$$

The m_r and σ_{14} for the (n, α) reactions are plotted as a function of s in Fig. 3 and 4, respectively. The fitting functions (3) and (4) are also shown in the figures.

3. Result and Discussion

The distributions of the deviations $((\sigma_{exp}-\sigma_{cal})/\sigma_{cal})$ for the (n, p) and (n, α) reactions in the energy range between 13.4 to 15.0 MeV are shown in Fig. 5 and 6, respectively. Seventy-one percent of the data are between −0.25 and +0.25 for (n, p) reactions, and 72 percent of the data are between −0.3 and +0.3 for the (n, α) reactions. It is concluded that the accuracy of our expressions for (n, p) and (n, α) reactions are ±25% and ±30%, respectively.

The present formulae would be useful for check of the decay data. We illustrate the cross section for ^{66}Zn(n, p)^{66}Cu and ^{69}Ga(n, α)^{66}Cu reactions in Fig. 7. The 1039 keV γ-ray emission probability (I_γ) of ^{66}Cu was evaluated to be (7.4±1.9)% in ref. 9. Recently the emission probability was precisely measured[10] to be (9.23±0.09)%, and the cross sections have been arranged to be smaller values by 25%. These newly arranged values show better agreement with the calculated values in comparison with the old values. Some of the deviations might be due to the used decay data.

References

(1) Katoh, T., et al.: JAERI-M 89-083 (1989) (in Japanese).
(2) Kawade, K., et al.: JAERI-M 90-171 (1990).
(3) Kawade, K., et al.: JAERI-M 92-020 (1992).
(4) Kasugai, Y., et al.: JAERI-M 93-124 (1993).
(5) Kasugai, Y., et al.: to be published in J. Nucl. Sci. Technol.
(6) Ikeda, Y., et al.: JAERI 1312 (1987).
(7) Konno, C., et al.: JAERI 1329 (1993).
(8) Kasugai, Y, et al.: Proc. Int. Conf. on Nuclear Data for Science and Technology, Gatlinburg, USA (1994).
(9) Browne, E., Firestone, R. B. and Shirley, V. S.: "Table of Radioactive Isotopes", John Wiley & Sons, New York (1986).
(10) Miyahara, H., et al.: Nucl. Instrum. and Methods, A324, 219 (1993).

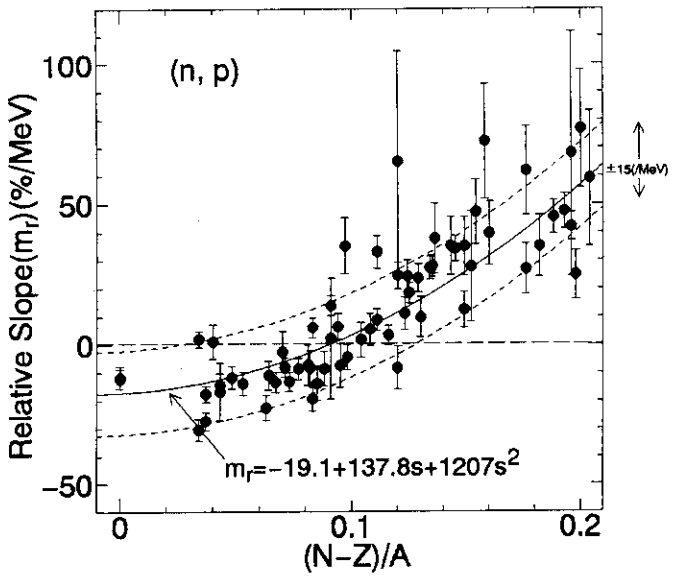

Fig. 1 The relative slopes (m_r) for the (n, p) reactions are plotted as a function of $(N-Z)/A$.

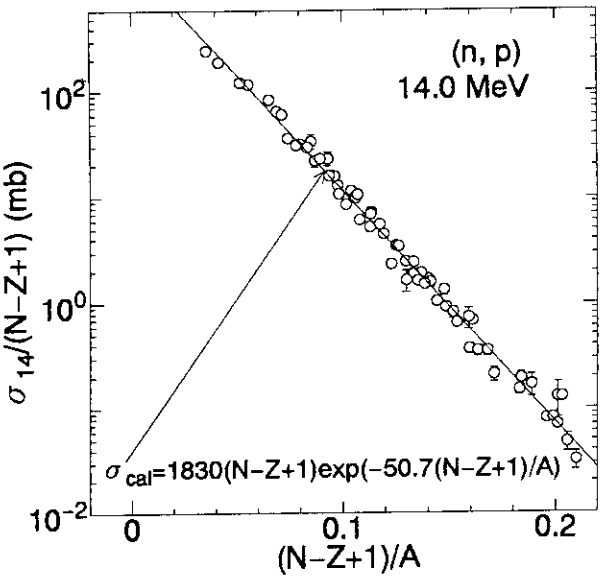

Fig. 2 The values of $\sigma_{14}/(N-Z+1)$ for the (n, p) reactions are plotted as a function of $(N-Z+1)/A$.

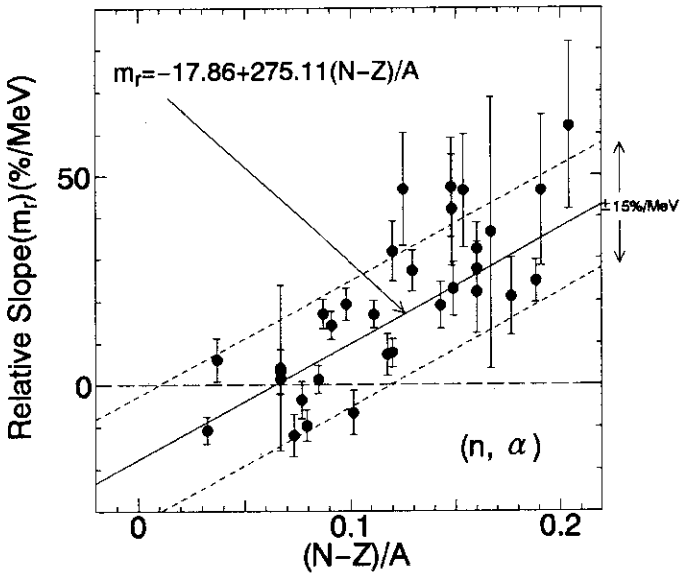

Fig. 3 The relative slopes (m_r) for the (n, α) reactions are plotted as a function of $(N-Z)/A$.

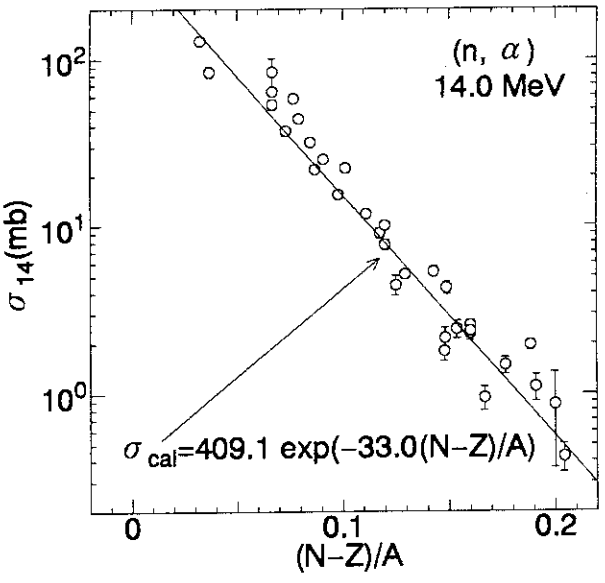

Fig. 4 The values of σ_{14} for the (n, α) reactions are plotted as a function of $(N-Z)/A$.

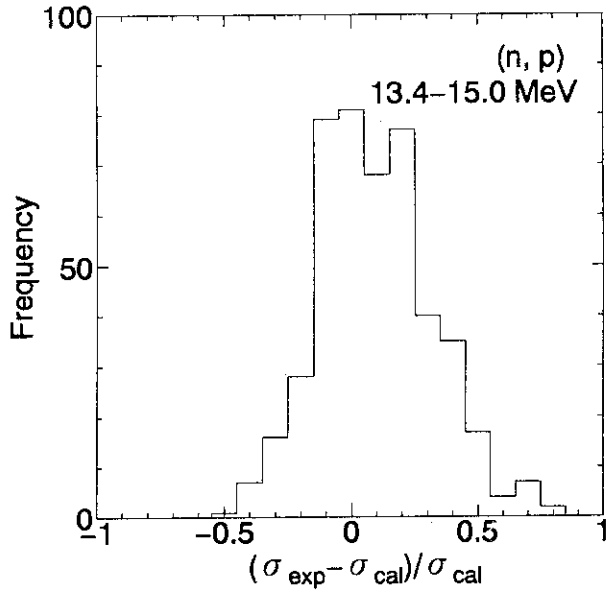

Fig. 5 The distribution of the deviations $((\sigma_{exp}-\sigma_{cal})/\sigma_{cal})$ for the (n, p) reactions in the energy range between 13.4 to 15.0 MeV.

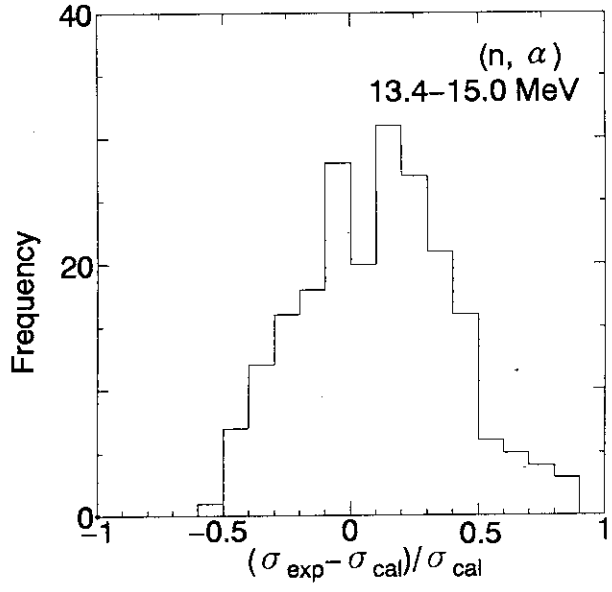

Fig. 6 The distribution of the deviations $((\sigma_{exp}-\sigma_{cal})/\sigma_{cal})$ for the (n, α) reactions in the energy range between 13.4 to 15.0 MeV.

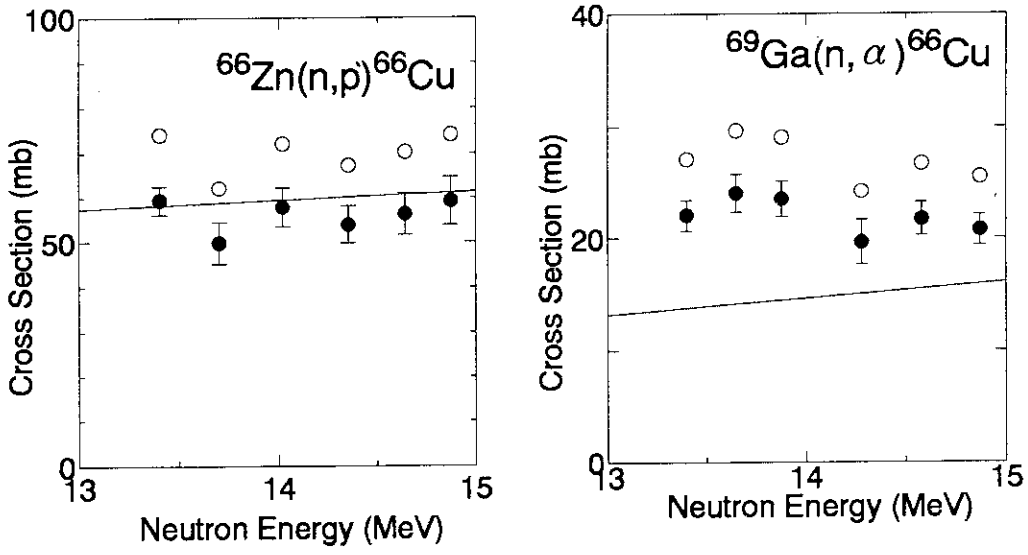

Fig. 7 The cross sections of ^{66}Cu(n, p)^{66}Zn and ^{69}Ga(n, α)^{66}Cu. The closed circles (●) show the experimental data deduced by using the new data of emission probability for ^{66}Cu [10]. The open circles (○) show the experimental data deduced by using the old data [9]. The solid lines are calculated excitation functions.

3.16 Measurement of Beta-decay Half-lives of Short-lived Nuclei by Using High-rate Spectroscopy Amplifier

S. Itoh, M. Yasuda, H. Yamamoto, *T. Iida, *A. Takahashi
and K. Kawade
Department of Energy Engineering and Science, Nagoya University
Furo-cho, Chikusa-ku, Nagoya, 464-01, Japan
*Department of Nuclear Engineering, Osaka University
Yamadaoka, Suita-shi, Osaka, 565, Japan

Abstract

The half-lives of short-lived nuclei produced by 14 MeV or thermal neutron bombardments were measured with Ge detectors and a High-Rate Spectroscopy Amplifier(EG&G ORTEC Model 973) in the multi-scaling mode. The corrections for pile-up and dead-time losses were performed by applying source and pulser methods. The half-lives of ^{16}N, ^{20}F, ^{19}O, ^{63}Co, ^{89m}Y, ^{118m}In, ^{139m}Ce, ^{161}Gd, ^{173}Er, ^{176}Tm, ^{185m}W and ^{186}Ta were determined with accuracy of 0.08 $\sim$ 1.2 % and the accuracy has been much improved.

1 Introduction

The half-life of β-decay is one of the most fundamental constants on radioactive isotopes. In the activation cross section measurements, the uncertainty brings a strong effect to the results. Most of the values previously published were obtained with GM counters, ionization chambers, proportional counters and scintillation counters. In order to improve the precision and reliability of the half-lives of short-lived nuclei ($T_{1/2}$ = 11 s $\sim$ 10 min), Ge detectors were used, and to measure at high counting rate, the High-Rate Spectroscopy Amplifier was used for the present work.

2 Experiment

The γ-rays were measured with ORTEC 22 % Ge detector and PGT LEPS(Low Energy Photon Spectrometer, crystal size of 50 mm$^{\phi}$ $\times$ 10 mm^{t}) in the spectrum multi-scaling mode. Decay was followed for about 10 times the half-life at equal intervals of 1/3 to 1/4 of half-life. A long-lived γ source and a constant-pulser were simultaneously measured together with the short-lived activity for the correction of the pile-up and the dead time losses (source method, pulser method). In Fig.1, the variation of peak intensity ratios of ^{60}Co and pulser. The ratios are constant when counting rates is less than 9.0$\times$10^{4} cps by

using the High-Rate Spectroscopy Amplifier. So the initial counting rate could be always kept about ten times higher than our previous method [1]. The detailed procedures are described elsewhere [1]. Sources of ^{16}N, ^{20}F, ^{63}Co, ^{118m}In, ^{139m}Ce, ^{173}Er, ^{176}Tm, ^{185m}W and ^{186}Ta were produced by 14 MeV neutron bombardment at OKTAVIAN of Osaka University. Sources of ^{19}O and ^{89m}Y were produced by 14 MeV neutron bombardment at 3.75 MeV Van de Graaff accelerator of Nagoya University. Source of ^{161}Gd were produced by thermal neutron irradiation at TRIGA-II reactor of Rikkyo University(100 kW).

3 Results

A decay curve of ^{161}Gd is shown in Fig.2. The results are summarized in Table 1 together with production reactions, γ-rays, reference sources, number of measurement, measured and previous values [2]. In Fig.3, the result is compared with previous works. The present result has shown good agreement with previous works, and the accuracy has been much improved. In Fig.4, relative deviations of previous values from the present ones are shown. It is clearly seen that previous values [3] shorter than about 10 min deviate systematically and those become larger as the half-lives become shorter. The cause might result from insufficient correction for pile-up and dead time losses. It is likely to start measurements at too high counting rates in order to get good statistics. If the corrections at high counting rates are not enough, the decay curve will show a longer half-life compared with the true value.

4 Summary

The half-lives of short-lived nuclei were determined with accuracy of 0.08 $\sim$ 1.2 %. By using the High-Rate Spectroscopy Amplifier, the initial counting rate(9.0×10^4 cps) could be always kept about ten times higher than our previous method. Previous values shorter than about 10 min deviate systematically and those deviations become larger as the half-lives become shorter.

References

[1] M. Miyachi et al., Nucl. Data for Sci. and Tech., 897(1988,Mito)

[2] E. Browne et al., *Table of Radioactive Isotopes*, (1986) John Wiley & Sons, New York

[3] C. M. Lederer and V. S. Shirley, *Table of Isotopes 7th Ed.*, (1978) John Wiley & Sons, New York

Table 1 Results of half-life measurement.

Nuclide	*Production reaction*	E_γ (keV)	*Reference*[a] (E_γ in keV)	*Number of measurement*	*Half-life* *Reference*[b]	*Present*
^{16}N	^{16}O(n,p)	6129.2	^{137}Cs(661.7)	6	7.13(4) s	7.13(3) s
^{19}O	^{19}F(n,p)	197.1	^{57}Co(122.1)	4	26.76(8) s	26.464(9) s
^{20}F	^{23}Na(n,α)	1632.6	^{137}Cs(661.7)	4	11.08(1) s	11.11(4) s
^{63}Co	^{64}Ni(n,np)	87.3	^{241}Am(87.3)	18	27.4(5) s	26.41(27) s
^{89m}Y	^{23}Na(n,n')	909.2	^{137}Cs(661.7)	3	16.06(4) s	15.663(5) s
^{118m}In	^{118}Sn(n,p)	683.4	^{137}Cs(661.7)[c]	4	4.40(5) min	4.364(7) min
		1050.8				
		1229.7				
^{139m}Ce	^{140}Ce(n,2n)	754.2	^{133}Ba(356.0)[c]	15	56.4(5) s	56.54(13) s
^{161}Gd	^{160}Gd(n,γ)	314.9	^{57}Co(122.1)	6	3.7(1) min	3.646(3) min
^{173}Er	^{176}Yb(n,α)	193.1	^{241}Am(87.3)	4	1.4(1) min	1.434(17) min
		199.3				
^{176}Tm	^{176}Yb(n,p)	189.8	^{241}Am(87.3)	4	1.9(1) min	1.853(27) min
^{185m}W	^{186}W(n,2n)	131.5	^{170}Tm(84.3)	15	1.67(3) min	1.597(4) min
		173.7				
		187.9				
^{186}Ta	^{186}W(n,p)	122.4	^{170}Tm(84.3)	6	10.5(5) min	10.390(27) min
		198.1				
		737.7				
		739.6				

a) These source were used for corrections of dead-time and pile-up losses.

b) Taken from ref.2.

c) No pulser was used. Source was only used.

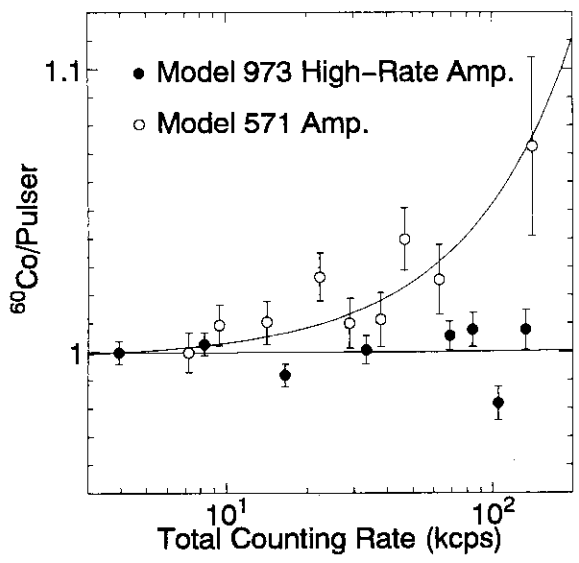

Fig. 1 Peak intensity ratios of ^{60}Co and pulser.

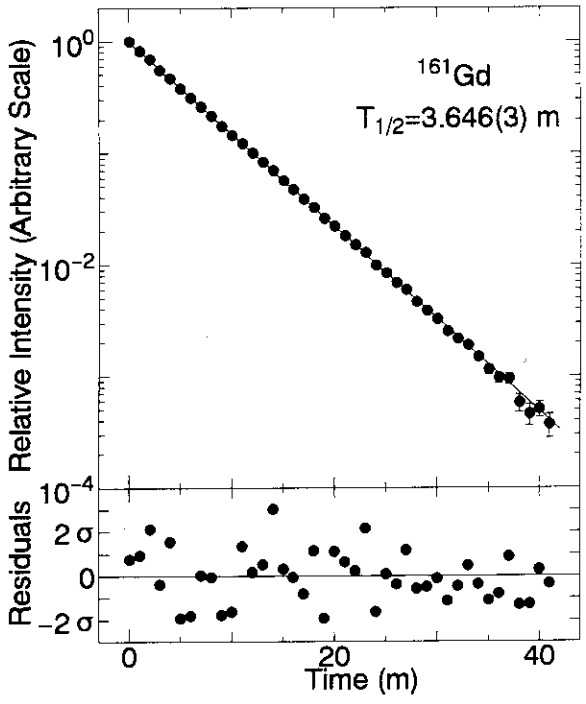

Fig. 2 Decay curve of ^{161}Gd and residuals from a least squares fitting analysis.

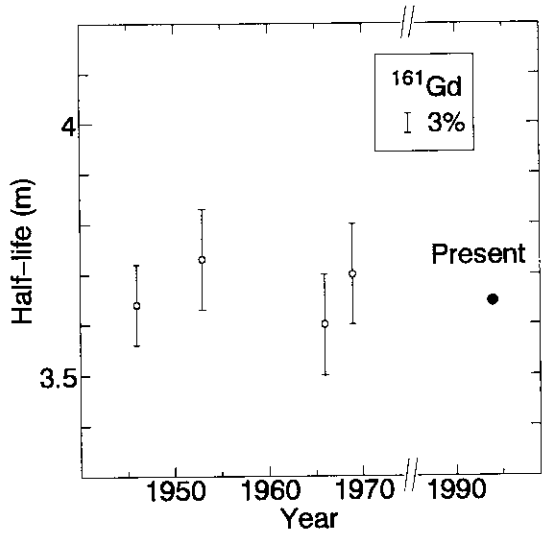

Fig. 3 Comparison with previous works taken from ref. 3.

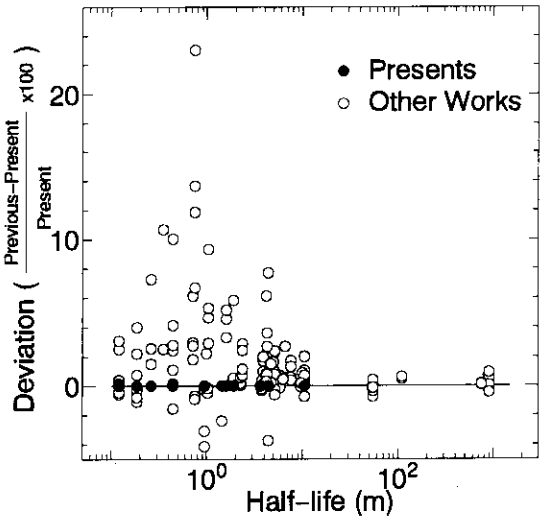

Fig. 4 Deviation of previous half-life values from the present.

3.17 Measurement of Formation Cross Sections Producing Short-lived Nuclei by 14 MeV Neutrons - Na, Si, Te, Ba, Ce, Sm, W, Os -

Y. Satoh, T. Matsumoto, Y. Kasugai, H. Yamamoto*,
T. Iida**, A. Takahashi**,and K. Kawade*
Department of Nuclear Engineering, Nagoya University
*Department of Energy Engineering and Science, Nagoya University
**Department of Nuclear Engineering, Osaka University

Abstract

13 neutron activation cross sections for (n,2n), (n,p), (n,np) and (n, α) reactions producing short-lived nuclei with half-lives between 4 s and 19 min were measured in the energy range from 13.7 MeV to 14.9 MeV for Na, Si, Te, Ba, Ce, Sm, W and Os. The cross sections of ^{123}Te(n,np)^{122m}Sb, ^{188}Os(n,p)^{188m}Re and ^{189}Os(n,np)^{188m}Re were measured for the first time. Measured (n,p) cross sections were compared with the excitation functions estimated by our systematics. Estimated excitation functions agreed well with experimental data.

1. Introduction

We have measured activation cross sections of short-lived nuclei by 14 MeV neutrons at the Intense 14 MeV Neutron Source Facility (OKTAVIAN) of Osaka University. Cross sections for the (n,2n), (n,p), (n,np) and (n, α) reactions leading to short-lived nuclei with half-lives between 4 s and 20 min were measured in a qualified experimental condition[1),2),3),4)].

In this work we measured 13 cross sections of short-lived nuclei ($T_{1/2}$= 4 s-19 min) at neutron energy from 13.7 to 14.9 MeV by activation method.

2. Experiments

Experiments were carried out at OKTAVIAN. A pneumatic sample transport system was used for the irradiation of samples. The angles of the irradiation position to the d^+ beam were 0° , 55° , 75° , 105° and 125° , which covered the neutron energies ranging from 14.9 to 13.7 MeV. The distance between the T-target and the irradiation position was 15 cm. When high neutron flux was required, an additional tube set at 0° and at 1.5 cm was set. The induced activity were measured by 12% and 16% HPGe detectors at an equivalent distance at 5 cm. The neutron flux at the irradiation position was measured by using substandard ^{27}Al(n,p)^{27}Mg ($T_{1/2}$=9.462 min) reaction, whose cross sections were determined by referring to the ^{27}Al(n, α)^{24}Na reaction (ENDF/B-V). The samples were sandwiched between two aluminum foils of 10 mm × 10 mm × 0.2 mm thick. The effective energy of incident neutron at the irradiation position was determined by the ratio of the ^{90}Zr(n,2n)^{89}Zr and ^{93}Nb(n,2n)^{92m}Nb cross sections (Zr/Nb method[5)]). The errors in the neutron energy were estimated to be about 90 keV. Mass separated isotopes and samples of natural abundance were used as samples. Powder samples were wrapped in powder papers (size: 10 mm × 10 mm and about 1 mm thick).

In Table. 1, measured reactions and associated data[6)] of the half-lives ($T_{1/2}$), the γ-ray energy (E_γ) and the absolute intensity in photons per disintegration (I_γ) are listed together with the Q-value.

Corrections were made for time fluctuation of neutron flux, thickness of samples, self absorption of γ-ray, sum-peak effect of γ-ray and contribution of low energy neutrons below 10 MeV. The details of the correction are described elsewhere[1),2),3),4)].

The total errors (δ_t) were described by combining the experimental errors (δ_e) and the errors of nuclear data (δ_r) in quadratic : $\delta_t^2 = \delta_e^2 + \delta_r^2$. Accuracy of the obtained cross sections were around 4.5% in case of good statistics.

3. Results

Numerical data table of cross sections are given in table. 2 and the example of graphs is given in Fig. 1 together with data reported previously. The cross sections of ^{123}Te(n,np)^{122m}Sb, ^{188}Os(n,p)^{188m}Re and ^{189}Os(n,np)^{188m}Re were measured for the first time. The obtained (n,p) cross sections were compared with the excitation functions estimated by our systematics[7)]. The example of them is given in Fig. 2. As shown in the figure, the excitation functions estimated by our systematics agreed well with the present experimental data.

4. Summary

Neutron activation cross sections were measured for 13 reactions producing short-lived nuclei in the neutron energy from 13.7 to 14.9 MeV for Na, Si, Te, Ba, Ce, Sm, W and Os. The cross sections of ^{123}Te(n,np)^{122m}Sb, ^{188}Os(n,p)^{188m}Re and ^{189}Os(n,np)^{188m}Re were measured for the first time. The excitation functions estimated by our systematics were shown good agreement with the obtained (n,p) cross sections.

References

1) T. Katoh et al.: JAERI-M 89-083 (1989) (in Japanese).
2) K. Kawade et al.: JAERI-M 90-171 (1990).
3) K. Kawade et al.: JAERI-M 92-020 (1992).
4) Y. Kasugai et al.: JAERI-M 93-124 (1993).
5) V.E. Lewis et al.: Nucl. Instr. Meth. 174, 141 (1980).
6) E. Browne et al.: "Table of Radioactive Isotopes", John Wiley & Sons, New York (1986).
7) Y. Kasugai et al. to be published.

Table 1 Measured reactions and decay parameters.

Reaction	$T_{1/2}$	E_γ(keV)	I_γ(%)	Q(MeV)
^{23}Na(n,p)^{23}Ne	37.24(12) s	439.8	32.9(30)	-3.60
^{30}Si(n,p)^{30}Al	3.60(6) s[b)]	2235.0	65.1(11)	-7.76
^{123}Te(n,np)^{122m}Sb	4.196(8) min[c)]	61.45	57.4(23)	-8.30
^{132}Ba(n,2n)^{131m}Ba	14.6(2) min	108.12	55(2)	-9.99
^{138}Ba(n,2n)^{137m}Ba	2.552(1) min	661.660	90.1(1)	-9.27
^{138}Ba(n,α)^{135m}Xe	15.65(10) min	526.563	81.2(10)	3.35
^{140}Ce(n,2n)^{139m}Ce	56.54(13) s[c)]	754.21	92.5(3)	-9.94
^{140}Ce(n,α)^{137m}Ba	2.552(1) min	661.660	90.1(1)	4.63
^{144}Sm(n,2n)^{143m}Sm	1.10(3) min	754.01	90.0(1)	-10.52
^{144}Sm(n,2n)^{143g}Sm	8.83(2) min	1056.48	1.75(18)	-11.27
^{186}W(n,p)^{186}Ta	10.390(20) min[c)]	198.05	59(10)	-3.11
^{188}Os(n,p)^{188m}Re	18.6(1) min	105.90	10.8(5)	-1.51
^{189}Os(n,np)^{188m}Re	18.6(1) min	105.90	10.8(5)	-7.43
^{27}Al(n,α)^{24}Na[f)]	14.959(4) h	1368.6	99.994(3)	-3.13
^{27}Al(n,p)^{27}Mg[g)]	9.462(11) min	843.8	72.0(4)	-1.83
^{30}Si(n,α)^{27}Mg[g)]	9.462(11) min	843.8	72.0(4)	-1.83

a) Taken from ref. 6.

b) Taken from Nucl. Phys A521, 1.

c) Measured in our previous work.

d) (n,np) means [(n,d)+(n,n'p)+(n,pn)]

e) Q(n,n'p) is given here. Q(n, d)=Q(n,n'p)+2.225MeV.

f) Standard reaction (ENDF/B-V) used in this work.

g) Secondary standard reaction used for short-lived nuclei.

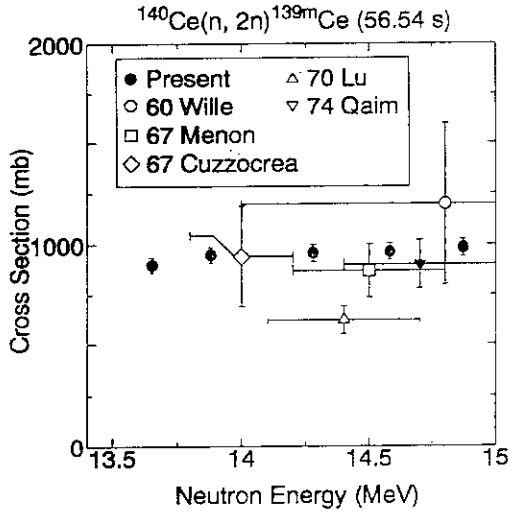

Fig. 1 Cross section of ^{140}Ce(n, 2n)^{139m}Ce.

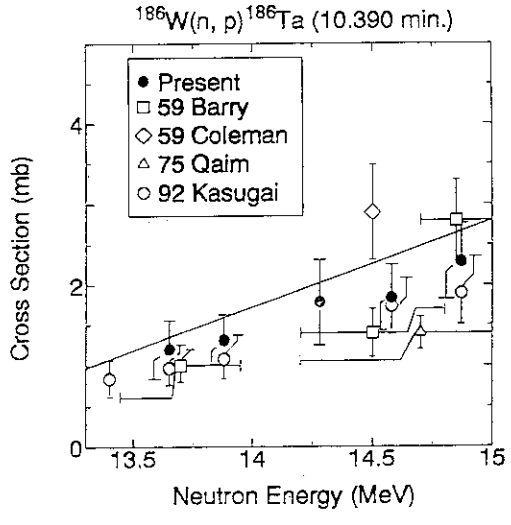

Fig. 2 Comparison between experimental data and excitation function estimated by our systematics (^{186}W(n, p)^{186}Ta).

Table 2 Activation cross sections of short-lived nuclei.

^{23}Na(n, p)^{23}Ne (37.24 s)					^{30}Si(n, p)^{30}Al (3.60 s)				
En(MeV)	σ(mb)	δ_e(%)	δ_r(%)	δ_t(%)	En(MeV)	σ(mb)	δ_e(%)	δ_r(%)	δ_t(%)
14.87	40.5	9.7	9.6	13.7	14.87	38.6	19.2	3.8	19.6
14.58									
14.28	42.1	8.6	9.6	12.9					
13.88									
13.65	43.4	9.7	9.6	13.7					
^{123}Te(n, np)^{122m}Sb (4.196 min)					^{132}Ba(n, 2n)^{131m}Ba (14.6 min)				
En(MeV)	σ(mb)	δ_e(%)	δ_r(%)	δ_t(%)	En(MeV)	σ(mb)	δ_e(%)	δ_r(%)	δ_t(%)
14.87	0.30	10.4	5.0	11.5	14.87	880	6.8	3.9	7.8
14.58					14.58	813	6.0	3.9	7.1
14.28					14.28	792	6.9	3.9	7.9
13.88					13.88				
13.65					13.65	698	6.2	3.9	7.3
^{138}Ba(n, 2n)^{137m}Ba (2.552 min)					^{138}Ba(n, α)^{135m}Xe (15.65 min)				
En(MeV)	σ(mb)	δ_e(%)	δ_r(%)	δ_t(%)	En(MeV)	σ(mb)	δ_e(%)	δ_r(%)	δ_t(%)
14.87	983	3.2	3.0	4.4	14.87	0.79	33.6	3.3	33.8
14.58	975	3.2	3.0	4.4	14.58	0.85	37.0	3.3	37.1
14.28	963	3.9	3.0	4.8	14.28	0.80	46.2	3.3	46.3
13.88	967	3.2	3.0	4.4	13.88	0.78	34.3	3.3	34.5
13.65	945	3.1	3.0	4.3	13.65	0.74	36.8	3.3	36.9
^{140}Ce(n, 2n)^{139m}Ce (56.54 s)					^{140}Ce(n, α)^{137m}Ba (2.552 min)				
En(MeV)	σ(mb)	δ_e(%)	δ_r(%)	δ_t(%)	En(MeV)	σ(mb)	δ_e(%)	δ_r(%)	δ_t(%)
14.87	983	3.1	3.0	4.3	14.87	3.02	25.8	3.0	26.0
14.58	966	3.0	3.0	4.3	14.58	3.01	28.1	3.0	29.5
14.28	958	3.2	3.0	4.4	14.28	2.64	37.5	3.0	37.6
13.88	948	3.0	3.0	4.3	13.88	2.83	26.5	3.0	26.7
13.65	899	3.0	3.0	4.3	13.65	2.51	31.8	3.0	31.9
^{144}Sm(n, 2n)^{143m}Sm (1.10 min)					^{144}Sm(n, 2n)^{143g}Sm (8.83 min)				
En(MeV)	σ(mb)	δ_e(%)	δ_r(%)	δ_t(%)	En(MeV)	σ(mb)	δ_e(%)	δ_r(%)	δ_t(%)
14.87	587	4.2	4.0	5.8	14.87	1088	11.3	10.4	15.4
14.58	574	3.2	4.0	5.2	14.58	946	9.6	10.4	14.1
14.28	495	3.3	4.0	5.2	14.28	839	11.2	10.4	15.3
13.88					13.88				
13.65	419	3.3	4.0	5.2	13.65	737	10.8	10.4	15.0
^{186}W(n, p)^{186}Ta (10.390 min)					^{188}Os(n, p)^{188m}Re (18.6 min)				
En(MeV)	σ(mb)	δ_e(%)	δ_r(%)	δ_t(%)	En(MeV)	σ(mb)	δ_e(%)	δ_r(%)	δ_t(%)
14.87	2.30	11.4	17.3	20.7	14.87	0.61	8.9	5.6	10.5
14.58	1.84	14.4	17.3	22.5					
14.28	1.78	24.6	17.3	30.1	^{189}Os(n, p)^{188m}Re (18.6 min)				
13.88	1.31	16.7	17.3	24.0	En(MeV)	σ(μb)	δ_e(%)	δ_r(%)	δ_t(%)
13.65	1.20	23.7	17.3	29.3	14.87	33.9	46.0	5.6	46.3

3.18 Measurement of C(n, z) Double Differential Cross Section at 40, 64 MeV

Takehide KIYOSUMI, Mamoru BABA, Tomohiko IWASAKI
Toshiya SANAMI, Shigeo MATSUYAMA, Naohiro HIRAKAWA
Department of Nuclear Engineering, Tohoku University, Aoba-ku, Sendai 980-77

Takashi NAKAMURA
Cyclotron Radioisotope Center, Tohoku University, Aoba-ku, Sendai 980-77

Susumu TANAKA
Takasaki Establishment, Japan Atomic Energy Research Institute, Takasaki 370-12

Hiroshi NAKASHIMA, Shin-ichiro MEIGO, Shun-ichi TANAKA
Tokai Establishment, Japan Atomic Energy Research Institute, Tokai-mura 319-11

Abstract

We measured (n,px), (n,dx) cross sections of carbon for 40MeV and 64MeV neutrons at the mono energetic neutron source facility of TIARA by using a ΔE-E counter telescope. These spectra are dominated by a continuum attributed to multi-particle breakup with some peaks corresponding to levels of residual nuclei. The high energy parts of the spectra show very strong angular dependencies that are not interpreted by the kinematic effect alone.

1.Introduction

Neutron cross section data for En>20MeV are required for development of large accelerators for nuclear transmutation and fusion materials irradiation tests, and for research of radiation effect and so on. However, these data are very scarce.

As a part of the neutron cross sections studies at the 20-90MeV mono energetic neutron source facility of TIARA (Takasaki Ion Accelerator for Advanced Radiation Application) (Fig.1)[1], we measured double differential (n,z) cross section (DDX) of carbon for 40MeV and 64MeV neutrons. The C(n,z) data are important in various applied fields. The results were compared with some model calculations.

2.Experimental

Details of experimental and data analyses have been reported previously[2]. Figure 2 shows the experimental set up for the measurement. We put a sheet of carbon (0.3mm thick at 40MeV, 0.5mm at 64MeV) on the neutron beam from the ^{7}Li(p,n) reaction and measured emitted particles by a ΔE(Si SSB)-E(NaI(Tl) 3cm thick) telescope. Data for 30° ~ 120° were obtained by rotating the telescope around the sample (Fig.2(a)). At forward angles (7.2° ~ 25°), we used an "annular" geometry (Fig.2(b)): The telescope was placed on 0° line and shielded from the neutron beam by a shadow bar (50-cm long brass) to avoid backgrounds from the detector themselves. Scattering angle was varied by changing the distance between sample and detector.

Particle identification was done using a two-dimensional ΔE versus E display. TOF between cyclotron RF and the E detector was used to select the events arising from the peak of the neutron beam (Fig.3). We determined the neutron flux by measuring H(n,p) recoil protons, and monitored neutron flux by proton beam current and two fission chambers around the target.

3.Data Reduction

The energy scale was determined from a linear response of the NaI(Tl) scintillator versus particle energies and the recoil proton energy for the peak neutrons of the ^{7}Li(p,n) spectrum. Background-subtracted spectra were corrected further for the energy loss in the sample, air, ΔE detector and window materials using averaged values for possible charged-particle paths. At last, DDX was deduced by dividing the spectra by $4\pi\phi NS\Omega$ (ϕ: neutron fluence, N: areal density of sample atom, S: sample

sample atom, S: sample area, Ω: solid angle).

4.Results and Discussion

Figures 4(a)~(d) show DDXs of proton and deuteron emission reactions of carbon for 40 and 64 MeV neutrons. These spectra show peculiar structure and strong angular dependencies in high energy region. Figures 5(a)~(d) show typical spectra in Figs.4. They consist of clear peaks at high energy end and continuum at low energy range. We compared our data with those by U.C. Davis[3]. Although the incident neutron energy is different between these data, our data are consistent with U.C.Davis both in shape and magnitude.

To estimate the underlying continuum, we compared with a three-body phase-space distribution[4]; the $^{12}C(n,pn)^{11}B$ reaction for proton and the $^{12}C(n,d\alpha)^{7}Li$ reaction for deuteron. They are assumed to be isotropic in C.M. system. As shown in Figs.4(a) ~ (d), the phase space reproduces qualitatively the 40MeV data except 120° proton case, but is much smaller than 64MeV data. Therefore, the angular dependence of the spectra at 64MeV is inexplicable by the kinematic effect alone. Then, we compared with the calculation by D.J.Brenner[5] (En=40, 60MeV) using an intranuclear cascade model. It traces the experimental data fairly well while it underestimating at backward angles.

Angular distributions of $^{12}C(n,p)^{12}B$, $^{12}C(n,p)^{12}B^{*}$, and $^{12}C(n,d)^{11}B$ are shown in Fig.6. They indicate very strong forward-rise and this tendency is clearer for En=64 than for En=40MeV. They are likely to be due to the direct reaction process. Then we are doing DWBA analysis of the data.

By the present telescope, it is not possible to measure the low energy region protons, deuterons (<15MeV) and α particles. Hence, the telescope will be extended to enable detection of low-energy protons, deuterons and other heavier particles.

The present work was undertaken as part of special project research between universities and JAERI. The authors thank operating crew of JAERI Takasaki cyclotron for their collaboration.

References:

1)Tanaka, S.,et al.;Proc. 2-nd Int.Symp. "Advanced Nuclear Energy Research -Evolution by Accelerators-" (JAERI 1992) p.342
2)Baba, M. et al.;JAERI-M 94-019(1994), p.200
3)Subramanian, T.S., et al.;Phys. Rev.,**C28(2)** 521(1983)
4)Ohlsen, G.G.;Nucl. Inst. Methods, **37** 240(1965)
5)Brenner, D.J.,et al.;Atomic Data and Nuclear Data Tables, **41** 71(1989)

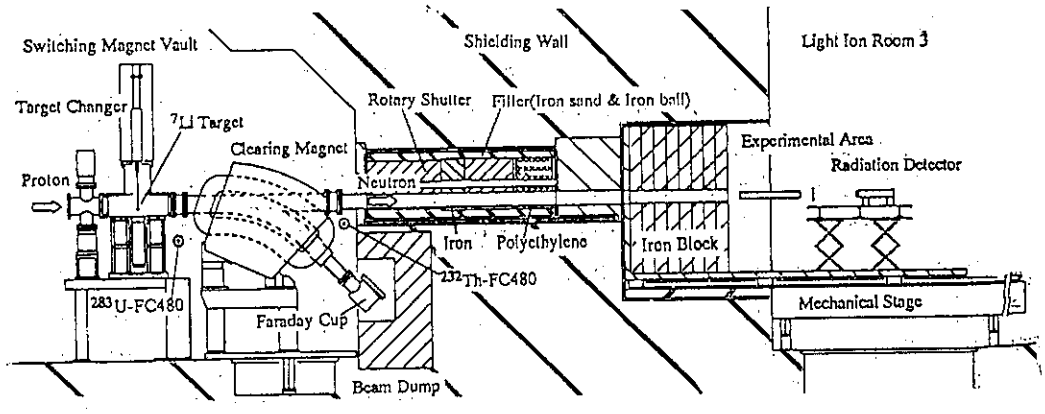

Fig. 1 Lay-out of quasi mono-energetic neutron source facility of TIARA and set up of telescope.

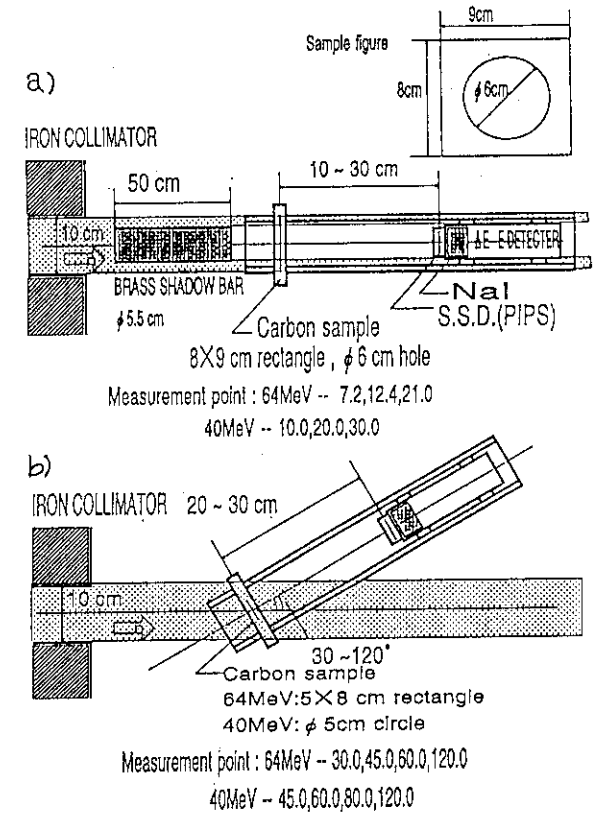

Fig. 2 a) Set up of θ <25° measurement
b) Set up of θ >30° measurement

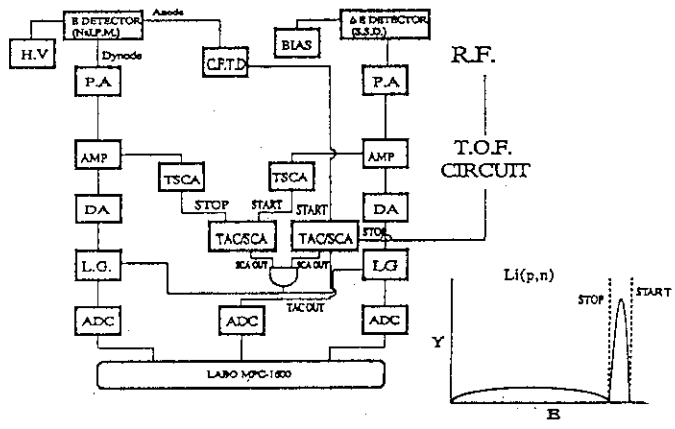

Fig. 3 Electrnic circuit for the measurement

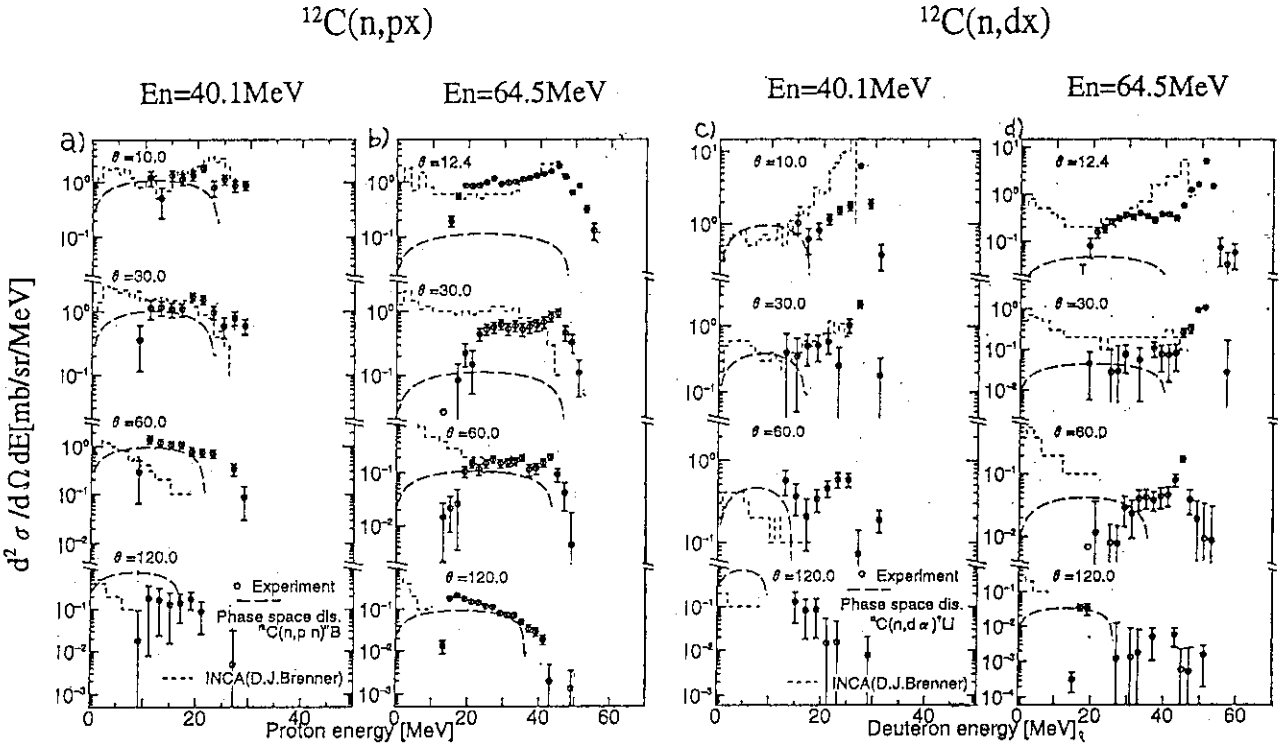

Fig. 4 Double differential cross-sections for ^{12}C(n,p;d) at laboratry angles between 10° and 120°

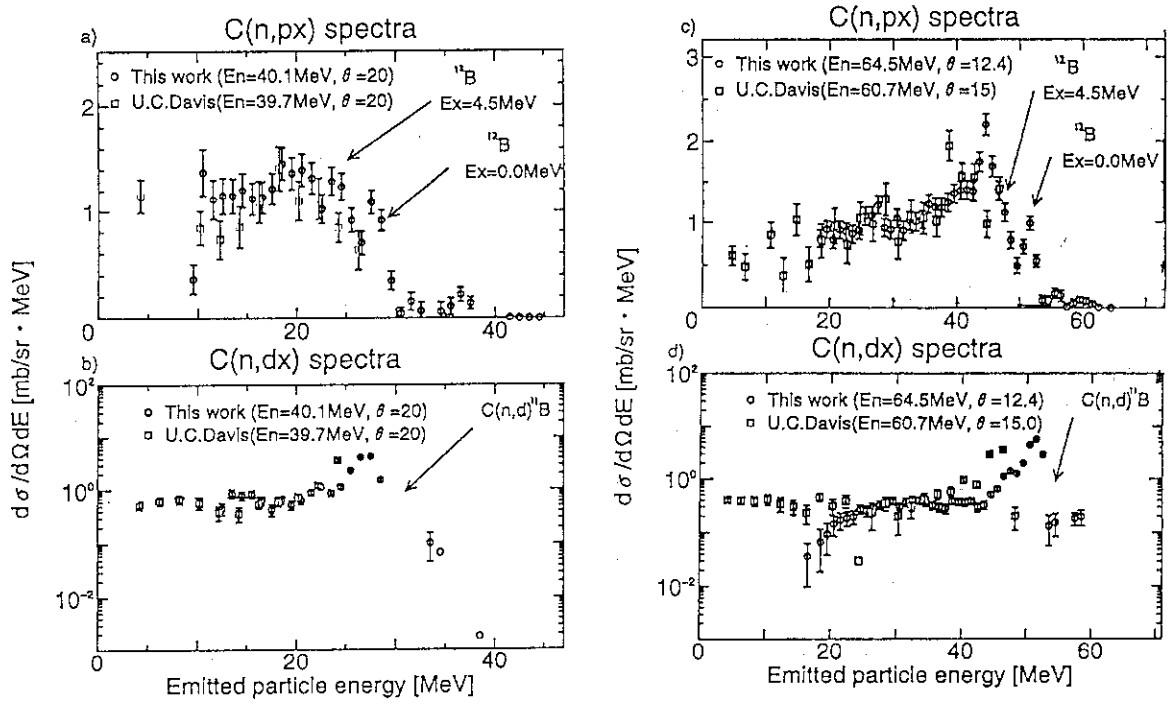

Fig. 5 Typical DDX of C(n,px) and C(n,dx)

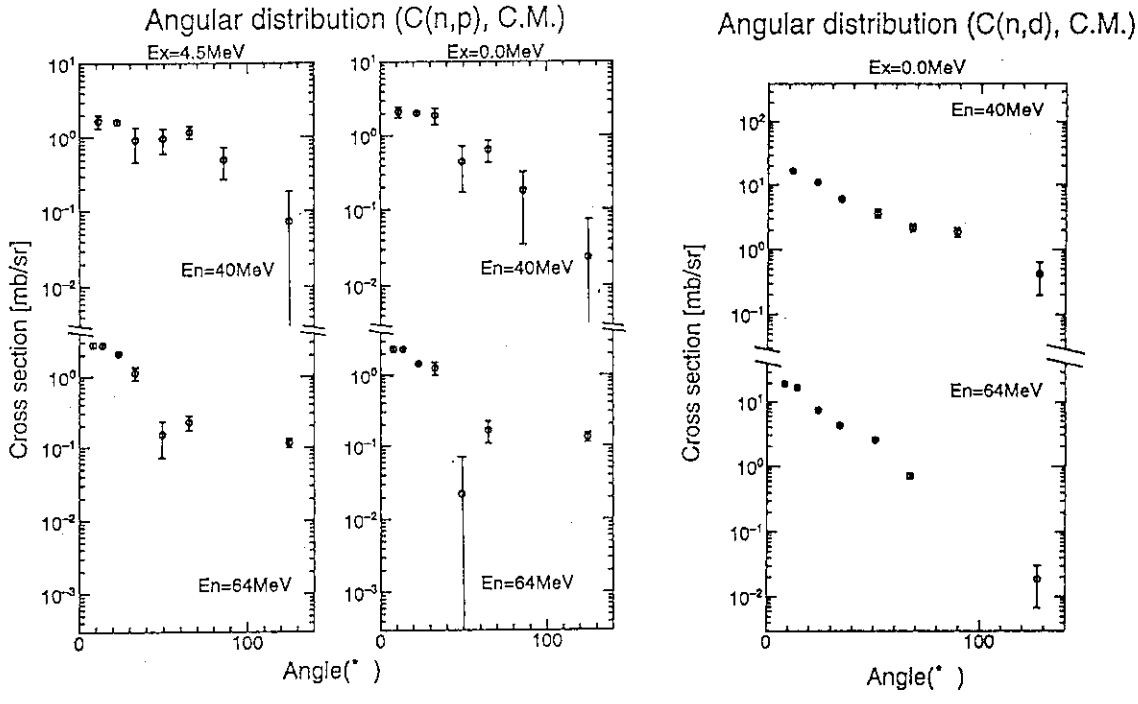

Fig. 6 Angular distribution of $^{12}C(n,p;d)$ reaction

3.19 Gamma Ray Albedo Data Generated by the Invariant Imbedding Method

Hiroyuki Kadotani
CRC Research Institute, Inc.
Nakase, Mihama-ku, Chiba 261-01

Akinao Shimizu
Research Laboratory for Nuclear Reactors
Tokyo Institute of Technology
Ookayama, Meguro-ku, Tokyo 152

The invariant imbedding method is used to generate gamma ray albedos for various materials. The accuracy of the calculated gamma ray albedos are established by comparing with the MCNP calculation. A new format for gamma ray albedo data base is proposed, from which one can easily obtain the various albedos (number, dose, energy, etc.). The invariant imbedding method can calculate gamma ray albedos very fast and accurately even on a PC, therefore, this method is most suitable for generation of gamma ray albedos.

I. Introduction

Albedos, in this paper the gamma ray albedos, which are defined as the ratios of incident to the reflected radiation have been recognized to be a useful data for a simplified shielding applications. However, albedos have not been used widely in practical shielding calculations, because the few albedo data bases have been available for shielding analysts, and no tools are available to re-arrange the albedo data for specific applications. We will demonstrate that the invariant imbedding[1),(2)] method is practically the best procedure to produce accurate gamma ray albedos.

2. Invariant Imbedding Re-visited[3)]

The meaning of the term "invariant imbedding or embedding" has not been directly explained. According to the recent paper by Nelson, "invariant imbedding" means in broad sense that, if a physical system is linear with regard to some properties, then that property is invariant to the system being embedded into a larger system. In the present application, the property is the fact that output fluxes depend linearly

on the other entering fluxes. In the same paper, Nelson explains this term in the narrower sense, that "the imbedded subsystem differs only differentially in some parameters (for instance, some measure of system size) from the larger system in which it is imbedded, and the invariance along with the fundamentals of the physical processes taking place in the differential layer is used to obtain a differential equation". For the calculation of gamma ray albedos from semi-infinite homogeneous medium, the change of the reflection function by adding the thin layer to the surface is calculated from the physical properties of the added layer, while the reflection function of the original layer is invariant.

The most apparent difference of the invariant imbedding method from the conventional transport method is that, in the invariant imbedding method, no information can be obtained for the flux within the medium. The available data are only the reflection or transmission functions. However, this is a very suitable feature for calculation of albedos.

3. Albedos of Gamma Rays for an Infinite Slab[4] and Format of Data Base

Albedos are simply defined as the ratios between incident and exiting gamma rays. For an infinite slab, differential albedos is defined as,

$$R(E_{in},\mu_{in},:E_{out},\mu_{out})=\phi_{ref}(E_{out},\mu_{out})/I_{in}(E_{in},\mu_{in})$$

where,

$R(E_{in},\mu_{in}:E_{out},\mu_{out})$: Azimuthal integrated differential albedo,

$\phi_{ref}(E_{out},\mu_{out})$: Reflected gamma ray flux,

$I(E_{in},\mu_{in})$: Incident gamma ray current,

with conventional symbols. From the above differential albedos, one can easily obtain number albedos, dose albedos, energy albedo, etc.

A new data base format is proposed for gamma ray albedos which is suitable for later use. The detailed description of the format will be discussed in elsewhere.

4. Calculation and Verification of Albedos by Invariant Imbedding Method

A computer program, GTIER0[5),(6)], is written to calculate gamma ray albedos based on the invariant imbedding method, The total cross sections for gamma rays are produced from PHTX[7)] library. The photo luminescence effect is included in the present program. The effect of the Bremsstrahlung is not treated in the current version of the program. The GTIER0 code is a short FORTRAN program and its computing time is short even on PC's.

Verification of the GTIER0 code is performed by comparing the calculations by the MCNP3A[8)] code. Reflected gamma ray fluxes are calculated for water and lead at 1 and 10 MeV gamma rays. Figs. 1 and 2 show the comparison between the invariant imbedding and the Monte Carlo calculations. The agreements between two calculation can be said fairly good, though it is still necessary to compare the calculation with the experimental results as benchmarking. This comparison had been done for several materials and it was found that the agreement is also good.

It can be concluded that the invariant imbedding method with modern cross sections calculates accurate gamma ray albedos. This method has an advantage over other existing methods in regard to the computing time and accuracy.

References

1) Shimizu and A., Aoki, K,: Application of Invariant Embedding to Reactor Physics", Academic Press, New York, 1972.

2) Mingle, J. O.: The Invariant Imbedding Theory of Nuclear Transport", America Elsevier Publishing Company, Inc. New York, 1973

3) Nelson, P.: "Invariant Embedding and Related Methods", Trans. Am. Nucl. Soc., 71, 223-224 1994.

5) Diop, C. M., Elhamzaoui, B. and Nimal, J. C: "Determination of the Double Angular and Energy Differential Gamma-Ray Albedo for Iron Material by Using the Monte Carlo Method", Nucl. Sci. & Eng., 117 201-226 (1994).

5) Shimizu, and A. Mizuta, H: "Application of Invariant Imbedding to the Reflection and Transmission Problem of Gamma Rays, (I)", J. Nucl. Sci. & tech., 3, 57-56 (1966).

6) Shimizu, A: Private communication, 1992.

7) Berger, M. H. and Hubbell, J. H.: "PHTX V2.0", DLC-136.

8) Briesmeister, J. F. (Ed.): MCNP-A General Monte Carlo Code for Neutron and Photon Transport, Version 3A, LA-7396-M, Rev. 2 (1986).

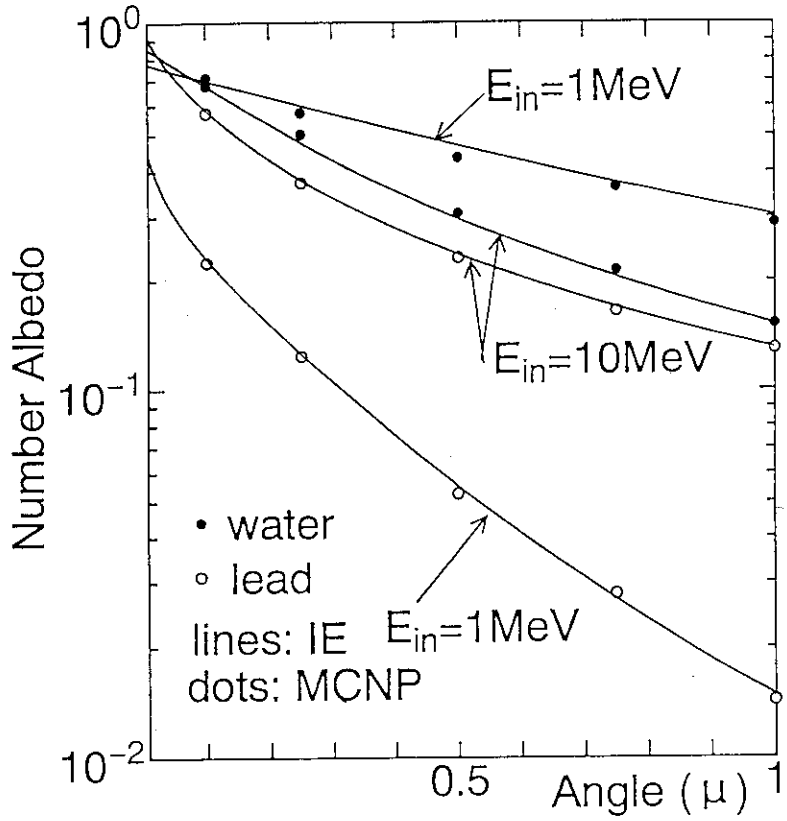

Fig. 1 Number Albedo of Obliquely Incident Gamma Rays on Water and Lead

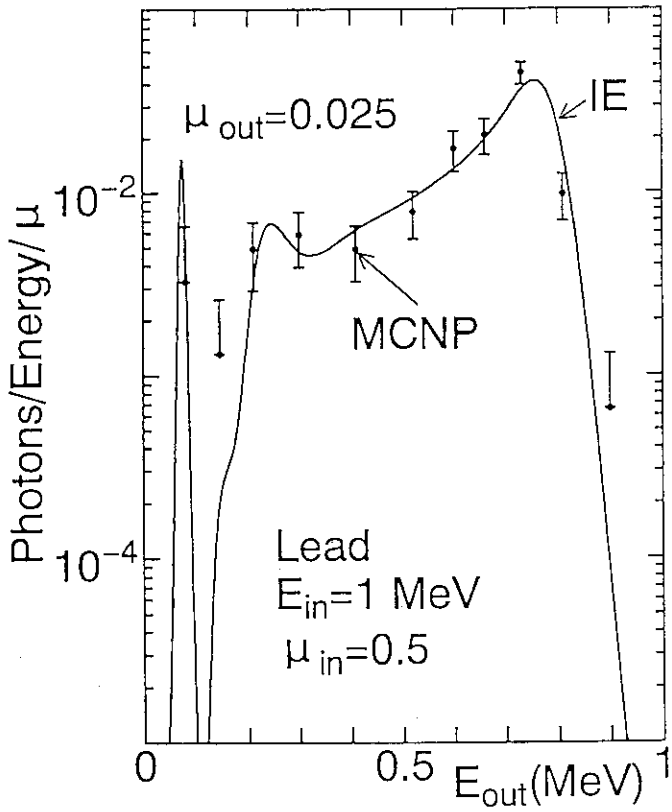

Fig. 2 Differential Albedo for Lead

3.20 A Subject of Activation Cross Section Library for IRAC Code System

Susumu TANAKA and Naoki YAMANO*

Japan Atomic Energy Research Institute, Takasaki Establishment
*Sumitomo Atomic Energy Ind., Ltd.

Abstract

The IRAC code system has a major activation cross section library, ACSELA94, which has been calculated using ALICE-F code on the basis of selection of geometry depended hybrid models with conditions of 9 incident particles and 136 target nuclides in the range of ^{1}H ~ ^{209}Bi. The incident energies of light ions (^{1}H, ^{2}H, ^{4}He) and neutrons are from threshold energy to 150 MeV, and of heavy ions (^{12}C, ^{14}N, ^{16}O, ^{20}Ne, ^{40}Ar) are from threshold energy to 500 MeV, respectively. To obtain the general tendency of the calculated cross section, the sum total of individual isotope production cross sections was compared with nonelastic cross section. It was found that they are in good agreement with the both in which the mass number of target nuclides is from 15 to 185. Furthermore some subjects of the cross section in ACSELA94 were found out.

1. Introduction

Induced radioactivity is an important consideration in the design and operation of any facility in which a significant activating particle flux is present. For the requirements on radiation protection, composition of structural materials and condition of operation have to select, to minimize the amount of induced activity, and to minimize radiation exposure to personnel. Therefore, it is advantageous to know what activity level will be present in the facility.

Regarding the design of nuclear reactor and fusion reactor, there are many kinds of code systems, for example, ORIGEN2, REAC2, ACTIVE and THIDA-2[1]. For studying nuclear physics, high energy Monte Calro codes NMTC, HETC, are used to calculate particle transport and product nuclides. A lot of accelerators have been widely used in material science, biology and industries. A wide variety of particles and target materials are used in that area. Thick-target yields data and calculations are usually used, but it is difficult to get radioactivity in the complex elements and geometry. The IRAC code system was developed to be fast and easy to use for calculation of induced radioactivities and related quantities in those accelerator facilities.[2]

The IRAC code system has a major activation cross section library, ACSELA94, which has been calculated using ALICE-F code system[3] on the basis of selection of geometry depended hybrid models and its default values with conditions of 9 incident particles and 136 target nuclides in the range of ^{1}H ~ ^{209}Bi. Projectile and target nuclide were selected in most provable combination to be used in experiments and accelerator components. The incident energies of light ions (^{1}H, ^{2}H, ^{4}He) and neutrons are from threshold energy to 150 MeV, and of heavy ions (^{12}C, ^{14}N, ^{16}O, ^{20}Ne, ^{40}Ar) are from threshold energy to 500 MeV, respectively.

2. Comparison with Nonelastic Cross Section and Measured Data

An error of induced radioactivity calculated by the IRAC code system is mostly caused by an uncertainty of the cross section. For verifying the cross section, it is the best way that the calculated cross sections directly compare with an experimental data, but the experimental data are scarce now. To obtain the general tendency of the calculated cross section, the sum total of

individual isotope production cross sections(SUM) was compared with nonelastic cross section calculated with optical model by ALICE-F.

The comparison was carried out with combination of 9 incident particles and 136 target nuclides. The results obtained with incident particles of neutron, proton, ^{12}C and ^{40}Ar are demonstrated in Figs.1(a)-(d), respectively, in which target nuclides of ^{12}C, ^{27}Al, ^{56}Fe, ^{93}Nb, ^{133}Cs, ^{181}Ta and ^{209}Bi are compared. It was found that they are in good agreement with the both in a case of all the target nuclides except ^{12}C for the incident particle of neutron and proton. The SUM of $^{12}C(p,x)$ reaction has discontinuous due to lack in production cross section of ^{4}He in the energy range of 40 MeV to 100 MeV, and wrong data existed far from what have been expected. For the heavy ions, such as ^{12}C and ^{40}Ar, the SUM of most target nuclides decreases at energy above 300 MeV. The SUM of $^{209}Bi(^{40}Ar, x)$ reaction was indicated much too small for comparing the nonelastic cross section.

An inelastic cross section by Guerra for $^{12}C(n,x)$ is shown in Fig.2, together with the SUM, nonelastic cross sections and $^{12}C(n,n3\alpha)$ obtained with cross section of outgoing alpha particle. A value in total including the SUM plus $^{12}C(n,n3\alpha)$ is in good agreement with the inelastic cross section.

Nonelastic cross sections with both the optical model and Pearlsttein's systematics by PEND6F in ALICE-F code system are compared with $^{12}C(n,x)$ and $^{12}C(p,x)$ in Fig.3. The Pearlsttein's systematics has discontinuous form at energy of 20 MeV.

Figs.4(a)-(d) show the comparison of calculated and measured[4] activation cross sections of $^{12}C(n,p)^{12}B$, $^{12}C(n,2n)^{11}C$, $^{12}C(n,t)^{10}B$ and $^{12}C(n,\alpha)^{9}Be$. The calculated cross sections of $^{12}C(n,p)^{12}B$ and $^{12}C(n,t)^{10}B$ are not in accord with the measured ones.

3. Conclusion

To obtain the general tendency of the cross section in ACSELA94, the sum total of individual isotope production cross sections was compared with the nonelastic cross section. It was found that they are in good agreement with the both in which the mass number of target nuclides is from 15 to 185. Furthermore some subjects of the cross section in ACSELA94 were found out.

References

1) Y.Seki et al., "THIDA-2: An Advanced Code System for Calculation of Transmutation, Activation, Decay Heat and Dose Rate", JAERI 1301 (1986).
2) S. Tanaka et al., "Development of IRAC code System to Calculate Induced Radioactivity Produced by Ions and Neutrons", Proc. of 8th ICRS, Texas, USA, April 25-29, 1994.
3) T. Fukahori, "ALICE-F Calculation of Nuclear Data up to 1 GeV," Proc. of the Specialists' Meeting on High Energy Nuclear Data, Tokai, Ibaraki, Oct. 3-4, 1991, p.114, JAERI-M 92-039, (1992).
4) V. McLane, "EXFOR Manual," IAEA-NDS-103(Rev.89/1), (1989)

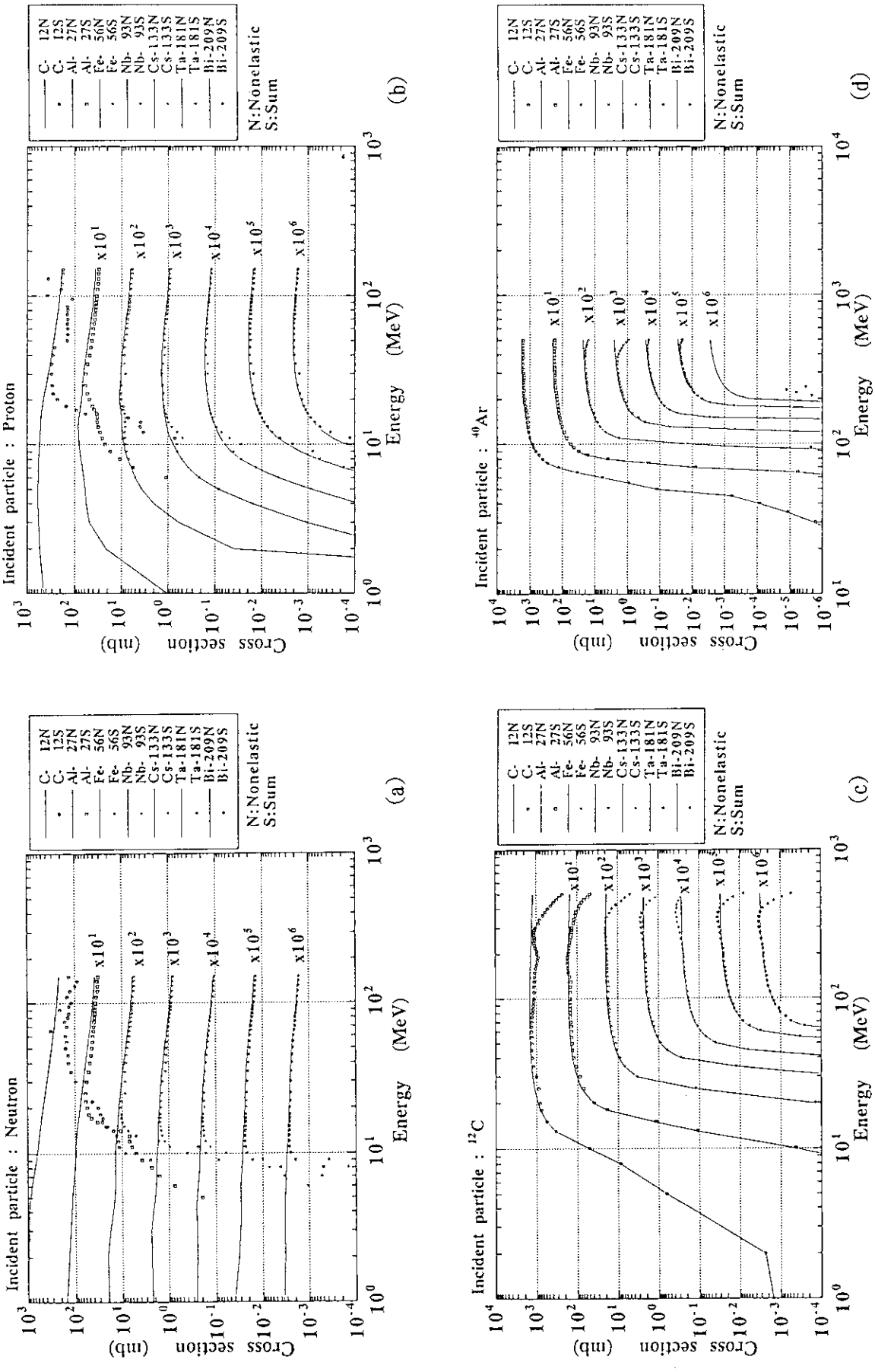

Fig. 1 Comparison of the sum total of individual isotope production cross sections and nonelastic cross section.

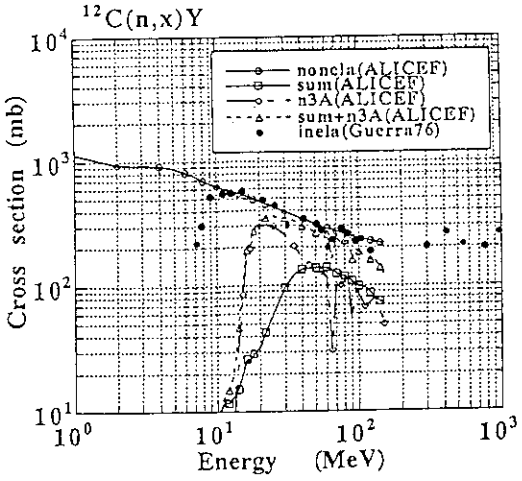

Fig. 2 Cross sections of ^{12}C(n, x)Y reaction.

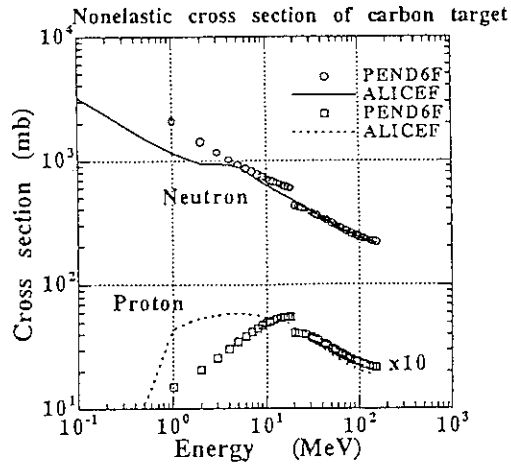

Fig. 3 Comparison of the optical model and Pearlsttein's systematics cross sections with ^{12}C(n, x) and ^{12}C(p, x) reactions.

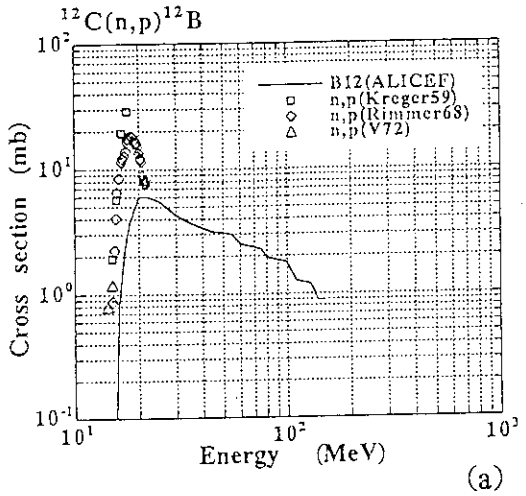

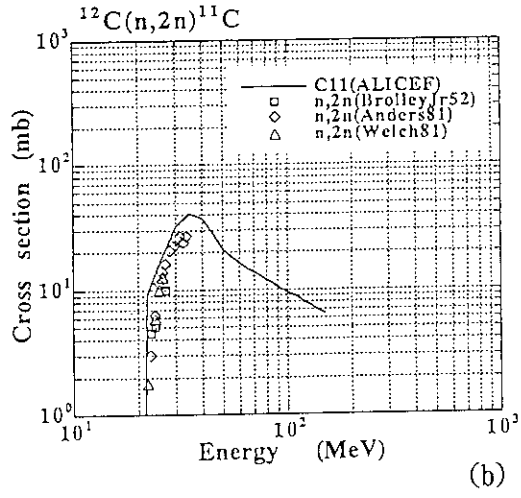

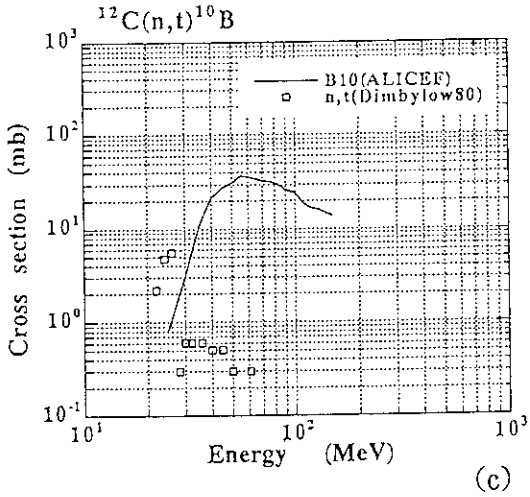

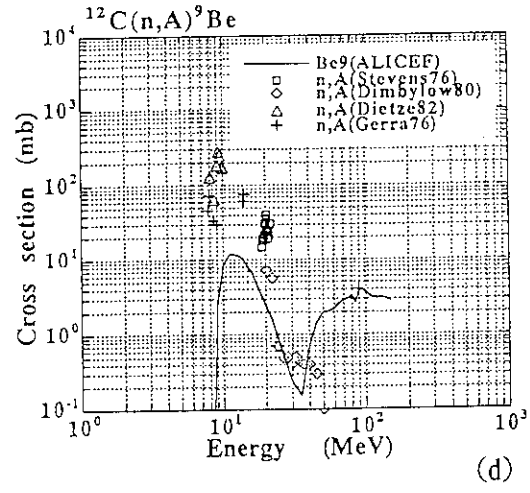

Fig. 4 Comparison of calculated and measured activation cross sections of ^{12}C(n, p)^{12}B, ^{12}C(n, 2n)^{11}C, ^{12}C(n, t)^{10}B and ^{12}C(n, α)^{9}Be.

3.21 Measurements of Gamma-ray Intensities of ^{231}Th with Semiconductor Detectors

Hiroshi CHATANI
Research Reactor Institute, Kyoto University
Kumatori-cho, Sennan-gun, Osaka 590-04

Thorium nitrate irradiated in the Kyoto University Reactor (KUR) core was purified chemically and used for γ-ray measurements. The Th-231 was produced by the Th-232(n,2n)Th-231 reaction. Most of the relative intensities are in good agreement with Hornshoj et al. within the experimental errors.

1 Introduction

Surprisingly few studies have so far been made at the intensities of Th-231 γ-rays. As far as the author know, they are the previous papers that Freedman M.S. et al./1/, Brown E. et al./2/, Teoh W./3/ and Hornshoj P. et al./4/. In particular, among these workers, Brown E. et al./2/ and Hornshoj P. et al./4/ have measured the intensities with high resolution Ge(Li) detectors in the range of γ-ray energy from 25 to 352 keV. Between these two studies the intensities are in fairly good agreement with each other, however some are in disagreement appreciably. Here we present the intensities with precise measurements. This study has been made twice.

2 Experimental

2.1 Preparations for ^{231}Th source

Thorium nitrate ($Th(NO_3)_4 4H_2O$) of about 100 mg was hermetically enclosed in a quartz tube under a reduced pressure less than 0.5 atm. and irradiated with neutrons at the center of the KUR core for 3 hours. About 1 day later on irradiation the Th sample was chemically purified with the procedures described in ref./5/6/7/8/9/.

2.2 Measurements of γ-rays and analysis

The γ-ray spectra have been taken by a Leps and 30 % HPGe with FWHM's of 0.593 and 1.28 keV at 122 keV, respectively. Analysis of the γ-ray spectra were performed by a Gaussian analysis program PKFIT /10/ on a personal computer. Some of the spectra were analyzed jointly with channel-summing method to ensure accuracy. Typical γ-ray spectrum is shown in Fig.1. In this spectrum we can see the photopeaks ascribed to the interference nuclides, however no serious obstacle existed in the analysis.

2.3 Detector efficiencies

Full energy peak (FEP) efficiencies for the detectors used were precisely calibrated using standard reference sources from Amersham Co. and/or LMRI (Laboratoire de Metrologie des Raynnements Ionisants).

2.4 Corrections for self attenuation and extended-area source

Attenuation of photons in the Th samples were measured with γ- and X-rays from Am-241, Co-57 and Ba-133, as shown in Fig.2. Self attenuation in the Th samples can readily be obtained from the data of the penetration experiments, in the following way. The observed intensity, I, passed through the sample is given as eq.(1), as widely known.

$$I = I_0 \exp (- \mu t) \quad (1)$$

where I_0 is the incident intensity, μ is the linear attenuation coefficient of the total contents of the Th sample and t is the thickness of the Th sample. The term μt is written as eq.(2), which can be directly calculated from the data in Fig.2.

$$\mu t = \ln (I_0 / I) \quad (2)$$

On the other hand, the equation describing the self attenuation factor f is given as eq.(3).

$$f = (1 - \exp (- \mu t)) / \mu t \quad (3)$$

Consequently, f can be obtained by substituting eq.(2) into eq.(3).

The efficiency correction for the extended-area source can not be neglected when the measurements are made in the vicinity of the Leps, at 1 cm. The mapping method was applied to this correction, which has been proposed by Kushelevsk A.P. et al./11/ and was systematized by the author/12/. The value B=0.256 cm^{-2} in Fig.3, obtained using 190 keV γ-rays, is a Gaussian width parameter in eq.(4).

$$\varepsilon_r = \varepsilon_0 \exp (- Br^2) \quad (4)$$

in which r is the distance away from the detector axis, ε_0 is the FEP efficiency on the detector axis and ε_r is the efficiency at r. Therefor, FEP efficiency of the extended-area

Table 1 Summary of the presented intensities of ^{231}Th γ-rays and that of the previous results.

Energy[a] (keV)	This work					Previous works			
	Leps[b]			HPGe[b]		Freedman+[f] (1952)	Brown+[g] (1973)	Teoh[h] (1973)	Hornshoj+[i] (1975)
	9mm PMMA[c] 5cm[d]	No[c] 7.10cm[d]	Cu+Cd[c] 1cm[d] r=5mm[e]	10mm PMMA[c] 15.10.5cm[d]	Result				
25.64	--	226 (9)	--	--	226 (24)	170 (+L x-ray)	202 (20)	--	228 (15)
42.86	0.84 (8)	0.83 (4)	--	0.76	0.83 (4)		0.87 (10)	--	0.89 (6)
44.06	--	--	--	--	--		0.06 (4)	--	0.011 (3)
58.57	6.8 (3)	6.8 (3)	--	6.29 (36)	6.8 (3)	<40 (59+63keV)	7.2 (7)	--	7.4 (3)
63.84	0.48 (3)	0.48 (5)	--	--	0.48 (3)		0.68 (14)	--	0.35 (3)
68.47	--	--	--	--	--		--	--	0.088 (22)
72.75	3.6 (2)	3.6 (2)	4.01 (22)	3.58 (12)	3.6 (2)		4.0 (4)	3.8 (2)	3.86 (23)
73.16	--	--	--	--	--		0.10 (4)	--	--
81.23	13.6 (6)	12.9 (6)	13.8 (7)	15.4 (5)	13.7 (6)		14.2 (14)	13.5 (9)	13.7 (8)
82.07	6.07 (22)	6.02(12)	6.14 (31)	7.28 (25)	6.1 (3)		7.2 (7)	6.8 (4)	6.2 (5)
84.21	100	100	100	100	100	100 (85keV)	100	100	100 (6) [6.5 (4)][j]
89.97	15.3 (6)	14.4 (6)	14.7 (7)	--	14.6 (6)		15.3 (15)	15.3 (8)	14.5 (9)
92.28 x	--	--	5.6 (6)	--	5.6 (6)		6.0 (6)	--	--
93.05	--	--	0.79 (15)	--	0.79 (15)		0.50 (5)	0.9 (2)	0.69 (8)
95.86 x	9.9 (4)	9.73 (40)	9.50(44)	--	9.7 (5)		10.3 (10)	--	--
99.29	2.15 (9)	1.92 (11)	2.02 (10)	--	2.1 (1)		2.1 (2)	2.2 (2)	1.85 (11)
102.27	6.78 (25)	6.63 (13)	6.65 (27)	6.41 (22)	6.65 (27)		6.7 (7)	6.8 (4)	6.3 (5)
105.81	0.149 (11)	0.119 (18)	0.108 (7)	--	0.12 (1)	6 (5)	0.14 (2)	0.13 (8)	0.11 (1)
106.58	0.251 (21)	0.245 (26)	0.278 (13)	--	0.267 (12)		0.34 (4)	0.33 (10)	0.26 (2)
107.60 x	1.20 (6)	1.14 (6)	1.20 (5)	--	1.20 (5)		1.29 (14)	--	--
108.42 x	2.32 (13)	2.25 (11)	2.29 (10)	--	2.30 (10)		2.43 (24)	--	--
109.07 x	0.15 (5)	0.24 (9)	0.163 (18)	--	0.16 (2)		--	--	--
111.49 x	--	1.09 (25)	0.91 (4)	--	1.0 (1)		0.9 (1)	--	--
112.38 x	--	(0.35)(20)	0.266 (28)	--	0.27 (20)		0.34 (4)	--	--
115.61	--	--	0.025 (15)	--	0.025 (15)		0.04 (1)	--	0.015 (3)
116.81	0.37 (2)	0.32 (2)	0.339 (15)	0.29 (1)	0.34 (2)		0.39 (4)	--	0.318 (20)
124.93	0.96 (5)	0.87(8)	0.902 (41)	0.86 (3)	0.90 (4)		0.95 (9)	--	0.86 (5)
134.03	0.41 (2)	0.32 (2)	0.385 (17)	0.40 (1)	0.39 (2)	2 (122keV)	0.42 (5)	--	0.37 (2)
135.68	1.28 (5)	1.15 (6)	1.21 (5)	1.18 (4)	1.20 (5)		1.3 (1)	--	1.20 (8)
136.73	0.082 (7)	0.13 (5)	0.075 (6)	0.088 (2)	0.082 (6)		0.09 (3)	--	0.065 (3)
140.55	--	--	0.0102 (16)	0.015 (1)	0.010 (2)		--	--	0.011 (1)
145.07	--	--	0.084 (4)	0.071 (6)	0.084 (6)		0.12 (3)	--	0.089 (6)
145.91	0.45 (3)	0.46 (3)	0.464 (20)	0.476 (17)	0.46 (3)		0.58 (6)	--	0.49 (3)
163.13	2.28 (8)	2.33 (9)	2.33 (10)	2.34 (8)	2.33 (10)	1.8 (167keV)	2.6 (3)	--	2.38 (14)
164.96	--	--	0.044 (2)	0.056 (6)	0.044 (4)		0.06 (3)	--	0.060 (6)
169.65	--	--	0.022 (1)	0.015 (1)	0.019 (4)		0.03 (1)	--	0.018 (2)
174.18	0.27 (3)	0.29 (2)	0.263 (12)	0.27 (1)	0.268 (15)		0.31 (3)	--	0.278 (17)
183.50	0.48 (3)	0.57 (3)	0.482 (19)	0.49 (2)	0.48 (2)		0.57 (6)	--	0.506 (20)
188.77	--	--	0.049 (2)	0.047 (3)	0.048 (3)		0.08 (1)	--	0.049 (3)
217.96	0.55 (4)	0.61 (4)	0.608 (24)	0.61 (2)	0.61 (3)	0.3 (210keV)	0.67 (7)	--	0.62 (5)
236.02	0.183 (24)	--	0.143 (6)	0.139 (5)	0.141 (6)	0.1 (230keV)	0.18 (2)	--	0.14 (1)
240.26	--	--	0.0056 (10)	--	0.0056 (20)		0.0050 (5)	--	0.0043 (5)
242.54	--	--	0.0141 (12)	--	0.014 (2)		0.0130 (6)	--	0.013 (1)
249.57	--	--	0.0092 (14)	--	0.009 (3)		0.010 (2)	--	0.012 (1)
250.41	--	--	0.011 (2)	0.010 (4)	0.011 (3)		0.011 (2)	--	0.010 (1)
267.63	--	--	0.0177 (10)	0.019 (1)	0.018 (2)		0.0230 (6)	--	0.018 (2)
274.15	--	--	--	--	--		--	--	0.00046 (15)
308.73	--	--	0.0058 (5)	0.0044 (9)	0.005 (2)		0.008 (1)	--	0.0060 (6)
311.01	--	--	0.0461 (24)	0.0459 (23)	0.046 (3)		0.054 (5)	--	0.045 (3)
317.95	--	--	--	--	--		0.0020 (2)	--	0.0012 (2)
320.23	--	--	--	--	--		0.0035 (3)	--	0.0017 (2)
351.84	--	--	--	--	--		--	--	0.0011 (2)

The numbers in parentheses denote the error in units of the last decimal place.

a: γ-ray energies are taken from the decay scheme in Ref. /4/ ; letters x beside the numbers refer to X-rays whose energies are taken from appendices of Ref. /14/.

b: Detector used.

c: Absorbers; " 9mm PMMA" refers to " Acrylic resin of 9 mm thick" ; " Cu+Cd" refers to " Pasted Cu (1mm) and Cd (1mm) together" .

d: Distance from the detector to a source.

e: Radius of the extended-area source.

f: Ref. /1/. g: Ref. /2/. h: Ref. /3/. i: Ref. /4/.

j: A number in square brackets denotes the absolute intensity.

source ε_R having a radius R, can be obtained by integrating eq.(4) with respect to R.

$$\varepsilon_R = \varepsilon_0 (1 - \exp(-BR^2)) / BR^2 \quad (5)$$

Measurements of the B were carried out using a few γ-ray sources which emit monoenergetic (i.e. coincidence free) γ-rays; Fig.4 shows B obtained according to γ-ray energy.

Peak area analyzed by PKFIT were corrected with FEP efficiency, self attenuation and extensity of the source.

3 *Results and Discussion*

Relative γ-ray intensities emitted from Th-231 have been measured with two semiconductor detectors. The results obtained are given in Table 1 with the literature values. Among several measurements in this work, most of the intensities (included X-rays) are in good agreement with each other. Resulted values in colum 6 are from the weighted averages of several measurements and the scatterings.

More detailed studies for the weak intensity lines which have not been measured here are being carried out. Moreover a study of the absolute values will also be necessary.

Acknowledgment

The author would like to thank Hisao KODAKA and Jitsuya TAKADA for their help. Thanks are also due to Kotoyuki OKANO for the use of the Leps; in particular I am extremely grateful to Shigeru YAMADA for comprehensive support during the course of this study and for suppling PKFIT. I also acknowledge Katsuhei KOBAYASHI for hearty support and discussion.

References

/1/ Freedman M.S., Jaffey A.H. et al.: Phys. Rev., 89 [1], 302–309 (1953). /2/ Brown E. and Asaro F.: Phys. Rev.,C7 [6], 2545–2566 (1973). /3/ Teoh W.: Nucl. Instrum. Meth., 109, 509–513 (1973). /4/ Hornshoj P., Petersson P.T. and Kaczarowski R. et al.: Nucl. Phys., A248, 406–428 (1975). /5/ Chatani H.: Nucl. Instrum. Meth., 205 [3], 501–504 (1983). /6/ Chatani H. and Kimura I.: Ann. Nucl. Energy, 19 [8], 425–429 (1992). /7/ Hyde E.K.: NAS-NS 3004, (1960). /8/ Chatani H. and Kimura I.: JAERI-M 91–032, (1991). /9/ Kobayashi K, Hashimoto T and Kimura I.:J. Nucl. Sci. Technol., 8 [9], 492–497 (1971). /10/ Yamada S.: Private communication. /11/ Kushelevski A.P. and Alfassi Z.B.: Nucl. Instrum. Meth., 131, 93–95 (1975). /12/ Chatani H.: KURRI-TR-370, " Efficiency correction for disk sources using HPGe" (in Japanese), (1992). /13/ Storm E. and Israel H. I.: Nucl. Data Tables, A7, 565–681 (1970). /14/ Brown E. and Firestone R.B.: " Table of Radioactive Isotopes" , John Wiley and Sons,(1986).

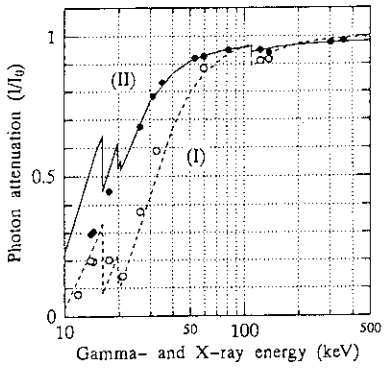

Fig. 2 Attenuation of photons in the purified Th samples: (I) for the 1st experiment and (II) for the 2nd. The lines fitted to the data points were calculated from calculation tables by Storm E. and Israel H. I. /13/.

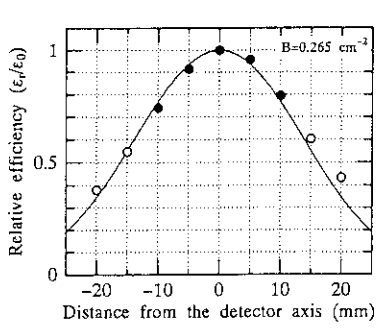

Fig. 3 Distribution of off-center detection efficiencies of the Leps at 1 cm with the Cu+Cd absorber. Solid line is a Gaussian distribution with the width parameter 0.265 cm^{-2} which was calculated from the solid circles only.

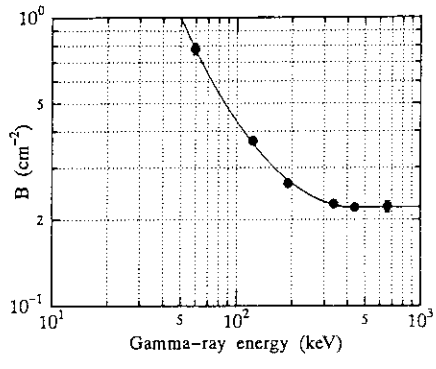

Fig. 4 Systematics of the B-value vs γ-ray energy for the Leps at 1 cm with the Cu+Cd absorber. Data were taken using the 60(^{241}Am), 122(^{57}Co), 190(^{114m}In), 336(^{115m}In), 439(^{69m}Zn), and 662 keV (^{137}Cs).

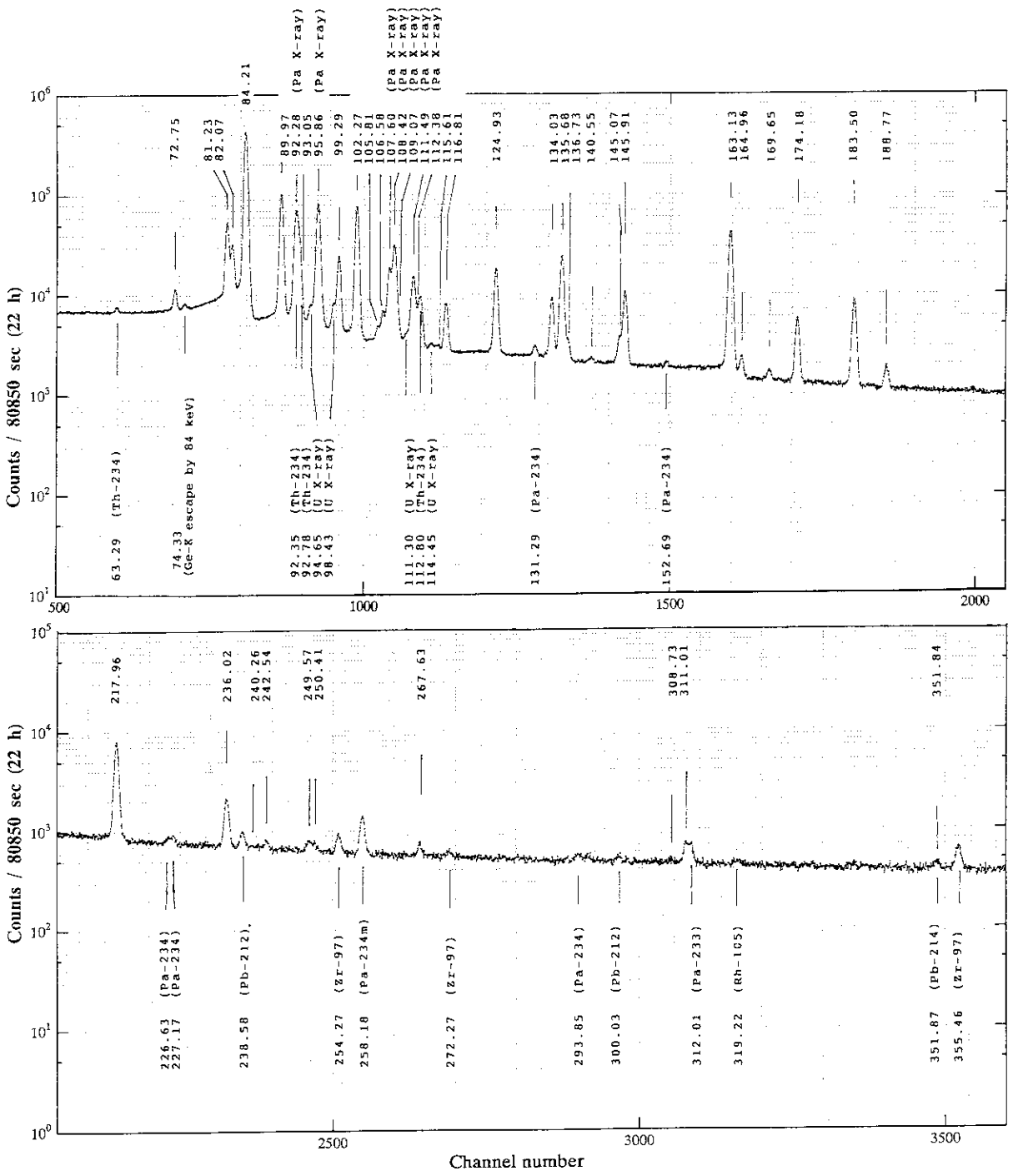

Fig. 1 Typical γ-ray spectrum of the Th sample purified after neutron irradiation, measured with the Leps at 1 cm with a Cu(1mm)+Cd(1mm) absorber. Figures above the spectrum are γ- and X-ray energies in keV in the decay of ^{231}Th. Figures below the spectrum are those associated with ^{234}Th, ^{234}Pa, ^{97}Zr, ^{233}Pa and Pb.

3.22 Measurements of Thermal Neutron Capture Cross Section and Resonance Integral of ^{129}I

Toshio Katoh, Yoshimune Ogata*, Hideo Harada**, Shoji Nakamura**

Department of Nuclear Engineering, Nagoya University,
Nagoya 464-01 JAPAN
**Radioisotope Center, Nagoya University, Nagoya 464-01, JAPAN*
***Power Reactor and Nuclear Fuel Development Corp.,*
Tokai, Ibaraki 319-11, JAPAN

Abstract: The thermal neutron capture cross sections(σ_0) and resonance integrals(I_0) of ^{129}I were measured to obtain the fundamental data for the transmutation of ^{129}I(one of fission products), by the neutron capture. The amount of target nucleus was determined from the specific activity and the weight of the target. Gamma-rays from the produced nuclei, ^{130}I and ^{130m}I, were measured by a high purity Ge detector to deduce the amount of ^{130}I and ^{130m}I. Results obtained are as follows:

For formation of ^{130m}I; $\sigma_0^{2+} = 17.5 \pm 0.8$ (b), $I_0^{2+} = 17.9 \pm 0.9$(b),

For formation of ^{130}I; $\sigma_0^{5+} = 12.6 \pm 0.5$ (b), $I_0^{5+} = 15.5 \pm 0.9$(b).

The thermal neutron capture cross sections and resonance integrals of ^{129}I were measured to obtain the fundamental data for the nuclear transmutation of ^{129}I(one of long-lived fission products) through the reaction $^{129}I(n,\gamma)^{130}I$.

The standardized solution, supplied from The Amersham, of ^{129}I contained in polyethylene tubes were irradiated by neutrons from the Rikkyo University Reactor. The amount of activity in the targets were about 2500 Bq for the targets within a Cd shield and 250 Bq for the targets without the Cd shield. The precise value of the amount of nucleus of each target was determined from the specific activity, 42.12 kBq/g, and the weight of solution in the target. The weight were measured

by a Mettler's micro-balance. The neutron irradiation of the samples were carried out within a Cd shield tube or without the Cd shield. The neutron fluxes were monitored by two kinds of flux monitors, Co/Al and Au/Al. The thermal neutron flux at the irradiation position was 4.6 x 10^{11} n/cm^{2}s and the Westcott's epithermal index $r\sqrt{T/T_0}$ 0.038. Gamma-rays from produced nuclei, ^{130}I and ^{130m}I, were measured by a high purity Ge detector. In the gamma-ray spectra obtained, peaks of gamma-rays from ^{130}I and ^{130m}I were observed at the energies of 536 keV, 586 keV, 668 keV, 739 keV, 1157 keV and 1614 keV. Decay of the gamma-ray peaks were followed. The average values of half-lives of decay of the peaks were 8.786 ± 0.012 min for the 2+ state and 12.338 ± 0.008 hours for the 5+ state. These values were close to the values reported[1] previously for these states, respectively.

The area of gamma-ray peaks of the spectra were analyzed with the following equation,

$$Y_i = \varepsilon_i \left[b_{2i} W_2 + b_{5i} W_5 \right]$$

where, Y_i : Area of gamma peak of energy i

ε_i : detection efficiency of gamma-ray of energy i

b_{2i}: emission rate of gamma-ray of energy i due to ^{130m}I

b_{5i}: emission rate of gamma-ray of energy i due to ^{130}I.

The factors W_2 and W_5 are expressed as follows,

$$W_2 = R_2 \frac{N_0}{\lambda_2} (1 - \exp(-\lambda_2 T_{irr}))(\exp(-\lambda_2 T_1) - \exp(-\lambda_2 T_2))$$

where, N_0: Number of the target nucleus

λ_2, λ_5: decay constants of ^{130m}I and ^{130}I, respectively

R_2, R_5: reaction rates for formation of ^{130m}I and ^{130}I, respectively

T_{irr}: irradiation time

T_1: start time of the measurement

T_2: stop time of measurement

b_{it}: isomeric transition probability(83%).

When the neutron is well thermalized, the reaction rate(R) can be combined with the effective cross section($\hat{\sigma}$) as follows,

$$R = nv_0\hat{\sigma}$$

where, nv_0 is the neutron flux including the thermal and epithermal components. The v_0 is the velocity of 2,200 m/s.

The effective cross section is expressed according to the Westcott convention with the thermal neutron capture cross section(σ_0) with the following relation.

$$\hat{\sigma} = \sigma_0(gG_{th} + r\sqrt{T/T_0}\, s_0 G_{epi})$$

where σ_0 is the cross section for 2,200 m/s neutron, g the deviation from the 1/v law, and $r\sqrt{T/T_0}$ the epithermal index.

The s_0 is related to the resonance integral(I'_0) above the 1/v component, and is

$$s_0 = \frac{2}{\sqrt{\pi}}\frac{I'_0}{\sigma_0}.$$

In this experiment, the parameter gG_{th} can be set as 1. With a simple calculation[2], the relation between the reaction rate and the thermal neutron cross section was deduced as follows,

$$\frac{R}{\sigma_0} = \phi_1 + \phi_2 s_0 G_{epi} \quad \text{for irradiation without the Cd shield}$$

and $$\frac{R'}{\sigma_0} = \phi'_1 + \phi'_2 s_0 G_{epi} \quad \text{for irradiation within the Cd shield.}$$

The values of neutron fluxes ϕ_1(') and ϕ_2(') were determined by flux

monitors(Co/Al and Au/Al). The reaction rates obtained for both irradiations are combined to the value s_0G_{epi} as follows;

$$s_0G_{epi} = -\frac{\phi_1 - \phi'_1(R/R')}{\phi_2 - \phi'_2(R/R')}.$$

By using this value and the relation of R/σ_0, the value of σ_0 can be obtained. The value of resonance integral(I_0) is also obtained from a relation of

$$I_0 = I'_0 + 0.045\sigma_0 .$$

Results obtained in this experiment are

$\sigma_0^{2+} = 17.5 \pm 0.8$ (b), $I_0^{2+} = 17.9 \pm 0.9$ (b) for ^{130m}I formation,

$\sigma_0^{5+} = 12.6 \pm 0.5$ (b), $I_0^{5+} = 15.5 \pm 0.9$ (b) for ^{130}I formation.

The present value of the cross sections are close to the value reported by Block et al[3]. However, their value is only a combined value of ^{130}I and ^{130m}I formation. The value of the resonance integral is 10% larger than the value reported previously[4], which does not include the contribution of isomeric transition. Our measurement includes this effects.

References:

1) Lederer,C.M.,Shirley,V.S.:*Table of Isotopes*(7th er.),(1978), John Wiley & Sons.,New York
2) Sekine,T.,Hatsukawa,Y.,Kobayashi,K.,Harada,H.,Watanabe,H., Katoh,T.: J. Nucl. Sci. Technol., 30(11), pp.1099-1106(1993)
3) Block,R.C. et al.: Nucl. Sci. Engineering, 8, p. 112(1960)
4) Roy,J.C.,Wuschke,D.: Canadian J. Chemistry, 36, p. 1424(1958)

3.23 Measurements of Neutron Spectra from a Thick Lead Target Bombarded by 0.5 and 1.5 GeV Protons

Shin-ichiro MEIGO[1], Hiroshi TAKADA[1], Satoshi CHIBA[1], Tatsushi NAKAMOTO[2], Kenji ISHIBASHI[2], Naruhiro MATSUFUJI[2], Keisuke MAEHATA[2], Nobuhiro SHIGYO[2], Yoshihisa WAKUTA[2], Yukinobu WATANABE[3], Takashi NAKAMURA[4] and Masaharu NUMAJIRI[5]

1. Japan Atomic Energy Research Institute, Tokai-mura, Naka-gun 319-11
2. Department of Nuclear Engineering, Kyushu University, Hakozaki, Fukuoka 812
3. Energy Conversion Engineering, Kyushu University, Kasuga-koen, Kasuga 816
4. Cyclotron and Radioisotope Center, Tohoku University, Aoba, Sendai 980
5. National Laboratory for High Energy Physics (KEK), Oho, Tsukuba 305

Abstract

Neutron spectra from a thick lead target bombarded by 0.5 and 1.5 GeV protons have been measured at 6 angles between 15° and 150° using the time-of-flight and the unfolding methods. The experimental results were reproduced by a Monte-Carlo calculation satisfactorily except for an energy region of several tens MeV where the calculated values were considerably lower than the measured data.

1. Introduction

For the design study of such facilities as spallation neutron sources and accelerator driven transmutation systems, it is necessary to use the calculation code which can simulate nuclear reactions and particle transport process in bulky matters in the energy region up to several GeV. In order to evaluate the validity of the calculation code, the neutron spectra from a thick lead target bombarded with 0.5 and 1.5 GeV protons have been measured at 6 angles between 15° and 150° and compared with the calculated values.

2. Experimental Procedure

The experiment was carried out at π2 beam line of the 12 GeV proton synchrotron facility of National Laboratory for High Energy Physics (KEK). An illustration of the experimental arrangement is given in Fig. 1. A rectangular lead target having a size of 15 cm in length, 15 cm in width and 20 cm in thickness was employed. The target was thick enough to stop 0.5 GeV proton completely inside, while it caused a loss of 0.24 GeV on average for 1.5 GeV protons.

The NE-213 scintillators (5" ϕ x 5") with veto counters were used for the neutron detectors. Two-gate integration method[1] was employed to discriminate events produced by neutrons and γ-rays, which could accept a large dynamic range ($\geq$4000:1).

3. Data Reduction

The neutron energy spectra were obtained primarily by the time-of-flight (TOF) method. The detector bias was set at half height of ^{137}Cs Compton edge (0.493 MeVee). For the neutron below 80 MeV, the detection efficiency was calculated with SCINFUL[2] code including the modified deuteron light output[3] and the angular distribution of H(n,n) reaction[4]. The efficiency above 80 MeV was calculated with Cecil[5] code which was connected to the value obtained by SCINFUL at 80 MeV.

If a neutron interacts with the target nuclei more than once in the target, some delay is generated in the flight time compared with the one which comes out the target without scattering. Consequently, the measured TOF spectra might be softer than the real one. In order to estimate this effect quantitatively, the measured data were also analyzed using the unfolding method. The unfolding was carried out with FORIST[6] code, where the response matrix was calculated with SCINFUL. Since the saturation was observed in the pulse height signal for neutrons above several tens MeV, the unfolding method was employed for the pulse height corresponding to the neutrons below 14 MeV.

The neutron spectrum obtained by the unfolding method is compared in Fig. 2 with one obtained by the TOF method. In the region below 3 MeV, a difference of more than 50 % is seen in the comparison between the two methods. This difference is thought to be caused by ambiguity of the efficiency around the ^{137}Cs bias, which is used in the TOF method. Therefore, we concluded that the neutron spectra obtained by the unfolding method was more reliable than ones obtained by the TOF method below 3 MeV. In the region between 3 and 14 MeV, however, the spectra obtained by unfolding method agree with the result of TOF quite well. It is concluded from these results that the neutron scattering effect is negligibly small above 3 MeV. Therefore, the overall spectrum was obtained by unfolding and by TOF methods in the region below 3 MeV and above 3 MeV, respectively. In the present work, the data have been deduced up to 200 MeV because the TOF resolution became drastically poor at higher energy (30 % at 200 MeV, 54 % at 500 MeV).

4. Calculation

The calculation of the particle transport and nuclear reaction was performed with NMTC/JAERI[7] code in the energy region above 20 MeV. NMTC/JAERI was modified to take the Baba's level density parameter and the nucleon-nucleus elastic scattering into account.

For the neutron transport calculation below 20 MeV, MCNP 4.2[8] was employed. The neutron cross-section library was processed from the evaluated nuclear data file JENDL 3.2.

5. Result

Comparisons between the measured and the calculated results are made in Figs. 3 and 4. The calculated results are in good agreement with the measured spectra at every emission angle, although they underestimate the measured data by about a factor of two in the region of several tens MeV. Origin of this discrepancy is under consideration now.

References

1) K.Ishibashi, et al., JAERI-M 93-046 p.82 (1993).
2) J.K.Dickens, ORNL-6436 (1988).
3) S.Meigo, et al., JAERI-Review 94-009 p.268 (1994).
4) R.A.Arndt, et al., Phys. Rev., D35, 128(1987).
5) R.A.Cecil, et al., Nucl. Instrum. Meth., 161 439 (1979).
6) R.H.Jonson and B.W.Wehring, ORNL/RSIC-40 p.33(1976).
7) Y.Nakahara and T.Tsutsui, JAERI-M 82-198 (1982).
8) J.F.Briesmeister, et al., RSIC/CCC-200 (1991).

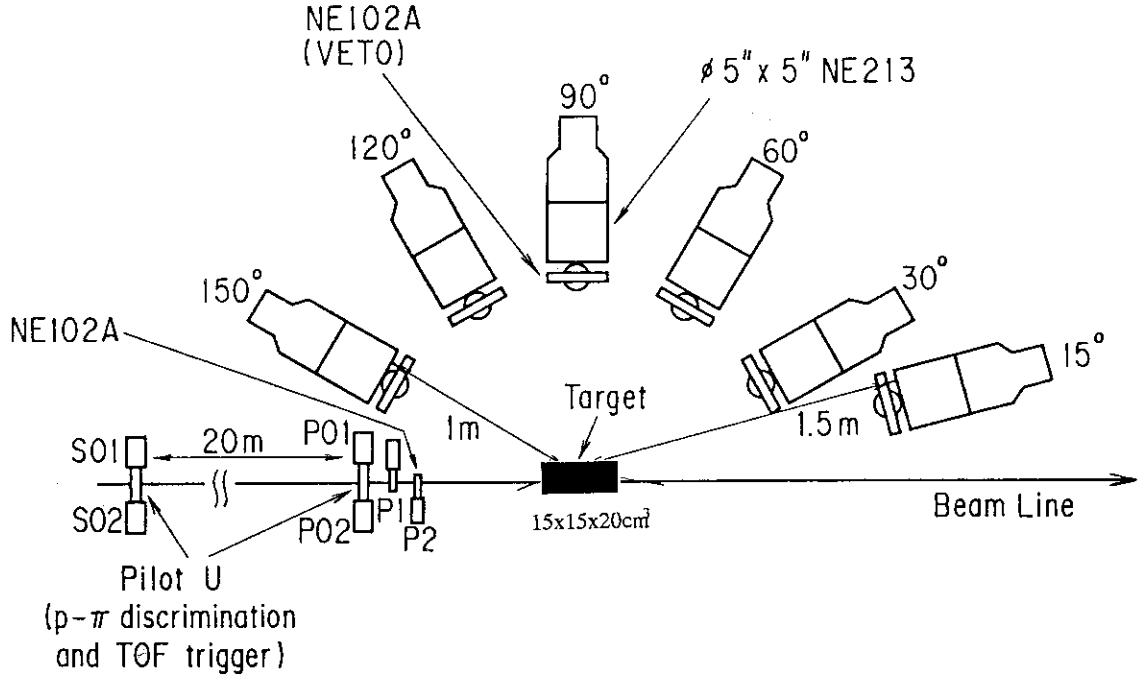

Fig. 1 Illustration of the experimental arrangement.

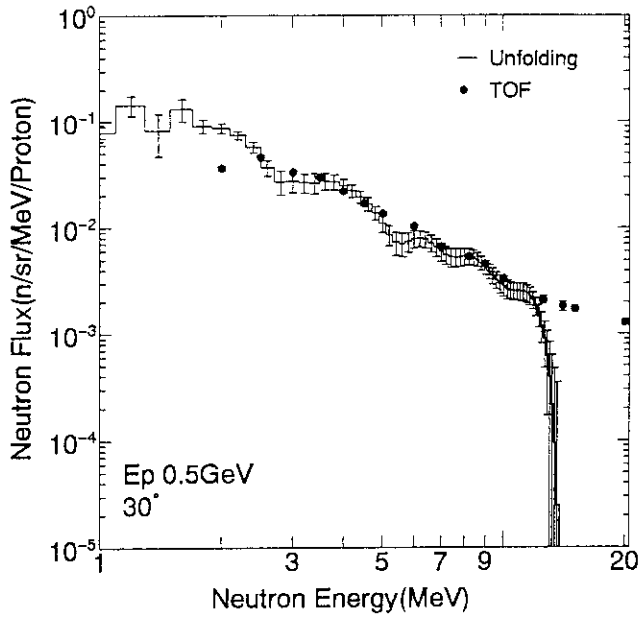

Fig. 2 Comparison of neutron spectra obtained by TOF and unfolding methods for 0.5 GeV proton incidence on thick lead target at 30°.

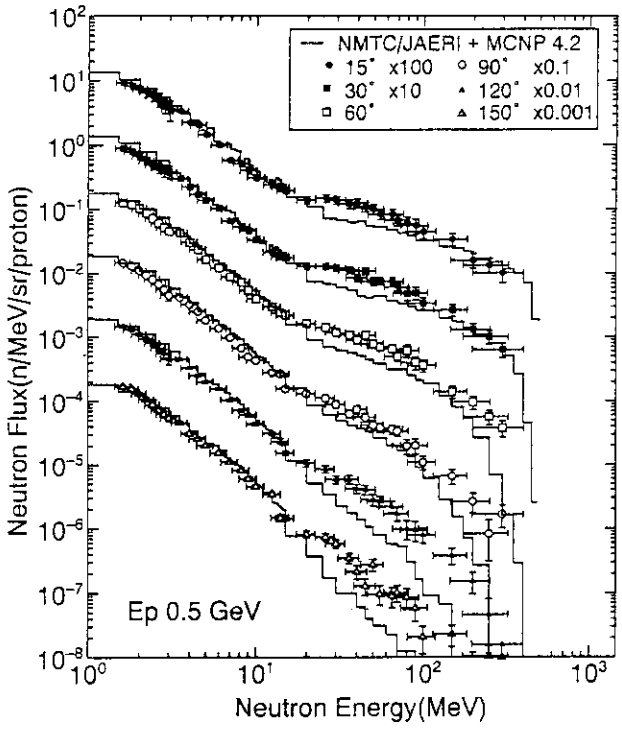

Fig. 3 Neutron spectra for 0.5 GeV proton incidence on thick lead target.

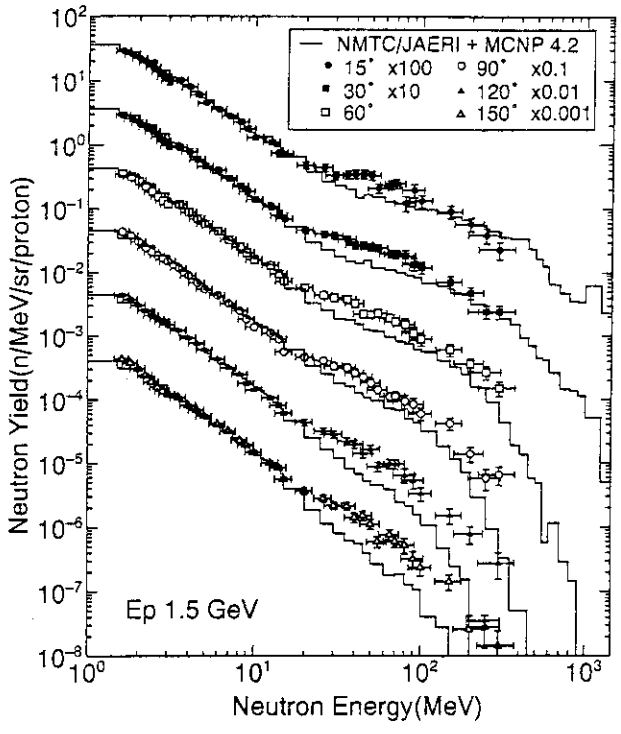

Fig. 4 Neutron spectra for 1.5 GeV proton incidence on thick lead target.

3.24 Systematics of Fragmentation Reaction and their Incorporation into HETC

Nobuhiro SHIGYO, Tatushi NAKAMOTO and Kenji ISHIBASHI

Department of Nuclear Engineering, Kyushu University
Hakozaki, Fukuoka-shi 812, Japan

We construct the systematics on the fragmentation reaction by means of the mass yields and the kinetic energy spectra of the fragments. The nuclear temperature obtained from the mass yields and the energy spectra are averaged to the same value for the specified incident proton energy. The systematics are incorporated as a subroutine set into HETC. The incorporation of this systematics is mostly appropriate for representing the experimental data.

1. Introduction

A computer code High Energy Transport Code (HETC)[1] is used for engineering purposes. This code describes the spallation reaction by the cascade-evaporation model. The model divides the reaction into two processes. In the cascade process, a nucleus emits nucleons by the intra-nuclear cascade collision. Subsequently, nucleons and light nuclei of low energies are emitted in the evaporation process. In some cases, the nucleus reaches a state of a very high excitation energy after the cascade process, and intermediate-mass fragments are emitted. The fragments are not released by the evaporation process at all. Since the fragmentation step is not included in HETC, we attempt to incorporate this process.

Before the incorporation of the fragmentation process, we construct the systematics on the reaction. We are interested in the mass yields and the kinetic energy spectra of the proton induced fragmentation reaction. We use the data of the mass yields and the energy spectra for incident proton energies of 0.48 GeV on Ag[2], 1.6, 2.3 and 3.1 GeV on Xe[3].

2. Systematics of Fragmentation

2-1. Mass Yields

Panagiotou et al.[4] have proposed the probability for the fragment formation by simplifying the liquid-gas phase transition model. In the energy range of the incident protons concerned, the mass yields were found to be described by modifying their probability as

$$Y\left(A_f\right)=\alpha A_f^{-2.0}\exp\left[-16\left(1-\frac{T}{17}\right)^2 A_f^{2/3}/T\right], \tag{1}$$

where α is the normalization constant, and T is written in units of MeV. Fig. 1 shows the fragment mass yields. Dashed curves indicate the results of fitting by Eq. (1).

2-2. Kinetic Energy Spectra

For the kinetic energy spectra of the fragments, Porile et al.[3] have assumed the thermal droplet model for estimating the Coulomb barrier, and described the kinetic energy spectra with a complex form with double integration. On the condition concerned, we found a simpler expression given by

$$\frac{d^2\sigma}{dE_f d\Omega}=\frac{K}{T}\left(\frac{E_f}{E^*}\right)^{1/2}\frac{1}{2}\left[1-\tanh\left(-\frac{E^*-C}{D}\right)\right]\exp\left(-\frac{E^*}{T/\nu}\right), \tag{2}$$

where C and D are the quantities corresponding to the most probable Coulomb barrier, and the variance of Coulomb barrier, respectively, and K is the normalization constant. Figs. 2 and 3 indicate the results of Eq. (2) with the dashed curves. These figures indicate that the systematics is suitable for reproducing experimental data.

2-3. Common Temperature

Both of the mass yields and the kinetic energy spectra are originated from the same phenomenon with a common nuclear temperature in principle. Then, the nuclear temperatures obtained for both affairs were averaged to be the same value for the specified incident proton energy. The empirical expression for the common nuclear temperature T(MeV) is given by

$$T=17\left[1-\exp\left(-\frac{E_p-120}{460}\right)\right], \tag{3}$$

where E_p is the incident proton energy in units of MeV. Figure 4 shows the common nuclear temperatures as a function of the incident proton energies.

3. Incorporation into HETC

The systematics thus constructed were incorporated as a subroutine set into HETC. In the calculation by this code, the probability of the fragmentation and the nuclear temperature are derived from an excitation energy of the nucleus after the cascade process, respectively.

$$P = 1.8 \times 10^{-5}\left(E_x - 50\right)^{1.5}, \tag{4}$$

$$T = 17.5\left[1 - \exp\left(-\frac{E_x - 50}{200}\right)\right], \tag{5}$$

where P is the probability of the fragmentation, and E_x is the excitation energy after the cascade process in units of MeV. The histograms in Figs. 1 - 3 show the results of the fragmentation-incorporated HETC. These figures show that the experimental data are reproduced by incorporating the fragmentation process into the code.

4. Summary

We constructed the systematics of the fragmentation reaction. The nuclear temperatures obtained from the mass yields and the kinetic energy spectra were averaged to the same value for the specified incident proton energy. The mass yields and the energy spectra of the fragments were represented by the systematics reasonably. The incorporation of this systematics into HETC was mostly appropriate for reproducing the mass yields and the kinetic energy spectra of the fragments.

References

(1) CHANDLER, K.C., ARMSTRONG T.W.: *ORNL*-4744, (1972)
(2) GREEN, R.E.L., et al.: *Phys. Rev.*, **C29**, 1806 (1984)
(3) PORILE, N.T., et al.: *Phys. Rev.*, **C39**, 1914 (1989)
(4) PANAGIOTOU, A.D., et al.: *Phys. Rev.*, **C31**, 55 (1985)

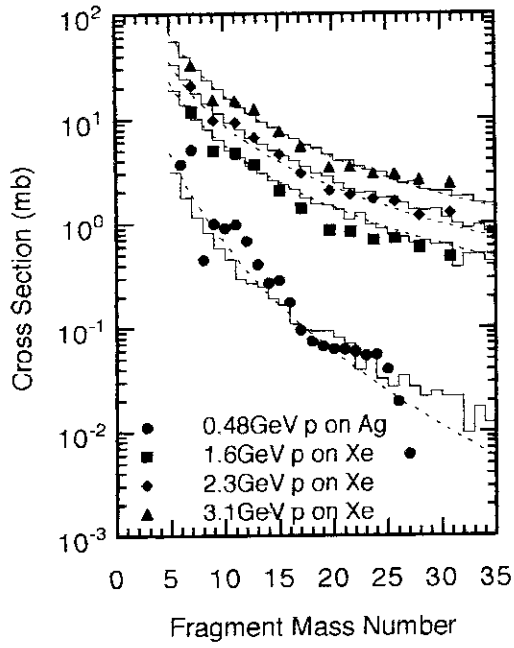

Fig. 1 Mass Yields of fragments for various targets and proton energies. Dashed curves are the results of the systematics, and solid lines are those of HETC.

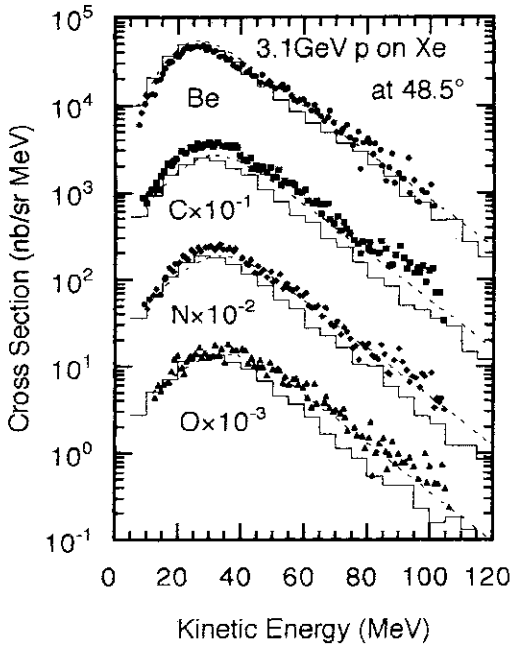

Fig. 2 Kinetic energy spectra of fragments in the reaction p + Xe for 3.1 GeV protons energy. (See Fig. 1)

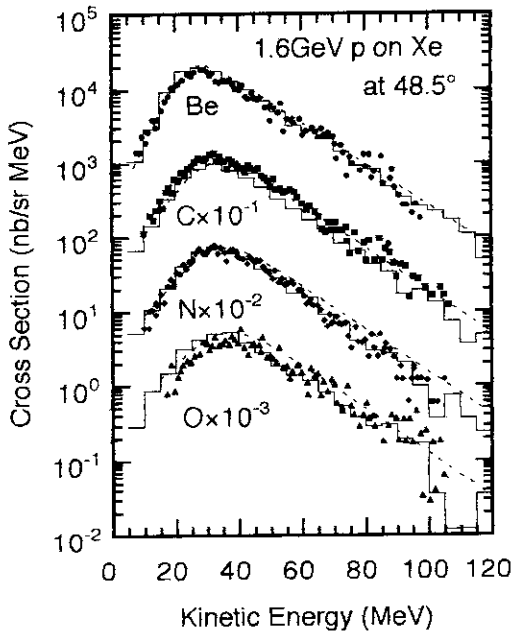

Fig. 3 Kinetic energy spectra of fragments in the reaction p + Xe for 1.6 GeV protons energy. (See Fig. 1)

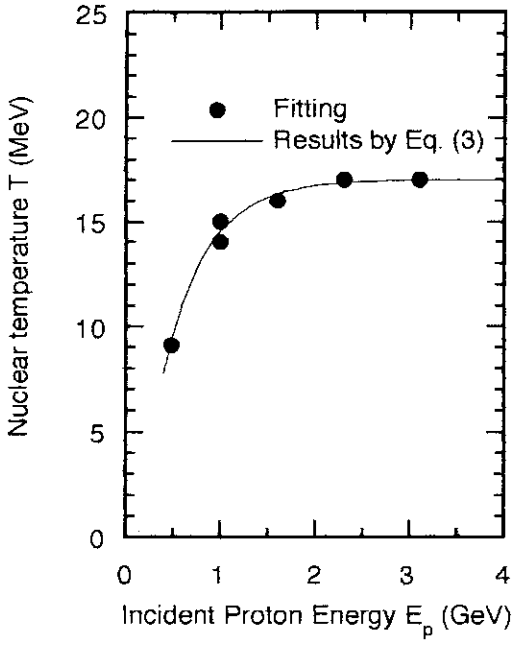

Fig. 4 Nuclear temperature as a function of incident proton energy.

3.25 Evaluation of High Energy Fission Models for High Energy Nuclear Reaction and Transport Codes

Nobuaki Yoshizawa[1], Takahiko Nishida[2] and Hiroshi Takada[2]

1. Mitsubish Research Institute Inc.

Otemachi , Chiyoda-ku, Tokyo 100

2. Japan Atomic Energy Research Institute

Tokai-mura, Naka-gun, Ibaraki 319-11

Abstract

Benchmark calculations were made to examine the accuracy of the high energy fission models proposed with Nakahara and Achison, respectively. We have calculated ^{238}U(p,f), ^{209}Bi(p,f) and ^{235}U(n,f) cross sections by using two high energy transport codes NUCLEUS and HETC-KFA2. For ^{238}U(p,f) cross section, differences between experimental data and calculated results were from 30 to 50 %. Those codes underestimate cross section for ^{209}Bi(p,f) reaction below 1000 MeV. For the residual mass distributions through the high energy proton induced ^{238}U reactions, the calculated results with HETC-KFA2 agreed well with the experimental data between the mass number from 100 to 140. For ^{235}U(n,f) cross section at 20 MeV, the codes estimated the cross sections significantly smaller than JENDL-3.2 since the underestimation of total cross sections in the codes.

Introduction

Evaluation of high energy fission cross sections of actinoids is important to estimate the amount of radioactive waste transmutated by using high energy particle. In high energy particle-induced reactions, estimations of high energy fission of sub-actinoides should be also taken into accounts because its cross section increases with the incident energy.

High Energy Fission Models

Atchison and Nakahara proposed high energy fission model [1, 2]. As shown in **Fig. 1**, the high energy fission process is treated as a competitive process to evaporation process after the cascade process in the models. Fission width of the excited compound nucleus is determined with experimental data and mass distributions of fission fragments are approximated by the weighted summation of the single and double peaked Gaussian distributions. The Atchison model is adopted in HETC-KFA2[3]. The Nakahara model is adopted in NMTC/JAERI[2] and NUCLEUS[4].

High Energy Fission Cross Sections

In **Fig. 2**, the calculated results with NUCLEUS and HETC-KFA2 are compared with the experimental data[5-15] for $^{238}U(p,f)$ cross sections. It is observed that the calculated results are lower than the experimental data by about 50% above 100 MeV. NUCLEUS gives the cross section about 20 % smaller than those of HETC-KFA2.

In **Fig. 3**, proton induced fission cross sections of ^{209}Bi calculated with NUCLEUS and HETC-KFA2 are lower than experimental data[5, 6, 8, 9, 13-21], below 1000 MeV. It is found that there is a room to be improved for the high energy fission in both models.

Residual mass distributions

After 300 and 2900MeV proton induced in ^{238}U reactions, residual mass distributions calculated with HETC-KFA2 well agree with experimental data[12, 22]in the mass number range about 100 to 140, as shown in **Figs. 4** and **5**. The residual nuclei in this mass range are mainly produced with high energy fission. NUCLEUS gives broader mass distributions than HETC-KFA2. This comes from the fact that the width of the Gaussian distribution is wider in NUCLEUS than in HETC-KFA2. Consequently, it seems that the width of the width of the Gaussian distribution should be adjusted in NUCLEUS.

Connection to JENDL-3.2

In **Fig. 6,** calculated results of $^{235}U(n,f)$ cross sections are compared with the evaluated value in JENDL-3.2[23] and experimental data[24]. Calculated cross sections are smaller than that of the evaluated value in JENDL-3.2 at 20 MeV. The major reason of this discrepancy seems to be the fact that the geometrical cross section is employed constantly as the total cross sections independent of the incident energy in NUCLEUS and HETC-KFA2. Since the total cross section exhibits energy dependence in energy below 100 MeV, it is necessary to take this energy dependence into account correctly in the codes. On the other hand, the difference between calculated results and experimental data are about 50% above about 50MeV. The cross sections calculated with HETC-KFA2 are greater than those with NUCLEUS about 30 % similar to $^{238}U(p,f)$ reactions.

Conclusion

Proton induced high energy fission cross section of ^{238}U and ^{209}Bi calculated with Nakahara and Atchison models are compared with experimental data. For ^{238}U, calculated results differ from experimental data about 50% above 100 MeV. Results of NUCLEUS are about 80% of HETC-KFA2. For ^{209}Bi, calculated results significantly underestimate experimental data. Residual mass distribution through the proton induced ^{238}U reaction calculated with HETC-KFA2 well agreed with experimental data for the fission fragments.

Neutron induced high energy fission cross section calculated with the two models are discontinuous to the evaluated cross section of the JENDL-3.2 at 20 MeV.

Acknowledgment

The authors wish to thank Dr. T. Fukahori for his useful discussion about the treatment of the high energy fission process and the introductions of the many experimental data collected by him. The authors also gratefully acknowledge Drs. Y. Nakahara and S. Iwai for their encouragement.

References

(1) ATCHISON, F. : *Jül-Conf*-34, (1980).

(2) NAKAHARA, Y., *et al.* : *JAERI-M* 82-198, (1982).

(3) CLOTH, P., *et al.* : *KFA-IRE-E AN*/12/88, (1988).

(4) NISHIDA, T., *et al.* : *JAERI-M* 86-116, (1986).

(5) KHAN, H. A., *et al.* : *Phys. Rev.* **C29** (1984) 2199.

(6) BYSHENKOV, V.S., *et al.* : *Sov. J. Nucl. Phys.* **17** (1973) 496.

(7) REMY, C., *et al.* : *Nucl. Phys.* **A163** (1971) 583.

(8) HUDIS, J., *et al.* : *Phys. Rev.* **180** (1969) 1122.

(9) KON'SHIN, V.A., *et al.* : *Sov. J. Nucl. Phys.* 2 (1966) 489.

(10) DOSTROVSKY, I., *et al.* : *Phys. Rev.* **139** (1965) B1513.

(11) BATE, G.L., *et al.* : *Phys Rev.* **133** (1964) B1471.

(12) STEVENSON, P.C., *et al* : *Phys. Rev.* **111** (1958) 886.

(13) JUNGERMAN, J., *et al.* : *Phys. Rev.* **79** (1956) 632.

(14) STEINER, H.M., *et al.* : *Phys. Rev.* **101** (1956) 807.

(15) LINDER, M., *et al.* : *Phys. Rev.* **94** (1954) 1323.

(16) VAISHNENE, L.A., *et al.* : *Z. Phys.* **A302** (1981) 143.

(17) BOCHAGOV, B.A., *et al.* : *Sov. J. Nucl. Phys.* **28** (1978) 291.

(18) HUDIS, J., *et al.* : *Phys. Rev.* **C13** (1976) 1961.

(19) BRANDT, R., *et al.* : *Revue de Physique Appliquee* **7** (1972) 243.

(20) MATUSEVICH, E.S., *et al.* : *Sov. J. Nucl. Phys.* **7** (1968) 708.

(21) JODRA, L.G., *et al.* : *Phys. Rev.* **99** (1955) 1470.

(22) FRIEDLANDER, G. : *" Fission of Heavy Elements by High-Energy Protons, in Physics and Chemistry of Fission," IAEA, Vienna* (1965).

(23) SHIBATA, K. *et al.* : *JAERI* 1319 (1990).

(24) RAPAPORT, J. *et al.* : *LA-11078-MS* (1987).

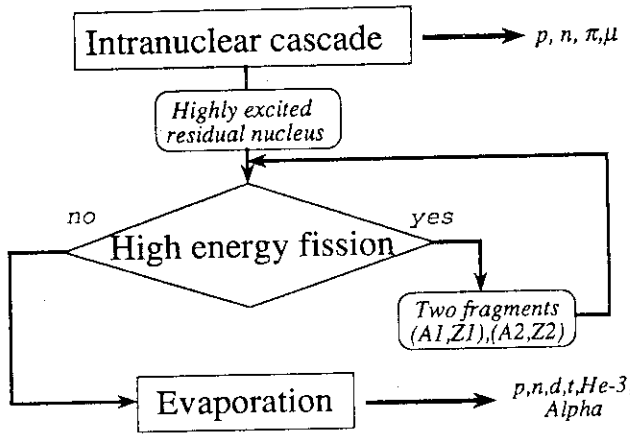

Fig.1 High energy fission calculation in the high energy transport codes

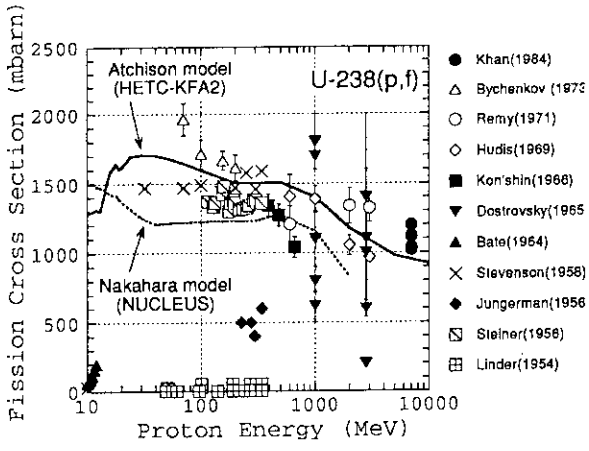

Fig.2 High energy fission cross sections calculated with Atchison (HETC) and Nakahara (NUCLEUS) models

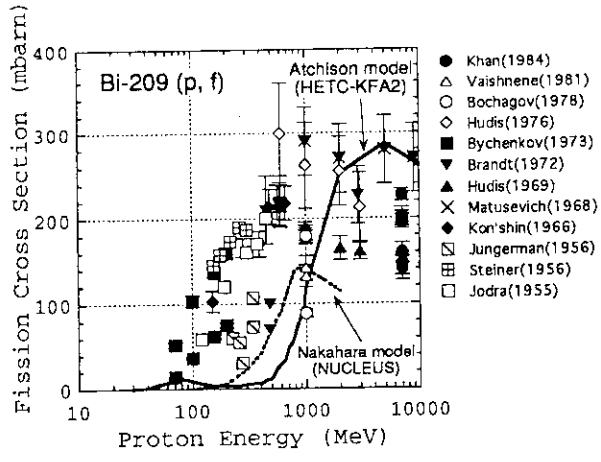

Fig.3 High energy fission cross sections calculated with Atchison (HETC) and Nakahara (NUCLEUS) models

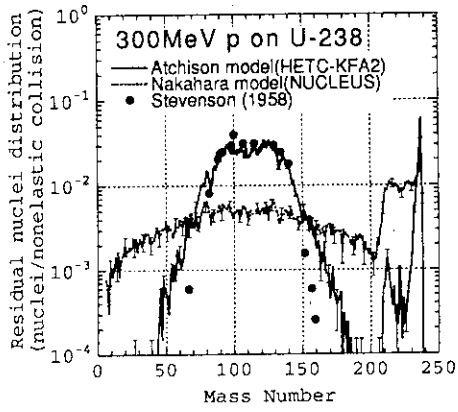

Fig.4 Comparison of residual nuclei distribution between calculation with the two models and experimental data

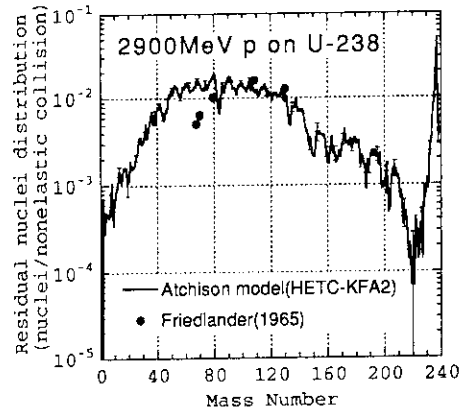

Fig.5 Comparison of residual nuclei distributions between calculation with Atchison model (HETC-KFA2) and experimental data

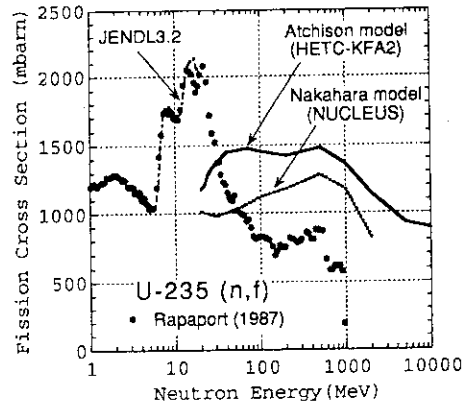

Fig.6 High energy fission cross sections calculated with Atchison (HETC) and Nakahara (NUCLEUS) models

3.26 Measurement of Preequilibrium (p, p') Spectra at Small Angles

M. Hayashi, Y. Nakao, S. Yoshioka, M. Harada, M. Higashi, H. Ijiri, and Y. Watanabe
Department of Energy Conversion Engineering, Kyushu University,
Kasuga, Fukuoka 816, Japan

A ΔE-E Si-detector counter telescope with an active collimator was developed in order to reduce backgrounds due to a large yield of elastically-scattered protons in measurements of continuum (p,p') spectra at small angles. Preequilibrium spectra of 14.1-MeV (p,p') for ^{60}Ni and ^{93}Nb were measured over a wide angle range from 15° to 160° using the developed detector system.

1. Introduction

In recent years, a variety of experimental data on proton-induced reactions (e.g., inclusive particle emission spectra, such as (p,xp) and (p,xn) spectra) are required in intermediate energy nuclear data evaluation. In general, one can obtain the data with better statistics in proton experiments than in neutron experiments. However, an extremely large yield of elastically-scattered protons by Coulomb interaction makes it difficult to measure (p,p') spectra at small angles, because the intense flux of elastically-scattered protons gives rise to the background tail of low energy pulses. The tail is known to originate mainly from two physical sources [1]: (I) slit-edge scattering effect of a defining slit placed in front of a detector, and (II) nuclear reactions generated in the detector.

In the present work, we have developed a ΔE-E silicon detector counter telescope system with an active collimator in order to reduce the above-mentioned backgrounds. In addition, the proton transportation in matter by multiple Coulomb scattering is simulated by a Monte Carlo method to understand the mechanism of slit-edge scattering, and the result is compared with the experimental one. Finally, the counter telescope system is applied to a measurement of 14.1-MeV (p,xp) spectra for ^{60}Ni and ^{93}Nb using a proton beam from the Kyushu University Tandem accelerator.

2. Counter telescope system

Figure 1 illustrates an experimental setup and a schematic side view of an active collimator used in the ΔE (75 μm) - E (2000 μm) silicon detector counter telescope. The active collimator consisting of a 1 mm thick NE102A plastic scintillator was connected with a photomultiplier (Hamamatsu model R5600U) through a light guide and operated as a veto detector. An event that an emitted proton passes through the active collimator was rejected in the data acquisition using the veto signal from the active collimator. Thus it is possible to

eliminate the background (I) due to the slit-edge scattering effect. Pulse height signals from each detector were processed with conventional NIM modules including a particle-identification (PI) module and stored as a two-dimensional list data (ΔE+E and PI pulse heights). Using the two-dimensional plot, one can separate the background events (II) from true events of (p,p') scattering as mentioned below.

3. Experimental results and discussions

3.1 Background due to slit-edge scattering

To estimate the slit-edge scattering background, we show a comparison between the energy spectrum measured with the active collimator (solid circles) and that with the passive collimator made of stainless steel (open circles) for ^{197}Au(p,p') at 16 MeV in Fig.2(a). It was found that the use of the active collimator led to about 70% reduction of the continuous background.

Next, a simulation of the slit-edge scattering process was carried out using a Monte Carlo method, assuming that protons are transported in the metallic collimator by the multiple Coulomb scattering. A comparison of the calculated result with the experimental spectrum of edge-scattering protons is shown in Fig.2(b). A good agreement is seen except for the low energy region below 6 MeV. This result indicates that the active collimator operated successfully so that the edge scattering background could be eliminated almost completely.

3.2 Nuclear reactions in E-detector

Some satellite peaks are observed at energies between 8 and 12 MeV in Fig.2(a). These peaks arise from the background events that elastic protons give rise to nuclear reactions (mainly, (p,p') scattering) with Si in the E-detector [2]. The events appear as a locus on a two-dimensional plot as a function of ΔE+E signals and PI signals as shown in Fig. 3. We can readily separate them from the events of inelastically-emitted protons .

3.3 Measurement of 14.1-MeV(p,xp) for ^{60}Ni and ^{93}Nb

Since we have found it possible to reduce the two kinds of background (I) and (II) by about an order of magnitude in the continuum region, we have applied the above-mentioned ΔE-E Si-detector counter telescope system to a measurement of double differential cross sections for 14.1-MeV (p,p') for ^{60}Ni and ^{93}Nb at angles from 15° to 160°. The experimental (p,p') spectra for ^{60}Ni are shown in Fig.4. We have obtained a preliminary result that the experimental continuum (p,p') angular distributions for ^{60}Ni are nearly isotropic in the c.m. system in the low outgoing proton energy region where the multistep compound process is dominant, as the statistical multistep theory, such as the FKK theory [3], predicts.

4. Summary

The active collimator installed in the ΔE-E Si-detector counter telescope was found to work well to reduce the slit-edge scattering contribution which is one of troublesome backgrounds in the measurement of continuum (p,p') spectra at small angles. Moreover, the ΔE-E two-dimensional measurement made it possible to eliminate the background due to nuclear reactions occurring in the thick E-detector. We have measured the 14.1-MeV (p,xp) spectra for ^{60}Ni and ^{93}Nb at angles from 15° to 160°, under the low background condition achieved with the ΔE-E Si-detector counter system.

Acknowledgments

The authors wish to thank Drs. K. Sagara and H. Nakamura for their kind help during the experiment. They gratefully acknowledge the Tandem Accelerator Laboratory, Faculty of Science, Kyushu University, for the financial support for the experiment. They also express their thanks to Mr. S. Meigo (JAERI) for allowing them to use the multiparameter data-acquisition unit belonging to his laboratory and his kind advice for use.

References

[1] F.E. Bertrand et al., Nucl. Instr. and Methods **101**, 475 (1972).

[2] M. Makino et al., Nucl. Instr. and Methods **81**, 125 (1970).

[3] H. Feschbach, A. Kerman, and S. Koonin, Ann. Phys. (N.Y.) **125**, 429 (1980).

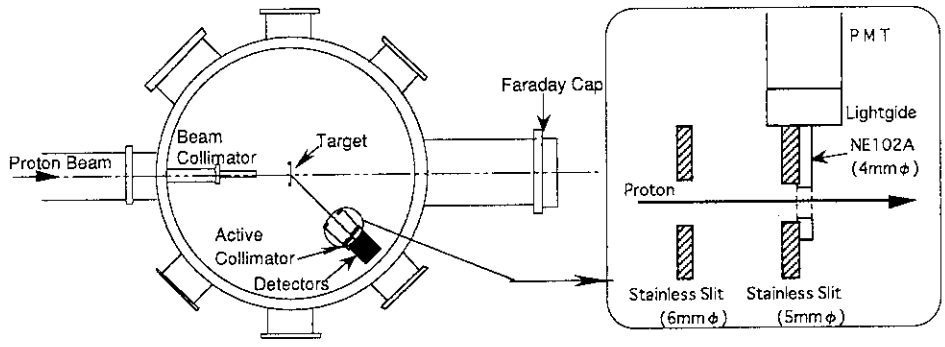

Fig. 1 Experimental setup in left and schematic side view of an active collimator used in ΔE-E counter telescope in right.

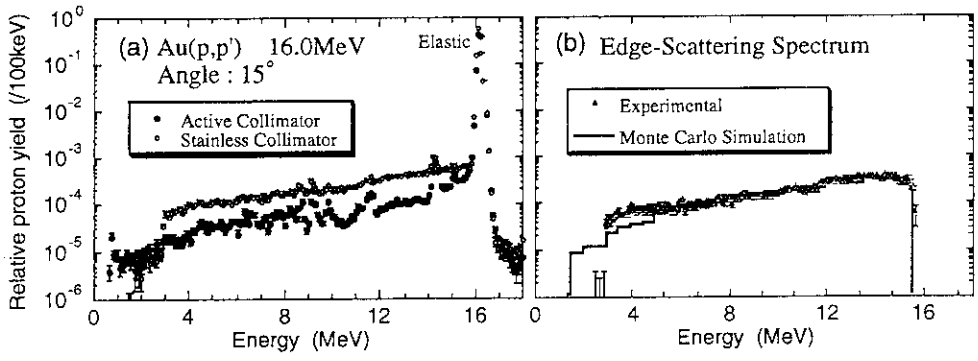

Fig. 2 (a) Proton emission spectra for ^{197}Au(p, p') at 16 MeV measured with active collimator (NE102A) and with passive collimator (stainless steel), (b) a comparison of the experimental slit-edge scattering spectrum with that calculated by the Monte Carlo simulation.

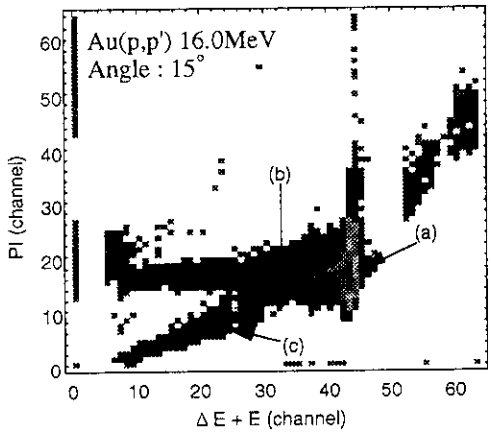

Fig. 3 Two-dimensional contour plot as a function of ΔE+E and PI signal pulse heights. The area indicated by (a) corresponds to the elastic proton peak and that denoted by (b) to inelastic protons and the remaining background of edge scattering. The background events due to nuclear reactions in the Si-E detector appears as a locus marked by (c).

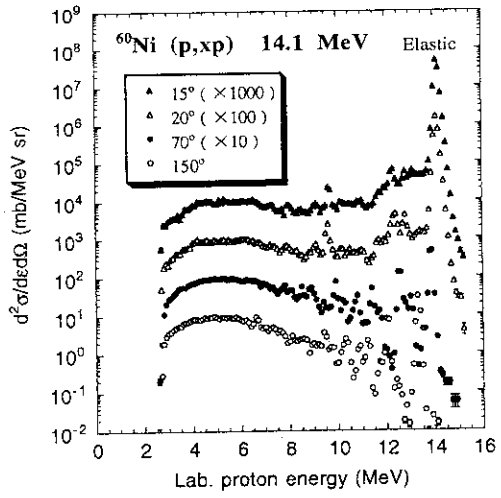

Fig. 4 Experimental proton emission spectra from ^{60}Ni(p, xp) reaction at 14.1-MeV. The cross sections are given in the lab. system.

3.27 Precise Measurement of γ-ray Emission Probabilities for Radioisotopes with Half-lives of a Few Hours

Gatot Wurdiyanto, Atsushi Yoshida and Hiroshi Miyahara
Nagoya University, Department of Nuclear Engineering
Furo-cho, Chikusa-ku, Nagoya 464-01

The γ-ray emission probabilities for ^{116m}In with half-life of 54.15 min have been measured by a 4πβ(PC)-γ(HPGe) coincidence apparatus using a live-timed bi-dimensional data acquisition system. Those for eleven γ-rays were determined with the uncertainties less than 1%.

Introduction

Accurate value of the decay data is an important factor for wide application of radioisotopes in various fields. There is, however, no doubt that the evaluated γ-ray emission probabilities for many nuclides (especially short-lived nuclides) have insufficient precision. When a nuclide transits directly to the ground state, the β-ray branching ratio in addition to the relative γ-ray intensity is required for determination of γ-ray emission probability. Since the uncertainty of β-ray branching ratio is usually large and affects the certainty of γ-ray emission probability. One method for improvement is to determine the emission probability from the measurement of disintegration rate and absolute γ-ray intensity.

Recently, we have been measuring precisely the disintegration rate and γ-ray spectrum in a short time by a 4πβ(PPC)-γ(HPGe) coincidence apparatus using a live-timed bi-dimensional data acquisition system. By using this apparatus, the following results have been obtained that the γ-ray emission probabilities for ^{175}Yb[1] were twice of the evaluated values[2], and that those for ^{128}I[3] were smaller than the evaluated values by about 25%.

We have carried out a precise measurement of the γ-ray emission probabilities for ^{116m}In with half-life of 54.15 min. All of authors[4~6] were convinced that ^{116m}In does not decay directly to the ground state, and they determined the γ-ray emission probabilities on the assumption that the sum of two γ-rays, 1294 keV and 2112 keV, equals to unity. Their results contain systematic uncertainties more than 5% due to the uncertainties of the relative γ-ray intensities. We show the results of our experiment and also the results for ^{139}Ba with half-life of 82.9 min and ^{188}Re with that of 16.98 hour that those are still on the stage of measurement.

Apparatus

A new system which has been developed is composed of a 4πβ(PC), an HPGe detector with a relative efficiency of 23% and coincidence apparatus using a live-timed bi-dimensional data acquisition system (Fig. 1)[7]. Outputs from each detector through the preamplifier are amplified and discriminated by Ortec 490B amplifier, then the digital outputs go to the coincidence controller which determines single or coincidence event within a resolving time. When the outputs are judged to be coincidence event, the ADCs analyze the pulse height of each analog input. An ADC controller has function to transfer information of β or γ channel, pulse heights and time relation to a microcomputer. After the data of 2^{12} events are stored on a dynamic random access memory (DRAM) in the

computer, then the data are written on a magnetic tape and following data are stored in another DRAM.

Source preparation

All sources were produced by thermal neutron irradiation (2.34 ~ 2.75 x 10^{13} $cm^{-2}.sec^{-1}$) at the Kyoto University Research Reactor. The samples were ^{115}In powder (enrichment : 99.9%), $^{138}BaCO_3$ powder (99.80%) and ^{187}Re powder (99.39%). The irradiated sources were dissolved in weak HCl solution, and one drop of solution was placed onto a metallized VYNS film. It was covered with similar film after drying under infrared lamp.

Results of measurement

The γ-ray detection efficiencies were determined from measurement of standard sources of ^{24}Na, ^{57}Co, ^{60}Co, ^{133}Ba and ^{152}Eu. The efficiencies were evaluated for about twenty energies after correction for the cascade-summing effect.

After the data have been collected on magnetic tape, the coincidence efficiency function can be derived by computer discrimination method[8] and γ-ray spectrum is obtained. The eight peaks of ^{116m}In were clearly recognized in the γ-ray spectrum. Coincidence efficiency functions were obtained for gate sets of the 138, 417, 819, 1097, 1294, 1507, 1754 and 2112 keV γ-rays, and an example of the coincidence efficiency function is shown in Fig. 2. The disintegration rate can be determined from extrapolation which carried out using a linear function fitted to the data. The mean value, however, was calculated from the results for the 417, 819, 1097 and 1294 keV γ-rays within the uncertainty less than 1%.

The measured γ-ray emission probabilities of ^{116m}In and published results are shown in Table 1, where the emission probabilities of the present results are the mean values of the four time runs, and 3 ~ 5 sources were measured at each run. The uncertainties of all present results are less than 1%. Fig. 3 shows the decay scheme calculated from the present results and the internal conversion coefficients shown in the Nuclear Data Sheets [9].

We also measured the γ-ray emission probabilities of ^{139}Ba and ^{188}Re shown in Tables 2 and 3, but the results are on the stage of measurement. The disintegration rate of ^{188}Re was determined for gate sets of the 155, 478 and 633 keV γ-rays, and ^{139}Ba was determined for gate set of the 166 keV γ-rays.

Summary

It is possible to measure the γ-ray emission probabilities for short-lived nuclides by a 4πβ(PC)-γ(HPGe) coincidence apparatus using a live-timed bi-dimensional data acquisition system.

For the strongest emission of the 1294 keV γ-rays of ^{116m}In, the measured emission probability agreed with those of the Nuclear Data Sheets[9] and Rabenstein[10]. On the other hand, our result for the 417 keV γ-rays was smaller by 8% than that of the Nuclear Data Sheets, and the uncertainty of our result was smaller than 1%.

References

1) Miyahara H., Matumoto H. and Mori C.; Appl. Radiat. Isot. **45** 219 (1994).
2) Browne E. and Firestone R.B.; "Table of Radioactive Isotopes", (1986) Wiley, New York.

3) Miyahara H. et al.; Nucl. Instrum. and Meth. **A336** 385 (1993).
4) Bolotin H.H.; Phys. Rev. **B1557** 136 (1964).
5) Fettweis P. and Vervier J.; Z. Phys. **201** 465 (1967).
6) Garcia-Bermudez G. et al.; Phys. Rev. **C9** 1060 (1974).
7) Miyahara H. et al.; J. Nucl. Sci. Technol. **31** 521 (1994).
8) Smith D.; Metrologia **11** 73 (1975).
9) Blachot J. et al.; Nuclear Data Sheets **32** 325 (1981).
10) Rabenstein D.; Z. Physik **240** 244 (1970).

Table 1. The measured γ-ray emission probabilities of ^{116m}In and published results (%).

Energy (keV)	Present work	P.Fettweis et al. (1967)	Rabenstein (1970)	Garcia-Bermudez et al. (1974)	Table of Isotopes (1978)	Nuclear Data Sheets (1981)
138.3	3.668(27)	4.0(4)	3.33(20)	4.7(2)	3.33(20)	3.29(12)
355.4	0.728(27)	0.85(8)	0.85(6)	0.78(5)	0.85(6)	0.83(4)
416.9	26.95(25)	33(3)	32.4(15)	29(2)	32.4(15)	29.2(14)
463.1	0.706(28)	0.89(9)	0.85(6)	0.77(6)	0.85(6)	0.83(5)
818.7	12.23(15)	14(1)	11.8(6)	12.3(7)	11.8(6)	11.5(4)
972.5	0.529(59)	-	0.46(3)	-	0.46(3)	0.454(16)
1097	58.52(24)	49(5)	55.7(15)	59(3)	55.7(15)	56.2(11)
1294	85.15(38)	82(8)	85.0(20)	84(4)	85.0(20)	84.4(4)
1507	9.89(6)	15(1)	10.2(5)	9.9(5)	10.2(5)	9.96(34)
1754	2.320(28)	1.7(2)	2.44(20)	2.3(2)	2.44(20)	2.48(8)
2112	15.05(9)	18(2)	15.0(10)	15.7(9)	15.0(10)	15.5(4)

Table 2. The evaluated γ-ray emission probabilities of ^{139}Ba (%) and the present results that are on the stage of measurement.

Energy (keV)	Present work				Nuclear Data Sheets (1989)	Table of Radioactive Isotopes * (1986)
	Series			Mean		
	1	2	3			
165.8	23.06(18)	22.95(15)	23.12(15)	23.04(9)	23.78(25)	22
1420	0.228(21)	0.242(8)	0.248(12)	0.239(6)	0.261(26)	0.30(3)

* Systematic uncertainty : 4.6 %

Table 3. The evaluated γ-ray emission probabilities of ^{188}Re (%) and the present results that are on the stage of measurement.

Energy (keV)	Present work				Table of Radioactive Isotopes * (1986)	ICRP (1978)
	Series			Mean		
	1	2	3			
155	14.77(38)	14.76(10)	14.94(9)	14.82(13)	14.9(4)	14.9
453.3	0.100(9)	0.083(1)	0.085(3)	0.089(3)	0.0705(19)	0.070
478	0.974(37)	0.978(6)	1.055(9)	1.002(13)	1.04(3)	1.04
633	1.405(43)	1.391(9)	1.501(12)	1.432(15)	1.25(10)	1.25
872.5	0.108(10)	0.118(1)	0.116(3)	0.113(3)	0.111(3)	0.11
829.5	0.419(17)	0.422(3)	0.452(6)	0.431(6)	0.408(11)	0.408
937.3	0.702(10)	0.561(4)	0.593(7)	0.815(4)	0.562(14)	0.561

* Systematic uncertainty : 3.8 %

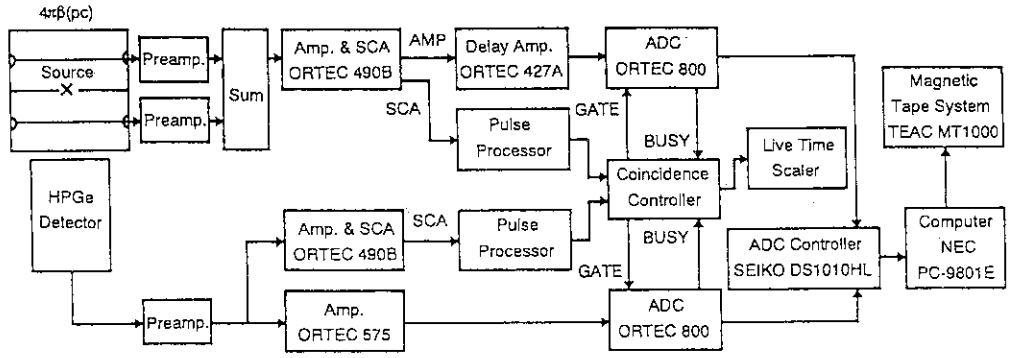

Fig. 1. A block diagram of the electronics for the live-timed bi -dimensional data acquisition system composed of the 4πβ(PC) and the HPGe detector.

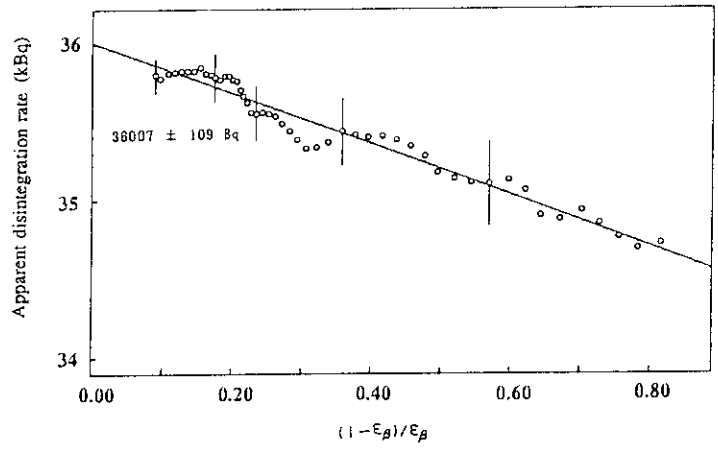

Fig. 2. An example of coincidence efficiency function of ^{116m}In derived by the computer discrimination method for gate set of the 417 keV γ-rays.

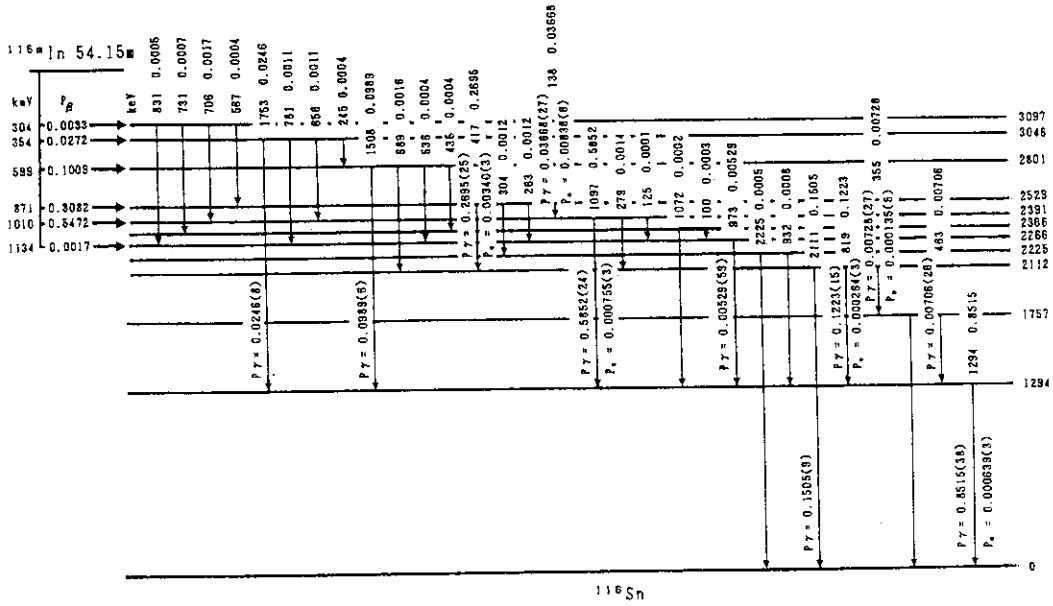

Fig. 3. The decay scheme and the proposed probability values for ^{116m}In.

3.28 Neutron Effective Charge for Primary E1 Transitions from Broad Neutron Resonance on p-shell and sd-shell Nuclei

Hideo KITAZAWA
Faculty of Engineering
Tokyo Institute of Technology
2-12-1 O-okayama, Meguro-ku, Tokyo 152

Strong retardation of primary single-particle E1 transitions from broad neutron resonances on p-shell and sd-shell nuclei, previously observed in E1 transitions from the $d_{5/2}$-wave neutron resonance on ^{9}Be at 622 keV and from the the $p_{3/2}$-wave neutron resonances on ^{24}Mg at 84 keV and 431 keV, is reasonably explained by coupling a single-particle motion with the giant electric-dipole reaonance mode.

1. Introduction

Based upon a viewpoint of the valence-capture model[1,2], we have observed strong E1 transitions from broad s-wave neutron resonances on even-even sd-shell nuclei to the final states with a large spectroscopic factor. In consequence those transitions were found to be quite well explained by this model[3]. Furthermore, valence E1 transitions were also confirmed for electromagnetic transitions from broad $p_{3/2}$-wave neutron resonances on even-even and even-odd nuclei to the final states with strong s-wave character[4,5,6].

The single-particle feature of primary transitions from those resonances is in striking contrast with a well-known fact of the extreme retardation of E1 transitions between low-lying bound states. Probably, a great success of the valence-capture model in the present study would be due to a strong cancellation of the E1 transition matrix element in the nuclear internal region (see Fig. 1(a)), which causes a decoupling between the s-wave or p-wave single-particle motion and the giant dipole-resonance (GDR) excitation in the target nucleus.

However, a remarkable fact was found, as shown in Table 1, that the E1 transitions from the $p_{3/2}$-wave resonances on ^{24}Mg to the final states with strong d-wave character and those from the $d_{5/2}$-wave resonance on ^{9}Be to the final states with strong p-wave character are considerably hindered, as compared with the valence-capture model calculations (valence 1)[6,7]. As expected from Fig. 1(b), this E1 retardation may be caused by an essential contribution of the overlap integral in the nuclear internal region into the valence-capture transition

Here, E_R is the giant dipole-resonance energy, ΔE_{21} is the single-particle transition energy, and j_1 and j_2 are the total-spin quantum numbers of the initial and final single-particle states, respectively. The reduction factor $\tilde{\alpha}$ is related to the non-energy-weighted sum rule S_{new} for the isovector dipole mode,

$$S_{new} = \tilde{\alpha} \frac{A}{4\pi} \langle r^2 \rangle . \qquad (6)$$

The factor $\tilde{\alpha}$ lies between 0.2 and 1.0 and takes into account the effect of nucleon correlations on the sum rule. In Eq.(5), the second term of the right-hand side is a polarization charge produced by the core-polarization effect due to excitation of GDR.

Using Eq.(5), we calculate the renormalized neutron effective charge $e_f(E1)$ for the valence-neutron E1 transition from the 622 keV resonance to the 3368 keV(2^+) state in ^{10}Be. The model parameters, $\tilde{\alpha}$=0.66 estimated by a pure harmonic-oscillator model[9], v_1=100 MeV, E_R=23.0 MeV, and ΔE_{21}=6.79 MeV produce $e_f(E1)=0.62\bar{e}$. Then, the valence-capture model calculation using this effective charge gives the partil radiative width Γ_γ=0.63 eV, which is in excellent agreement with the observed value.

In the capture process, the dipole transition moment may receive an appreciable contribution from the external region of the nucleus, and thus the polarization effect depends on a radial form factor for the dipole field. How strongly a specific transition will be affected by the form factor depends on the shape of the relevant wave function in the neighborhood of the nuclear surface. In the case of ^{9}Be, the polarization effect is not so sensitive to the radial form factor of the particle-core coupling hamiltonian Eq.(3), because the radial wave functions of the initial and final single-particle states are nodeless in the nuclear internal region. On the other hand, the renormalized effective charge for the E1 transitions from the p-wave resonances on ^{24}Mg strongly depends on the form factor, because of a zero-crossing of the initial-state wave function in the nuclear internal region. However, a suitable choice of model parameters within reasonable values generates $e_f(E1)\approx 0.6\bar{e}$. In Table 1, the valence-capture model calculations with $e_f(E1)=0.6\bar{e}$ (valence 2) are comparable in substantial agreement with the observed values.

3. Summary

The E1 transitions from the $p_{3/2}$-wave neutron resonances on ^{24}Mg at 84 keV and 431 keV to the final states with strong d-wave character, and those from the $d_{5/2}$-wave resonance on ^{9}Be at 622 keV to the final states with strong p-wave character are considerably hindered, as compared with the Lane-Mughabghab valence-capture model calculations. This noticeable E1 retardation originates from a large reduction of the single-particle transition strength due to the repulsive coupling of the GDR mode.

matrix element, resulting in a repulsive coupling of the GDR mode to those single-particle motions. It is quite different from the fact that for the E1 transition from a single-particle p-state to a single-particle s-state (or vice versa), the transition matrix element strongly cancels out in this region. The repulsive coupling of the GDR mode may in turn lead to a large reduction of the single-particle E1 transition strength[8].

2. Theoretical Analysis and Discussion

In the present analysis, we assume a coupling scheme between a valence-nucleon single-particle motion and the isovector dipole mode of the core(target) nucleus in a resonance state[7]. The two-body interaction Vi between the valence nucleon and the ith core nucleon, which is responsible for the excitation of the dipole mode, is given by the zero-range force approximation as

$$V_i = P\tau_3\tau_{3i}\delta(\mathbf{r}-\mathbf{r}_i). \tag{1}$$

The interaction strength P is combined with the Lane symmetry potential, $V_L = (1/2A)(\boldsymbol{\tau}\cdot\mathbf{T}_t)v_1 f(r)$, for coupling between the nucleon isospin ($\boldsymbol{\tau}/2$) and target isospin $\mathbf{T}_t$:

$$P = \frac{1}{4}\frac{v_1 f(r)}{\rho_0(r)} \ . \tag{2}$$

The quantity $\rho_0(r)$ is the total isoscaler density and f(r) is a Woods-Saxon potential form factor. The symmetry-potential strength v_1 is repulsive and of order of 100 MeV. Then, the particle-core coupling hamiltonian $\hat{H}$ can be written

$$\hat{H}_{1\mu} = \frac{\pi v_1}{A\langle r^2\rangle}\tau_3 r f(r) Y^*_{1\mu}(\Omega)\alpha_{1\mu}, \tag{3}$$

with the collective coordinates for an isovector dipole oscillation

$$\alpha_{1\mu} = \sum_i \tau_{3i} r_i Y_{1\mu}(\Omega_i) \ , \tag{4}$$

where $\langle r^2\rangle$ is the mean square distance of a nucleon from the center of mass of the nucleus. Finally, we find a renormalized neutron effective charge $e_f(E1)$ for the E1 transition,

$$e_f(E1) = -\frac{Z}{A}e\left(1-\frac{1}{2}v_1\tilde{\alpha}\frac{\langle j_2|rf(r)|j_1\rangle}{\langle j_2|r|j_1\rangle}\frac{E_R}{E_R^2-\Delta E_{21}^2}\right). \tag{5}$$

References

1) A.M. Lane and J.E. Lynn, *Nucl. Phys.* **17** (1960) 563.
2) A.M. Lane and S.F. Mughabghab, *Phys. Rev.* **C10** (1974) 412.
3) H. Kitazawa, M. Igashira, M. Shimizu, K. Muto, T. Oda, Y. Achiha, Y. H. Lee, and N.Mukai, *Phys. Rev.* **C46** (1992) 2364.
4) S. Raman, M. Igashira, Y. Dozono, H. Kitazawa, M. Mizumoto, and J.E. Lynn, *Phys. Rev.* **C41** (1990) 45.
5) M. Igashira, H. Kitazawa, and K. Takaura, *Nucl. Phys.* **A536** (1992) 285.
6) T. Uchiyama, M. Igashira, and H. Kitazawa, *Phys. Rev.* **C41** (1990) 862.
7) H. Kitazawa, M. Igashira, S. Shibata, K. Tanaka, H. Takakuwa, and K. Masuda, *Nucl. Phys.* **A575** (1994) 72.
8) A. Bohr and B.R. Mottelson, *in Proceedings of the International Symposium on Neutron Capture Gamma-Ray Spectroscopy*, Studsvik, Sweden, 1969 (IAEA, Vienna, 1969), p.3.
9) A. Bohr and B.R. Mottelson, *Nuclear Structure*, Vol. I (Benjamin, New York, 1969), p. 222.

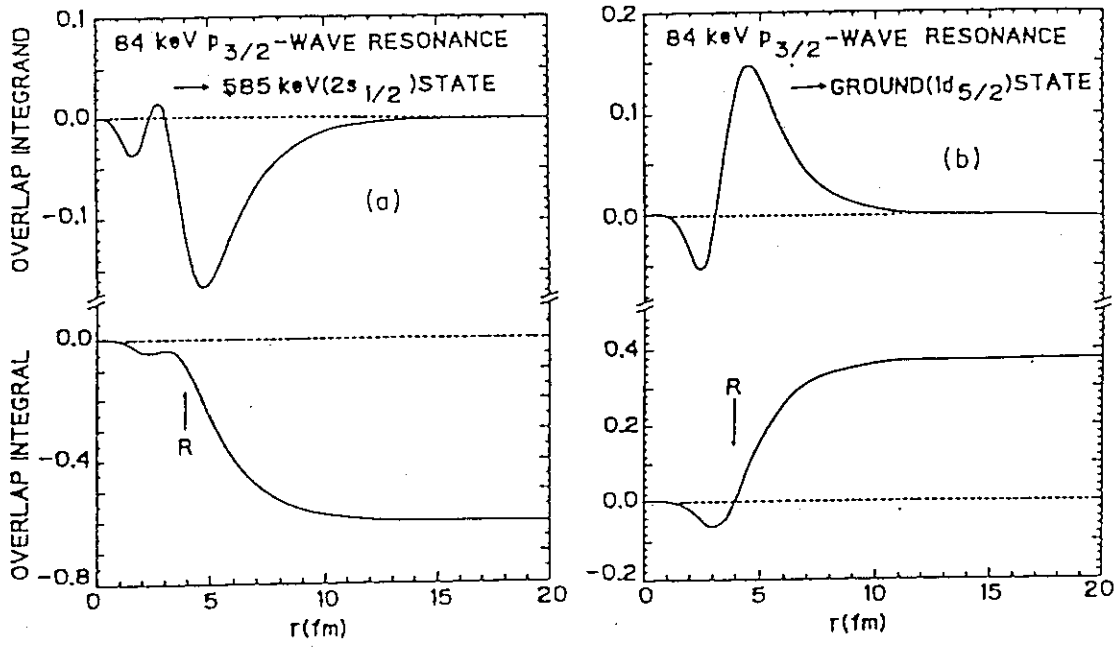

Fig.1. Radial overlap integral and integrand of the valence-transition matrix element for the 84 keV $p_{3/2}$-wave resonance capture by ^{24}Mg.

Table 1. Retardation of single-particle E1 transitions.

Nuclei	E_R(keV)	E_x(keV)	θ_f^2	Γ_γ(eV)		
				measured	valence 1	valence 2
^{9}Be	622(3^-)	3368(2^+)	0.126	0.62±0.06	1.65	0.59
^{24}Mg	84($3/2^-$)	0($5/2^+$)	0.37	0.93±0.14	2.78	1.00
		1965($5/2^+$)	0.11	0.20±0.03	0.44	0.16
	431($3/2^-$)	0($5/2^+$)	0.37	0.35±0.07	1.86	0.67

3.29 Nuclear Level Density Formula with Shell-pairing Correlation Terms

H. Nakamura

Nuclear Engineering Division, Fuji Electric Co., Ltd.
1-1 Tanabe-Shinden, Kawasaki-shi 210

The systematics of parameters for the level density formula based on the SPC model[1] is studied by using the neutron and the proton resonance spacings over a wide range of mass number A=40~254. The present model prediction for the level densities is superior compared with those of the traditional Fermi-gas and the KRK-model[2]. The present improvement seems to be due to considering the shell-pairing correlation terms in the analytic expression of single-particle state, and also to no use of the prescription for the effective excitation energy by using the so-called odd-even correction energy.

1. Introduction

The subjects of the present work were: (1) Analytic expression for single-particle states, in particular, considering the shell-pairing correlation terms, (2) Nuclear level density formula based on a model to be used for describing both the ground and the excited states.

By using the analytic expression for the single-particle state density[1] and the traditional Saddle-Point approximation, the nuclear level density formula is written as

$$\rho(U, J, \pi) = \tfrac{1}{2} W(J) R(U) K_{rot}(U), \tag{1}$$

where the factor $\frac{1}{2}$ is assumed for equal probability of parity states π, $W(J)$ and $R(U)$ are the components depending on the total spin J and the excitation energy U respectively, and K_{rot} is the rotational enhancement factor[3].

2. Nuclear mass formula

For the difinition of the ground state energy, the empirical mass excess data[4] are used to determine parameters of a mass formula, based on the foregoing single-particle state expression. This model relates the shell, pairing and deformation effects on the level density to the ground state corrections

$$E_S + E_P + E_D = M_{exp} - M_{drop} \tag{2}$$

defined as the differences of the experimental mass M_{exp} and the liquid drop mass M_{drop} (gross terms). The present status of the mass formula is presented by the fitting error ΔM = 0.373MeV. This error are defined by the following quantity;

$$\sigma_{th} = [\Sigma W\{(M_{th}-M_{exp})^2 - \sigma_{exp}^2\}/\Sigma W]^{1/2}, \quad W = 1/(\sigma_{exp}^2 + \sigma_{th}^2) \tag{3}$$

3. Systematics of level density parameters

Free parameters to be fitted by using the resonance spacing data are

$a_0 = A_0 \cdot A$: asymptotic level density parameter,
$W = W_0 \cdot A^{1/3}$: main-shell spacing,

where the constants A_0 and W_0 are found by minimizing the quantity

$$\chi^2 = \Sigma (a_{0i} - A_0 \cdot A_i)^2, \quad a_{0i}: \text{fitted } a_0 \qquad (4)$$

The following two different fits are performed ;

mass range: 40<A<70 resonance spacings[5],
systematics : [Fig. 1]

mass range: 40<A<253 resonance spacings[6],
systematics : [Fig. 2]

4. Conclusion

With the exception of a mass range 40<A<90, the asymptotic level density parameter a_0 of the KRK and SPC models are quite well described by the relation $a_0 = A_0 A$ as seen in Fig. 2. The empirical prescriptions of the KRK for the spin cut-off factor and the effective excitation energy disappear in the SPC model. An analogous fit for the range of 40<A<70 shown in Fig. 1 by using the different resonance spacings[5], where is max. 30% discrepancy compared with those of Fig. 2 in the same mass range, presents another problem associated with the resonance spacing data processings.

References ;

1) Nakamura H. : JAERI-M 94-019, No. 5. 20, P342. "Proceedings of the 1993 symposium on nuclear data", Nov. 18-19, 1993, Tokai.
2) Kataria S. K., Ramamurthy V. S. and Kapoor S. S. : Phys. Rev., C18, 549 (1978).
3) Ignatyuk A. V., Istekov K. K. and Smirenkin G. N. : Sov. J. Nucl. Phys. 29 (4), 1979.
4) Wapstra A. H., Audi G. and Hoekstra R. : Atomic Data and Nuclear Data Tables, 39, 281 (1988).
5) Vonach H., et al: Phys. Rev., C38, 2541 (1988).
6) Zhongfu H et al, CNDP, No. 5, 59 (1991).

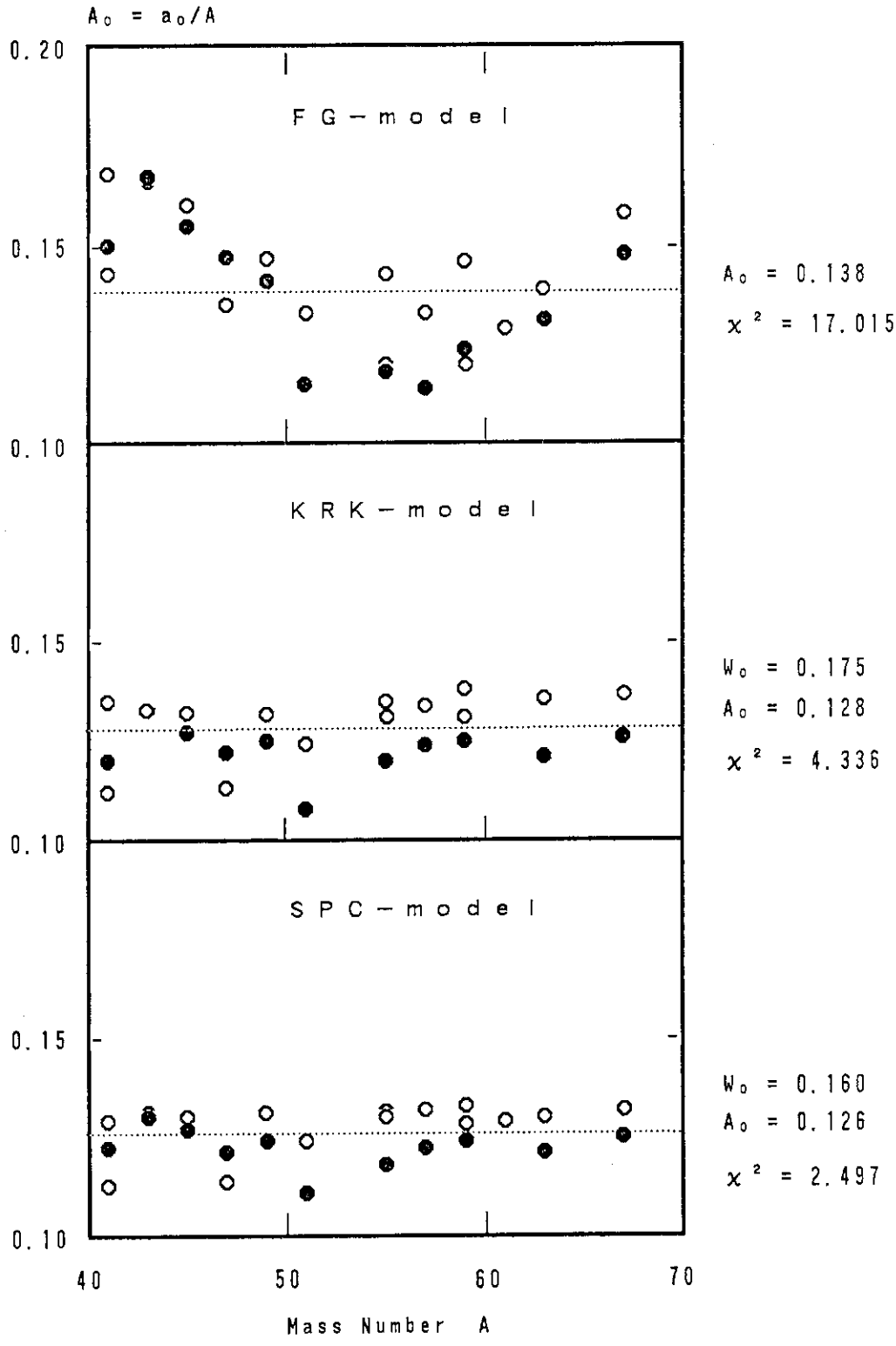

Fig. 1 MASS NUMBER DEPENDENCE OF ASYMPTOTIC LEVEL DENSITY PARAMETER a_o. REDUCED VALUES OF $A_o = a_o/A$ ARE FROM THE NEUTRON-(○) AND THE PROTON-(●) RESONANCE DATA. ---------- RESULTS OF THE LEAST-SQUARES FITS FOR A_o VALUE.

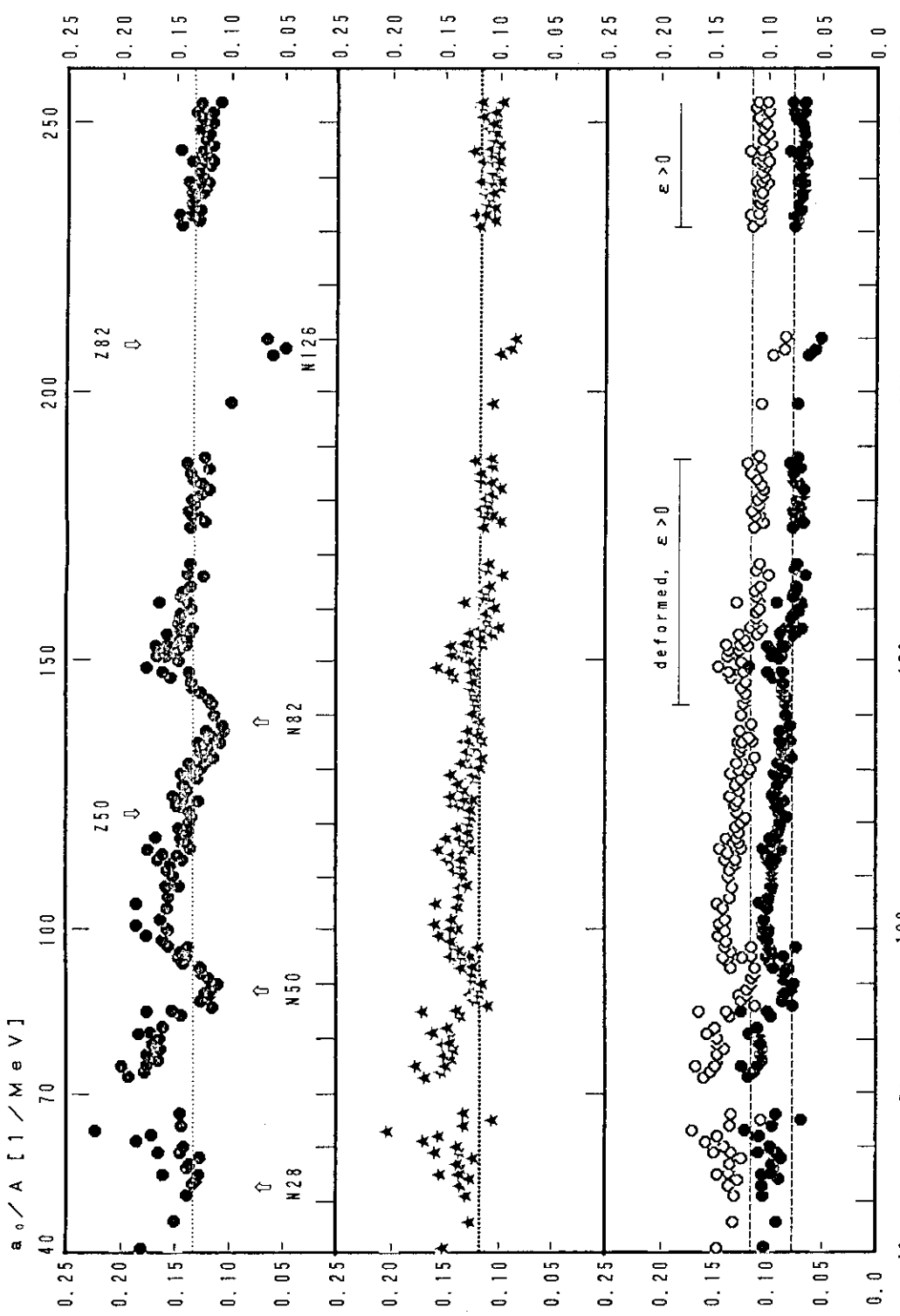

Fig.2 RATIO OF ASYMPTOTIC LEVEL DENSITY PARAMETERS TO MASS NUMBER A. RESULTS OF LEAST-SQUARES FITS (DOTTED LINES) DESCRIBED IN THE TEXT.

3.30 Neutron Bound State Potentials

O. Iwamoto, A. Nohtomi, Y. Uozumi, T. Sakae, and M. Matoba
Department of Nuclear Engineering, Kyushu University
Hakozaki, Higashi-ku, Fukuoka 812

Single particle / hole states of medium weight nuclei were studied using polarized proton / deuteron beams. Real and imaginary parts of neutron bound state potentials have been calculated from single particle energies and spreading widths of the single particle / hole states and compared with optical potentials obtained by the dispersion relation approach to neutron scattering cross section.

1. Introduction

Recently nucleon-nucleus cross sections at low incident energies have been studied with the dispersion relation theory that connects real and imaginary parts of the potentials[1]. In their studies the optical model potentials at positive energy are extrapolated to the bound state potentials at negative energy. Therefore the bound state potentials have both real and imaginary parts. The real parts of the shell model potentials are evaluated to reproduce the single particle / hole state energy, the imaginary parts are deduced from spreading widths of fragmentations of single particle / hole states. Experimental data of spreading widths are not sufficient and the discussions are restricted to spherical nuclei.

Our group has studied neutron particle / hole states systematically in several medium weight nuclei with one nucleon transfer reactions at the Research Center for Nuclear Physics (RCNP), Osaka University, which has been installed an AVF cyclotron with a polarized ion source and a high resolution spectrograph.

In the present work we report the results of the evaluation of the bound state potentials having both real and imaginary parts, which are calculated from the one nucleon transfer reaction data. They are compared with the results from the dispersion relation approaches to neutron scattering cross sections.

2. Experiment

The ^{40}Ca,$^{58-64}$Ni(p,d) and ^{40}Ca, reaction experiments with polarized 65 MeV proton and 56 MeV deuteron beams were carried out at the AVF cyclotron facility of RCNP to study the neutron hole / particle states. The deuteron and proton spectra from (p,d) and (d,p) reactions were measured in excitation energy region 0-10 MeV. The typical proton spectrum from ^{58}Ni(d,p) reaction is shown in Fig. 1. Angular distributions of the cross sections and analyzing powers were measured at 5° to 45° laboratory angles.

The cross section and analyzing power data were analyzed with the distorted wave born approximation code DWUCK under the zero-range local energy approximation model. From the comparison between experiment and theory, the transferred angular momenta l, j were assigned, and the spectroscopic factors were determined in the excitation energy region from 0 to 10 MeV. For almost all the strong excited states, the diffraction patterns are clear to assign the l, j values. The details of the experiment and analysis and the references were described in Ref. 2).

3. Neutron bound sate potentials

The single particle and hole energy for nlj state are obtained by calculating the center of gravity of the spectroscopic strength function or spectroscopic factor $C^2S_{nlj}(E_i)$ as a function of energy, and the width Γ_{nlj} is obtained from the second moment of the spectroscopic strength function. The potential depths of real and imaginary parts for nlj state are calculated using a complex potential parameter search code CXBOUND[3] that solves the complex eigenvalue equation,

$$\left\{\frac{\hbar^2}{2m}\frac{d^2}{dr^2}+\frac{\hbar^2}{2m}\frac{l(l+1)}{r^2}+V(r)+iW(r)+V_{ls}(r)l\cdot s+V_c(r)\right\}u_{nlj}(r) = \left(E_{nlj}+i\frac{\Gamma_{nlj}}{2}\right)u_{nlj}(r) \quad (1)$$

where E_{nlj} and Γ_{nlj} are the single particle energy and the spreading width for the nlj state, respectively. V(r) and W(r) are the real and imaginary parts of the nuclear potential, respectively. $V_C(r)$ is the coulomb potential and $V_{ls}(r)$ is the spin orbit potential. The $u_{nlj}(r)$ is the single particle radial wave function. The volume type contribution to the imaginary potential was disregarded, since the volume type contribution is negligible in this energy region near Fermi surface. The geometrical parameters used were assumed to be constant of r_0=1.25 fm, a_0=0.65 fm for all central potentials.

The volume integrals of the real and the imaginary parts of the neutron potentials for ^{40}Ca are shown as a function of the neutron energy in Fig. 2. The general tendency of both the real

and imaginary parts of the bound state potentials are in agreement with ones obtained by dispersion relation approaches. Optical potentials may be connected to bound state potentials smoothly for both real and imaginary parts. The energy dependence of bound state potentials for Ni isotopes exhibits almost same tendency as for Ca isotopes except the imaginary parts near Fermi surface. The imaginary parts for Ca vanish near Fermi surface but for Ni isotopes.

References

1) C. Mahaux, R. Sartor, Adv. in Nucl. Phys., **20**, 1 (1991)
2) O. Iwamoto, A. Nohtomi, Y. Uozumi, T. Sakae, M. Matoba, M. Nakano, T. Maki, N. Koori, Nucl. Phys., **A576**, 387 (1994)
3) Y. L. Luo, M. Kawai, code CXBOUND, Kyushu University, private communication.
4) C. H. Johnson, C. Mahaux, Phys. Rev. **C38**, 2589 (1988)
5) C. Mahaux, R. Sartor, Nucl. Phys., **A528**, 253 (1991)

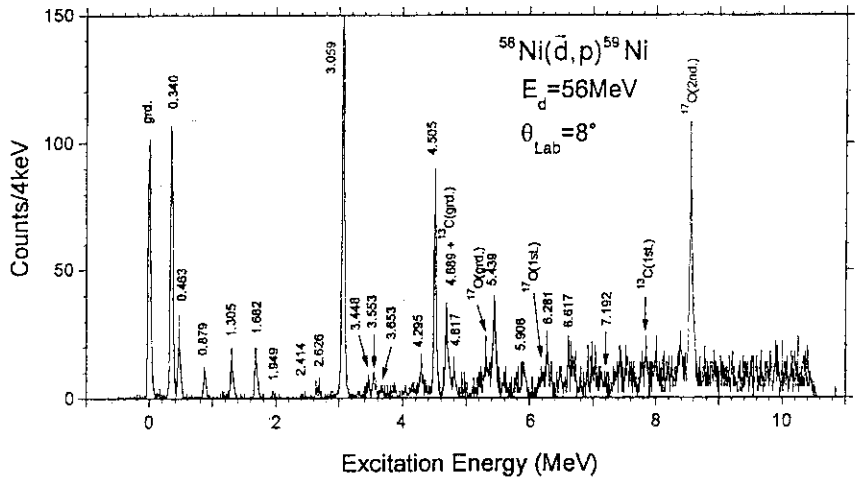

Fig. 1. Typical energy spectrum of protons from ^{58}Ni(d,p)^{59}Ni reaction at 56 MeV for deuteron-spin up; θ_{Lab}=8°

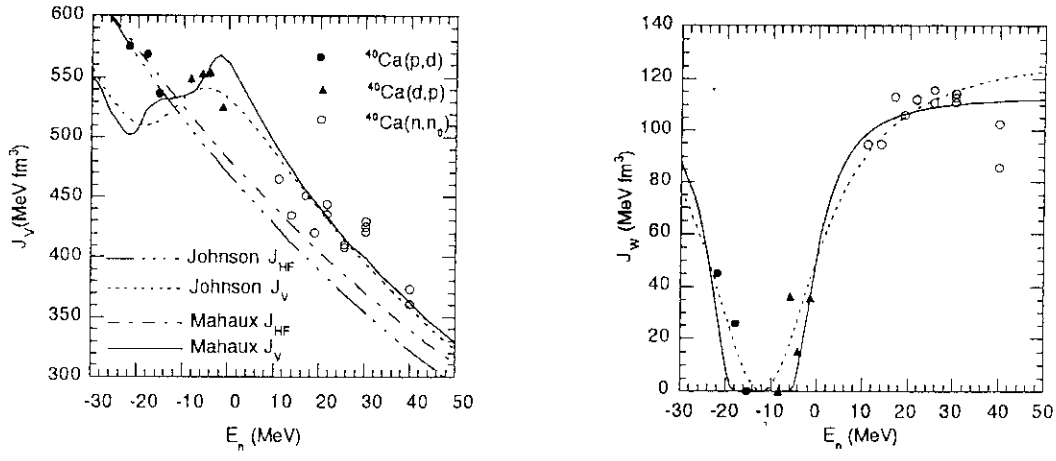

Fig. 2. Volume integrals of real (left) and imaginary (right) parts of the neutron potentials for ^{40}Ca. The closed symbols show one obtained from single particle states and the lines show ones obtained from dispersion relation approaches of Johnson et al.[2] and Mahaux et al.[3] J_{HF} and J_V show volume integrals of Hartree-Fock components and full potentials (HF + dispersion-contribution), respectively.

3.31 Evaluation of Covariance for ^{238}U Cross Sections

Toshihiko Kawano, Masahiro Nakamura, Nobuyuki Matsuda and Yukinori Kanda

Department of Energy Conversion Engineering,
Kyushu University

6-1, Kasuga-kouen, Kasuga-shi, Fukuoka 816, Japan

Abstract : Covariances of ^{238}U are generated using analytic functions for representation of the cross sections. The covariances of the $(n, 2n)$ and $(n, 3n)$ reactions are derived with a spline function, while the covariances of the total and the inelastic scattering cross section are estimated with a linearized nuclear model calculation.

1. Introduction

So far no covariance data has been given in JENDL-3.2. The covariance data is under preparation in order to meet requirements of the nuclear data users. The covariance data of U, Pu, C, O, Na, and structural materials have higher priority especially for design of the fast/thermal reactors and shielding. The objective is generation of the covariance data of ^{238}U for JENDL-3.2.

It is difficult to derive the covariance of the existent evaluated nuclear data, since derivation of the covariance data depends on the cross section evaluation methods, one must trace the evaluation procedure and calculate error propagation rigorously at each evaluation step. In order to evade this complication we adopt an analytic function for representation of the cross section and give the covariance for the function. Then the given covariance is rehashed into the covariance of the existent evaluated nuclear data.

2. Calculation Method

A covariance matrix for the spline-smoothed cross sections $\mathbf{M}$ is given by the least squares method, $\mathbf{M} = \mathbf{D}'\mathbf{V}^{-1}\mathbf{D}$, where $\mathbf{V}$ is a covariance matrix of experimental data, and $\mathbf{D}$ is a design matrix. The experimental data $\boldsymbol{y}$ is written as $\boldsymbol{y} = \mathbf{D}\boldsymbol{x}$, where $\boldsymbol{x}$ is a vector whose elements are the cross sections at the spline knots. The matrix $\mathbf{D}$ is arranged so as to average or to interpolate the experimental data between the spline knots.

The covariace matrix of the nuclear model calculated cross section can be generated from the covariance of the model parameters. The nuclear model calculation is linearized with the first order Taylor series expansion around a certain parameter set $\boldsymbol{x}_0$, $\boldsymbol{f}(\boldsymbol{x}) \simeq \boldsymbol{f}(\boldsymbol{x}_0) + \mathbf{C}(\boldsymbol{x} - \boldsymbol{x}_0)$, where $\mathbf{C}$ is a sensitivity matrix. The least squares method is feasible with this linearized function. The covariance of the model parameters $\mathbf{P}$ is calculated

by $\mathbf{P} = (\mathbf{X}^{-1} + \mathbf{C}'\mathbf{V}^{-1}\mathbf{C})^{-1}$, where $\mathbf{X}$ is the prior covariance matrix of the parameters. The covariace matrix of the cross sections is given by $\mathbf{M} = \mathbf{CPC}'$

Usually the covariance matrix $\mathbf{M}$ is multiplied by a scale factor, χ^2. In order to rehash the covariance of the analytic function into the evaluated cross sections, we refer the χ^2 of the evaluation instead of the χ^2 of the analytic function. Note that the covariance matrices sited in the following section are not multiplied by this factor, but the χ^2's are quoted in figures.

3. Results and Discussion

Figures 1 and 2 show the covariance matrices of the $(n, 2n)$ and $(n, 3n)$ reaction cross sections. We employed the spline function assisted least squares method with interval average for $\mathbf{D}$. The spline function well reproduces the experimental $(n, 2n)$ cross sections, and that is almost equal to the JENDL-3.2 evaluation. The obtained covariance does not multiplied by χ^2 since $\chi^2 < 1$. In the case of the $(n, 3n)$, few available experimental data gave rise to large uncertainties and the ambiguous spline function.

The covariance of the total cross section was evaluated with a coupled-channels (CC) method. Optical potential parameters and deformation parameters (β_2, β_4) were taken as the model parameters. The obtained covariance matrix is shown in Fig. 3. The uncertainties are very small because there are a large number of data points.

The covariance of the inelastic scattering cross section was also evaluated with the CC method. Compound process contribution is significant below $E_n < 5$ MeV. In order to avoid the calculation being complicated, the compound cross section was calculated with a Hauser-Feshbach-Moldauer (HFM) model and the cross section was renormalized. The normalization constant was taken as the one of the model parameters. The covariance matrices of the inelastic scattering cross sections to the first excited state and the second excited state are shown in Figs. 4 and 5, respectively. There are no experimental data above 5 MeV. This method, however, is able to generate the covariance in this enegy range.

The CC calculation with 0^+-2^+-4^+ coupling scheme yields a correlation matrix of the inelastic scattering cross sections between the first and the second levels. This is shown in Fig. 6. This information is required for completion of a consistent covariance file.

4. Conclusion

Covariances of the ^{238}U reaction cross sections were evaluated using analytic functions — a spline function and a linearized nuclear model calculation. The spline method went well for the $(n, 2n)$ but for the $(n, 3n)$ because of the lack of the experimental data. The linearized nuclear model method was able to generate the covariance although the experimental data were insufficient.

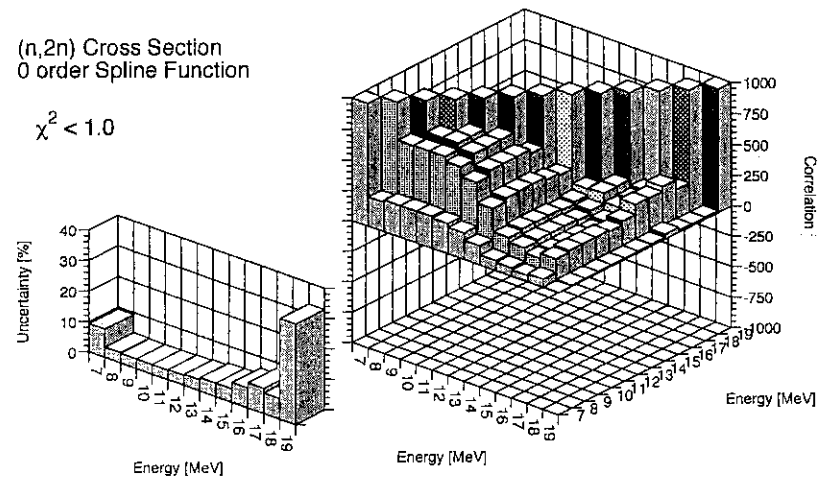

Fig.1 Covariance matrix of $^{238}\mathrm{U}(n,2n)$ reaction cross section

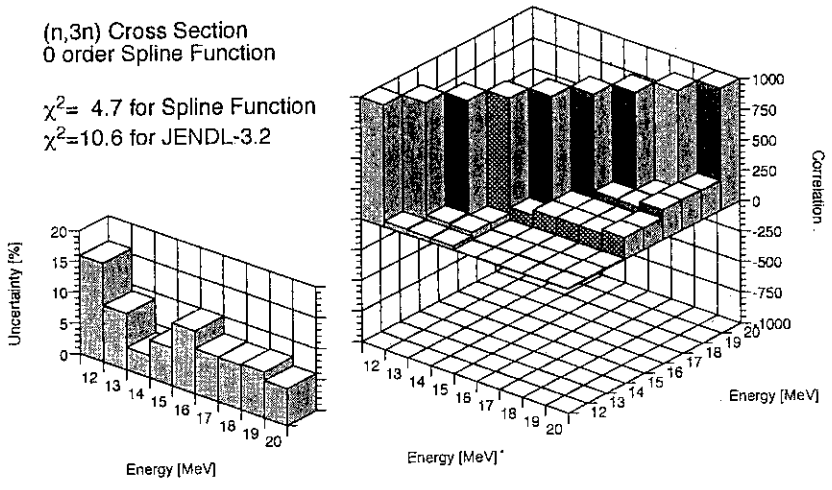

Fig.2 Covariance matrix of $^{238}\mathrm{U}(n,3n)$ reaction cross section

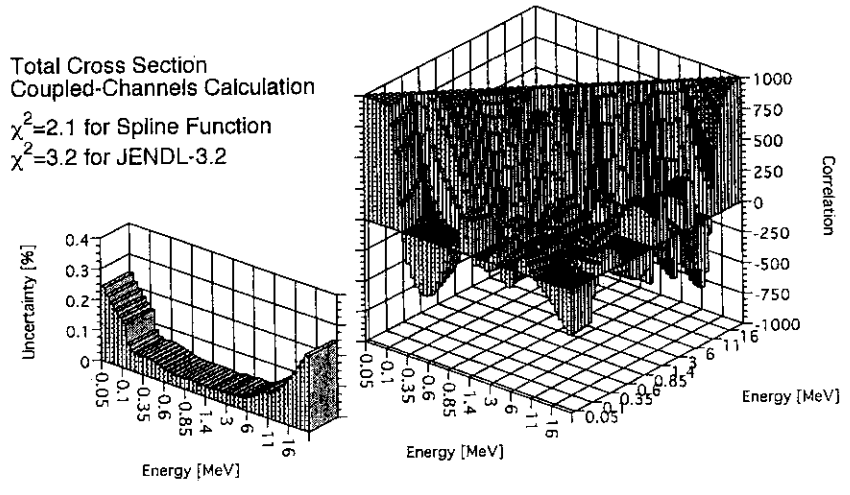

Fig.3 Covariance matrix of $^{238}\mathrm{U}$ total cross section

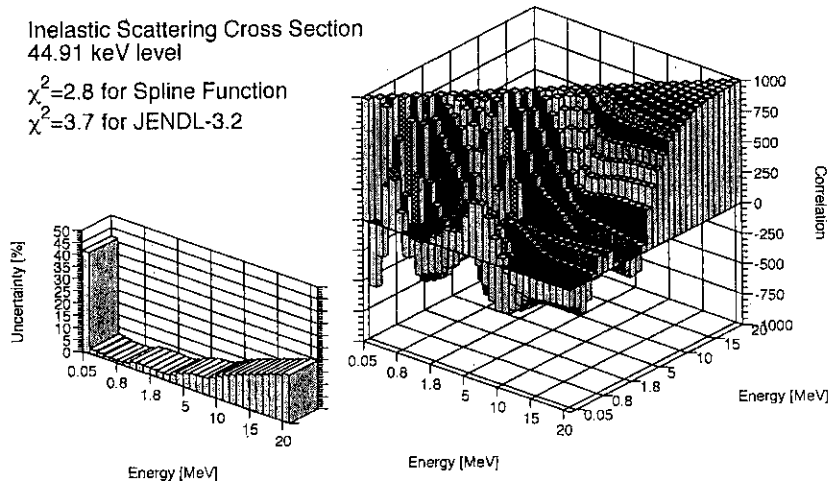

Fig.4 Covariance matrix of $^{238}\mathrm{U}(n,n')$ cross section

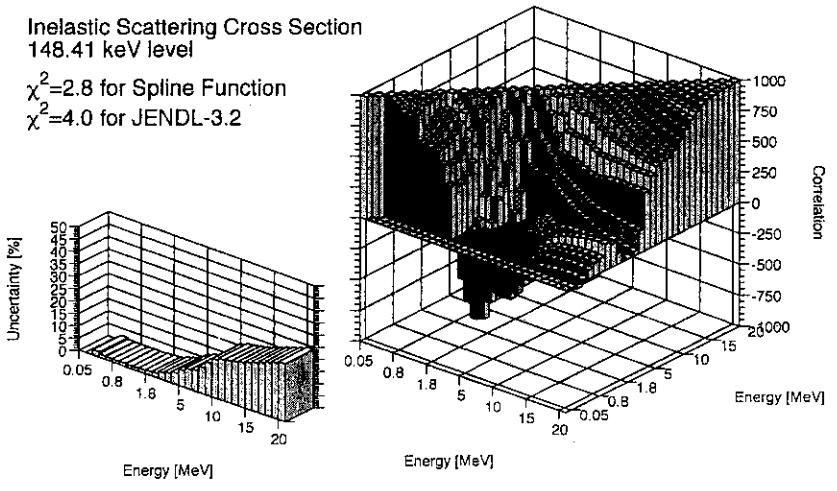

Fig.5 Covariance matrix of $^{238}\mathrm{U}(n,n')$ cross section

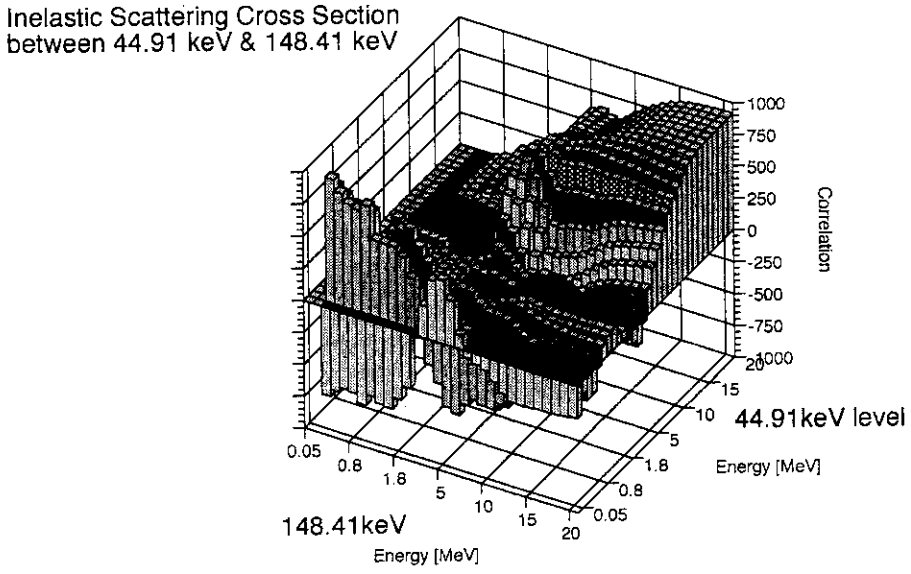

Fig.6 Correlation matrix of $^{238}\mathrm{U}(n,n')$ cross sections between the first and the second levels

3.32 Determination of Shell Energies and a Mass Formula

H. Koura, T. Tachibana*, M. Uno** and M. Yamada*

Department of Physics and Applied Physics, Waseda University
*Advanced Research Center for Science and Engineering, Waseda University
**Ministry of Education, Science and Culture

Abstract

Our group has been studying a method of calculating nuclear shell energies and incorporating them into a mass formula. The first result with this method was reported at the 1990 Symposium on Nuclear Data. Here we report the advances of this method focusing on nuclear deformations, and give some preliminary results.

§1. Introduction

For several years we have been developing a method of calculating nuclear shell energies on the basis of single-particle energies. This method is composed of the extraction of the proton and neutron (crude) shell energies from sums of single-particle energies and the refinement of them so as to include effects of residual interaction, i.e., pairing and deformation.[1,2] The shell energies thus obtained were incorporated into the TUYY-type nuclear mass formula.[3]

In this report, we improve this method in two points: we firstly use an extended Woods-Saxon potential, and secondly modify the refinement procedure with respect to pairing and deformations. We briefly explain how to obtain crude shell energies in section 2, how to refine them in section 3, and the mass formula in section 4.

§2. Crude Shell Energy

As for neutrons, for example, we adopt an extended Woods-Saxon central potential and a conventional type of *l-s* potential,

$$V(r) = V_0 \frac{1}{\left\{1+\exp[(r-R_v)/a_v]\right\}^{a_v/\kappa}} + V_{ls0}\frac{\hbar^2}{2m}\frac{1}{r}\frac{d}{dr}\left\{\frac{1}{1+\exp[(r-R_{ls})/a_{ls}]}\right\} l\cdot s \ , \qquad (1)$$

where V_0, R_v, a_v, V_{ls}, R_{ls}, a_{ls} and κ are functions of Z and N with some parameters. The values of these parameters are determined from comparison with the single-particle levels of 16 doubly-magic or magic-submagic nuclei from ^{4}He to ^{208}Pb and their neighboring nuclei. As for protons, the same type potential as Eq. (1) supplemented by the Coulomb potential is used. Here, the charge symmetry is taken into account in the functions of Z and N.

We start from this spherical potential, Eq. (1). When n particles are put in the potential, we refer to the sum of single-particle energies as $E_{i\mathrm{SP}}(n;\ Z,\ N)$ [i=p for proton and i=n for neutron]. This quantity is a function of n and fluctuates due to the shell effects. In order to get significant shell energies, we subtract smooth energies from $E_{i\mathrm{SP}}(n;\ Z,\ N)$ using the Thomas-Fermi approximation and the other method of averaging. The main procedure is the same as that mentioned in Refs.1 and 2. In Ref.1, we wrote $E_{i\mathrm{cl}}(n;\ Z,\ N)$ and $\Delta E_{i\mathrm{av}}(n;\ Z,\ N)$ as $E_{i\mathrm{T\text{-}F}}(n;\ Z,\ N)$ and $E_{i\mathrm{sm}}(n;\ Z,\ N)$ for the present symbols.

$$E_{ics}(Z, N) = E_{iSP}(n=N; Z, N) - E_{iT-F}(n=N; Z, N) - E_{ism}(n=N; Z, N) \qquad (2)$$

In Eq. (2), i = p for proton and i = n for neutron. In this report, $E_{ism}(n; Z, N)$ is changed into appropriate polynomial functions of $(n/Z)^{1/3}$ for proton and of $(n/N)^{1/3}$ for neutron. The crude shell energies thus obtained are shown in Fig. 1.

§3. Refinement of the Crude Shell Energy

We refine the crude shell energies with consideration of the effects of residual interactions, i.e., pairing effect, configuration mixing and nuclear deformation.

(a) Pairing

In our model, the shell energy with the pairing effect is expressed as

$$E_{ipr}(Z, N) = \min_{V^2}\left[\left\langle E_{ics}(Z, N)\right\rangle_{pr} + \overline{\Delta E_{ipr}}\right] \qquad [i \text{ = p for proton, } i \text{ = n for neutron}], \qquad (3)$$

where, $\left\langle E_{ics}(Z, N)\right\rangle_{pr}$ is a weighted average of crude shell energies. The weight function used here corresponds to the BCS type occupation probability V^2. The second term in Eq.(3), $\overline{\Delta E_{ipr}}$, is the pairing energy derived from the single-particle levels without shell effect.

(b) Configuration mixing

The occupation probability V^2 has a long tail even in the high energy region of the single-particle levels. Accordingly, the shell effect is reduced by the configuration mixing. In order to take into account this effect, we just multiply a reduction factor μ to the modified energies $E_{ipr}(Z, N)$. The value of μ is adjusted with reference to nuclear masses and is given in section 4.

(c) Deformation

In (a) and (b), the shell energies are considered as those for the spherical nucleus. In our model, it is assumed that the shell energy of a deformed nucleus is obtained as a weighted sum of spherical shell energies of neighboring nuclei. Thus the shell energy with the deformation effect is expressed as

$$E_{sh}(Z, N) = \min_{\alpha_2,\alpha_4}\left[\mu\left\langle E_{npr} + E_{ppr}\right\rangle_{def} + \Delta E_{DFLD}\right], \qquad (4)$$

with

$$\left\langle E_{npr} + E_{ppr}\right\rangle_{def} = \sum_{N'} W_{ndef}(N'; Z, N)\, E_{npr}(Z, N') + \sum_{Z'} W_{pdef}(Z'; Z, N)\, E_{ppr}(Z', N) \ , \qquad (5)$$

and

$$\Delta E_{DFLD} = \Delta E_{surf} + \Delta E_{Coul}, \qquad (6)$$

where W_{idef} [i = p or n] are weight functions determined by considering the nuclear shape, and ΔE_{surf} (ΔE_{Coul}) is the difference of the surface (the Coulomb) energy caused by deformation. The weight function W_{idef} is assumed to be proportional to the solid angle corresponding to each spherical nucleus, as shown in Fig.2. In this report, we describe the nuclear shape in terms of Y_2 and Y_4 deformations and derive the weight function from this shape according to the above-mentioned prescription. The nuclear radius divided by $A^{1/3}$ is ,

$$r(\theta) = \frac{r_0}{\lambda}\left[1 + \alpha_2 P_2(\cos\theta) + \alpha_4 P_4(\cos\theta)\right], \tag{7}$$

with

$$\lambda = \left[1 + \frac{3}{4\pi}\left(\frac{4\pi}{5}\alpha_2^2 + \frac{4\pi}{9}\alpha_4^2\right)\right]^{1/3}, \tag{8}$$

where α_2 and α_4 are deformation parameters. We determine the parameter values by minimizing the shell energies (See Eq.(4)). From a certain consideration on experimental deformations, we slightly change the optimization function so as to prefer a prolate shape. The example of α_2 and α_4 thus obtained and FRDM prediction[3] are shown in Fig. 3 and 4, respectively.

Finally, we get the refined shell energies and show them in Fig. 1.

§4. Mass formula

Our previous mass formula[4] is expressed as,

$$M(Z, N) = M_{gross}(Z, N) + M_{even\text{-}odd}(Z, N) + M_{sh}(Z, N). \tag{9}$$

In this formula, the shell energies, $M_{sh}(Z, N)$, were obtained by using an empirical method, and therefore this formula is available only in the nuclidic region with Z<112 and N<160. In order to improve this mass formula, we use the refined shell energies obtained in the previous section as the shell term $M_{sh}(Z, N)$. The new mass formula thus obtained is available over the very wide nuclidic region as long as the single particle level is bound. The parameter values in the gross part $M_{gross}(Z,N)$ and the value of μ are determined in order to reproduce the experimental masses.[5] The results are still preliminary ones, in which the root mean square deviation is 946 keV. We are now undertaking a determination of better parameter values, and results will be reported elsewhere.

References

1) T. Tachibana, M. Takano and M. Yamada, JAERI-M 91-032
2) M. Uno, T. Tachibana, M. Takano, K. Koura and M. Yamada, *Nuclear Far From Stability / Atomic Masses and Fundamental Constants 1992* (IOP 132), p. 117
3) P. Möller and J. R. Nix, *ibid.*, p. 43
4) T. Tachibana, M. Uno, M. Yamada and S. Yamada, Atomic Data and Nuclear Data Tables **39** (1988), 251
5) A. H. Wapstra, G. Audi and R. Hoekstra, *ibid.*, **39** (1988), 281

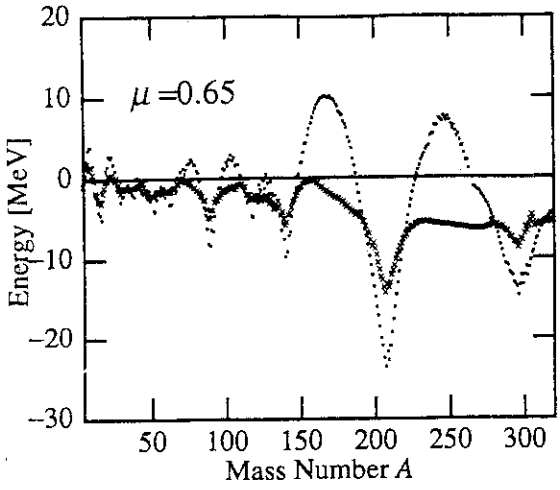

Fig. 1 The crude shell energies (•) and the refined shell energies (x) on the β - stability line. The parameter value μ=0.65 is adopted.

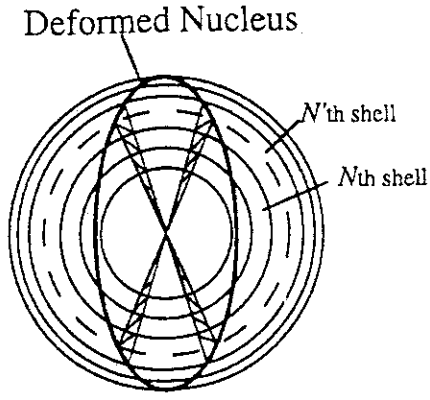

Fig. 2 Decomposition of a deformed nucleus into fractional spherical nuclei. The shaded part corresponds to the solid angle.

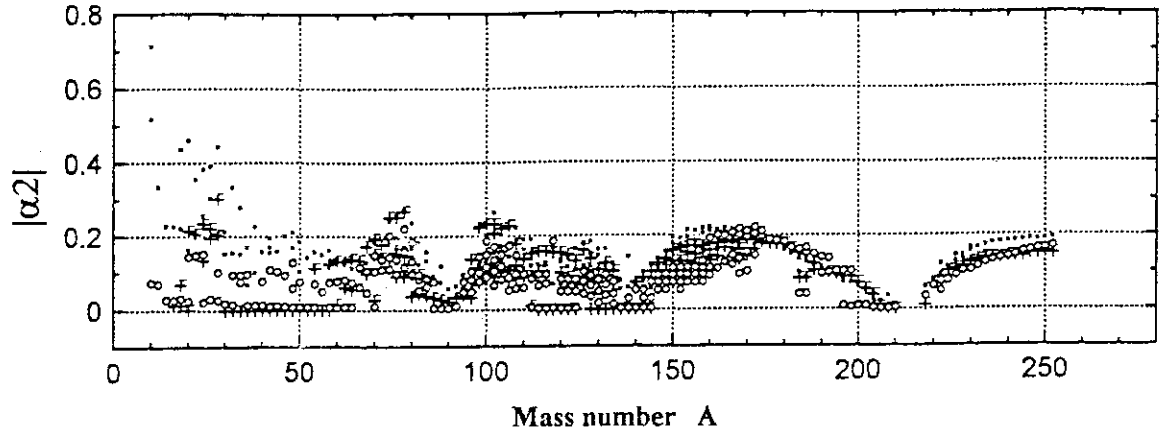

Fig. 3 The deformation parameter α_2.
o : This work, + : FRDM calculation in Ref.3, ▪ : Experimental value.
The absolute values of the predicted α_2 are shown so as to correspond to the experiment.

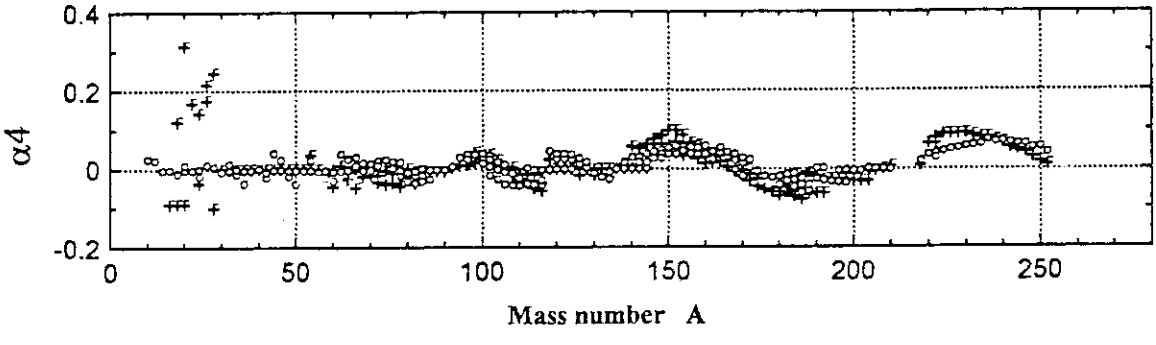

Fig. 4 The predicted deformation parameter α_4. See also the notation of Fig. 3.

3.33 Neutron Irradiation Effect of Silicon

Itsuro KIMURA,Ikuo KANNO,Takumi MIKAWA
Takashi INBE,Mitsuo KOHNO* and Kei MATSUMOTO*

Department of Nuclear Engineering, Kyoto University
Yoshida, Kyoto 606-01
*Komatsu Electronic Metals Co Inc.
Shinomiya, Hiratsuka, Kanagawa 254

Several kinds of silicon wafers were irradiated at four neutron fields with different energy spectra.Electrical resistivity and deep level defect concentrations after the neutron irradiation, and their changes against number of displacement atoms (DPA's) for different neutron fields were compared. The number of DPA's was calculated by N. Yamano's data.

1. Introduction

Although various irradiation effects of silicon by neutrons have been extensively investigated by many groups for more than 40 years, the dependence of its irradiation effects on neutron energy is not very clear even at present. Several groups have irradiated silicon wafers and silicon devices at various neutron fields with different neutron spectra, and compared irradiation effects each other [1)-3)]. T.Iida and K.Sumita showed the correlation of fusion and fission neutron damage in transistors by the number of displacement atoms, DPA. The DPA cross section or kerma of silicon has been calculated by several authors [4) 5)] and is now available in a standard of ASTM.[6)] However it is still necessary to evaluate these cross sections and to examine the relation between various irradiation effects and the number of DPA or its kerma.

Several kinds of silicon wafers were irradiated at four neutron fields with different energy spectra, and then electrical resistivity and deep level defect concentrations were measured. Their changes against the number of DPA for four neutron fields were compared.

2. Experimental Methods

2.1 Silicon Samples

We irradiated wafers of n-type single crystals of silicon as tabulated in Table 1. The size of a wafer was about 1cm square and 0.5 mm in thickness.

2.2 Neutron Irradiation

The silicon wafers were irradiated at the following four neutron fields:

(1) The pneumatic tube of Kyoto University Reactor KUR, Pn-2 (typical thermal

reactor spectrum),

(2) The pneumatic tube in the graphite thermal column of KUR, TC-Pn (mainly thermal neutrons),

(3) The through tube (Glory hole) in Fast Source Reactor, YAYOI of the University of Tokyo, and

(4) The rotating target of Intense 14 MeV Neutron Source, OKTAVIAN of Osaka University.

The neutron fluence for the irradiation at (1),(2) and (3) was measured by the $^{58}Ni(n,p)^{58}Co$ reaction and that at (4) was done by the $^{93}Nb\ (n, 2n)\ ^{92m}Nb$ reaction. The numerical value of DPA cross section was given by N. Yamano [5) 7)] as seen in Fig, 1.

2.3 Measurement of Electrical Resistivity

The specific electrical resistivity of silicon wafers were measured by the four point probe method at constant temperature, 20.5℃. The experimental error can be estimated to be about 3%.

2.4 Deep Level Transient Spectroscopy, DLTS

After the irradiation, the surface of a silicon wafer was etched by a mixed solution of HF, CH_3COOH and HNO_3 (1:1:3), and a Schottky junction and an ohmic contact were formed by evaporating gold and aluminum, respectively. This element was set in a cryostat with liquid nitrogen and its temperature was controlled. The deep level defect concentrations were measured with a transient capacitance spectrometer of type DA-1500 manufactured by HORIBA. This spectrometer is capable to carry out both deep level transient spectroscop, DLTS and isothermal capacitance transient spectroscopy, ICTS.

3. Results and Discussion

In Fig.2, the changes of the electrical resistivity are plotted against the number of DPA. The solid curves show the modified Buehler's formula [8)] in which the average neutron energy is assumed to be 1 MeV.From these figures,it is seen that the resistivity changes at KUR-Pn, YAYOI and OKTAVIAN reasonably agree each other, but those at TC-Pn obviously show rather slower rise than others.Therefore, the DPA caused by thermal neutrons are thought less effective to increase the electrical resistivity than those caused by both reactor neutrons and by 14 MeV neutrons.

A typical pattern of the DLTS spectrum of an irradiated silicon wafer is shown in Fig.3.In this figure we can recognize three predominant peaks which had been assigned to correspond the following deep levels and centers [9)]:

E1 - 0.15 eV O-V

E2 - 0.21 eV $(V\text{-}V)^{2-}$

E3 - 0.39 eV $(V\text{-}V)^{-}$

The energy of each level is slightly different among references. Number of defects, N in each level was obtained, and the ratio of N/DPA is depicted in Fig.4.The values of N/DPA for both reactor neutrons and for 14 MeV neutrons reasonably agree each other, while those for thermal neutrons obviously smaller than the others. Therefore, the less effectiveness of the DPA caused by thermal neutrons to electrical resistivity change is probably due to this smaller N/DPA value for thermal neutrons. More precise measurement of deep level defect formation through DPA by fast and thermal neutrons is expected.

3. Conclusion

The changes of electrical resistivity and deep level defect concentration after the irradiation of neutrons with four different spectra were measured. From these results, we can conclude that the DPA caused by thermal neutrons is less effective to produce deep level defects and to increase electrical resistivity.

4. Acknowledgments

This work was partly supported by Grant-in-Aid of Ministry of Education, Science and Culture. And the cooperations of the KURRI and OKTAVIAN groups are deeply appreciated.

References

1) V.V.Verbinski, et al.,IEEE Trans. Nucl. Sci., **NS-25**, No.6,1629 (1978).
2) T. Maekawa,et al., Semicond. Sci. Technol., **3**, 645 (1988).
3) T.Iida and K.Sumita, J.Nucl.Sci. Technol., **26**, 231 (1989).
4) V.C.Rogers,et al., IEEE Trans. Nucl.Sci., **NS-22**,No.6, 2326 (1975).
5) N. Yamano, JAERI-M91-043, p.107 (1991).
6) E722-93 Standard, Annual Book of ASTM Standards, Vol.12.02, American Soc. for Testing Materials (1993).
7) N.Yamano Private Communications.
8) M.G.Buehler, IEEE Proc.**56**,1741 (1968).
9) Y. Tokuda and A. Usami, IEEE Trans. Nucl. Sci., **NS-28**,3564 (1981)

Table 1 Data of irradiated Silicon Wafers

Group	Method	Crystal face	Resistivity [Ω · cm]	Oxygen Conc. [cm^{-3}]	Phosphorus Conc.[cm^{-3}]	Boron Conc. [cm^{-3}]
I	CZ	(100)	7.33	8.56×10^{17}	6.08×10^{14}	$\leqq5\times10^{12}$
IV	CZ	(100)	1.81	1.55×10^{18}	1.96×10^{15}	$\leqq1\times10^{13}$

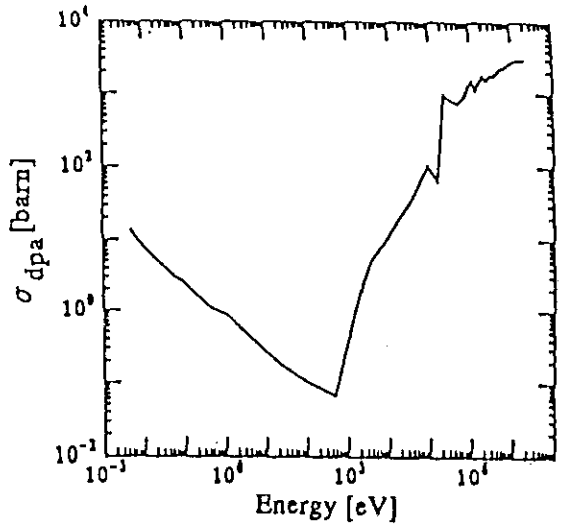

Fig. 1 DPA cross section

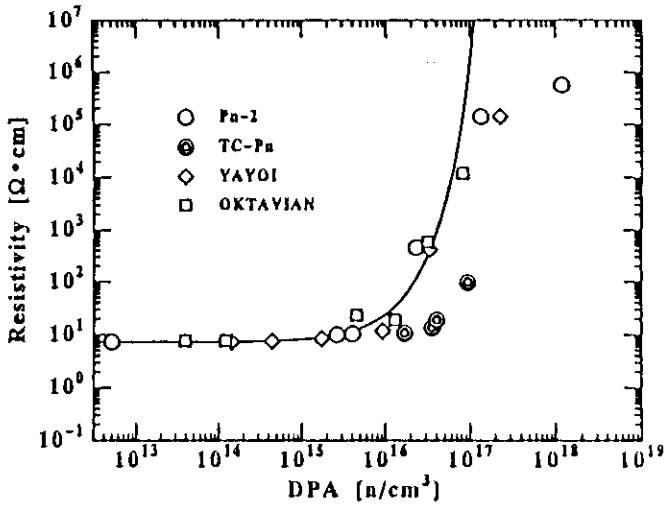

Fig. 2 Changes of the electrical resistivity

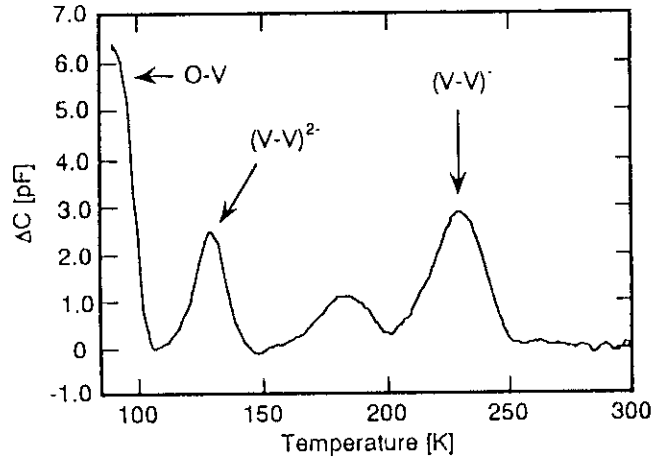

Fig. 3 Typical pattern of the DLTS spectrum

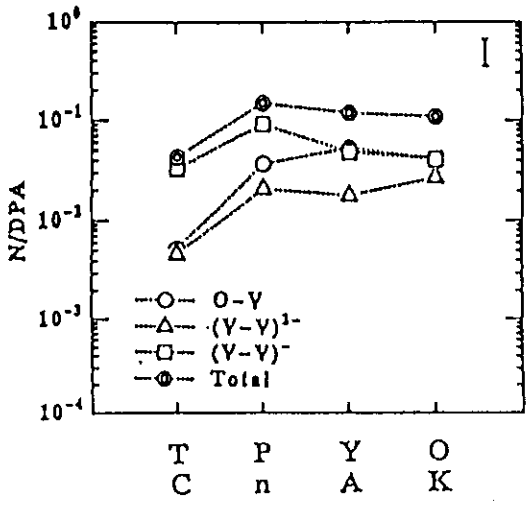

Fig. 4 N/DPA for four neutron fields

3.34 Possible In-lattice Confinement Fusion (LCF): Dynamic Application of Atomic and Nuclear Data

Yuuki KAWARASAKI
Central Research Lab., Hamamatsu Photonics K.K.
5000 Hirakuchi, Hamakita-shi, Shizuoka-ken 434

New scheme of a nuclear fusion reactor system is proposed, the basic concept of which comes from ingenious combination of hitherto developed techniques and verified facts; 1) so-called cold fusion(CF), 2) plasma of both magnetic confinement fusion(MCF) and inertial confinement fusion(ICF), and 3) accelerator-based D-T(D) neutron source. Details of the LCF reactor physics require dynamics of atomic data as well as nuclear data; interaction of ions with matters in solid and the problems of radiation damage.

Historically the controlled fusion research can be regarded as based on the nuclear physics research which has initiated early in 1930s with the discovery of neutron. The D-T(D) nuclear reaction by use of accelerated D^+ ions impinging upon a T(D)-containing target has been widely used for production of fast neutrons. This should have motivated the fusion research. However, this scheme has a fatal drawback. The bombarding particles lose their energy very quickly, mainly in collisions with electrons. The ratio of nuclear output over the input energy is usually very small, i.e., less than 10^{-2}. It is thus obvious that this process can not be exploited for power generating purposes[1]. To overcome this drawback, the use of accelerated ion-beams(in non-Maxwellian distribution) can still nowadays be found in MIGMA[2].

The origin of the solar energy, a long-term enigma, had been successfully explained by H.A.Bethe and C.F.von Weiszäcker in 1939, as through thermonuclear reactions: either of the proton-proton(p-p) chain in stars of the size of our sun or of the carbon-nitrogen(C-N) chain in larger stars. Both the reactions can be reduced to as nuclear-mass extinguishment converted to energy, where finally four protons get together to one alpha-particle, ^4He. The stellar thermonuclear reactions can be sustained through the confinement of solar-gas plasma by the huge gravity of such solar bodies. With the advent of a new field of plasma physics, the controlled fusion studies, somewhat later after the hydrogen-bomb explosion tests, have started to produce high-density and high-temperature plasma, such as Z-pinch experiments mid in 1950s, then leading to the todays' magnetic confinement fusion(MCF) schemes. From this viewpoint, magnetic force plays a role for confinement of the plasma under the terrestrial environment, instead of the gravity on solar bodies. In MCFs, typical facilities are Tokamaks and Helical Devices. Late in 1960s, the availability of high-power lasers made another scheme of the fusion power studies, known as inertial confinement fusion(ICF). Here the laser power is applied to compress the fusion fuel gas to high density and then high temperature through the implosion of a pellet, containing the fuel gas, of some (sub-)millimeter in size, the mechanism of which resembles to the hydrogen bomb, being driven to extreme implosion by a fission nuclear power. In ICFs, Laser Fusion Facilities are the first runners followed by those of proposed heavy-ion inertial confinement fusion after many proposals of the candidates for the energy drivers such as relativistic electron beams and light-ion beams. Both schemes(MCF and ICF) use Maxwellian high-temperature plasmas of D(or D-T mixture) ions.

In March, 1989, M.Fleishmann and S.Pons had abruptly announced the so-called cold fusion scheme[3]. They had carried out an electrolysis experiment of D_2O+Pd system and claimed that the excess heat generation had been observed due to nuclear fusion reaction inside the lattices of Pd-metal. As well known, some metals, e.g., Ti, Zr, Pd, etc., can solve isotopes of hydrogen in their lattices up to more than $10^{22}cm^{-3}$ in density. The metal-hydrogen system reveals the characteristic features, phases, depending on both concentration and temperature; a phase diagram represents it well. Under some condition, say, in α-phase, the occluded hydrogens behave like plasma. In other words, the confinement time τ, one of the important parameters of plasma fusion, becomes infinite. The occluded hydrogen of $10^{22}cm^{-3}$ in density means that the quantity in a metal block of only 1 cm^3 is almost the same as those in large Tokamas' plasma of 100 m^3, because the density of Tokamaks' plasma is around 10^{14} cm^{-3}. This should implicitly give a physics-basis of the CFs, even though the kinetic energy of the occluded plasma is far small for nuclear reaction threshold; at room temperature, it is at the same order of thermal neutron, 0.025 eV.

J. D. Lawson and W. B. Thompson showed a criterion that the minimal requirement of the plasma for power application must be fulfilled; three parameters, i.e., density n, confinement time τ and temperature T, often a product $n \cdot \tau$ and T, must exceed the critical values. The Lawson diagram indicates conveniently the chronological achievement of both MCFs' and ICFs' performance. The expanded one of Fig. 1 includes the possible location of the CFs, far upmost and far left-sided, indicated by an arrow, and the position of D-T neutron source reduced from the Q-value and of the MIGMA. The superposition of both D-T neutron sources' and MIGMA's may be out of the rigorous definition of statistical property of plasma in the figure. However, this procedure can offer us a good guide to further proceed to a new scheme establishment. A line drawn from the position of D-T neutron source toward the CFs' can fortunately cross the area of $Q_{D-T} \gg 1$. To move the CFs' part toward the D-T neutron source may be equivalent to letting the occluded Ds or Ts be energized in an ordinary sense, differing from the so-called cold fusion that explores a possible new mechanism of nuclear fusion reaction inside the lattices.

A technique of the plasma-heating by the fast(of high energy) neutral beam injection(NBI) in e.g., Tokamaks suggests that the use of fast neutrons favours in this case of LCFs, because the difference(10^8) in desity of between MCF and LCF inevitably leads to use neutral particles much smaller than those of atomic size; the unique candidate is neutron and it should be conceivable that the use of fast neutrons can make other advantages: deep-penetrability inside materials, identical usability of D-T(partially D-D) neutrons, and fuel self-production through the nuclear combination with slow proton after D-D reaction. Fission reactor physics treats well the process of neutron slowing down, where the neutrons lose their energy through multiple collision with nuclei; in turn, the nuclei get the recoil energy dependent on their mass. After the head-on collision of a neutron of energy E_0 against a nucleus of atomic mass A, the resulting neutron energy E can be expressed as $E = \alpha E_0$, where $\alpha \equiv ((A-1)/(A+1))^2$. The transferred(recoil) energy to the nucleus is thus given as $(1-\alpha)E_0$. For a hydrogen ion(a proton), the complete energy transfer can take place, the incident neutron being stopped.
For heavier nuclei, the recoil energy becomes much smaller.
For deuteron or triton, an adequate amount of energy transfer can be expected. Some corrections, however, are practically needed to the above discussion due to possible nuclear reactions such as (n, n'), (n, p), (n, 2n), etc. and due to the fact that the collision angles are never fixed and then the recoil energies show a wide spectrum. Thus the quantitative discussion requires computational simulations. However, it could qualitatively be demonstrared that the fast neutron bombardment onto an occluding block yields the selective energization of only light ions, D^+s or T^+s, while the lattice structure may remain unchanged or slightly damaged; whereas damage healing at high temperature takes place. Energized (or recoiled) Ds can easily attain energy high enough to fuse together with other Ds or Ts. As a typical fact, it is well known that the operation of heavy-

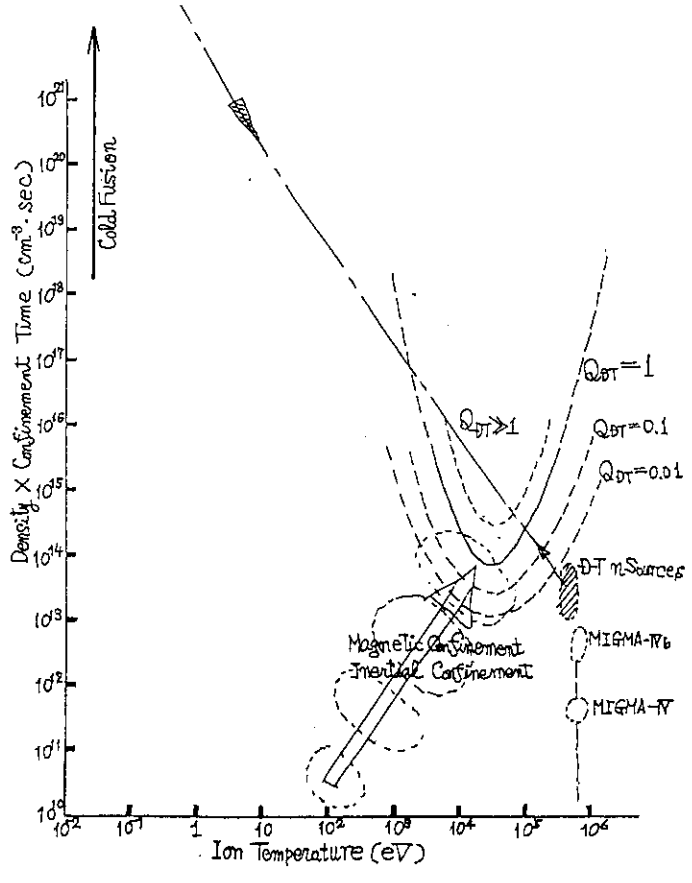

Fig. 1 Expanded Lawson Diagram

water reactors produces resultantly tritiums in moderating and/or cooling heavy water, which can be explained as due to D-D reactions; the first D is recoiled by unmoderated fission neutrons and then energized high enough to fuse with another D in D_2O. This reaction has two branches almost in equal probability as presented below;

$^2D + ^2D \rightarrow$ $^3T(1.01) + p(3.03)$ [4.04], …… (1)
$^3He(0.82) + n(2.45)$ [3.27], …… (2)

where the numbers in round and square parentheses are the energy in a unit of MeV of each reactioned particle and of totally released one, respectively. In the second branch, helium-3(^3He) is produced as much as tritium in amount. The detection of ^3He, however, should be hindered by a huge volume of natural helium(containing 0.00014% of ^3He) gas filled up atop of the heavy water. Instead, ^3Ts is radioactive, emitting β-rays of 18.6 keV, thus being easily detectable. Another source of tritium production may be conceived as in the neutron-capture by deuterons. Howevre, the neutron-capture (absorption) cross-section of deuteron is so small that heavy water is preferred to light water as moderator in a sacrifice of smaller slowing-down power, even if this can not completely be ruled out. In addition, the tritium production may be rather troublesome for the operation of heavy-water reactors; the less in amount, the more favorable.

The energy gain Q of any accelerator-based D-T(D) reaction is less than 10^{-2}, even though such the reactions are genuine for the first(and second) candidate of fusion power application and widely used for fast neutron sources. The D-T reaction is expressed as below together with a hopeful aneutronic D-^3He reaction, if ^3He were supplied enough,

$^2D + ^3T \rightarrow ^4He(3.52) + n(14.06)$ [17.58], …… (3)
$^2D + ^3He \rightarrow ^4He(3.67) + p(14.67)$ [18.34]. …… (4)

The terminology, energy gain Q, here has a few synonymous ones: fusion energy(or power) multiplication factor, Q-value, or pellet gain(limited to ICFs), which is defined as $Q = E_{out}/E_{in}$(or $= P_{out}/P_{in}$), where P_{out} is the nuclear output power while P_{in} is the input power to driving the nuclear reactions. When Q=1, the situation is called "Break Even". In MCFs, the self-ignition condition is defined as that the energetic alpha-particles(of 3.5 MeV as seen in (3)) can serve enough for the plasma heating by themselves; Q-value looks virtually infinite. This α-particle heating should be effective also in ICFs. As seen in (3), 80% of the nuclear fusion energy is carried out by fast neutrons, so that both MCFs and ICFs have to provide a blanket, in which the neutron energy is converted to thermal energy with optionally fortunate tritium production and gain amplification through the reaction, $n + ^6Li \rightarrow ^3T + ^4He$. The break-even condition, as well known as Lawson's, for D-T fuel gas plasma, at T=10 keV, the product $n \cdot \tau$ should be above $10^{14} sec \cdot cm^{-3}$.

Typical neutron sources such as RTNS(Rotating Target Neutron Source-I(II), LLNL), INS(Intense Neutron Source, ANL, proposal), OKTAVIAN(Osaka Univ.), and FNS(Fusion Neutron Source, JAERI) use D-T reaction, because their primary mission is for D-T fusion material testing and nuclear data measurement. This D-T reaction is much easier and then preferable at the first step for fusion power application, because its reaction cross section shows at maximum 5 barns at 107 keV releasing totally 17.58 MeV, while D-D's is less promising. If only the D-T reaction can take place without any electronic or non-nuclear processes, which is, of cource, absolutely improbable, then the Q-value yields 164, being calculated plainly from the ratio of 17.58MeV/107keV. When colliding particles can be realized, the Q-value will roughly be doubled. In reality, the obtained Q-Values lie under the value of 10^{-2}; the nuclear reaction rate is less than 10^{-4}; the accelerated D^+ particles of more than 10,000 can only generate one neutron dependent on the target condition; the above exampled sources show the similar rate. Charged particles such as D^+s can not penetrate deep into material, so that the neutron target is usually thin, where only alpha-particles heat the target; however, sometimes this causes a problem of the target cooling. Almost all neutrons escape from the target; this is the true purpose of neutron generation. Here let us assume that the target is made enough thick and wide, and occluding D ions or D-T mixture: something like a large block or core assembly, the size of which covers the mean-free path λ of fast neutron by several times. Then the neutrons recoil Ds or Ts that can react with neighbouring ones; such the reaction generates again neutron inside the target, acting as the primary one. Thus the regenerative effect can take place. Taking β as the probabilty of how many neutrons the primary ones can next produce in solid, the regenerative(or amplification) factor α will follow in a simplified manner as;

$$\alpha = 1 + \beta + \beta^2 + \beta^3 + \cdots = 1/(1 - \beta) > 1.$$

For the estimation of α or β, the following discussion would be helpful;In the case of the neutron sources, the acceleration voltage of D^+s is experimentally adjusted as 400 to 600 keV for giving a maximum yield as a whole, while the cross-section maximum appears at 107 keV. The reason seems due to the energy losses of the incident D^+s through electronic interactions during penetration near at the surface of the target; the stopping power of materials becomes important. On the other hand, one 14-MeV neutron, for example, can most optimistically produce 100 particles of 140 keV inside the target without the surface effect;this implies that the efficiecy increases nearly by hundred. This approach can be regarded as to move the position of D-T neutron source toward the area of $Q_{D-T} \gg 1$ in the direction to the CF's in Fig. 1.

The neutron yield n is usually linear to the beam power P_{in} of D^+s; $n \propto P_{in}$ or $n = \eta \cdot P_{in}$, where η is the D-to-n conversion efficiency. The output power P_{out} due to the nuclear reaction is also proportional to n; $P_{out} \propto n$ or $P_{out} = \varepsilon \cdot n$, where the coefficient ε depends on the incident neutron energy, D,T-concentration, and the protonic number, Z, of the target material and includes the previous α. Here the Q can be expressed by ε and η; howevre it seems far deficient. Thus the key issue at this point is how to increase the Q-value above unity, break-even or more, overcoming the linear relationship between the input and output. The plasma fusion suggests that the output power density P_{FS} can be expressed in the D-T case as, $P_{FS} = n_D n_T \langle \sigma v \rangle E_{DT}$, where n_D and n_T are, respectively, the density of Ds and Ts, $\langle \sigma v \rangle$ is the fusion reaction rate, and E_{DT} is the nuclear energy released thereby. For the same kind particle, the above equation is to contain a part of square proportionality; this should be the basis of plasma-fusion power application, guaranteeing the Q-increase.

In order that the reaction rate of the present case could include a term proportional to the square number of incident neutrons, the assembly geometry should be invented together with both the spatial and temporal control of the incident neutrons, so as to generating many transient micro-plasmas, the individual particles of which have kinetic energy high enough to fuse together. The word, transient micro-plasma, comes from an empirical figure of energetic charged particles' collision with occluded ions; fast neutrons recoil charged particles of similar mass; the situation may be the same except that neutrons can travel long distance(mean free path λ), while charged ones interact with others very closely; making a so-called shower found in high-energy particle experiments or a unidirectional star or a jet. When two showers in reverse direction take place simultaneously at the same spatial position, the resultant one can be regarded as a micro-plasma, whose life-time is very short compared with an ordinary Tokamaks' or Helical devices' plasma, but longer than ICFs'. Thus the output power P_{out} can include a term proportional to square number of n, where the Q can be increased in principle; $P_{out} = \varepsilon_1 \cdot n + \varepsilon_2 \cdot n^2$, where the previous ε is suffixed as ε_1, and ε_2 depends on both the number and the density of micro-plasmas; They further depend on the configuration(size and shape of the core, the number and position of the neutron injectors) and the peak neutron intensity(in pulse-operation inevitably).

Details of the LCF reactor physics require dynamics of the atomic data as well as nuclear data; specifically the microscopic stopping power, including channeling effect, of energetic light ions inside the lattice of such materials, i.e., the interaction of ions with matter in solid and the problems of (neutron)radiation damage.

A proposed system consists of a reactor core of D- or D,T-occluding metal block assembly with several pulsed fast neutron injectors symmetrically equipped similar to the configuration of direct ICFs' drivers. Here six units of the neutron injector are equipped, as the core being simply cubic, perpendicular to each facet. The core is not necessarily a one block of metal, but a pile of laminated sheet of the metal. The generated heat is transferred by liquid metal, e.g., lead eutectic, flowing through the cooling pipes. The core is encased by a pressure vessel, with which an inlet of fuel D- or D-T mixed gas and an outlet of burnt alpha are connected.

Author would like to thank Mr. T. Hiruma, the President of Hamamatsu Photonics K.K. and Dr. Y. Suzuki, the Director General of the Central Research Laboratory, to support this work. Acknowledgement also goes to the members of the Researcg Group No. 1 with Prof. M. Koshiba, Tokai Univ., for motivation and discussion.

1) J. G. Linhart, "Plasma Physics", p. 202-205, North-Holland, Amsterdom, 1960
2) B. C. Maglich, Nucl. Instr. and Method in Phys. Res., A271(1988)13-36
3) M. Fleishmann and S. Pons, J. Electroanal. Chem., 261(1989)301